Noncommutative Biology: Sequential Regulation of Complex Networks and Connected Matter

Thesis by
William Letsou

In Partial Fulfillment of the Requirements for the
degree of
Doctor of Philosophy in Chemistry

CALIFORNIA INSTITUTE OF TECHNOLOGY
Pasadena, California

2018
Defended April 24, 2018

William Letsou
ORCID: 0000-0002-4969-2330

ACKNOWLEDGEMENTS

I could not have completed my degree without the loving support of my parents, Peter and Felicity, who were there for all my trials and triumphs, despite living 2000 miles away. My younger siblings Tina and Ted, who have followed me on the path of continual education, lent critical but encouraging ears to all my funny ideas, and have consistently reminded me that I am doing what I love. I hope you find the same inspiration on your own journeys. I would like to thank members of the Cai lab, past and present, for being great friends and supportive colleagues. I am especially grateful to Timur for looking out for me when I first started graduate school. Your guidance has continued to influence my growth as a scientist. Eric was a great friend who tolerated all my bad habits and patiently listened to all my concerns. I'll miss our discussions over frisbee golf. Seoyeon, with her quiet determinism, taught me the valuable lesson that sometimes all you need is a four-leaf clover. Proximity surely makes the heart grow fonder, and I want to especially thank two of my long-time office mates: Yandong, who joined me in the depths of the Noyes subbasement; and Mike, who provided some much-needed older-brotherly advice.

I have had a number of great academic advisers during my time at Caltech. Long cannot know how much I appreciate the freedom and trust he gave me to work on a project so unorthodox in traditional biology. His guidance and support helped me see connections others would have surely missed. Jim Heath and Leo Goentoro are two of the best teachers I have encountered; they showed me the great joy there is in working with students. My committee, consisting of Daniel Weitekamp, Judy Campbell, and Richard Murray, were very supportive and never failed to point me in the right direction when I fell short.

I would not have gotten through graduate school were it not for a number of indispensable individuals who improved my life in countless small ways. Maria Oh was an invaluable source of support and positivity at a moment when things were most difficult. I want to thank the lifeguards and other staff at the Caltech Athletic Center, especially Rowena, Claudia, Amy, Kirsten, and Leslie, for keeping me safe and for being so friendly and cheerful. The ever-reliable Memo, Joe, Armando, and Gregory made trips to the CCE stockroom one of the more enjoyable escapes from work. Margarita Davis, Alison Ross, Liz Ayala, and Agnes Tong provided tireless administrative support, without which I would never have even begun my journey at Caltech. Finally, thank you to Engracia: you have taught me never to be afraid of getting my hands dirty.

ABSTRACT

During animal development from zygote to adult, a limited set of regulatory molecules are autonomously deployed in the service of tissue-specific gene expression (reviewed in chapter 1). Inherent in the process is the tension that single cells sample heterogeneous expression states while robustly maintaining a collective final outcome. This thesis addresses theoretical issues that help resolve the paradox that one cell simultaneously contains the fate information of many.

Previous models of development have likened cell fate to minima on a smooth potential energy surface. Such static pictures can be misleading because they suggest the egg knows the path it will take to the adult before it divides even once. Recognition that the potential analogy is an oversimplification has led others to propose that the surface is actually nonsmooth. Chapter 2 reviews the theoretical basis for smooth potentials and resolves these problems by appealing to the tangent space of gene expression. It is then shown that if the potential difference is sufficient to characterize the difference between egg and adult, then the tangent space controls on gene expression are one-dimensional. Furthermore, a shortcoming of models ignoring the connectivity and common origin of dividing cells is that they erect artificial barriers between alternative fates. A fundamentally different picture is sketched wherein the difference between egg and adult is schematized as the shape of the locus of equipotential fates accessible at the same point in time. The conjugacy of space and time is invoked to explain how the requirement that each fate be on a line of equipotential is the same as requiring that each alternative fate move the same distance down the surface at each step. The developmental trajectory is deterministic but not known in advance because it needs to be ascertained at each step which way cells "turn" in order to maintain their equipotential relationship. Chapters 3 and 4 refine this sequential model of collective development with specific examples.

A simple solution to the problem of cell-type specific gene expression is combinatorial binding of transcription factors at promoters. It is shown in chapter 3 that such models result in substantial information bottlenecks, because all cell fate information is concentrated at the start. We explore a novel, noncommutative model of gene regulation—known as sequential logic—that spreads the information out over time. It is shown using time sequences of noncommutative controllers that targets which otherwise would have been activated together can be regulated independently. We derive scaling laws for two noncommutative models of regulation, motivated by phosphorylation/neural networks and chromosome folding, respec-

tively, and show that they scale super-exponentially in the number of regulators. It is also shown that specificity in control is robust to loss of a regulator. Consequently, sequential logic overcomes the information bottleneck in complex problems and enables novel solutions through roundabout strategies. The theoretical results are connected to real biological networks demonstrating specificity in the context of promiscuity.

Noncommutative sequential logic has improved storage capacity, but it does not specify who or what supplies the sequences of input that determine cell fate. Chapter 4 offers a solution by way of the seemingly unrelated problem of looping in twisted strings. Cells and strings obey a set of common space-time constraints, ultimately due to the conservation of energy. It is argued that the most parsimonious allocation of energy from the straight to strained string is the one in which each segment sees the same share of the total. Planar looping is shown to be a consequence of the parsimony principle and the Euler-Poincaré equations for rotational motion in the presence an applied torque. We then solve the problem for the looping of a twisted string; with two strains, the Euler-Poincaré equations predict a different answer than the classical Frenet-Serret equations. Using the results of chapter 2, it is concluded that the Frenet-Serret curvatures assigned ahead of time are not guaranteed to generate space curves that conserve energy: the predicted string has localized strains the Euler-Poincaré solution lacks. Rotational dynamics of strings are connected to developing organisms by postulating conserved RNA polymerase as an analog of angular momentum, and transcriptional activity as energy. Alternative fates along a one-dimensional "string" of dividing cells are possible by finding the RNAP distribution that conserves transcriptional activity along a curve of constant developmental potential. Consequently, each alternative fate samples a different sequence of changes to the distribution as it follows a local gradient downhill from high to low developmental potential over time.

In conclusion, regulation in the tangent space of gene expression resolves the paradox that development has a unique solution specified in the DNA of the egg which cannot be determined with certainty until completion of the adult. Noncommutative sequential logic generates complexity that cannot be realized at the start, while interdependent cells (and strings) require time to ensure that each fate is at the same potential difference from a common ancestor. This fundamental reimagining of the Waddington framework can be tested using new multiplexed mRNA imaging technologies that preserve the spatial context of cells in developing tissue.

PUBLISHED CONTENT AND CONTRIBUTIONS

1. Letsou W, Cai L. Noncommutative Biology: Sequential Regulation of Complex Networks. PLoS Comput Biol. 2016; 12: e1005089. DOI: 10.1371/journal.pcbi.1005089.
   W.L. participated in the conception of the project, derived formulas and proofs, wrote computer code, prepared figures, and participated in the writing of the manuscript.

CONTENTS

LIST OF FIGURES

NOMENCLATURE

Ad_g Adjoint action of a Lie group on its Lie algebra by $L_g \circ R_{g^{-1}} \circ \xi$.

ad_g adjoint action of a Lie algebra on itself by $T_e\left(L_g \circ R_{g^{-1}}\right) \circ \xi = T_e L_g R_{g^{-1}} \circ \xi + L_g T_e R_{g^{-1}} \circ \xi \to \eta \circ \xi - \xi \circ \eta$ as $g \to e$ at the identity of the group.

$\mathrm{adj}\,\mathbf{A}$ Adjugte or classical matrix adjoint defined by the transpose of the cofactor matrix of signed determinants of the matrices formed by deleting the i^{th} row and j^{th} column of $\mathbf{A}$; it satisfies $\mathbf{A}^{-1} = (\det \mathbf{M})^{-1} \mathrm{adj}\,\mathbf{A}$ for $\mathbf{A}$ non-singular.

$\mathrm{am}\{x \mid p\}$ Elliptic amplitude, defined as the circular angle required to subtend the arc length x on an ellipse with eccentricity p.

$\boldsymbol{\chi}_i, \boldsymbol{\Gamma}_i$ Body frame representation of the i^{th} body frame and fixed axis unit vectors.

$\boldsymbol{\kappa}, \hat{\boldsymbol{\kappa}}$ Spatial angular velocity of RNAP exchange as a vector or skew-symmetric matrix of with units dist.$^{-1}$

$\boldsymbol{\omega}, \boldsymbol{\Omega}$ Angular velocity as a vector or skew-symmetric matrix with units dist.$^{-1}$ or time^{-1}.

$\boldsymbol{\phi}, \boldsymbol{\psi}$ Orthogonal vector fields (f, g) and $(-g, f)$ of the gradient system corresponding to flow along curves of constant potential and constant stress.

$\boldsymbol{\Theta}(s')$, $\boldsymbol{\Theta}^0(s')$ Vector of current and initial cumulative distribution functions $\Theta_{x_i}(s')$ of RNAP allocation.

$\boldsymbol{\Xi}$ Applied torque with units force.

κ, τ Curvature and torsion of a space curve with units dist.$^{-1}$

κ_i^j Angular rate of transfer of RNAP from locus i to j, with units of dist.$^{-1}$

λ Loading parameter of the elastica $\sqrt{\frac{T}{E\mathbb{I}}}$ with units dist.$^{-1}$

λ, μ Spatial and temporal delays expressing the space time constraints.

$[\cdot, \cdot]$ The matrix commutator $[\mathbf{A}, \mathbf{B}] = \mathbf{AB} - \mathbf{BA}$ or the Lie bracket $[\mathbf{X}, \mathbf{Y}] = a^i \frac{\partial b^j}{\partial x^i} \frac{\partial}{\partial x^j} - b^j \frac{\partial a^i}{\partial x^j} \frac{\partial}{\partial x^i}$ of vector fields.

$\langle \cdot, \cdot \rangle$ The vector inner product $\langle \xi, \mu \rangle = \xi^T \cdot \mu = \mu^T \cdot \xi$ assigning a real number to two n-dimensional vectors.

$\mathbb{I}_{ij}$,$\mathbb{I}^{ij}$ Cost function tensors for the amount of RNAP (number of transcripts) at locus i freed from one transcript (worth one RNAP) at locus j, with units RNAP $\times$ trans.$^{-1}$ (RNAP^{-1} $\times$ trans.).

$\mathbb{J}_i^j$ Worth of transcripts (RNAP) at j in terms of the number of transcripts (amount of RNAP) produced by a single unit of RNAP (freed from a single transcript) at i.

$\mathbf{A}, \mathbf{B}$ Vector fields corresponding to torsion and curvature.

$\mathbf{A}_{i_1,i_2,\ldots,i_k}$ State of a target regulated by i_1 from pool 1, etc.

$\mathbf{d}_i$ i^{th} director basis vector.

$\mathbf{E}_i$ i^{th} basis vector in an orthonormal frame attached to the body's center of mass.

$\mathbf{e}_i$ i^{th} fixed basis vector.

$\mathbf{I}, \mathbf{J}$ The identity matrix on $\mathbb{R}^n$ and the symplectic matrix $\begin{pmatrix} 0 & \mathbf{I} \\ -\mathbf{I} & 0 \end{pmatrix}$ on $\mathbb{R}^{2n}$.

$\mathbf{n}, \mathbf{b}, \mathbf{t}$ Principal normal, binormal, and tangent vectors.

$\mathbf{r}, \mathbf{R}$ Coordinates of space curve in fixed and body-centered representations.

$\mathbf{u} \otimes \mathbf{v}$ Dyadic or tensor product defined by $(\mathbf{u} \otimes \mathbf{v})\,\mathbf{w} = (\mathbf{v} \cdot \mathbf{w})\,\mathbf{u} = (\mathbf{u} \otimes \mathbf{w})\,\mathbf{v}$.

$\mathbf{x}, \mathbf{x}_g$ Vector of states of the targets controlled by all regulators and the subset g.

$\mathbf{X}, \mathbf{X}_q$ A (contravariant) vector field with coordinates $a^i \frac{\partial}{\partial x^i}$ or $(a^1, \ldots, a^n)$ in the tangent space at point $q \in \mathbb{R}^n$.

$\mathcal{E}(\phi \mid p)$ Elliptic integral of the second kind defined by $\mathcal{E}(\phi \mid p) = \int_0^\phi \sqrt{1 - p^2 \sin^2 t}\, dt$ for an ellipse with eccentricity p subtended by the circular angle ϕ; said to be *complete* when $\phi = \frac{\pi}{2}$.

$\mathcal{K}(\phi \mid p)$ Elliptic integral of the first kind defined by $\mathcal{K}(\phi \mid p) = \int_0^\phi \frac{dt}{\sqrt{1-p^2 \sin^2 t}}$, giving the elliptic arc length subtended by a circular angle ϕ on an ellipse with eccentricity p; said to be *complete* when $\phi = \frac{\pi}{2}$.

$\mathcal{L}_{\mathbf{X}}$ Lie derivative with a vector field $\mathbf{X}$.

$\mathcal{R}_\phi$ Two-dimensional counterclockwise rotation through an angle ϕ.

μ Element of the dual Lie algebra $\mathfrak{g}^*$.

$\Omega_{\mathbf{X}}, \Xi^{\mathbf{X}}$ n-dimensional vector and covector of the components of a $2n$-dimensional symplectic vector field.

ϕ Euler angle between $\mathbf{n}$ axis and $\mathbf{d}_1$; gene regulatory potential $fx + gy = xy$; elliptic amplitude $\operatorname{am}\{x \mid p\}$.

$\Phi^t_{\mathbf{X}}$ Flow along vector field $\mathbf{X}$ for time t, defined as a path $\sigma(t)$ in the group whose Lie algebra is realized by $\mathbf{X}$.

ψ Euler angle between fixed x axis and $\mathbf{n}$; conjugate gene regulatory potential $-gx + fy = \frac{1}{2}(x^2 - y^2)$.

$\sharp, \flat$ Mapping from vectors to forms and forms to vectors by the association $v^1\mathbf{e}_1 + \cdots v^n\mathbf{e}_n \overset{\flat}{\underset{\sharp}{\leftrightarrow}} v^1 dx^1 + \cdots v^n dx^n$; also denotes a linear map $\Omega^\flat$ ($\Omega^\sharp$) acting from the left (right) sending column vectors (row covectors) to row covectors (column vectors) via the symplectic matrix $\mathbf{J}^T$ ($\mathbf{J}$).

$\sigma(t, s)$ Curve in the Lie group parametrized by time and space.

$\mathrm{sn}(x \mid p), \mathrm{cn}(x \mid p)$ Jacobi elliptic functions defined by $\mathrm{sn}(x \mid p) = \sin(\mathrm{am}\{x \mid p\})$ and $\mathrm{cn}(x \mid p) = \cos(\mathrm{am}\{x \mid p\})$.

$\star$ Hodge dual to the k-form $\omega = dx^{i_1} \wedge \cdots \wedge dx^{i_k}$ defined such that $\omega \wedge \star\omega = dx^1 \wedge \cdots \wedge dx^n$, the volume element in $\mathbb{R}^n$ for $k \leq n$.

τ_0 Initial axial strain $\frac{2\pi n}{L}$ of n turns.

θ Euler angle between fixed z axis and $\mathbf{d}_3 = \mathbf{t}$.

Θ, Ω Canonical one- and two-forms with basis elements dq^i and $dp_i \wedge dq^i$.

$\Theta_{x_i}(s')$ Cumulative distribution functions for the fraction seen at spatial position s' of the total amount of RNAP that locus i will see.

$\widehat{\cdot}$ The hat map $\widehat{\ }: \mathbb{R}^3 \to \mathbb{R}^{3\times 3}$ defined such that $\boldsymbol{\omega} \times \mathbf{v} = \widehat{\boldsymbol{\omega}}\mathbf{v}$ for all $\mathbf{v} \in \mathbb{R}^3$.

ξ, η Elements of a Lie algebra $\mathfrak{g}$.

B_m^{-n} Poly-Bernoulli number with indices n, m.

$dx^{i_1} \otimes \cdots \otimes dx^{i_n}(\mathbf{v}_1, \ldots \mathbf{v}_n)$ Covariant tensor product of a covectors (rows) on vectors (columns) defined by $dx^{i_1}(\mathbf{v}_1) \cdots dx^{i_n}(\mathbf{v}_n)$.

$dx^{i_1} \wedge \cdots \wedge dx^{i_n}$ Wedge product of n covectors defined by $\sum_\sigma dx^{i_1} \otimes \cdots \otimes dx^{i_n} \circ \sigma$, with the sum taken over for all permutations σ in the symmetric group; volume element in $\mathbb{R}^n$.

$E\mathbb{I}, G\mathbb{J}, G\mathbb{I}_l$ Bending, torsional, and localized spiral rigidities with units force×dist.^{2}

f, g Gene regulatory functions $-\dot{x}$ and $-\dot{y}$ of the gradient potential system.

$G, \mathfrak{g}, \mathfrak{g}^\star$ Lie group, its Lie algebra, and dual Lie algebra.

I Information at time t and position s.

K_i, P_i Activating and deactivating regulators in a switching network.

L, ℓ Total length in linear and logarithmic coordinates.

L_g, R_g Left and right translation by an element $g \in G$ of a Lie group.

l_n, l_m The number of regulators to which each target connects.

N Number of unique targets in a switching network.

n, m The number of K's and P's in the network.

p Eccentricity $p = \sqrt{1 - \frac{b^2}{a^2}}$ of an ellipse with semimajor and semiminor axes a and b, also defined as the ratio of the focal length to the length of the semimajor axis; related to the initial angular deviation $\theta(0) = \alpha$ of the planar elastica by $p = \sin\left(\frac{\alpha}{2}\right)$.

$p(s), g(s)$ Angular momentum matrix $\widehat{\mathbb{I}\boldsymbol{\omega}}$ (with units force × dist.) and rotation matrix.

s' Log-transformed distance coordinate $s' = \log s$.

$s, \mathbf{r}(s)$ Arc length and space curve parametrized by arc length.

$SE(n), \mathfrak{se}(n)$ Special euclidean group $SO(n) \times \mathbb{R}^n$ of rigid n-dimensional rotations plus translations, and its Lie algebra.

$SO(n), \mathfrak{so}(n)$ Special orthogonal group of rigid n-dimensional rotations and its Lie algebra.

T Number of steps in a sequence; activation threshold in the ratchet network; string tension; tangent space of a manifold; (when superscripted) matrix transpose.

u, n_i, l_{ni} The number of pools, the number of regulators in pool i, and the connectivity to regulators in pool i.

X_i, Z^i Spatial rates of RNAP allocation and transcription at locus i.

x_i, z^i RNAP and transcripts at locus i.

Chapter 1

INTRODUCTION: AUTONOMOUS DECISION-MAKING IN THE EMBRYO AND BEYOND

1.1. Biological mechanisms of development

Multicellular life starts from a single fertilized egg cell called the zygote. After many rounds of division, the zygote is transformed into an adult composed of $\mathcal{O}(10^2)$ cell types, each expressing different subsets of $\mathcal{O}(10^4)$ genes, under the control of $\mathcal{O}(10^3)$ transcription factors [176, 275, 282]. The task of assigning each cell its proper expression state is not a trivial one. It is made more complex by the fact that early development has only $\mathcal{O}(10^1)$ intercellular signaling pathways to channel cell fate information [90]. Hinegardner and Engleberg have argued that the biological complexity of the adult is not much greater than that of the fertilized egg [117], a position sustained by the general conservation of body plans across metazoans [90, 91]. But Valentine and coworkers have countered that complexity should include the sequential process of ordering and arranging expression states among cells [275]. While the adult and zygote refer to the same list of parts in the DNA, it is unknown where the instructions for putting them together reside. Does the egg "know"—in the sense that, is there sufficient information at the egg stage to know—what it will look like as an adult? Even if the egg were so prescient, it would appear that there is an information bottleneck between the instructions and their execution: development does not occur all at once, but in a robust series of steps, as has been repeatedly observed in nature [80, 227] and in *in vitro* culture [21, 67, 276]. Alternatively, the instructions could change over time in such a way that the egg doesn't know where it's going until it gets there. Which (if either) of each these two strategies do cells in the embryo use to learn what fate they should adopt in the adult? And how do so many fates emerge from such a limited number of signals? The aim of this thesis is to provide theoretical insight into these questions.

It has long been known from fluorescent tracer and microscopy studies that model organisms have a predictable [262] yet flexible [143, 151, 180] fate map from the earliest embryonic stages. Pioneering experiments have revealed numerous mechanisms that descendent cells use to realize their fates. Maternal transcripts in the oocyte guide gene expression for the first several cell divisions, after which time the zygote takes over production of the essential factors for transcription,

metabolism, and DNA replication [186, 304]. By the 16-cell stage in mouse, progenitors have segregated into layers known as that trophectoderm and the inner cell mass. The latter subsequently differentiates into the primitive ectoderm and the epiblast, which later becomes endoderm, mesoderm, and ectoderm (reviewed in [306]). Differentiation into the three primary germ layers is controlled by alleviating repression mediated by the so-called pluripotency factors Oct4, Sox2/3, and Nanog in the stem cell stage, which are then repurposed for repressing incompatible fates [271, 293]. For example, *Oct4*-expressing embryonic stem cells (ESCs) respond to a BMP signal for the transcription of genes such as *Brachyury* (*T*), associated with the mesoderm fate, whereas *Sox2* knockdown relieves repression of *T* [293]. Additional regulation occurs at the chromatin level, allowing poised ESCs to choose between alternative fates. For example, the neural *Olig1* gene in ESCs is marked bivalently with repressive (H3K27me3) and activating (H3K4me3) modifications on lysine residues of the histone proteins, but monovalently in fibroblasts and neural progenitors, respectively [177].

Once the basic radial symmetry of the germ layers is established, the anterior-posterior, left-right, and dorso-ventral body axes, which underlie metazoan body plans, must be specified. Initial asymmetries in shape and gene expression at the early stages are the basis of polarity in subsequent ones, as has been seen in organisms as diverse as flies [152], worms [185, 188, 191], frogs [264, 285], fish [17, 30, 31, 202], chicken [11, 205], mice [197, 276, 210, 266], and humans [294]. A unifying mechanism is that directional transport of vesicles and proteins regionalizes gene expression [69, 188, 202, 266]. The role of hydrodynamics during symmetry-breaking was elegantly shown by culturing mouse embryos in a specialized chamber and subjecting them to fluid flow both parallel and antiparallel to the intrinsic direction of ciliary rotation in the node: the latter condition reversed the pattern of a normally asymmetrically-expressed gene [197]. Cortical flow and cytoskeletal reorganization following sperm entry in *C. elegans* embryos lead to asymmetric localization of the PAR proteins at the one-cell stage [185, 188]. Once localized, posterior PAR2 excludes other anterior PARs by phosphorylating PAR1, typifying a general mechanism whereby upstream genes restrict transcripts that otherwise would be found ubiquitously in the embryo [30, 185, 191, 285, 294]. Homologs of the conserved TGF-β family members Lefty and Nodal act in a similar manner though a complex feedback loop during left-right patterning of the fish heart: Wnt signaling activates *Lefty* [17], which is promoted by, and subsequently inhibits, *Nodal* in an asymmetrical manner [30, 285]; *Nodal* is responsible for the

localization of the transcription factor Brachyury to the mesoderm [294]; loss of *Nodal* results in bilateral *Lefty* expression [31].

Once started down a developmental path, cells maintain their unique identities through contact inhibition [114, 251] and asymmetric cell division [118, 216]. The balance between progenitors and differentiated cells is regulated during neural fate specification, for example, when cells expressing the Delta ligand prevent cells with Notch receptors from differentiating as neurons [114]. It was also shown in the ascidian *Ciona* that ephrin signaling in the 8-cell stage induced polarization of notochord/neural mother cells and led to suppression of notochord fate in half of the embryo [216]. Whereas in these examples interactions serve to prevent neighboring and daughter cells from adopting the same fate, cell-cell contact also plays a role in regulating the arrival time of signals. It was shown that during *C. elegans* vulva induction, secondary progenitor cells differentiate normally even if they are blocked from receiving an upstream signal: they receive a downstream signal instead from primary cells [251]. In many cases, diffusible molecules provide the inductive signal, while cell context determines the interpretation. For example, the ubiquitous signaling molecule Wnt, which has multiple roles in axis formation (reviewed in [90, 116]), is kept under tight regulation to avoid misexpression. In a study of Wnt signaling in the intestine, several hundred target genes were found to be specifically and significantly co-bound by an intestine-restricted transcription factor and a Wnt effector [280]. But in another study of anterior development in the mouse, a homeobox transcription factor drove expression of Wnt antagonists specifically in the anterior mesendoderm, forestalling head defects [81]. Although in these cases cofactors mediate Wnt specificity, in other tissues cofactors are dispensable. For example, the Wnt transducer β-catenin requires the *Xenopus* transcription factor XTcf3 for target gene activation in dorsal, but not ventral, tissue in early embryogenesis [110]. XTcf3 was also shown to regulate β-catenin-mediated transcription during mesoderm induction, but not to be required for later patterning [160]. Although it is not always clear what causes the change in cofactor dependency over time, it is possible that the effects of an early deficiency are merely delayed to a later checkpoint. For instance, it is not necessary for mouse β-catenin to bind Tcf1 protein in order for cells progress through the DN1 and DN2 stages of thymogenesis, although complete absence of Tcf1 later results in apoptosis by the DN3 stage [299]. Of course, cell death need not indicate a patterning error: interdigital cartilage [88], plant embryos [36], and motoneurons [204] all undergo programmed apoptosis during development as a means of shape remodeling.

Knock-out studies like those cited above can reveal the causal role of each gene in a developmental regulatory network of interrelated components. An alternative view of development, informed by conventional and single-cell sequencing technologies, is that stochasticity and heterogeneous gene expression in the early stages lead to different fates in the adult [54, 99, 306]. In support of this idea, heterogeneous expression of pluripotency regulators [53, 135, 252] and asymmetric partitioning of maternal transcripts [247] have been shown to influence which fates embryonic cells are likely to adopt. For example, there is a small but reproducible population of pluripotent cells with transiently low *Nanog* and high *Gata6* expression biased toward endoderm fate [135, 252]. Populations of cells appear to control their overall level of heterogeneity: sorted cells eventually recapitulate the original distribution of expression states by stochastic switches [53, 135]. Heterogeneity is not restricted to cell culture assays, but also occurs in intact blastomeres. It has been shown by sequencing that transcriptional noise increases expression variation in individual genes between single blastomeres over time [247]. Increasing variation is in line with Markovian models of evolution in which multicellular lineages (i.e., cells) stochastically choose to add or remove a cell type (change the expression level of a gene) independently of their history [275]. Nevertheless, heterogeneity and stochasticity should be regarded in light of the observation that development is extraordinarily robust, not only in the final outcome it achieves, but also in the timing and coordination of steps along the way. Genetic circuits have been found that modulate embryos' sensitivity to inductive signals like retinoic acid [44] and BMP [208], with the result that animals have reduced variation in organ size [208]. Other testaments to reproducibility include the following: less than 10% variation of *bicoid* copy number in individual fly embryos [213], characteristic morphological transitions that occur at predictable times in mouse epiblast culture [21], and intransigence of chick forebrain development to hypoblast transplantation experiments [80]. The tension between robustness and stochasticity has been partially resolved by highly multiplexed *in situ* single-cell mRNA profiling heterogeneity in the mouse hippocampus [244] and chicken neural tube [157]. With cells' spatial context preserved, these studies make it possible to resolve broader organization underlying single-cell heterogeneity, suggesting that cells' stochastic decisions do not happen in isolation. It is therefore desirable to find a framework that reconciles top-down (deterministic) and bottom-up (stochastic) decision-making processes in development.

1.2. The potential landscape analogy

It is relatively easy to mathematically formulate development when cell fate is characterized by expression of a single gene: changes that increase expression from a referrence level are positive, those that decrease it are negative, and the desired level is a minimum with respect to some regulatory function. It is not so clear what it means to increase or decrease such a function when there are multiple genes, because alternative fates increase the expression of some genes and lower the expression of others. In the hematopoietic lineage, for example, *Gata1* and *PU.1* have alternate extremes of expression during myeloid and erythroid specification, respectively [53]. With increasing numbers of genes to define cell types, there are correspondingly more minima, and more paths between minima. As an example, astrocyte fate can be reached not only from the natural developmental trajectory of neural progenitors, but also from mature neurons by transcriptome transfer of mRNA from a mature astrocyte host [261], showing that recipient cells sense a different stable state after traversing a potential barrier. In multiple dimensions, figuring out which direction is "up" out of the basin of a stable fate is accomplished by the use of a *gene regulatory function*. This function sees attempted changes dx in the genes' expression levels and outputs a tangent vector df of changes permitted by the regulatory logic. There is no universal direction in a multidimensional space that is "up", but if a state is stable, then *no* tangent vectors can point "down". The preceding observation, making no reference to any fixed coordinate system, implies that the tangent vectors span a positive volume of gene expression space. It turns out that the enclosed volume is the determinant of the matrix spanned by the tangent vectors $\frac{\partial f}{\partial x_i}$ (see Appendix 1.5.1). Therefore, stable states are those points where the (linearized) regulatory function has a positive determinant.

The linear theory outlined above is the mathematical basis of the Waddington landscape of cell fate canalization during development [288]. As long as the landscape is constant in time, the gene regulatory function permits pluripotent progenitors to fluctuate within a delimited region of gene expression space without lineage commitment. The cue to differentiate from initially homogeneous starting conditions is often modeled as a bifurcation [26, 125, 155, 224, 245, 290, 291], or as the creation or elimination of a fixed point on a vector field of a multistable circuit [75, 125, 135], both of which change the underlying landscape. The model has had some success, for example, in explaining the progressive restriction of *Drosophila* olfactory receptors: deletion of a transcription factor (Rotund) required by two trichoid sensilla subtypes converts the gene expression profiles of those subtypes into

that of an Rn-independent upstream subtype, suggesting that differentiation lowers a potential barrier [155]. Another study demonstrated that erythropoietin changes the landscape felt by bone marrow progenitors: whereas progenitors are metastable, addition of growth factor eliminates barriers to the alternative erythroid and myeloid fates (via a supercritical pitchfork) [125]. This was an important finding because it (i.) showed that the same initial conditions (growth factor) can lead to different final conditions (myeloid or lymphoid fate) and (ii.) fit within the mathematical theory of gene regulatory logic. It was proven mathematically that when the gene regulatory functions corresponding to two different fate minima intersect at a midpoint a in gene expression space, their determinants (i.e., derivatives) at a are both positive, implying that gene-gene interaction network must have a nonlinear cycle [254]. A cycle in which two genes mutually repressed each other was in fact the basis of the bistability results in [125]. Nonlinearity in the interaction between genes and their regulators can lead to other unexpected effects, such as the context-specific interpretation of a signal. BMP was recently found to repress the *Vg1* gene in the posterior of the chick embryo, but to promote it in the anterior [11]. This effect could be reproduced by mathematical modeling if BMP promoted transcription factors of both genes, and if the transcription factors mutually repressed each other via a nonlinear circuit.

Despite the success and conceptual simplicity of the Waddington landscape, it has its limitations. Bhattacharya and coworkers have emphasized that biological landscapes need not represent a *gradient* potential like gravity [26], which obeys a clear conservation law. In cells, gene 1 can change more or less independently of a functionally unrelated gene 2, but in a gravitational field, the height of a tossed ball necessarily trades off against its upward velocity. A hyperbolic landscape is illustrated in Figure 1.1A to show the implications of a gradient system. The difference $\Delta\phi\left(x,y\right)$ in heights of the surface at two points represents the tendency of the expression levels x,y of two genes to change in the direction between those points. The red and blue lines in the lower plot, which represent the time derivatives $-\frac{\partial x}{\partial t}=f\left(x,y\right)=\frac{\partial\phi}{\partial x}$ and $-\frac{\partial y}{\partial t}=g\left(x,y\right)=\frac{\partial\phi}{\partial y}$ in the x and y directions, are the resultants of forces on the genes, analogous to those of a circulation-free stress field in an elastic material (see [79] ch. 2, 4 and 7, [163] ch. II and XIV, [242] ch. 2, [243] ch. 4). And like an elastic sheet at equilibrium, the continuity equations require that the y-rate-of-change of f balance the x-rate-of-change of g (see section 2.2.1). The two functions "know" about each other in the sense that, at fixed transcriptional activity (see section 4.2.5), the x rate of change is completely

determined by the rate of change of y. As a consequence, the tendency to transit between any two points in space (as measured by the difference in heights on the surface) is path-independent.

As has been pointed by others [182, 295], it is unrealistic to expect regulatory landscapes to be gradient potentials with symmetric interactions between expression states. One alternative non-gradient landscape is the spiral surface of Figure 1.1B, having a discontinuity at the origin. In this picture, the same expression state (x, y) can be associated with high potential or low potential depending on how it is reached. Path-dependence is quantified by the curl $\nabla \times (f, g) = \frac{\partial f}{\partial y} - \frac{\partial g}{\partial x}$ of the velocity field. Some authors have likened such cross product terms to a *curl-flux* force associated with oscillations in gene activity due to the input of external energy [290, 291], while others have interpreted them as manifestations of discontinuous transition states [182]. According to the elastic sheet analogy, it is possible to understand "tearing" of the surface as the decoupling of expression state dynamics that occurs when one gene is hidden from the regulatory influence of another, perhaps by the chromatin. Nevertheless, recent single-cell RNA sequencing data in actively differentiating lineages have painted a picture where (inferred) transitions between cell types are largely smooth [148, 238, 295], even when velocities are measured independently of the assumption of an underlying field [148]. One of the main contributions of this thesis is the idea that a smooth landscape is compatible with path-dependence or *noncommutativity* if controls are taken, via differentiation, to the *tangent space* of gene expression, where rates (both in time over space) are independently controlled. Indeed, recent results on RNA velocity [148] imply that cells select their fate indirectly by modulating intron splicing of new transcripts. Section 2.2.2 in chapter 2 shows how a non-gradient potential arises in gene expression space as the system traverses a certain vector field with nonzero circulation in the tangent space. As a consequence, the dynamics projected to the base space circulate as well, even as the surface itself remains smooth. Different realizations of noncommutativity are the subjects of chapters 3 and 4.

Aside from the theoretical issue of the potential is the more immediate problem that gene expression differences alone do not always account for fate selection. In a recent example, the photo-induced decision of individual plasmodial cells to sporulate did not appear to have an obvious relationship with gene expression: divergent responses occurred even among cells with highly similar transcription profiles [224]. Recent theoretical research has explored the possibility that, in addition to expression levels, factors such as speed [194] and direction [206] through

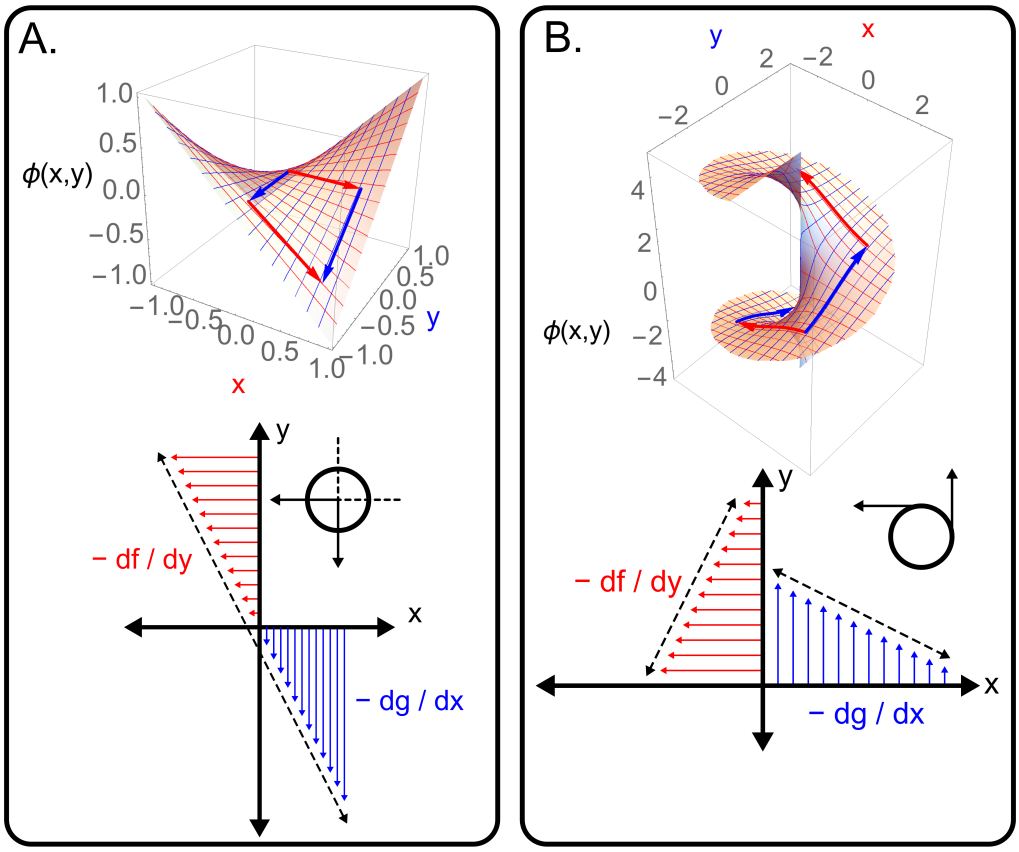

Figure 1.1: Potential landscapes in gene expression. **(A)** A gradient landscape described by the surface $\phi(x,y) = xy = fx + gy$, with f and g the negative rates of change of gene expression in the x and y. Height measures the tendency for gene expression to change. The tangent vectors in the lower plot move the system between different states. The direction of change is determined by the sign of dx or dy, and the magnitude by vector length. The red paths on the surface are mappings of the intervals $x \in [0,c], y = 0$ and $x \in [\phi(0,y)/y, \phi(c,y)/y], y = -c$, and the blue paths $y \in [0,-c], x = 0$ and $y \in [\phi(x,0)/x, \phi(x,-c)/x], x = c$ with with $c = 0.8$. Note that the negative derivatives point in the direction of expression change. The inset illustrates the circulation-free nature of vector field, as all tangent vectors entering a region subsequently leave it. **(B)** A pseudo-potential landscape not described by a gradient having a discontinuity at the origin. Alternate pathways differ because the curl of the vector field (f,g) is nonzero. The two-dimensional surface is parametrized by $(v\sin(u), v\cos(u), u)$ for $v \in [0,3]$ and $u \in \left[-\frac{3\pi}{2}, \frac{3\pi}{2}\right]$. The red paths are parametrized by $(r\tan\theta, r\tan\theta_0, \theta - 2\theta_0)$ for $\theta \in \left[\frac{\pi}{4}, -\frac{\pi}{4}\right], r = 1.5, \theta_0 = \frac{\pi}{4}$ and $(r\tan\theta, r\tan\theta_0, \theta)$ for $\theta \in \left[\frac{-\pi}{4}, \frac{\pi}{4}\right], r = 1.5, \theta_0 = \frac{\pi}{4}$. The blue paths are defined similarly. The inset illustrates the divergence-free nature of the vector field, as all tangent vectors circulate around a region.

gene expression space may play a role in cell fate canalization. In a model of Delta-Notch signaling, for example, physically connected cells could transit from an all-Delta no-Notch state to a hexagonally-patterned some-Delta some-Notch state by

first increasing the production rate of Notch and then lowering the production rate of Delta, but not if the order of the paths was reversed [206]. The result is similar to a model showing that "cheater" bacteria can invade a social population if they first evolve a novel "deaf" receptor, but not if they first evolve a novel signal: the first pathway gives them transient immunity to production cues, but the second has them doing double duty in responding and signaling [68]. These toy models are valuable because they are far more parsimonious than the simple-minded explanation that context-dependence of gene expression is the result of yet another cofactor: pursuing their implications will likely yield more biological insight in the long term. Finally, only a single prior state needed to be remembered for path-dependence to emerge in the models of [68, 194, 206]; chapter 3 of this thesis considers what happens when networks remember longer sequences of input.

1.3. Combinatorial logic in development

Combinations of inputs specify cell fate, but whether or not those inputs are remembered over time makes different outcomes possible. The theoretical framework broadly known as *combinatorial logic* (Figure 1.2A) is a memoryless (i.e., Markovian) scheme which postulates that different outcomes result for inputs A, B, and A AND B, and additionally when A is replaced with C. The probabilistic nature of DNA binding has made combinatorial logic a popular model for analyzing the statistical mechanics of independent and synergistic transcription factor binding at promoters [29, 113, 137, 239, 246], and therefore has helped inform the design of many synthetic circuits (see below). Perhaps more important than thermodynamics, however, are the propositions that combinatorial logic extracts additional diversity from a limited number of transcription factors [25, 39, 225], and that it tunes the response of undifferentiated cells to morphogen gradients [14, 46, 101]. How could a single transcription factor have different effects in different contexts? By acting in combination with others. One comprehensive microarray study found that several genes involved in *Drospholia* wing development could be turned on or off in response to Myc (A) binding at the promoter, and that the response depended on the presence or absence of alternate (B and C) elements at a distal enhancer or *cis*-regulatory element [199]. An even clearer example was observed in the action of signaling molecules cAMP and DIF on the three cell types of the amoeba *Dictyostelium discoideum*: cAMP alone promoted prespore and prestalk A cell fate; DIF alone prestalk A and prestalk B; and the combination prestalk A specifically [23]. Morphogens are diffusible signals that act in a dose-dependent manner to

control gene expression [14]. FGF and activin act as morphogens in the *Xenopus* embryo, generating muscle alone when activin is low and FGF high, or notochord alone when both are high [101]. The advantage of controlling development with overlapping gradients in this manner is that there is less need for precision in the inputs; robustness is thereby enhanced. For example, it was demonstrated that when *Drosophila* embryos are assumed to function as optimal decoders of a few combinatorial inputs, segmented gene expression can be reproduced to within 1% accuracy [214].

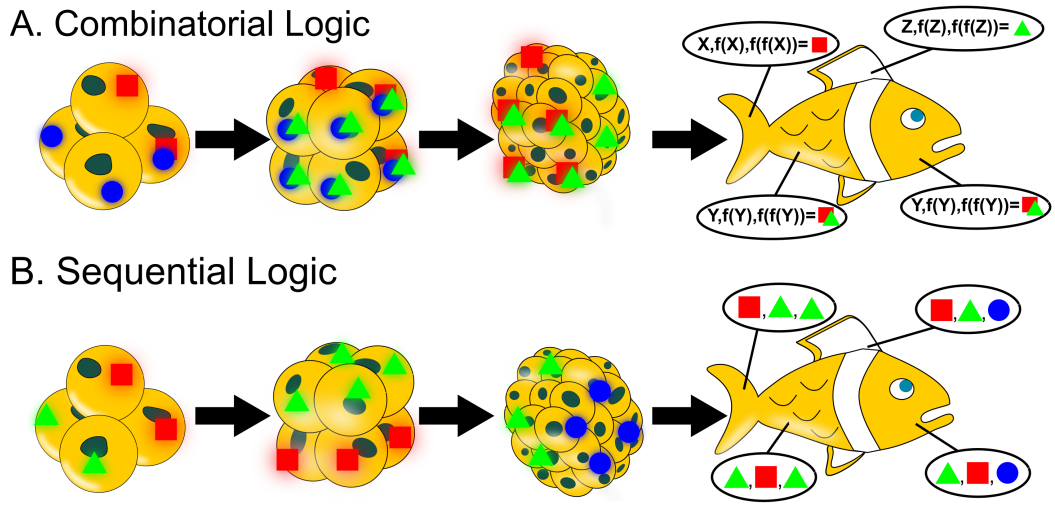

Figure 1.2: Combinatorial and sequential logic. Developmental signals (square, triangle, circle) can be interpreted in two different ways. **(A)** In memoryless combinatorial logic, iteration of the same tristable regulatory function f produces three stable expression states. Here the signals are also gene products, and the combination of expressed genes is the state. **(B)** In sequential logic, each cell remembers the sequence of the inputs it has seen when choosing its fate.

Despite its advantages, the unavoidable consequence of combinatorial logic is that cell fate is set at time zero (Figure 1.2A). Using the language of the gene regulatory function of the previous section, three signals (square, triangle, circle) lead to a change in gene expression in each cell at step one, a different change at step two, and so on until the minima have been reached and development is complete. Might such a process permit a switch in basins of attraction midway? In the absence of noise, the answer is, No. A cell initially poised to adopt fate 1 using combinatorial logic cannot later find out it adopts fate 2. The paradox of a Markovian process like combinatorial logic is that since information cannot be created over time, any changes to the regulatory function must be programmed at the start. It is the nature of a potential minimum that all states sufficiently close by get no farther away as

time goes on, unless energy or information is supplied. Conversely, it is not possible to say that the information for the adult (parts and order) is present in the egg if it can't be known until later. The foregoing reasoning leads to the conclusion that if a cell uses combinatorial logic, then it must know its fate at time zero (see also section 4.3).

To be sure, there are well-documented cases in *C. elegans* [10, 221], *Drosophila* [24, 78, 155, 309], rodents [259, 260, 308], and amoeba [23] in which combinatorial inputs explain gene expression choice in different tissues. Two *Drosophila* photoreceptor proteins Tsh and Hth promote (or fail to inhibit) the *Eya* gene when expressed alone, but function as repressors when expressed in combination [24]. Suppression of *Eya* in a specific context ensures that tissue anterior to the pre-proneural zone ahead of the morphogenic furrow is maintained in a proliferative state antagonistic to photoreceptor differentiation. In the *C. elegans* pharynx, PHA-4 and two HRL factors regulate the gland-specific *hlh6* gene, activating it in gland and suppressing it in non-gland cells [221]. Deletion or mutation of one of the HRL sites results in derepression, showing that a different complement of factors regulates the gene in non-gland tissue. In addition to single genes, combinatorial inputs operate on the cell fate level. Sox9 in the mouse spinal cord represses motoneurons and promotes astrocytes [259], while Olig2 represses astrocytes and promotes both oligodendrocytes and motoneurons [308]. These two genes give rise to a combinatorial code whereby oligodendrocyte identity is specified by high levels of Sox9 and Olig2 together; motoneurons and astrocytes are favored by the respective absence of either antagonist. Finally, a hybrid scheme was identified in the fly eye, involving combinatorial signaling molecules Notch and EGF regulating combinatorial input to *Pax2*, which designated the fates of at least four different cell types [78]. These examples show how combinatorial logic concisely explains expression differences in individual genes [23, 24, 221] and the emergence of specific cell types [24, 46, 101, 78, 155, 259, 260, 308]. Yet shortcomings are apparent when combinatorial logic is used to regulate groups of genes and cells at once, particularly in that specificity appears to require a specialized factors for each fate (see chapter 3). As the example in the amoeba shows, combinatorial codes can result in some cell types (e.g. pre-stalk A) emerging under all conditions [23], clearly an undesirable and unrealistic outcome in organisms with diversified cell types. Therefore, simple combinatorial logic may not be suitable for explaining *de novo* development from a symmetric starting state. New technology for characterizing combinatorial transcription binding on the whole-genome level [10, 309], although valuable for identifying these

diverse cell types, may not be appropriate for addressing the question of initial symmetry breaking. Alternative models, which are the subject of this thesis, will be necessary for the design of experiments that leverage the increasingly rich data now at our disposal.

An alternative to combinatorial logic, proposed in [153] (and reproduced in chapter 3 of this thesis), is that all inputs are remembered in the process of gene regulation. In this model, termed *sequential logic* (Figure 1.2B), several inputs act in sequence to specify developmental fate. In this way, cells seeing the same signal in the egg stage can later adopt divergent fates if they see different signals later (cf. fin versus tail in Figure 1.2B), or even if they see some of the same signals in different orders (tail versus scale, tail versus mouth fin versus scale, fin versus mouth). This noncommutative model addresses the information bottleneck inherent in the Markovian nature of combinatorial logic: information is spread out over time instead of concentrated in the egg. The idea that there is such a bottleneck has to some extent been anticipated. One study found that the *Drosophila* transcription factor Rn acts in nested fashion in patterning the fates of olfactory receptor neurons on progenitors that have already reached a certain state [155]. Another showed that the timing of neurogenesis and gliogenesis in the mouse spinal cord depends on when the patterning factors Pax6, Olig2, and Nkz2.2 are turned off, and when pro- and anti-neural factors are turned on [260]. This result is similar to the subjugation of the switch from early neurogenesis to later generation of oligodendrocytes to the timing of Sox9 activation [259, 308]. While the role of time in sequential development is well-established, the extent to which it demands revised models going beyond static landscapes and simple combinatorial logic has been under-appreciated.

It might reasonably be asked of Figure 1.2B what accounts for the different sequences seen by each cell. Although the zygotic cells don't know their fate at time zero, it appears that something does. Put another way, abandoning combinatorial logic is *sufficient* to make the time dimension informative. But in order for sequential logic to be a *necessary* feature development, the landscape must change as cells move along it. Although some authors have included the a time-dependent remodelling of the landscape [75, 125, 290, 291], truly autonomous development needs to be free of external influences once initiated. Chapter 4 develops a new hypothesis that autonomy emerges from the space-time constraints of limited transcriptional resources.

1.4. Combinatorial and sequential logic in synthetic biology

An alternative approach to studying cellular decision-making during development *in vivo* is to build synthetic gene circuits. Implementation of combinatorial and sequential logic circuits in live cells as components of biological computers is an ongoing project in synthetic biology. Rational design of genetic circuits is useful not only for engineering purposes, including designing oscillators for therapeutics [112] and long-term storing of data [55], but also for gaining insight into how cells use circuits for processing information *in vivo* (e.g. [8]). Just as computers built from a small variety of electronic components have widespread functionality, cells use limited signals to solve the problem of development [214]; it is imperative to understand how.

In the last two decades, the purview of synthetic biology has expanded from combinatorial transcriptional circuits in *E. coli* to stably writing into the DNA of eukaryotes. Studies thus fall on three (not-quite-orthogonal) axes spanning circuit type (combinatorial versus sequential), computational platform (RNA versus DNA), and cell system (eukaryotic versus prokaryotic). Although work continues in all regions of this space, the general desire is to engineer circuits with memory for application in human systems. This section reviews the different synthetic systems with an eye toward understanding the information-processing strategies that may be used in development *in vivo*.

Fluorescence in bacterial cells is driven by a limited number of small-molecule inducers to gene promoters, in a manner that is strongly dependent on circuit topology. Arabinose (Ara) and acyl homoserine lactone (AHL) directly activate the *AraC* and *LuxR* promoters pBAD and pLux [20, 59, 181, 289, 307], leading to reporter expression, but LacI and TetR repress the operators pLacO and pTetO controlling lactose metabolism and tetracycline resistance [59, 89, 105, 181, 189]; they must be repressed with the small molecules isopropyl β-D-1-thiogalactopyranoside (IPTG) and anhydrotetracycline (aTc). Additionally, the λ phage repressor cI inhibits transcripts from the pR promoter controlling the lytic response [105, 161], but it must be supplied transcriptionally. There are a number of caveats to the use of inducers in cells. Although repression of repressors and activation of activators logically have the same outcome, it has been shown that repression is in general dominant: when pBAD and pTetO jointly controlled downstream gene expression, Ara alone could not activate a GFP reporter, while aTc alone could [59]. In another study of co-regulated genes, cooperativity between TFs bound at primary and auxiliary sites was asymmetric with respect to activation and repression [115].

Auxiliary sites bound their regulators more tightly in activating circuits, whereas primary sites did so in repressive ones. Assuming that the higher affinity regulator is the first on and the last off, then the most switch-like response occurs when the primary activator (repressor) is the last be added (removed), in agreement with the observed affinities. Even the relative placement of activators from the transcription start site can influence the sharpness and leakiness of the response [189]. These and other concerns regarding genetic context and promoter strength [105, 289] mean that small molecule inputs to prokaryotic circuits are best treated as approximations of Boolean inputs to electronic circuits. Optimization through directed evolution [161, 237, 307] and other methods [181, 289] is a necessary first step in circuit design.

Once optimized, prokaryotic circuits can activate reporter expression *in cis* or *in trans*. When multiple binding sites are inserted upstream of a single promoter, fluorescence is a function only of the inputs [20, 40, 59, 105, 189, 237, 307]. This strategy has lent itself to circuits that compute AND [40, 237], NOR [40, 307], NOT [20, 40], and OR [40]. The more complex IF/ANDN (one of two inputs being on by itself is uniquely forbidden/allowed) appears to require regulation *in trans* (see below). The same elements were realized in a mammalian system using as input various antibiotics to disrupt the regulator-DNA interaction [144]. These simple circuit elements can be used to generate large-scale patterns: in one experiment, a mixed population of cells placed at different distances from a signal source with promoters of different strengths were induced to form fluorescent bulls' eyes [20]. With more than two inputs to a promoter, a range of computations are possible if one or more inputs is held constant [40]. Exhaustive sampling of different promoter architectures has shown that cells actually compute a linear combination of AND and OR, leading to a ladder of increasing fluorescence when A, B, and A + B are added [59]. When multiple promoters are used, input-output circuits become bistable. In one highly-cited study, IPTG relieved repression of pLacO by LacI, leading to *TetR* transcription and further repression of *LacI* at a locus *in cis* [89]. The opposite LacI-high state could be induced in real-time by adding aTc following IPTG, showing that the circuit was operating in a bistable region of parameter (i.e., promoter strength) space. Although integrated on a single plasmid, the circuit in this study was actually a special case of regulation *in trans* with two promoters regulated by separate but interconnected promoters, a necessary feature for circuits with memory.

Not all circuits regulated *in trans* are bistable, but in general they are more

modular than their counterparts *in cis*. This is because the products of the first input layer can be fed into a second, swappable layer downstream. The architecture of such circuits can be funnel-like [7, 16, 181, 289] or nonlinear [84, 161]. The funnel variety feed inputs into two different promoters, and the expressed products interact in some way to control transcription at a third. For example, input promoters have been engineered to produce enhancer-binding factors that interact with RNA polymerase [289], bacterial chaperones [181], and suppressors of amber stop-codons [7]. In all cases, both inputs were necessary to control output at a third locus, showing that funnel gates are similar to electronic summing junctions. The modularity of such systems was demonstrated by Moon and colleagues, who showed that orthogonal chaperone-transcription factor pairs could be chained together to produce a four-input AND gate with minimal faults, owing to different kinetics of the separate two-input modules [181]. A two-input one-output circuit that computes the logical XOR from two linked ANDN modules was also constructed using regulation *in trans* in a mammalian system [16]. The major difference between the prokaryotic and eukaryotic contexts is that small molecule repressors are replaced by antibiotics. Briefly, antibiotic A at one promoter inhibited the RNA-binding repressor of a fluorescent reporter transcribed from a distant locus, itself transcriptionally inhibited by antibiotic B. Because transcription is upstream of RNA-binding, the circuit computed the ANDN operation, only generating fluorescence when A is present alone; it is the complement of A $\rightarrow$ B.

Besides the funnel-type circuits that take multiple inputs to produce a single output, regulation *in trans* can be adapted to produce sequential circuits with memory. In this type of circuit, a single input initiates a chain of events that delays the output by virtue of a nonlinearity. Nonlinearity (i.e., a feedback loop) is necessary for memory (i.e., multiple steady states) [254]. In one example of a sequential-counting circuit, T7 RNA polymerase and GFP were both tagged with a mutated ribosome binding sequence [84]. Because mRNA binding was downstream of transcription, Ara-mediated post-transcriptional relief of riborepression was achieved only while the inducer was present. With GFP under the control of T7 RNA polymerase, this system during the first Ara pulse effectively functions as an incoherent feedforward loop [6]; it is not until a second pulse of Ara appears that GFP mRNA is translated. This report was widely cited as an example of a genetic circuit that can count pulses. In another study of sequential logic, a memory module was combined with a NOR gate to reversibly switch a circuit between RFP- and GFP-expressing states using the UV-triggered RecA proteasome pathway [161]. The RFP-GFP module, a bistable

switch controlled by mutually repressive cI inhibitors, operated in a monostable regime thanks to the superior strength of the GFP promoter. But a UV pulse that triggered proteolysis of cI also induced transcription of third cI variant, giving the system an additional "kick" to the RFP-expressing state. The final component was the production of LacI by the RFP operon, resulting in repression of cI number 3, so that a second UV pulse could restore the GFP-RFP switch to its default GFP-expressing state. Although highly complex, and showing only middling switching efficiency, the push-on push-off switch is a unique realization of a circuit able to remember sequences of input. In a final example, yeast cells were engineered with a feedback loop in which a GFP gene expressed from a *CYC1* locus was activated by Gal1-driven LexA DNA-binding at the promoter [2]. The system could transit between high- and low-GFP states depending on the kinetic parameters. The high-GFP state persisted in the absence of galactose, although it ultimately decayed to the low state due to dilution during cell growth. These examples show the great versatility of genes driven from multiple promoters to generate sequential logic circuits that do much more than simply produce a fixed output to a given input.

Uniting the examples discussed above is their reliance on fluorescence output. A parallel approach to logic functions in cells is to write changes directly into the DNA using recombinases [35, 74, 84, 108, 121, 253] or CRISPR-Cas9 DNA-editing technologies [71, 83]. DNA is a more stable storage medium than the transcriptional circuitry, because it persists for multiple generations and can even be read after cell death. Thus, DNA recombinases are a natural avenue for pursuing sequential logic in cells. Different recombinases such as Fim (B and E) [74, 108], HbiF [74], Cre [84], Hin [108], and Bxb1 [35, 121], and TP901-1 [121] recognize specific DNA sequences and have different levels of reversibility, but their overall mechanism is conserved. In the Bxb1 serine integrase system, the phage attP site (palindromic except for a central dinucleotide) undergoes recombination with the host attB site, generating attR and attL sites from alternate halves of the original partners; the reverse reaction is not allowed [92]. In order for proper synapsis to occur, the DNA strands must be in opposite $\rightarrow$ and $\leftarrow$ orientations when corresponding halves of the double helix pair as $\leftrightarrows$. Imagine the arrows being cut in the middle and the heads being attached to opposite tails (Figure 1.3). When the sites lie *in cis* on a circular plasmid, the cuts necessarily remove a contiguous portion of the DNA, which may contain two heads (panel A), or a head and a tail from opposite sites (panel B). Therefore, case A with the geometry $\rightarrow \ \leftarrow$ results in the the intervening DNA being reversed, and case B with $\rightarrow \ \rightarrow$ in looping out.

In A, intervening elements such as transcription start- and termination sites can be rotated with respect to one other and with respect to downstream genes, but they must be collinear in order to have an effect on transcription. For example, a DNA bit was switched from off to on (i.e., GFP-expressing) by introducing a pulse of HbiF recombinase to flip a start site from up to down, and FimE to flip it back again [74]. Strikingly, the recombinases recognize opposite sites irreversibly, and can be arranged to make a NOT gate if one is expressed constitutively. State-sensitive recombination is a useful feature, as the authors of a prior study were compelled to express the recombinase together with an excisionase in order to effect the reverse flip; as a result, they observed a mixed population of on and off states, a situation termed stoichiometric mismatch [35]. Nevertheless, once the kinetic parameters were adjusted, both studies observed stability of the DNA switching devices over time and upon multiple cycles, suggesting that such systems may be useful for long-term memory storage. A major drawback, however, is the problem of addressing specific bits with only one or two molecules available to catalyze the switch reaction at any bit. The synthetic biology toolbox has several different parts [284], and one solution is to try to supplement it with newly designed recombinases; this strategy is likely to have diminishing marginal returns. Another way to circumvent the bottleneck of limited switches is to spread them out in time. Friedland and coworkers employed a type of recombinase sequential logic to expose transcription start sites and terminators in an ordered fashion to build a DNA device capable of counting pulses [84]. A novel strategy employed by both Hsiao and colleagues and Ham and colleagues was to stagger the sites recognized by different recombinases, and then to expose cells to different sequences of events [108, 121]. Examination of the DNA state afterward by either fluorescence [121] or culture PCR [108] showed that it was possible to detect which recombinase was seen first. A theoretical version of this switching strategy in explored chapter 3.

Besides building bacterial computers, there is an emerging interest in using circuits with memory to learn about the dynamics of living cells using the DNA molecule as a recording device. In principle, any locus in the bacterial genome can be "written" into by expression of a retron unit in the SCRIBE system [71]. A single-stranded DNA molecule containing the edited gene is reversibly incorporated into the parent locus by the Beta recombinase, and the state is stored at the population level (i.e., only some cells are edited). It was shown that multiple edits could be made using multiple plasmids, albeit with low efficiency, providing one solution to the scalability problem of recombinase circuits. Alternatively, recorded events can be

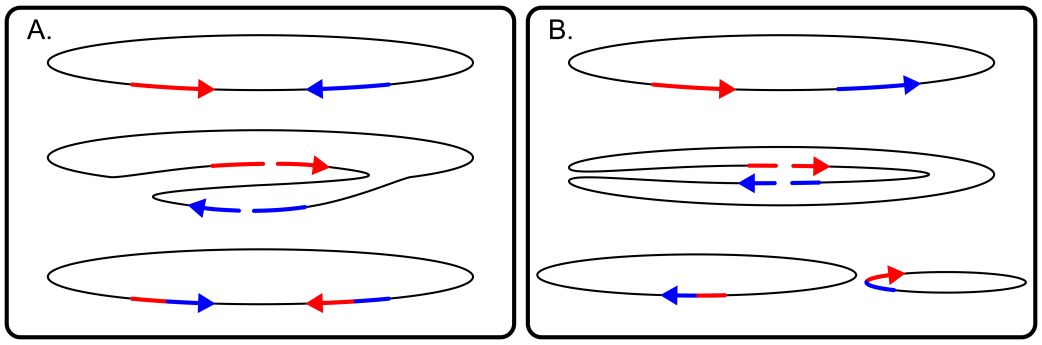

Figure 1.3: Two outcomes for oppositely oriented DNA recombinase switches. Phage-derived recombinases are able to flip or cut DNA when recognition sites are aligned head-to-tail. **(A)** Antiparallel recognition sites are flipped because the arrowheads are connected when the recombinase introduces a nick. **(B)** The intervening stretch is excised and the sites are parallel because the arrowheads are disconnected.

"read" off the genome by the marks they leave there using the MEMOIR system [83]. Frieda and coworkers introduced 28 DNA stem loop "scratchpads" into the genome of proliferating mouse embryonic stem cells, and used CRISPR-Cas9 to introduce an irreversible deletion. Probing the state of transcripts from the scratchpad loci using smFISH allowed the relatedness of daughters to be quantitatively assessed. This scheme makes it possible to answer the question of whether single cells remember the history of signals presented to them.

1.5. Appendix

1.5.1 The n-dimensional volume element

Let $a_1, \ldots, a_{n-1}, b \in \mathbb{R}^n$ be elements of a vector space with unit magnitude, each having the form $a_i = a_i^j \mathbf{e}_j$ relative to the standard basis $\{\mathbf{e}_i\}$. If each of these n elements is referred to the origin, then they span an n-dimensional volume element no bigger than the n-cube. Let

$$\mathbb{A} = \left[\begin{pmatrix} a_1 \end{pmatrix}, \ldots, \begin{pmatrix} a_{n-1} \end{pmatrix}, \begin{pmatrix} b \end{pmatrix} \right] \tag{1.1}$$

be the column span of the n elements. We seek to prove

Theorem 1.5.1. *The volume spanned by n elements of $\mathbb{R}^n$ is* $\det \mathbb{A}$.

Proof. The theorem is proved by induction on the dimension of $\mathbb{A}$. For the $n = 2$ case, it is easy to see that the parallelogram spanned by orienting $a_1 = a$ and b at the

origin is the area $(a^1 + b^1)(a^2 + b^2)$ of the square subtending them, less the areas $2a^2b^1$ of the corners and $a^1a^2 + b^1b^2$ of the external triangular elements. The sum of these contributions is $a^1b^2 - a^2b^1 = \det \mathbb{A}$, relative to a right-handed coordinate system. Note that if the roles of axes $\mathbf{e}_1$ and $\mathbf{e}_2$ are reversed, then the area $b^1a^2 - b^2a^1$ has the opposite sign.

For the general case, assume A is the volume of the region ∂R spanned by $n-1$ vectors $a^1, \ldots, a^{n-1}$. Adjoin b to the list, and refer it to a basis $(b^{\parallel}, b^{\perp})$, where $b^{\perp} \cdot a^i = 0$ for all i. Let $\mathbf{X} = \frac{\partial}{\partial b}$ be the vector field everywhere defined by tangent vectors in the direction of b; then $\nabla \cdot \mathbf{X} = 1$. The divergence theorem [50] shows that the volume V of the n-dimensional region R subtended by the n vectors is

$$V = \int_R dV = \int_R \nabla \cdot \mathbf{X} dV = \int_{\partial R} \mathbf{X} \cdot \mathbf{n} dA = b^{\perp} A, \tag{1.2}$$

where $\mathbf{n}$ is the unit normal to the boundary ∂R, and $\frac{\partial \mathbf{n}}{\partial \mathbf{b}} = b^{\perp}$ is the amount of $\mathbf{n}$ traversed when traveling on $\mathbf{b}$. Eq. (1.2) is equivalently interpreted as summing up small volume units V over the entire region R, or flowing along b and adding "slices" of the $n-1$-dimensional area A. Now let $a^1, \ldots, a^{n-1}, b \in \mathbb{R}^n$ be referred to the standard basis so that $b^{\perp} = b \cdot \mathbf{e}_i$ is perpendicular to the "face" (see [13] ch. 7) of ∂R with no components in $\mathbf{e}_i$. The area of this face is $\det \begin{bmatrix} a^1 & \ldots & a^{i-1} & a^{i+1} & \ldots & a^{n-1} \end{bmatrix} := \det \mathbb{A}_{\bar{i}}$, the i^{th} principal minor of $\mathbb{A}$; its orientation $(-1)^{i+1}$ corrects the sign error that results when a^{i+1} is an even number column. Therefore the n-dimensional volume with vectors referred to the standard basis is

$$b^{\perp} A = \sum_{i=1}^{n} b^i (-1)^{i+1} \det \mathbb{A}_{\bar{i}} = \det \mathbb{A}. \tag{1.3}$$

□

If the columns of $\mathbb{A}$ are vectors $\frac{\partial f}{\partial x_i}$ of gene expression changes due to attempted changes in the expression values x_i of each of the n genes, then $\det \mathbb{A} > 0$ at a point a is the condition that a stationary point is stable.

Chapter 2

THEORY OF SMOOTH POTENTIALS

2.1. Introduction

Waddington's theory [288] of a potential landscape for differentiating cells has recently become experimentally testable thanks in part to advances in single-cell sequencing technologies [182]. The gene expression states of individual cells at various time points in the process of hematopoietic [133, 179, 295] and neural [148, 217] differentiation, cellular reprogramming [147, 238], and preimplantation development [107, 169, 201] have been visualized as clusters in a high dimensional space, supporting a picture of hierarchical development in which cells roll down a surface. Taking cells out of their biological context was a necessary first step in perfecting these powerful techniques, but an unintended consequence has been neglect of the role of time in development. In particular, the Waddington landscape suggests that in the absence of expression noise, a cell picks its fate by falling into the basin of its nearest attractor state. And although the landscape may change due to the tuning of some external control parameter [75, 290, 291], development is an autonomous process that proceeds robustly with minimal guidance. These features beg the question, Why don't cells start at the end if they know the end at the start?

To resolving the paradox, it is necessary to reexamine the mathematical basis for the theory of potential landscapes. The Waddington landscape is a smooth surface, but as others have pointed out, gene expression levels need not reflect a gradient potential [26, 295]; both concepts are made precise in section 2.2.1. It is shown in section 2.2.2 that non-gradient dynamics arise on a smooth surface by transportation to the tangent space where rates (in space and time) of gene expression are independently controlled. Development proceeds as the flow from high to low potential of a locus of accessible states during which time information in the DNA of the progenitor is unpackaged; the condition for the potential difference to uniquely determine the trajectory at time zero is shown in section 2.2.3 to be the one-dimensionality of the controls. It is suggested that a system with many controls becomes one-dimensional as it orients to the direction of the applied forces at each step; in so doing, the trajectory is no longer known in advance. In 2.2.4, the conjugacy of space and time is invoked to explain how connected cells moving down a potential surface as group, abolishing the need for additional barriers between

alternative fates. By spreading out information in both space and time, the so-called parsimony principle resolves the fundamental information paradox that a single progenitor cell encompasses the fates of all its progeny.

2.2. Results and Discussion

2.2.1 Consequences of a smooth potential

Generalized forces can be defined from a smooth potential function $\phi(x, y)$ by its derivatives. It is the objective of this section to show that smoothness of the gene regulatory function leads to a gradient system in gene expression space. By a *gradient system* it is meant that transcripts at any point in expression space change in a direction that is a right angles to lines of equipotential relative to a reference state; motion of the (conservative) system is entirely due conversion of potential energy into kinetic. The consequences of a non-gradient potential are characterized by the negation of the sufficiency conditions.

Let the gene regulatory function of a two-gene system (x, y) be defined by the vector field $(f(x, y), g(x, y))$, where $-\dot{x} = f$ and $-\dot{y} = g$ are the negative rates of escape from two states x and y, similar to the assumptions of [26]. Define the potential function $\phi : \mathbb{R}^2 \to \mathbb{R}$ over regions in gene expression space by

$$\phi(x, y) = f(x, y)\, x + g(x, y)\, y, \tag{2.1a}$$

with differential

$$d\phi(x, y) = f(x, y)\, dx + g(x, y)\, dy. \tag{2.1b}$$

The condition (2.1b) is equivalent to the requirement that potential differences $f = \frac{\partial \phi}{\partial x}$ and $g = \frac{\partial \phi}{\partial y}$ reflect the tendency of the system to transit between two points. Then flow of the system is represented by the (bold face) vector field

$$\boldsymbol{\phi} = f\frac{\partial}{\partial x} + g\frac{\partial}{\partial y} = (f, g). \tag{2.2}$$

Because ϕ in (2.1a) defines a surface, it may assume the role of the warping function of a torsion bar in the St. Venant problem from continuum mechanics [79, 163, 243]. A surface ϕ is said to be *continuous* in a neighborhood containing (x, y) if $\lim_{(h,k)\to(0,0)} \phi(x + h, y + k) = \phi(x, y)$ for all directions $\mathbf{v} = (h, k)$, and *smooth* if $\lim_{\mathbf{v}\to 0} \frac{1}{\|\mathbf{v}\|} (\phi(x + h, y + k) - \phi(x, y))$ exists and is always equal to a tangent vector (f, g) for continuous functions f and g. These definitions suffice to prove the following version of the Implicit Function Theorem.

Lemma 2.2.1. *If ϕ is a smooth surface with a continuous differential $d\phi = f\,dx + g\,dy$, then there is a path in gene expression space with constant ϕ.*

Proof. If (x, y) is not an extremum of ϕ, then there are at least two tangent vectors $\mathbf{v}_1, \mathbf{v}_2$ with $\mathbf{v}_i = (f^{(i)}, g^{(i)})^T$ such that $\det\left[\left(\mathbf{v}_1\right) \quad \left(\mathbf{v}_2\right)\right] = 0$. Otherwise attempted changes dx and dy would always result in changes f and g of the same sign, which is only the case for extrema. Because the sign of the volume element spanned by the output tangent vectors must change, and because f and g are continuous, the determinant must at some point vanish. Therefore, the system of equations which must hold for the condition $d\phi = 0$ to be true, viz.

$$f^{(1)}dx + g^{(1)}dy = 0 \tag{2.3a}$$

$$f^{(2)}dx + g^{(2)}dy = 0, \tag{2.3b}$$

has a nontrivial solution $(dx, dy)^T$ (see Lemma 2.2.2 below). Upon substituting this solution into (2.1b), we find that

$$\frac{dy}{dx} = -\frac{f}{g}. \tag{2.4}$$

The differential equation (2.4) defines the locus of points in the (x, y) plane with constant ϕ. □

The solvability of system (2.3) is a consequence of the following technical lemma:

Lemma 2.2.2. *Let $\mathbb{A}$ be a linear operator with $\det \mathbb{A} = 0$. Then there is a nonzero vector $\mathbf{v}$ such that $\mathbb{A}\mathbf{v} = 0$.*

Proof. In general, $\mathbb{A}$ maps vectors to vectors by $\mathbb{A}\mathbf{v} = \mathbf{w}$. Because $\mathbb{A}$ is linear, $\mathbf{w} = (w^1, \ldots, w^n)^T$ may be written as $(\lambda^1 v^1, \ldots, \lambda^n v^n)^T$ for some constants λ^i. By appropriate choice of the v^i as $v^i \mapsto \frac{\lambda^1}{\lambda^i} v^i$, $\mathbf{w}$ may instead be written $\lambda\,(v^1, \ldots, v^n)^T$ for $\lambda = \lambda^1$. This transformation is well-defined if it is restricted to $\lambda^i \neq 0$. Assuming without loss of generality that this substitution has been made, we may solve for λ by taking the determinant of both sides of the equation $\mathbb{A}\mathbf{v} - \lambda\mathbf{I} = 0$, which follows from $\mathbb{A}\mathbf{v} = \mathbf{w} = \lambda\mathbf{I}\mathbf{v}$. The permutation definition of the determinant satisfies

$$\begin{aligned}\det\left(\mathbb{A} - \lambda\mathbf{I}\right) &= \sum_{\sigma} \operatorname{sign}(\sigma) \prod_i \left(\mathbb{A}_i^{\sigma(i)} - \lambda\delta_i^{\sigma(i)}\right) \\ &= \sum_{\sigma} \operatorname{sign}(\sigma) \prod_i \mathbb{A}_i^{\sigma(i)} + \text{ homogeneous polynomial in } \lambda,\end{aligned} \tag{2.5}$$

using the $\mathbb{A}^{\text{column}}_{\text{row}}$ convention [172]. Because $\det \mathbb{A} = 0$, Eq. (2.5) is itself a homogeneous polynomial in λ (i.e., having no constant term), and must therefore have at least one root $\lambda = 0$. Therefore, $\mathbb{A}\mathbf{v} = \mathbf{w} = 0$. □

Being a velocity potential, the locus of constant ϕ not only determines a relationship between x and y, but also how the (negative) velocities f and g must change in order for y and x to maintain their equipotential relationship. This idea is generalized using the language of vector fields in the tangent space of gene expression, where directions rather than positions are the independent variables. The next result shows that if f and g are well-behaved, like common gene regulatory functions, then the vector field $\boldsymbol{\phi}$ can be defined as the harmonic conjugate of another field $\boldsymbol{\psi}$. The relationship between these two fields determines how the velocities change in order to maintain constant potential and constant stress, respectively.

Theorem 2.2.3. *If f and g are velocities of a smooth potential ϕ, then there is an orthogonal vector field $\boldsymbol{\psi}$ such that*

$$\nabla \cdot \boldsymbol{\phi} = -\nabla \times \boldsymbol{\psi} \tag{2.6a}$$

$$\nabla \cdot \boldsymbol{\psi} = \nabla \times \boldsymbol{\phi}. \tag{2.6b}$$

Proof. Using Eq. (2.1b), the total derivative of ϕ becomes

$$\begin{aligned} d\phi &= df \cdot x + f\,dx + dg \cdot y + g\,dy \\ 0 &= df \cdot x + dg \cdot y. \end{aligned} \tag{2.7}$$

This is the Legendre transformation of ϕ. On a curve of constant ϕ, which must exist by Lemma 2.2.1, Eq. (2.1b) also vanishes:

$$0 = f\,dx + g\,dy. \tag{2.8}$$

Rearranging (2.7) and (2.8) and taking their ratio gives the constraint

$$\begin{aligned} \frac{df/dy}{dg/dx} &= \frac{y}{x} \cdot \frac{g}{f} \\ \left(\tfrac{\partial^2 \phi}{\partial y \partial x}\right) \Big/ \left(\tfrac{\partial^2 \phi}{\partial x \partial y}\right) &= 1 = \tfrac{g}{x} \Big/ \tfrac{f}{y} \end{aligned} \tag{2.9}$$

that must hold between the expression states x, y and their velocities f, g on the equipotential curve. Eq. (2.9) shows that $\frac{g}{x}$ and $\frac{f}{y}$ may not depend on different variables; the simplest case is that they are both lines with the same slope, i.e.,

$g(x) = \alpha x$ and $f(y) = \alpha y$. This condition is assumed in the torsion problem [163, 243], and is the one illustrated in Figure 1.1A.

Now, the vector field $\boldsymbol{\phi} = (f, g)$ of velocities is

$$\boldsymbol{\phi} = (\alpha y, \alpha x), \tag{2.10}$$

with divergence and curl given by ([50] ch. 1, [255] ch. 7)

$$\nabla \cdot \boldsymbol{\phi} = \frac{\partial f}{\partial x} + \frac{\partial g}{\partial y} = \alpha \left(\frac{\partial y}{\partial x} + \frac{\partial x}{\partial y} \right) = 0 \tag{2.11a}$$

$$\nabla \times \boldsymbol{\phi} = \frac{\partial f}{\partial y} - \frac{\partial g}{\partial x} = \alpha \left(\frac{\partial y}{\partial y} - \frac{\partial x}{\partial x} \right) = 0. \tag{2.11b}$$

The field $\boldsymbol{\psi}$ defined by

$$\boldsymbol{\psi} = (-g, f) = (-\alpha x, \alpha y) \tag{2.12}$$

has divergence and curl given by

$$\nabla \cdot \boldsymbol{\psi} = -\frac{\partial g}{\partial x} + \frac{\partial f}{\partial y} = \nabla \times \boldsymbol{\phi} \tag{2.13a}$$

$$\nabla \times \boldsymbol{\psi} = -\frac{\partial g}{\partial y} - \frac{\partial f}{\partial x} = -\nabla \cdot \boldsymbol{\phi}, \tag{2.13b}$$

and is at right angles to $\boldsymbol{\phi}$. □

Theorem 2.2.3 shows that ϕ defines a smooth gradient system in expression space because the field $\boldsymbol{\psi}$ specifies the direction of motion that at any point moves the system between level sets of the function ϕ. An example for the two-gene system is shown in Figure 2.1. The concentric circles represent the loci of x^2 = const. and $-y^2$ = const.,[1] relative to a reference level. Then at any point in space there is an imbalance $x^2 - y^2$ by virtue of the fact that the system lies on exactly two of these circles. The motion of the system from any point (x, y) is found by flow along $\boldsymbol{\phi} = (y, x)$, i.e., by moving by the amount y along the $\hat{x}$ unit vector and by x along $\hat{y}$; in contrast, flow along the orthogonal field $\boldsymbol{\psi} = (-x, y)$ changes the potential. In this way, the system always knows the allowed directions of motion at any point in space.

The landscape analogy cannot be taken as too literal a metaphor for development, at least not until a few modifications are made. In a physical landscape, you walk uphill and over a ridge into another valley; in a potential landscape, you

[1] The minus sign indicates that increasing x is attendant on decreasing y, e.g., if y is an inhibitor of x.

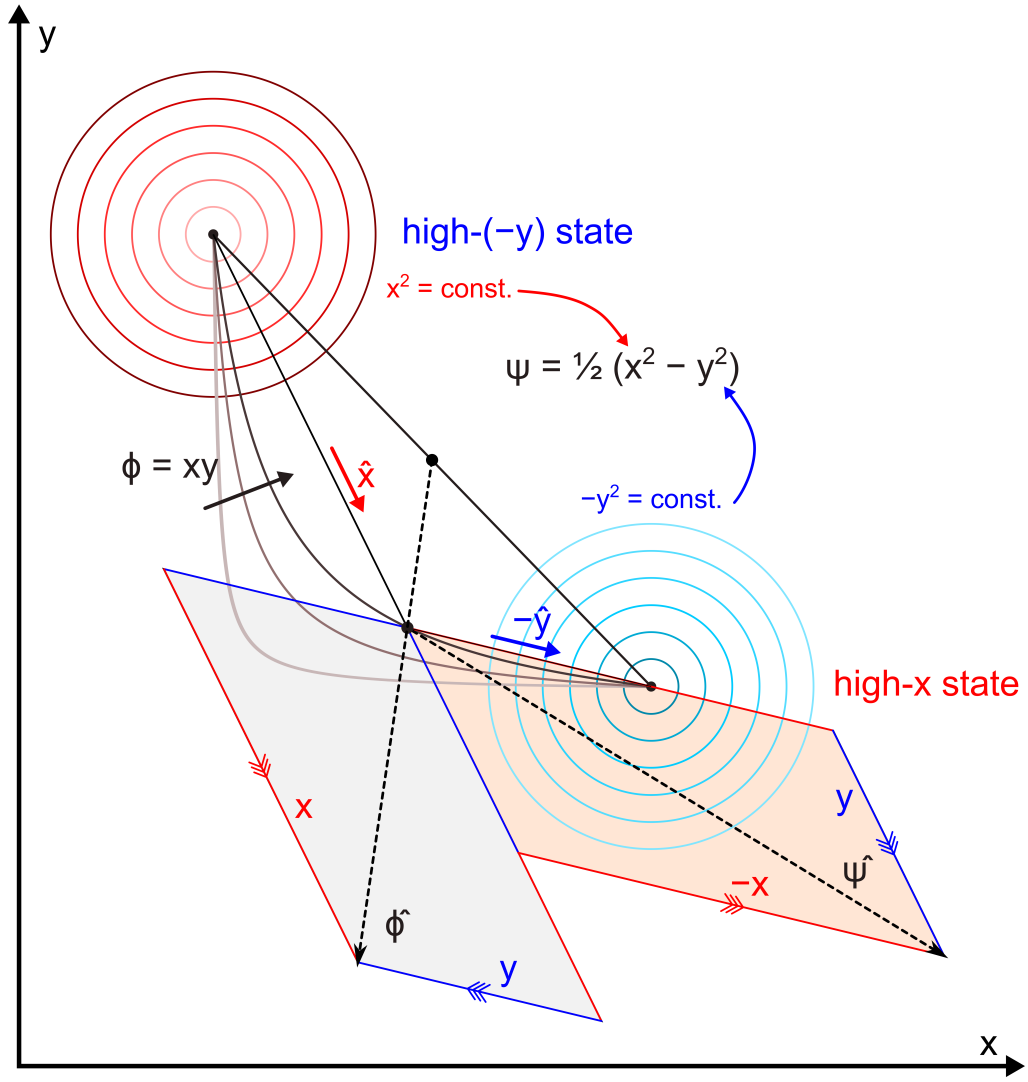

Figure 2.1: A gradient potential in gene expression space. Gene expression transfers population from the y state (blue) to the x state (state) in a conservative two-gene system in such a manner that the potential $\phi = xy$ is constant as $\phi = \frac{1}{2}\left(x^2 - y^2\right)$ is adjusted. Circles are loci of constant transcripts x^2 and $-y^2$, so that the sum of any two circles is the imbalance. As the energy ϕ increases, the midpoint of zero imbalance moves up and to the right. The senses in which the distances x and $-y$ are increasing (toward darker hues) are shown with red and blue arrows pointing to/from the current state of the system. The local coordinate system corresponds to the fixed axes drawn in black. The dashed lines show the tangent and normal directions along a curve of xy = const. The conjugate vector fields $\boldsymbol{\psi} := \hat{\psi} = (-x, y)$ and $\boldsymbol{\phi} := \hat{\phi} = (y, x)$ defining these respective directions are orthogonal relative to the skew coordinate system. Colored lines with chevrons show how the distance vectors are projected along the (signed) unit vectors $\hat{x}$ and $-\hat{y}$.

walk on a path where $\phi(x, y)$ is constant. Going up- or downhill in the potential landscape changes the depths of the valleys in the physical landscape, in the

sense that the more energy you have, the higher the hill you can climb. Notice that the several hyperbolic paths in Figure 2.1 connect the same endpoints at different heights, a feature that appears to violate the injectivity (one-to-one-ness) of a smooth ϕ. The interpretation is that adding energy to the system lowers the entire surface, so that the equipotential hyperbolas approach a straight line. A spaceship flying between two planets rather than marbles rolling downhill is perhaps a more accurate picture of the gene regulatory potential. Figure 2.1 is an attractive analogy for development because high-energy progenitors can exist in a bipotent intermediate state associated with high levels of multiple lineage-promoting factors, whereas low energy differentiated cells have to go around a barrier. Although some studies have found that progenitors stochastically turn on separate lineages programs [207, 217], there is ample single-cell evidence that stem cells in the kidney [42], intestine [142], bone marrow [82], hematopoietic lineages [122, 203, 219], and early blastula [201] simultaneously express genes associated with alternative fates. These bipotent progenitors are extremely rare and may not always translate nascent transcripts into protein products, but the very fact that single bipotent cells can be trapped and converted to alternative fates [203] suggests that the picture in Figure 2.1 of a high potential locus of states is not farfetched. Even reports suggesting that fate is fixed by mutually exclusive stochastic events at the progenitor stage have found latent capacity for stem cells to adopt multi-lineage transcription states when certain genes are knocked down [207]. This is an important refinement to the Waddington landscape, because it suggests that cells do not roll downhill independently. Instead, a collection of cells at the same potential take different trips downhill in such a way that they remain at the same height throughout the process (see section 2.2.4 below). There is no need to invoke additional barriers between states of low developmental potential, because alternative fates can only be reached by going back in time.

What are the allowed equipotential trajectories the system? The conjugate vector fields $\boldsymbol{\phi}$ and $\boldsymbol{\psi}$ are the equivalent of the Cauchy-Riemann equations for the imaginary and real parts of a harmonic function of a complex variable [77]. Vector fields (2.10) and (2.12) give the x and y components of the derivatives of functions ϕ and ψ. Comparing like terms shows that

$$\frac{\partial \phi}{\partial y} = \frac{\partial \psi}{\partial x} \tag{2.14a}$$

$$\frac{\partial \phi}{\partial x} = -\frac{\partial \psi}{\partial y}, \tag{2.14b}$$

by which it is clear that ϕ defines the imaginary part of an analytic function in the

complex plane. With $\alpha = 1$, Eqs. (2.14) lead to

$$\psi = \frac{1}{2}\left(x^2 - y^2\right) \tag{2.15a}$$

$$\phi = xy, \tag{2.15b}$$

the latter being the surface plotted in Figure 1.1A and the level sets plotted in Figure 2.1. Eqs. (2.15) correspond to the strain and warp, respectively, of a rod with an elliptical cross section under torsion. Moving on an hyperbolic trajectory $xy = \text{const.}$ means that ϕ is constant as the system moves between different circles of constant x^2 and $-y^2$. Depending on the value of ϕ, the point at which x and y are equal moves to progressively higher levels until the allowed trajectory between the two states is a straight line; otherwise the system goes around the barrier on an hyperbolic curve. Also observe that

$$\phi = -\dot{x}x - \dot{y}y = -\frac{d}{dt}\frac{1}{2}\left(x^2 + y^2\right), \tag{2.16}$$

so that in a gradient system, constant transcriptional activity corresponds to the total amount of transcripts changing at a fixed rate.

The foregoing reasoning asserts that a smooth potential surface and linear gene regulatory functions lead to a gradient system in gene expression. In this case, the velocities are uniquely determined from the difference $\Delta\phi$ between two points: by the commutativity of the controls (see below), the path between endpoints is always broken up into flows $\boldsymbol{\phi}$ and $\boldsymbol{\psi}$ parallel and perpendicular to the gradient. Conversely, if the system is not a gradient, the controls f and g may be noncommutative. Hence the change in velocity between two points is path dependent.

2.2.2 Projection of the dynamics in the tangent space leads to noncommutative paths in gene expression space

The smooth potential $\phi = fx + gy$ need not be a gradient if the second line of (2.9) does not hold: if the mixed partials of ϕ are not equal, then alternative paths from (x_0, y_0) to (x_1, y_1) in general have different values of ϕ (as in the spiral landscape of Figure 1.1B). Although it is relatively easy to construct such a discontinuous surface in the base space, it is more illuminating to derive it from the curl of a vector field in the tangent space, where gene expression is actually controlled. Denote by $\mathcal{M}$ the manifold of gene expression states (x, y), and by $T\mathcal{M}$ its tangent space with local coordinates $(x, y, \dot{x}, \dot{y}) = (x, y, -f, -g)$. In section 2.2.1, it was shown that flow along the field $\boldsymbol{\psi}$ on $\mathcal{M}$ restricted gene expression to level sets of the function ϕ by virtue of its being everywhere perpendicular to $\nabla\phi = \boldsymbol{\phi}$.

The content of the following theorem is that level sets of a candidate potential ϕ on $\mathcal{M}$ are not invariant to the curl of a vector field (f, g) of controls in $T\mathcal{M}$.

Theorem 2.2.4. *If f and g are the conjugate forces of a smooth potential ϕ defined on $\mathcal{M}$, then there is a projection mapping $\pi : T\mathcal{M} \to \mathcal{M}$ such that the following diagram commutes:*

$$\begin{array}{ccc} (f,g)\Big|_{T\mathcal{M}} & \overset{\nabla\times}{\longrightarrow} & \nabla\times(f,g)\Big|_{T\mathcal{M}} \\ \pi\downarrow & & \downarrow\pi \\ (x,y)\Big|_{\mathcal{M}} & \underset{\nabla\times}{\longrightarrow} & \nabla\times(x,y)\Big|_{\mathcal{M}} \end{array} \tag{2.17}$$

Proof. Define the real-valued function $\phi : \mathbb{R}^2 \to \mathbb{R}$ on $\mathcal{M}$ by

$$\phi(x,y) = f(x,y)\,x + g(x,y)\,y \tag{2.1a}$$

$$d\phi(x,y) = f(x,y)\,dx + g(x,y)\,dy, \tag{2.1b}$$

as in Eqs. (2.1). It follows from Eqs. (2.10) and (2.12) in Theorem 2.2.3 that there is a field $\boldsymbol{\phi} = (f, g)$ and a conjugate field $\boldsymbol{\psi} = (-g, f)$ at right angles to $\boldsymbol{\phi}$ such that $\nabla\cdot\boldsymbol{\phi} = \nabla\times\boldsymbol{\psi}$ and $\nabla\cdot\boldsymbol{\psi} = -\nabla\times\boldsymbol{\phi}$. The field $\boldsymbol{\phi}$ was found by stipulating that the function ϕ be constant. Then the fact that $\nabla\phi$ and $\boldsymbol{\psi}$ are orthogonal implies that the direction $\nabla\psi$ that maximizes the rate of change of a function ψ (and hence transfers population from y to x the fastest) is orthogonal to $\boldsymbol{\phi}$. Therefore, the divergence $\nabla\psi$ of $\boldsymbol{\psi}$ (the net change in ψ over a region) is the total change in the components f and g of $\boldsymbol{\phi}$ around a loop in $(x, y, -f, -g)$ that maintains constant ϕ. In a gradient potential, there is no change when returning to the same point; in a non-conservative potential, there is a nonzero circulation $\nabla\times\boldsymbol{\phi}$ when returning to (x_0, y_0).

If π is the projection mapping $(x, y, -f, -g) \mapsto (x, y)$, then the matrix of the inverse mapping

$$\pi^{-1} = -\begin{pmatrix} \frac{\partial f}{\partial x} & \frac{\partial f}{\partial y} \\ \frac{\partial g}{\partial x} & \frac{\partial g}{\partial y} \end{pmatrix} \tag{2.19}$$

is the differentiation map $\pi^{-1} : \mathcal{M} \to T\mathcal{M}$. The strategy to prove the theorem will be to use Eq. (2.19) to find the forward transformation π and show that it commutes with the cross product in diagram (2.17). For small Δt the instantaneous x derivative is approximated by

$$-f = \dot{x} = \frac{\Delta x}{\Delta t} = \frac{\overline{x} - x}{\Delta t}, \tag{2.20}$$

and similarly for $\dot{y}$. Here, $(\overline{x}, \overline{y})$ is a fixed intermediate point on the (approximate) tangent vector through a point $\mathbf{r}(t) = (x(t), y(t))$ of the trajectory $\mathbf{r}$. Then

$$\pi^{-1} = \frac{-1}{\Delta t}\begin{pmatrix} \frac{-\partial\overline{x}}{\partial x} + 1 & -\frac{\partial\overline{x}}{\partial y} \\ -\frac{\partial\overline{y}}{\partial x} & -\frac{\partial\overline{y}}{\partial y} + 1 \end{pmatrix} = \frac{1}{\Delta t}(\mathbf{F} - \mathbf{I}) = \frac{-1}{\Delta t}\mathbf{I}, \tag{2.21}$$

where $\mathbf{I}$ is the identity on $\mathbb{R}^2$ and $\mathbf{F} = \frac{\partial \overline{z}_i}{\partial z_j}$ is the *deformation gradient* [50] relating the intermediate to the original coordinates; it vanishes in the tangent space where the dependent variable is Δz instead of $\overline{z}$. Inverting (2.21) using the classical adjugate gives the projection mapping as

$$\pi = \frac{1}{\det \pi^{-1}} \operatorname{adj}\left(\pi^{-1}\right) = \frac{\Delta t^2}{J} \frac{1}{\Delta t} \left(\operatorname{adj}\left(\mathbf{F}\right) - \mathbf{I}\right) = -\Delta t \cdot \mathbf{I}, \tag{2.22}$$

where $J = \det \mathbf{F} - \operatorname{Tr} \mathbf{F} + 1 = 1$. Therefore, the top/right path in diagram (2.17) is

$$\pi \circ \nabla \times \boldsymbol{\phi} = -\Delta t \cdot \nabla \times \left(\frac{\Delta x}{\Delta t}, \frac{\Delta y}{\Delta t}\right) = \left[\left(\frac{\partial x\left(t\right)}{\partial y} - \frac{\partial y\left(t\right)}{\partial x}\right) - \left(\frac{\partial \overline{x}}{\partial y} - \frac{\partial \overline{y}}{\partial x}\right)\right] = \nabla \times \left(x, y\right), \tag{2.23}$$

which shows that the circulation of a trajectory $\left(x\left(t\right), y\left(t\right)\right)$ is exactly balanced by circulation in the opposite direction of the chord $\left(\Delta x, \Delta y\right)$. For the left/bottom path, observe that the (transpose) adjugate deformation gradient acting on $\boldsymbol{\phi}$ from the right can be written

$$\begin{aligned} \operatorname{adj}\left(\mathbf{F}\right) \circ \boldsymbol{\phi} = \boldsymbol{\phi} \cdot \operatorname{adj}\left(\mathbf{F}\right)^T &= \left(\frac{\partial \overline{y}}{\partial y} f + \frac{\partial \overline{x}}{\partial y} g, \frac{\partial \overline{y}}{\partial x} f + \frac{\partial \overline{x}}{\partial x} g\right) \\ &= -\frac{1}{dt}\left(\frac{\partial \overline{y}}{\partial y} dx + \frac{\partial \overline{x}}{\partial y} dy, \frac{\partial \overline{y}}{\partial x} dx + \frac{\partial \overline{x}}{\partial x} dy\right). \end{aligned} \tag{2.24a}$$

Then using the constancy of $\left(\overline{x}, \overline{y}\right)$ and the identity $\frac{\partial}{\partial z^j} dz^i = \delta^i_j$,

$$\nabla \times \boldsymbol{\phi} \cdot \operatorname{adj}\left(\mathbf{F}\right)^T = -\frac{1}{dt}\left(\frac{\partial \overline{x}}{\partial y} - \frac{\partial \overline{y}}{\partial x}\right) = 0. \tag{2.24b}$$

We are left with

$$\nabla \times \pi \circ \boldsymbol{\phi} = -\nabla \times \Delta t \cdot \left(f, g\right) = -\nabla \times \left(\Delta x, \Delta y\right) = \nabla \times \left(x, y\right), \tag{2.25}$$

exactly as in Eq. (2.23), and where the time-dependence of $\left(x, y\right)$ is understood. Therefore, diagram (2.17) is commutative. □

The consequence of Theorem 2.2.4 is that if the actions f and g controlling the rates of change of gene expression do not commute, then the potential landscape in gene expression space is not a gradient, even if the potential surface itself is smooth. If the expression levels x and y are the independent variables, then it is only in the commutative case (2.9) when $\frac{\partial f}{\partial y} - \frac{\partial g}{\partial x} = 0$ that the rate at which one gene changes is balanced by the rates and expression levels of the other gene(s) (cf. Figure 1.1A). A physical example of this balance is the way in which a spaceship's rate of escape from Earth depends on its distance from Earth, as well as its distance

and rate of escape from the moon. A similar coupling between distances and rates is at work in Michaelis-Menten kinetics, where the too much of a substrate inhibits the catalysis rate of an enzyme. When a cell receives an independent signal to increase transcription of gene x, however, there is no balance law that says how the rate of transcription of gene y must change, and so the potential cannot be a gradient. Theorem 2.2.4 permits us to project the tangent space dynamics back into gene expression space in a manner that preserves the degree $\frac{\partial f}{\partial y} - \frac{\partial g}{\partial x}$ to which they fail to commute. The foregoing arguments show that appealing to the tangent space of gene expression alleviates the need for unrealistic potentials in the base space.

2.2.3 When the potential difference alone determines the trajectory

Theorem 2.2.4 shows that when f and g are independent controls, there is no guarantee that ϕ is conserved. It is of interest to know when ϕ can be used to determine the trajectory of the system in advance. The following corollary of Theorems 2.2.3 and 2.2.4 characterizes the necessary and sufficient conditions when control in the tangent space defines a gradient system in the base space.

Theorem 2.2.5. *When only one dimension is controlled in the tangent space $T\mathcal{M}$ of a manifold $\mathcal{M}$, the potential ϕ on $\mathcal{M}$ defines a gradient.*

This is an important corollary which will be appealed to in chapter 4 for making statements about when prior knowledge of forces provides advance knowledge of position. We prove it in two different ways, first geometrically by referring to the level sets of ϕ in Figure 2.1, and second using a more general, algebraic approach without refernce to the preceding theorems.

Geometric proof of Theorem 2.2.5. This is a statement of the form $A \iff B$, meaning $A \implies B$ and $B \implies A$. To prove it we show both that $A \implies B$ and $\overline{A} \implies \overline{B}$; the latter is the same as $\overline{\overline{B}} = B \implies \overline{\overline{A}} = A$.

The potential $\phi = fx + gy$ is smooth if and only if Eq. (2.9) holds, i.e., mixed partials $\frac{\partial^2 \phi}{\partial x \partial y}$ and $\frac{\partial^2 \phi}{\partial y \partial x}$ are equal. By Theorem 2.2.3, the field $\boldsymbol{\phi}$ corresponding to ϕ has a conjugate field $\boldsymbol{\psi} = (-g, f)$. First suppose the one dimensional control is $f = \alpha y$; then $g = 0$ by definition. But since $g = -\dot{y} = 0$, we must have that $f = \alpha y_0$ for some constant y_0. Then the smoothness condition $\frac{\partial f}{\partial y} - \frac{\partial g}{\partial x} = 0$ holds, and the system is a gradient. The condition holds for any general function $f = f(x, y)$ because y is constant and $g = 0$.

Conversely, assume the controls are two-dimensional; then the applied force $\boldsymbol{\lambda}$ is not parallel to the direction vector $\mathbf{v}$ of the current point. There is an

orthogonal matrix $\mathbb{T} = \begin{pmatrix} \cos\theta & -\sin\theta \\ \sin\theta & \cos\theta \end{pmatrix}$ such that $\mathbf{v} \in \mathbb{R}^2$ has a one-dimensional representation via the transformation $\mathbb{T}\mathbf{v} = \begin{pmatrix} 0 \\ u \end{pmatrix}$ if $\theta = \tan^{-1}\frac{v^1}{v^2}$ and $u = \|v^1 + v^2\|^2$. If the controls f, g are applied for sufficient times t_1, t_2 such that

$$\boldsymbol{\lambda} \cdot \mathbf{v} = \begin{pmatrix} t_1 & t_2 \end{pmatrix} \begin{pmatrix} v^1 \\ v^2 \end{pmatrix} = \begin{pmatrix} t_1 & t_2 \end{pmatrix} \mathbb{T}^T \begin{pmatrix} 0 \\ u \end{pmatrix} = (t_1 \sin\theta + t_2 \cos\theta)\, u \neq 0$$

$$\implies t_1 \neq -\frac{v^2}{v^1} t_2, \tag{2.26}$$

then the controls are two-dimensional. Now assume that an external source of energy promotes the system between two level sets ϕ_1 and $\phi_2 > \phi_1$ of the potential, and let this change be broken down into two sequential steps via a (variable) intermediate state ϕ^*. The control f promotes the system in the $\hat{x}$ direction toward the x origin, and g takes it along $\hat{y}$ toward the y origin. By adjusting the durations t_1, t_2 of the first and second steps, the alternate paths f, g and g, f have the same energy endpoints. Because of the constancy of ϕ on a level set, the tangent vectors are uniquely determined at each spatial point: the direction $\hat{y}^*$ after the application of control f differs from $\hat{y}$; similarly, $\hat{x}^*$ after the application of control g points in a different direction than $\hat{x}$. For if it were possible to reach curve ϕ^* along $\hat{x}$ with $\hat{y}$ intact, say, then the y origin would be at the terminus of the same direction vector emanating from two different points; this can only happen if the two points are one, in which case the controls are one-dimensional (e.g. the path parallel to the line of increasing x in Figure 2.1). Now, both sequences of input f, g and g, f change the potential from ϕ_1 to ϕ_2 via ϕ^*, but the uniqueness of the tangent vectors shows that it is impossible for x and y to change by the same amounts on the alternate paths. That the same $\Delta\phi$ is associated with different translations $(\Delta x_1, \Delta y_2)$ and $(\Delta y_1, \Delta x_2)$ at steps 1 and 2 implies that

$$\begin{aligned} \frac{\partial f}{\partial y} - \frac{\partial g}{\partial x} \approx \frac{\Delta f}{\Delta y_1} - \frac{\Delta g}{\Delta x_1} &= \frac{\Delta^2\phi}{\Delta y_1 \Delta x_2} - \frac{\Delta^2\phi}{\Delta x_1 \Delta y_2} \\ &= \frac{\Delta^2\phi}{\Delta x_1 \Delta x_2 \Delta y_1 \Delta y_2} (\Delta x_1 \Delta y_2 - \Delta x_2 \Delta y_1) \neq 0. \end{aligned} \tag{2.27}$$

The last equality holds because $\det \begin{pmatrix} \Delta x_1 & \Delta x_2 \\ \Delta y_1 & \Delta y_2 \end{pmatrix} = 0$ only if the columns (or rows) are linearly dependent; they are not if the paths start together and end apart. Thus by Theorem 2.2.4, a system controlled in the tangent space by two-dimensional inputs is not a gradient. □

Algebraic proof of Theorem 2.2.5. First we prove sufficiency. Let $f_1, \ldots, f_n$ be column vectors of controls $f_i = \mathbb{F}_i^j e_j$ relative to the standard basis $e_1, \ldots, e_n$. Then the condition that, given an input set of controls, the energy completely determines the trajectory of the variables $x_1, \ldots, x_n$ on $\mathcal{M}$ is expressed as

$$\begin{pmatrix} d\phi \\ 0 \\ \vdots \\ 0 \end{pmatrix} = \left[\begin{pmatrix} \\ f_1 \\ \\ \end{pmatrix} \quad \cdots \quad \begin{pmatrix} \\ f_n \\ \\ \end{pmatrix} \right] \begin{pmatrix} dx^1 \\ \vdots \\ dx^n \end{pmatrix}, \tag{2.28}$$

meaning that the only output channel containing information about the inputs dx^i is the energy. System (2.28) is a single equation; it is solvable if it has at most one unknown. By hypothesis, this condition is met, because it is another way of expressing the one-dimensionality of the controls. Observe that there is an orthogonal matrix $\mathbb{T} = \mathbb{T}_{d\mathbf{x}}$ dependent on the current direction such that

$$\mathbb{T} \begin{pmatrix} dx^1 \\ \vdots \\ dx^n \end{pmatrix} = \begin{pmatrix} 0 \\ \vdots \\ 0 \\ du \end{pmatrix}. \tag{2.29}$$

For if

$$\mathbb{T}^{(i)} = \begin{pmatrix} \ddots & & & \\ & \cos\theta_{in} & \cdots & -\sin\theta_{in} \\ & \vdots & & \vdots \\ & \sin\theta_{in} & \cdots & \cos\theta_{in} \end{pmatrix} \quad \text{where } \theta_{in} = \tan^{-1}\left(\frac{dx^i}{dx^n}\right), \tag{2.30a}$$

then

$$\mathbb{T} = \prod_{i=1}^{n-1} \mathbb{T}^{(i)} \tag{2.30b}$$

is an orthogonal matrix that maps the direction vector $d\mathbf{x}$ by successive rotations of the projections in the i, n plane onto a single direction (the n^{th}), with magnitude equal to the sum of the squares of the components. Using $\mathbb{T}$ to refer the dynamics to a one-dimensional trajectory parallel to $d\mathbf{x}$, we can rewrite the solubility condition

of Eq. (2.28) as

$$d\phi = \left[\begin{pmatrix} \\ f_1 \\ \\ \end{pmatrix} \quad \cdots \quad \begin{pmatrix} \\ f_n \\ \\ \end{pmatrix}\right] \mathbb{T}^T \mathbb{T} \begin{pmatrix} dx^1 \\ \vdots \\ dx^n \end{pmatrix}$$

$$= \left(\mathbb{T} \left[\begin{pmatrix} \\ f_1 \\ \\ \end{pmatrix} \quad \cdots \quad \begin{pmatrix} \\ f_n \\ \\ \end{pmatrix}\right]^T \right) \begin{pmatrix} 0 \\ \vdots \\ 0 \\ du \end{pmatrix} = \begin{pmatrix} 0 & \cdots & 0 & \lambda \end{pmatrix} \begin{pmatrix} 0 \\ \vdots \\ 0 \\ du \end{pmatrix} = \lambda du. \tag{2.31}$$

Thus, the controls of a solvable system are written as a potential of mean force

$$\lambda = \frac{\partial \phi}{\partial u}, \tag{2.32a}$$

or upon taking the Legendre transform

$$u = \frac{\partial \phi}{\partial \lambda}. \tag{2.32b}$$

Therefore, the energy differential is sufficient to characterize the trajectory u on $\mathcal{M}$ if the controls can be reduced to a single vector λ.

When is this reduction possible? To prove necessity, observe that in order that the first of $n-1$ columns of the control matrix vanish under the action of $\mathbb{T} = \left[a^i_j\right]$, we must have that

$$a^1_1 f_1 + a^2_1 f_2 + \cdots a^n_1 f_n = 0. \tag{2.33}$$

This is the condition that n vectors be linearly dependent. Rearranging (2.33) and inserting $f_1 = -\frac{1}{a^1_1}\left(a^2_1 f_2 + \cdots a^n_1 f_n\right)$ into the equation for the second column

$$a^1_2 f_1 + a^2_2 f_2 + \cdots a^n_2 f_n == -\frac{a^1_2}{a^1_1}\left(a^2_1 f_2 + \cdots a^n_1 f_n\right) + a^2_2 f_2 + \cdots a^n_2 f_n = 0 \tag{2.34}$$

expresses the condition that $n-1$ vectors be linearly dependent. In general, the equation for the k^{th} column is a statement about the linear dependence of control vectors $f_k, \ldots, f_n$, conceived of as an equation for f_k in terms of the other $n-k$. The penultimate condition is

$$a^1_{n-1} f_1 + a^2_{n-1} f_2 + \cdots a^n_{n-1} f_n = \alpha f_{n-1} + \beta f_n = 0, \tag{2.35}$$

expressing the requirement that two vectors be linearly dependent. Thus, all vectors are parallel to f_n, and we conclude that the controls are one-dimensional. □

The consequence of Theorem 2.2.5 is that controlling the deviation from two reference states in general makes it impossible to know the trajectory of the system in advance. Because there are many possible paths between the same energy endpoints, the system does not know to which reference state it converges unless it also knows its position. In contrast, the reference state is always the same for a single potential well; the unique position trajectory $x(t)$ is dual to the velocity trajectory $f(t)$ specified at the start. As the same level set of ϕ is reached when controls are applied for different times, different level sets ϕ_1 and ϕ_2 are reached if f and g are applied for equal times but in different orders. The "extra" energy $\phi_2 - \phi_1$ in the noncommutative system must be stored if it is not translated into motion. A possibility considered in chapter 4 is that the dynamics can slow down if certain of the genes have more resistance or "inertia" to being transcribed than others.

Alternatively, the trajectory is completely determined by the input controls if at each step they are linearly dependent under the action of $\mathbb{T}$, i.e., if they add up to the (orthogonal) direction of motion $d\mathbf{x}$. The reaction force vector $f_i = \frac{\partial \phi}{\partial x^i}$ is orthogonal to the direction vector dx^i so that the area they span is equal to the energy increment (see Materials and Methods section 4.4.1.3 in chapter 4). With only one reference state, the Legendre transform of ϕ is always directed along level sets of ϕ, and the direction $d\mathbf{x}$ achieving the specified potential difference $d\phi$ is the orthogonal one down the gradient. In other words $\mathbb{T}$ is always a rotation of $90°$. But with n directions, $\mathbb{T}_{d\mathbf{x}}$ represents a $90°$ rotation in a skew coordinate system (cf. tan and gray areas in Figure 2.1); the rotation relative to fixed coordinates is not known until the position in space is known, and so the sequence of $\mathbb{T}_{d\mathbf{x}}$'s is not known before the trajectory is. Therefore, the n-dimensional controls determine the trajectory in advance only if you check at all steps that they induce transport between level sets of ϕ. By the time you've done this, the system is no longer determined in advance! The interpretation favored here is that it is possible to have advance knowledge of the future, but that interpreting this knowledge requires all time up until when the future becomes the present.

2.2.4 The parsimony principle

The results so far paint a picture of progressive lineage restriction on a smooth potential surface. The requirement for time is shown here to be conjugate to the spatial connectivity of developing cells. We argue that there is a "kernel" of information in the egg that can be made to fit within the adult either by specifying all fates at once or letting development proceed over time. The minimal size

requirement for fitting this information in space-time follows from the parsimony principle.

Development is at heart a process taking a system from high to low potential over time. Theorem 2.2.5 states that the potential difference between the end points is sufficient to characterize the trajectory when there is only one velocity being independently controlled. We can understand this statement as a condition on energy partitioning using the *parsimony principle*. The conversion of energy is measurable in single-cell data that show increased RNA splicing velocity [148] and decreased expression heterogeneity [182, 217]. The simplest or most parsimonious explanation for why cells moves faster (through expression space) when their fate is more certain is that potential energy is converted into kinetic. In more abstract terms, one dimensionality means that the trajectory never leaves the surface ϕ, because one direction $\frac{\partial f}{\partial y}$ is always balanced by another $\frac{\partial g}{\partial x}$ during the step $\Delta\phi$. One-dimensionality also means that the higher derivatives of the curve of ϕ versus t are zero, although this does not mean the surface ϕ has to have a constant slope: the marble follows a zig-zag (or "canalized") path down the hill if the path suddenly becomes too steep. In the absence of other information, the most we can say is that each time point is the same as the last, being characterized by the same decrease in potential.

The tradeoff between pluripotency and certainty of fate reflects a tradeoff in a conserved quantity called information. Just as the sum of potential and kinetic energy is conserved for the marble, so the total information present in the egg is constant in the space and time of development. The increment of a function $I(z) = I(t,s)$ of conjugate variables can be regarded as the pairing $\langle \boldsymbol{\phi}, \boldsymbol{\psi} \rangle$ of conjugate n-dimensional vector fields (see Materials and Methods section 4.4.1.3 in chapter 4), so that its space-time derivative of I can be written using a $2n$-dimensional vector field

$$\frac{dI}{dz} = \mathbf{X}(I) = dI \cdot \mathbf{X}, \tag{2.36}$$

where the second equality follows from writing $\mathbf{X} = (\boldsymbol{\phi}, \boldsymbol{\psi}) = \phi(t,s)\frac{\partial}{\partial t} + \psi(t,s)\frac{\partial}{\partial s}$ in coordinates and applying the chain rule. We hypothesize that development can be schematized in Figure 2.1 as the transformation of the locus of equipotential fates from a straight line to a curved one. If information is conserved during development, we should find it entirely contained in the area spanned by two equipotential lines. According to the parsimony principle, we are agnostic as to how the information is distributed; our best guess is that the areal distribution is uniform. We may write

this condition as the vanishing of the variation

$$\delta I = \delta \oint dI\,(\mathbf{X}) = \oint \phi ds + \psi dt = \delta \int\int \left(\frac{\partial \phi}{\partial t} - \frac{\partial \psi}{\partial s}\right) ds dt = 0, \tag{2.37}$$

where we have applied Green's theorem [77] to a counterclockwise loop in the (t, s) plane. The condition holds for all bounding space-time curves if the integrand on the r.h.s. of (2.37) vanishes, i.e., if

$$\frac{\partial \phi}{\partial t} = \frac{\partial \psi}{\partial s}. \tag{2.38}$$

Compare this equation with the Cauchy-Riemann equations (2.14), where now the transformed time variable $t \mapsto x + y$ is associated with increasing distance from the reference states and the transformed space variable $s \mapsto x - y$ with balance between them.

Eq. (2.38) hypothesizes that collective development is more like flow of an incompressible fluid or straining of a rubber band than it is a marble rolling downhill. Cell fates that are nearby (with respect to the expression space coordinate s) are related to each other by how far back in time they diverged. There is no need for extra extra barriers between alternative fates in the present because the only way they communicate is by going backwards in time. We can also understand the balance implied in Eq. (2.38) by the idea that the egg contains a "kernel" of information to be distributed among alternative fates (Figure 2.2A). With a small number n of signaling inputs, each fate is encoded in time by one of n^T possible sequences over T discrete events. That these fates are encoded in the egg implies that the total information is bounded by

$$I \leq n^T \tag{2.39a}$$

$$\log I \leq T \log n. \tag{2.39b}$$

Eq. (2.39b) shows that it is much more efficient to increase the number of steps T when assembling complex instructions than it is to increase the number of inputs. Both strategies lead to the same total information I, but it requires an exponential increase in n to specify all fates in a single step (blue area in Figure 2.2A); a linear increase in T encompasses the same information using only a few n (red area). This tradeoff is examined in chapter 3 with specific coding models.

The infinitesimal version of Eqs. (2.39) expresses the idea of local balance. If at some point in time or expression space the information contained in one cell exceeds the amount allocated to in by the parsimony principle, its neighbors in time

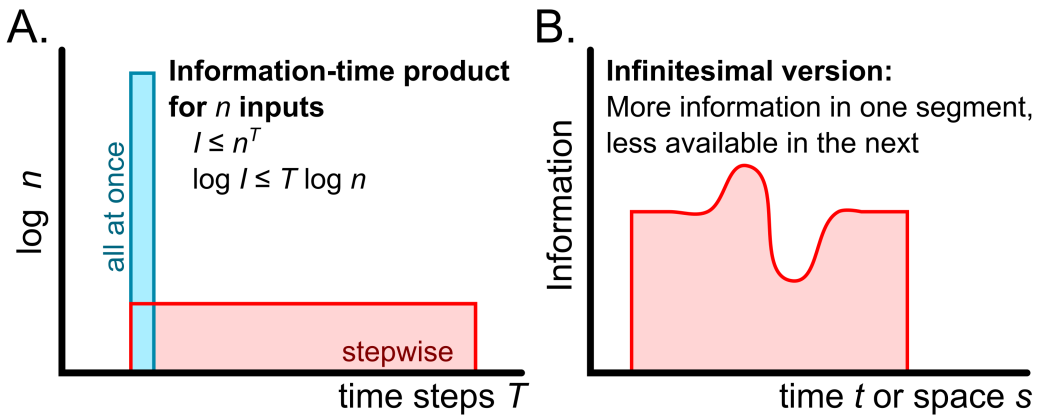

Figure 2.2: The information kernel. (**A**) The parsimony principle is at work in two alternative plots of total information. With an exponential number of inputs, all fates can be specified in one step, whereas using more steps and fewer inputs results in a fatter rectangle of the same area (not to scale). Conservation reflects the fact that the egg contains the total information content of the adult. (**B**) The infinitesimal version of the parsimony principle shows that locally increasing the number of signaling inputs necessarily decreases the information allocated later.

and space must have less (Figure 2.2B). A biological example is lateral inhibition in the Delta-Notch signaling pathway. A cell expressing the Delta ligand inhibits its Notch-expressing neighbors from adopting a neural fate [9, 114]. Delta is a very informative gene, defining the fate of both the expressing and receiving cell. But by the balance condition (2.38), excess information that flows into one cell now must flow out again later. In other words, the cost of extra knowledge is a limited horizon; the future moves toward the present until the information rectangle becomes a spike. An investigation of such space-time trade-offs in the physics of strings is described in chapter 4.

2.3. Conclusions

Here we have provided a two-gene example of how a cell can fail to know its fate in advance. The parsimony principle required that the cell at each step see the same decrease in information instead of following its original trajectory to a minimum. In answer to the paradox posed in section 2.1, although a cell might know its end at the start, it does not know how to get there. The biological basis for the parsimony principle was that multipotent cells have a range of expression states along a level set of the potential. Absent of other sources of information during the process, development was autonomous if cells maintained this relationship in time. The balance condition (2.38) meant that some steps could break the equipotential

relationship by locally increasing the signaling input into other cells, but at the cost of the endpoint being reached earlier. Development of connected cells entails a reimagining of the Waddington's analogy of the marble in terms of an elastic string or an incompressible fluid. Single-cell sequencing technologies that maintain cells' spatial context [157, 244] are beginning to make this hypothesis testable.

Chapter 3

NONCOMMUTATIVE BIOLOGY: SEQUENTIAL REGULATION OF COMPLEX NETWORKS

1. Letsou W, Cai L. Noncommutative Biology: Sequential Regulation of Complex Networks. PLoS Comput Biol. 2016; 12: e1005089. DOI: 10.1371/journal.pcbi.1005089.

3.1. Introduction[1]

A fundamental question in systems biology is how a small number of signaling inputs specifies a large number of cell fates through the coordinated expression of thousands of genes. This problem is especially challenging given that gene regulatory and other types of networks in biology tend to be highly interconnected and their regulators promiscuous, with regulators affecting multiple targets and targets being affected by multiple regulators. Examples of this architecture include: transcription factor binding networks in bacteria [166], yeast [18, 103], plants [215], and animals [195, 226]; cellular signalling pathways involved in growth and differentiation [123, 130, 164]; the interactome of protein kinases and phosphatases [232, 279]; and synaptic connections between different layers of the brain [234]. Furthermore, because the targets and regulators are often well-mixed and mutually accessible in the cell, most actions are likely to have nonspecific and undesired effects.

At the same time, regulatory molecules drive networks to a large number of highly specific outcomes or cell fates. Although there are approximately four hundred canonical cell types in the adult human [281], recent single-cell RNA expression profiling experiments in the developing embryo [201, 300], brain [303], hematopoietic system [133, 179], and other organs [42, 273] have indicated that there may be thousands more.

Given there are only a few signaling pathways used in metazoan development [91, 283], understanding how cells reach their final outcomes when there are fewer regulators than fates and/or targets is an unsolved problem. One extensively

[1]The formatting of the original article has been made to agree with the rest of this thesis. Typos have been fixed, the word "the" was deleted before theorems in Materials and Methods sections 3.4.4, 3.4.5, and 3.4.8, and a few non-critical mathematical errors were corrected in section 3.2.8.

studied solution for the control of promiscuous gene networks is combinatorial binding of DNA-binding transcription factors (TFs) at the promoter [43, 63, 72, 113, 137, 138, 268, 212, 298]. At the level of individual promoters, combinatorial binding ensures that individual genes are ON only when specific combinations of TFs are present (Figure 3.1A). However, on the genome level, combinatorial regulation restricts which sets of genes may be ON at the same time. For example, using AND logic, gene H in Figure 3.1A is only ON in the case that the three TFs K_1, K_2, and K_3 are concurrent at the H promoter; but these stringent requirements mean that H can never be transcribed independently of the less highly-regulated genes A-G. (A similar conclusion holds for OR logic.)

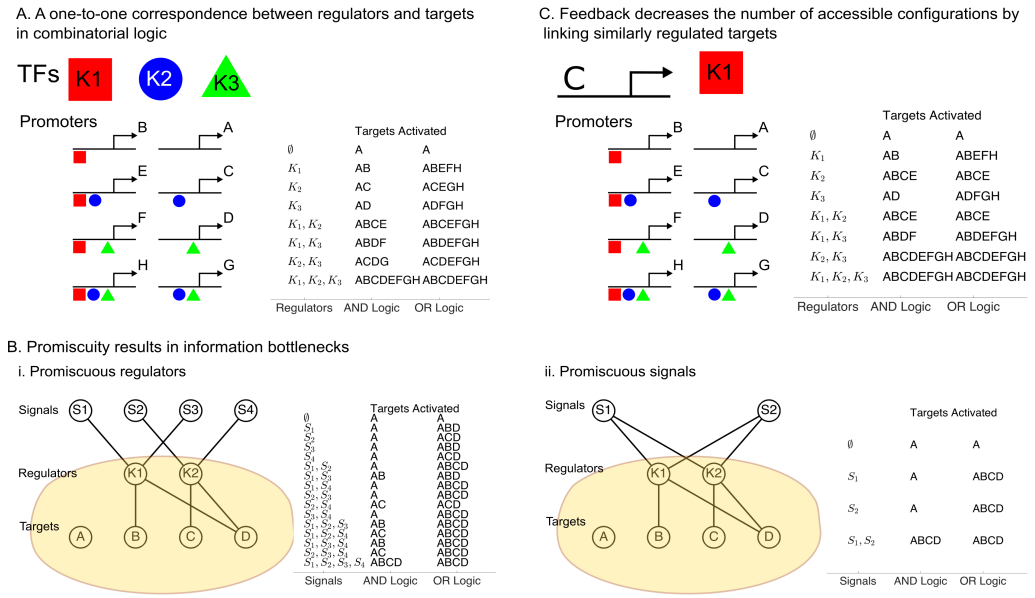

Figure 3.1: Combinatorial logic bottlenecks information flow in networks. **(A)** The number of ways that three TFs (K_1, K_2, K_3) can be ON or OFF (tabulated at right) is the same as the number of ways they can bind at promoters (left). An equal number of gene expression states are observed whether the TFs use AND logic (requiring all factors be present) or OR logic (requiring at least one of the factors). **(B)** Signal-to-target information flow is bottlenecked by regulators if (*i.*) the regulators respond to multiple targets, or (*ii.*) if the signals activate multiple regulators. The allowed target states are tabulated for signals using AND logic and regulators using AND/OR logic. **(C)** A feedback loop causes constitutive activation of a regulator (K_1) and leads to fewer accessible configurations (tabulated at right).

In fact, using combinatorial control, there is a one-to-one correspondence between configurations of the targets and configurations of the regulators. As shown in Figure 3.1A, the ON/OFF states of 3 TFs uniquely define the binding combinations

at $2^3 = 8$ promoters. A similar conclusion holds when the regulators are expressed in a graded fashion.

This one-to-one correspondence is the fundamental limitation of combinatorial regulation: it requires an equal number of regulators and independently controlled targets and/or cell fates. Applied to embryonic development, combinatorial control requires that hundreds or thousands of cell-type specific TF combinations be generated in a spatially precise manner at the start. However, the combinatorial scheme does not explain how the TF states are regulated in the first place, and thus it offers no new insight into how cell fate is specified.

The limitations of combinatorial logic can also be understood from an information theoretic point of view. In particular, it is impossible to specify arbitrary cell fates if the regulatory layer bottlenecks the capacity of the targets to receive messages from extracellular signals. It is known that some ten to twenty types of signals [91, 283] converge onto membrane-bound regulators in many different combinations, permitting messages to be passed to the downstream targets. Much of this information stands to be lost, however, if the network relies on combinatorial logic alone: the regulatory layer simply cannot transmit messages in their entirety if there are more signals than regulators. Thus, combinatorial logic strongly circumscribes what fates are ultimately reachable. Cell fate information is lost not only if the signals are more numerous than the regulators, but also if the connections between signals and regulators are promiscuous (Figure 3.1B). When different signals activate the same regulators (Figure 3.1B.i), certain signaling inputs become redundant. On the other hand, when same signal activates different regulators (Figure 3.1Bii), some of the regulators become redundant. One may determine by direct enumeration exactly how redundancy decreases the number of configurations available to the targets (Materials and Methods sections 3.4.1 and 3.4.2). These preliminary conclusions are at odds with the observation that signaling molecules are deployed over time in a complex code [129]. How do these messages in the signal space reach the targets if the regulatory layer imposes a bottleneck on information flow?

In addition, feedback regulation—a common feature of regulatory networks—exacerbates information bottlenecks when coupled with combinatorial logic. Stated another way, feedback merely widens the basin of attraction of certain promoter configurations at the expense of the number of distinct configurations. In Figure 3.1C, constitutive expression of K_1 by C means that C is never ON independently of the targets regulated by K_1. Thus, the number of accessible configurations decreases from 8 to 6 without allowing new target configurations to be explored.

We need an alternative to combinatorial logic in cell fate specification that overcomes information bottlenecks. Here, we considered time-ordered control schemes, which we refer to as sequential logic. In this scheme, regulators can be applied in a stepwise manner; the entire sequence matters, so the final configurations can differ if the same regulators are permuted in time. In order for different temporal sequences to carry distinct information, the actions of the regulators must be *noncommutative*. This is the case, for example, when a regulator protects its targets from the action of another regulator, as when loci recruited to repressive chromatin compartments are protected from further modification [52, 236].

While it is not surprising that noncommutative sequences like this result in different outcomes at the single promoter level, these simple mechanisms may have nontrivial implications for regulation at the genome level. In particular, noncommutativity permits the same regulators to be used at different times with distinct effects. This is seen in development when ubiquitous signaling molecules like FGF family members exert different effects depending on the time and context of their expression [132, 178, 249, 287]. Reuse of factors could greatly expand the information capacity of the major signaling pathways.

A number of examples show that noncommutativity may be a general strategy in other areas of biology. In hematopoietic stem cells, activation of GATA2 and C/EBPα in different orders results in different cell fates [131]. In neurobiology, different temporal orderings of the same inputs lead to distinct firing patterns [1, 93, 183]. In the field of synthetic biology, a DNA switch was developed that could detect the order in which invertase enzymes were applied [108]. And in evolutionary biology, the order in which mutations arise was recently implicated in determining a genotype's fitness [34, 68, 209, 292]. There is also accumulating evidence for sequential logic in transcriptional control: signaling molecules and TFs in mammalian cells, including ERK [5], NF-$\varkappa$B [139, 193], p53 [150], as well as in yeast [45, 61, 158] have been observed to pulse, suggesting that TF timing may be used to control the transcriptional state of the cell.

By applying sequential logic, we show that, even in complex and promiscuously regulated networks, specific target configurations can be reached using a temporal sequence of regulators. In particular, we consider two models inspired by (i.) kinase/neural networks and (ii.) chromosome folding and show analytically that both scale super-exponentially. We further show that noncommutative networks are robust to the loss of regulators, suggesting a mechanism for regulator evolution. We also show that regulators induce different orbits in expression space, which is

related to the number of networks that can be controlled in parallel. We conclude by discussing how these models apply to interconnected networks in and outside biology and by providing possible experimental tests of the theoretical concepts. Theorems and proofs are given in the Materials and Methods.

3.2. Results

3.2.1 A time-sequence ratchet model generates more diversity than combinatorial logic in multiply-connected networks

To consider how time-ordered sequences of regulators can specifically control groups of targets, we begin by analyzing a generic two-layer network that is an extension of combinatorial logic (Figure 3.2, Materials and Methods sections 3.4.1 and 3.4.2). In this model, each regulator controls multiple targets, and each target is accessible to any of its regulators. The model is meant to be analogous to the cellular environment wherein regulators and targets are well-mixed. For example, targets could be substrate proteins capable of multi-site phosphorylation [228, 270], and regulators the kinases and phosphatases. Targets could also be neurons and regulators their upstream excitatory and inhibitory inputs [234]. We denote by K the set of activators (i.e., kinases) and P the set of deactivators (i.e., phosphatases). Each target has a ladder of (integer-valued) *states*, and together the states of the targets are a *configuration* of the network. (This distinction is in contrast to the common usage of "state" as a gene expression vector.) An additional parameter, the threshold T, determines the number of rungs on the ladder. Regulators ratchet the targets through their states, and only targets that have reached threshold will be ON at the end of a sequence of regulators. If each target in the group can be controlled by a unique combination of K's and P's, what ON/OFF configurations are possible?

In this model, termed the ratchet network (Figure 3.2A), each of n K's and m P's control $N = \binom{n}{l_n}\binom{m}{l_m}$ unique targets, with the connectivity parameters l_n and l_m specifying the number of regulators to which each target connects. Consider the sequence $K_1K_2P_1$ acting on the targets A, B, C, and D (Figure 3.2B). In the final configuration, B and D are ON together even though no single K connects to both, and A and C are OFF, even though both share and activator with B and D. Therefore, this simple model illustrates the important point that similarly regulated targets can be in independently controlled using sequential logic.

With threshold $T = 1$, not all configurations are reachable. Observe that there is no way to specifically activate A and D while leaving B and C OFF. This result is surprising given that A and D share no regulators: specificity depends

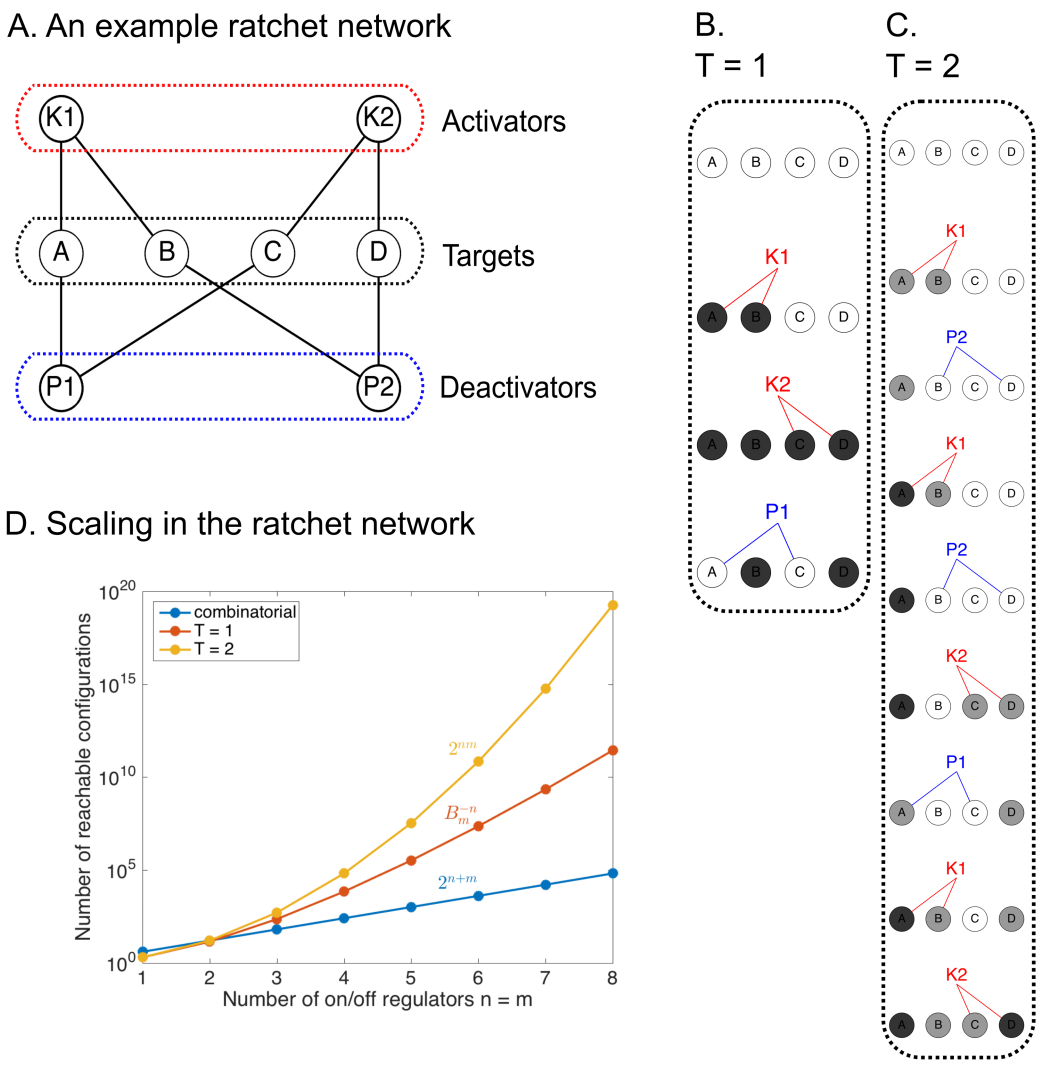

Figure 3.2: The ratchet model attains configurations not reachable by combinatorial logic. **(A)** The ratchet model for $n = m = 2$ and $l_n = l_m = 1$. Activators (K's) and deactivators (P's) turn targets ON and OFF, respectively. **(B)** An example temporal sequence for the network with a threshold equal to 1. Black targets are in the 1 state. **(C)** An example sequence for the same network with threshold equal to 2. Gray targets are in the 1 state, and black targets are in the 2 state. **(D)** Scaling laws for the threshold $T = 1$ (red) and $T = 2$ (yellow) are shown for symmetric networks ($n = m$). A comparison to combinatorial logic with an equivalent number of regulators ($n + m$) is shown in blue.

on the network as a whole, not just individual targets. By going to $T = 2$, the forbidden configuration becomes accessible (Figure 3.2C), along with all ON/OFF states (below).

3.2.2 A combinatorial formulation of the model as a connectivity matrix

The model described above can be formalized as a combinatorial object that we refer to as the *connectivity matrix* $\mathbf{A}$. This formulation is useful because it is amenable to studying scaling, and it permits a direct comparison between non-commutative ratchet networks and standard combinatorial logic. For the interested reader, the models considered in this paper have a universal formulation as non-commutative matrix operators on the vector space of configurations (Materials and Methods section 3.4.9).

Typically, the state of N targets is represented as an N-dimensional vector. If each target is controlled by a unique (K_i, P_j) pair (i.e., $l_n = l_m = 1$), the $N = nm$-dimensional vector can be re-formulated as an $n \times m$ matrix

$$\mathbf{A} = \begin{array}{c} \\ K_1 \\ \vdots \\ K_n \end{array} \begin{array}{c} \begin{array}{ccc} P_1 & \cdots & P_m \end{array} \\ \begin{pmatrix} A_{1,1} & \cdots & A_{1,m} \\ \vdots & \ddots & \vdots \\ A_{n,1} & \cdots & A_{n,m} \end{pmatrix} \end{array}, \tag{3.1}$$

where each entry $\mathbf{A}_{i,j} \in \{0, 1, \ldots, T\}$ is the state of the target regulated by K_i and P_j. For example, the connectivity matrix for the network in Figure 3.2 is

$$\mathbf{A} = \begin{array}{c} \\ K_1 \\ K_2 \end{array} \begin{array}{c} \begin{array}{cc} P_1 & P_2 \end{array} \\ \begin{pmatrix} A & B \\ C & D \end{pmatrix} \end{array}. \tag{3.2}$$

In general, a regulator may connect to multiple targets (i.e., $l_n, l_m > 1$, see below), so that each entry of $\mathbf{A}$ may be thought of as an M-dimensional vector (M determined in Materials and Methods section 3.4.1). It turns out that this is an unnecessary complication; we instead let each $\mathbf{A}_{i,j} = 1$ if at least one of the M targets regulated by K_i and P_j is ON, and $\mathbf{A}_{i,j} = 0$ only if all M targets are OFF.

In this formulation K_i and P_j are raising and lowering operators that map $n \times m$ matrices to $n \times m$ matrices via the rules

$$\begin{aligned} K_i(\mathbf{A}_{i,j}) &= \begin{cases} \mathbf{A}_{i,j} + 1 & \text{if } \mathbf{A}_{i,j} < T \\ \mathbf{A}_{i,j} & \text{if } \mathbf{A}_{i,j} = T \end{cases} \\ P_i(\mathbf{A}_{i,j}) &= \begin{cases} \mathbf{A}_{i,j} - 1 & \text{if } \mathbf{A}_{i,j} > 0 \\ 0 & \text{if } \mathbf{A}_{i,j} = 0. \end{cases} \end{aligned} \tag{3.3}$$

From Eq. (3.3), any sequence $K_{i_1} K_{i_2} \cdots K_{i_k}$ of all K's is commutative, because any target controlled by $t \leq k$ of the K's will be in state $t \leq T$ at the end of the

sequence, regardless of the order. A similar argument holds for the P's. However, sequences consisting of both K's and P's are in general noncommutative. This is due to edge effects when $\mathbf{A}_{i,j} = 0$ or T. If $\mathbf{A}_{i,j} = T$, for example, then $K_i P_j$ results in $\mathbf{A}_{i,j} = T - 1$, whereas $P_j K_i$ gives $\mathbf{A}_{i,j} = T$. Therefore, $\mathbf{A}$ gives insight into both the configuration of the targets and the noncommutativity of the regulators.

The problem of determining the number of accessible configurations in a network is reduced to finding the number of matrices satisfying certain patterns. For example, combinatorial logic with $T = 1$ corresponds to the special case in which the only sequences are the 2^n combinations of the n K's. In an $n \times 1$ connectivity matrix, activating K_i corresponds to turning all 0's in row i into 1's. There are 2^n matrices generated by this procedure. More complicated cases of combinatorial logic can be studied this way (Materials and Methods section 3.4.2), but it turns out that the total number of network configurations is always less than 2^{n+m}, with $n+m$ the total number of regulators. This is important because noncommutative models can bypass the exponential limit.

3.2.3 The ratchet model scales as the poly-Bernoulli numbers

We used the connectivity matrix representation of the ratchet network to determine the scaling as function of the number of regulators n and m, with each target connected to a unique (K, P) pair (i.e., $l_n = l_m = 1$) and the threshold $T = 1$. K_i turns 0's to 1's in row i and P_j turns 1's to 0's in column j. The rules are consistent with the one-pot reaction model in which all substrates receptive to K_i are promoted when K_i is active. For example, the sequence $K_1 K_2 P_1$ in Figure 3.2B can be recast as

$$\begin{pmatrix} 0 & 0 \\ 0 & 0 \end{pmatrix} \xrightarrow{K_1} \begin{pmatrix} 1 & 1 \\ 0 & 0 \end{pmatrix} \xrightarrow{K_2} \begin{pmatrix} 1 & 1 \\ 1 & 1 \end{pmatrix} \xrightarrow{P_1} \begin{pmatrix} 0 & 1 \\ 0 & 1 \end{pmatrix}. \tag{3.4}$$

The main result is that $\mathbf{A}$ must avoid the patterns $\begin{pmatrix} 1 & 0 \\ 0 & 1 \end{pmatrix}$ and $\begin{pmatrix} 0 & 1 \\ 1 & 0 \end{pmatrix}$ in any 2×2 sub-block (Materials and Methods section 3.4.3). Brewbaker [38] enumerated the $n \times m$ binary matrices avoiding these patterns and showed that they scale as the poly-Bernoulli numbers [136]

$$B_m^{-n} = B_n^{-m} = \sum_{j=0}^{m} (-1)^{(n+j)}\, j!\, (j+1)^n \left\{ {n \atop j} \right\} = \sum_{j=0}^{\min(n,m)} (j!)^2 \left\{ {m+1 \atop j+1} \right\} \left\{ {n+1 \atop j+1} \right\}, \tag{3.5}$$

where $\left\{ {n \atop j} \right\}$ is a Stirling number of the second kind, defined combinatorially as the number of ways to put j labelled balls into n unlabelled boxes such that no box

is empty [175]. These numbers scale not quite as fast as $2^N = 2^{nm}$, but much faster than 2^{n+m}, the maximum number of states in the equivalent combinatorial network (Figure 3.2D). Thus, a simple time-sequence model is able to generate super-exponential scaling.

3.2.4 All binary ON/OFF states are reachable for an increased threshold

Are more configurations accessible if multiple activation events are needed before reaching threshold? For example, neurons require the summation of multiple excitatory inputs to reach action potential, and proteins need to be phosphorylated at multiple sites before they are activated [228, 270]. We found that by increasing the threshold to $T = 2$, all 2^N ON/OFF configurations of the N targets become reachable. In the connectivity matrix formulation, $\begin{pmatrix} 1 & 0 \\ 0 & 1 \end{pmatrix}$ and $\begin{pmatrix} 0 & 1 \\ 1 & 0 \end{pmatrix}$ are no longer forbidden, which we show with an inductive proof (Materials and Methods section 3.4.4). This scaling law (Figure 3.2D) achieves the maximum of reachability and specificity; it far exceeds the scaling 2^{n+m} of the combinatorial model.

Being able to reach the entire ON/OFF space of N targets is overkill for most biological networks, which only display a relatively small number of stable configurations. The major implication of this result is that multiple levels of activity permit more targets to be controlled independently.

3.2.5 Increased regulatory connectivity generates robustness

As sequential logic allows a large number of configurations to be reached in a complex network, we asked whether increasing the connectivity of the network (l_n and l_m) can maintain the specificity of the network while making it robust to the loss of a regulator. This is potentially relevant to evolution of biological networks, because redundant connections allow the network to repurpose regulators for new functions without severely impairing existing ones [267].

In the ratchet model, an increase in the connectivity parameters to $l_n = 2$ K's and $l_m = 2$ P's permits multiple targets to share a common (K, P) pair (Figure 3.3A). The connectivity matrix incorporating the extra links in the network in Figure 3.3A is

$$\mathbf{A} = \begin{array}{c} \\ K_1 \\ K_2 \\ K_3 \end{array} \begin{array}{c} \begin{array}{ccc} P_1 & P_2 & P_3 \end{array} \\ \begin{pmatrix} ABDE & ACDF & CDEF \\ ABGH & ACGI & BCHI \\ DEFG & DFGI & EFHI \end{pmatrix} \end{array}. \tag{3.6}$$

Now that each entry of $\mathbf{A}$ is a group of $M > 1$ targets, it makes sense to track the state

of the group as a whole with a single number $\mathbf{A}_{i,j}$. Even though a target appears in multiple entries of $\mathbf{A}$, the rules prevent a regulator from altering the state of groups at remote locations (e.g. K_1 cannot change the state of the group at $\mathbf{A}_{2,2}$).

We prove in the Materials and Methods that all sequences using at least $n - l_n + 1$ K's and $m - l_m$ P's are redundant with shorter sequences (Figures 3.3B and C, Materials and Methods section 3.4.5). For example, the sequences $K_1K_2K_3$ is required to turn ON all targets in the case $l_n = l_m = 1$, but if $l_n = l_m = 2$, the shorter sequences K_1K_2, K_1K_3, and K_2K_3 have the same effect. We derived a recursive formula that eliminates the redundant sequences in each (n, m, l_n, l_m) instance to derive the number of sequences in $(n, m, l_n + 1, l_m)$ and $(n, m, l_n, l_m + 1)$ (Figure 3.3D and S2 Fig). The formula agreed exactly with an algorithm designed to find all minimal length sequences (Materials and Methods 3.4.5). Notably, increasing l_n, l_m reduced the number of configurations. We observed a similar effect in combinatorial logic (S1 Fig).

To investigate the robustness of sequential logic networks, we studied the effect of deleting regulators in increasingly connected networks on the number of reachable configurations (Figure 3.4A). We hypothesized that sequences that activate similar subsets of targets should be able to recoup permanently lost configurations. To test this, we computed the normalized correlation coefficient between configurations in the network using all K's (the full network) and configurations in the network without K_1 (the impaired network), subject to the constraint that those configurations were reached using longer sequences (Figure 3.4B). To focus on the recoverable fraction, we deleted all configurations that had an exact match. Highly similar configurations (yellow) clustered to the right of the plot, indicating that longer sequences can be used to recover lost configurations.

How similar are the recouped configurations? As connectivity increased, the maximum similarity became increasingly concentrated above 0.8 (Figure 3.4C). There is generally a tradeoff between reachability and the size of the fraction above 0.8 (Figure 3.4D). The tradeoff is nonlinear, however: using $l_n = 2$ gave the greatest increase recoverability for the smallest loss of configurations, showing that an intermediate level of redundancy can buffer the network to loss of regulators. The above analyses demonstrate that specificity of control is not compromised when regulators are lost or repurposed in heavily interconnected networks.

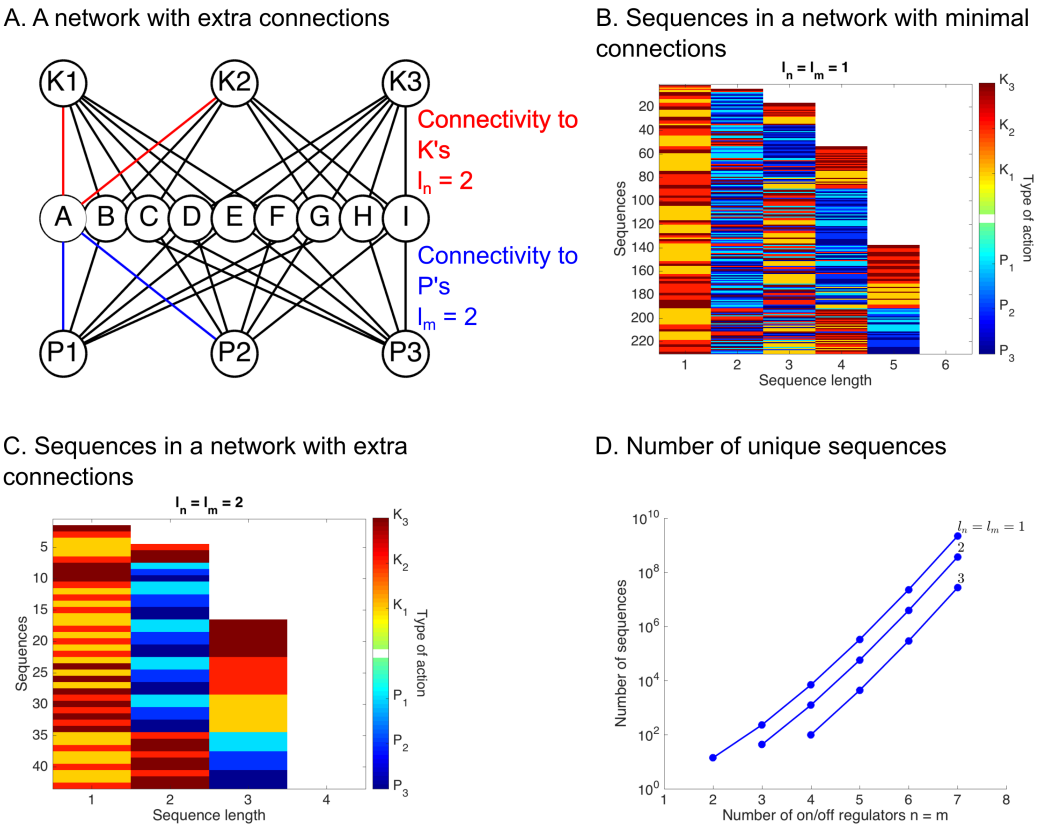

Figure 3.3: Multiple connections in the ratchet network decreases the number of configurations. **(A)** An example network where each target has $l_n = 2$ connections to the K's (red) and $l_m = 2$ connections to the P's (blue). **(B)** A list of the minimal length sequences generating unique configurations in the network in when $l_n = l_m = 1$. Red bars are K actions and blue bars are P actions. **(C)** The list of minimal length sequences when $l_n = l_m = 2$. Some sequences now map to the same configuration. **(D)** Analytical solution for the number of sequences as a function of $n = m$ for different $l_n = l_m$ families.

3.2.6 Sequestration networks generate diversity through protected states

In the ratchet model, all targets are accessible to their regulators at all times. However, in some cases targets may be shielded from regulators: for example, genes can be silenced by sequestration in various nuclear compartments [211, 310]. This was seen in a landmark study by Filion and coworkers [76], who used a DNAse accessibility assay to show that genes associate with different regulators depending on their chromatin "color" or accessibility status.

To study the effect of accessibility and silencing on activating specific subsets of genes, we constructed the following sequestration model. In addition to the OFF state 0 and the ON state 1, each target/gene is endowed with additional orthogonal states 2 to n (allowing for a total of $2^{n-1} - 1$ genes). If RNA polymerase

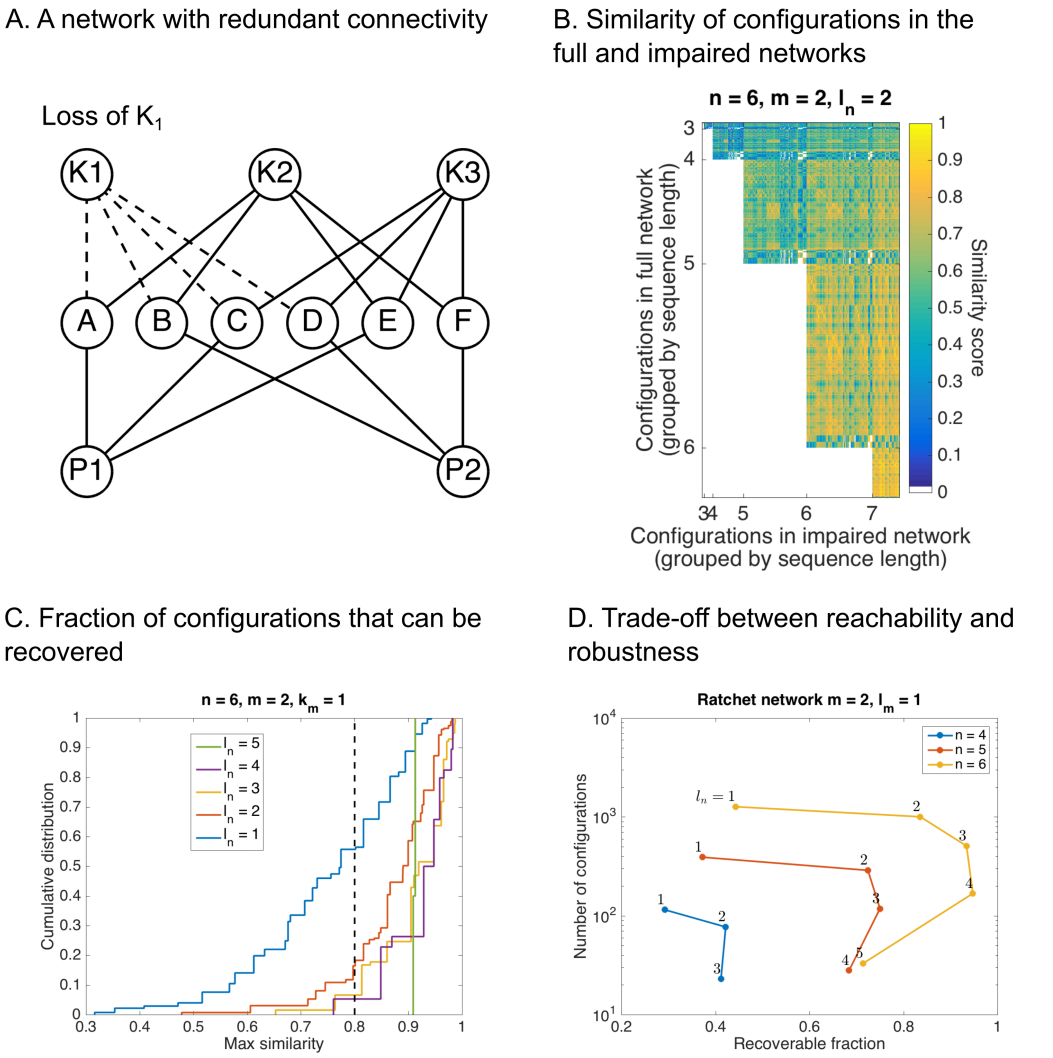

Figure 3.4: The ratchet network is robust to loss of a regulator. (A) A schematic illustration of the experiment. The regulator K_1 was deleted from networks with $m = 2$ P's and variable n for different values of the connectivity l_n. The resulting number of configurations was computed by simulation. **(B)** Correlation coefficient between configurations in the full network (all K's; rows) and the impaired network (without K_1; columns). All rows with exact matches were deleted. **(C)** Cumulative distribution $F(x)$ of the maximum correlation coefficient x for each row in C for different values of l_n. The dashed line is the similarity cutoff 0.8. **(D)** Tradeoff between reachability and robustness. The number of reachable configurations as a function of (n, l_n) is plotted versus the fraction of states above the similarity cutoff 0.8 (i.e., $1 - F(0.8)$) for different values of n.

(RNAP) is associated with K_1, what genes can be independently activated? In this model (Figure 3.5) a regulator K_i promotes targets in the 0 state to state i, and P_i returns targets in state i to 0. Any target in state i is protected from regulators other than P_i. As an example of gene regulation on a three-dimensional chromosome

(Figure 3.5A), the sequence $K_3K_4K_1P_3P_4$ first clusters all genes having a 3 in a repressive compartment, and then the remaining genes having a 4 in another repressive compartment. The net effect is that RNAP can only act on the gene represented by $\{1, 2\}$. We represent this abstractly as a configuration vector of k-armed targets (Figure 3.5B), where each entry corresponds to the state $\{0, 1, \ldots, n\}$ of a gene able to access $k \leq n$ of the states (see below for a mathematical description of the model). Therefore, protected states in the sequestration model allow genes to be transcribed specifically in a well-mixed environment.

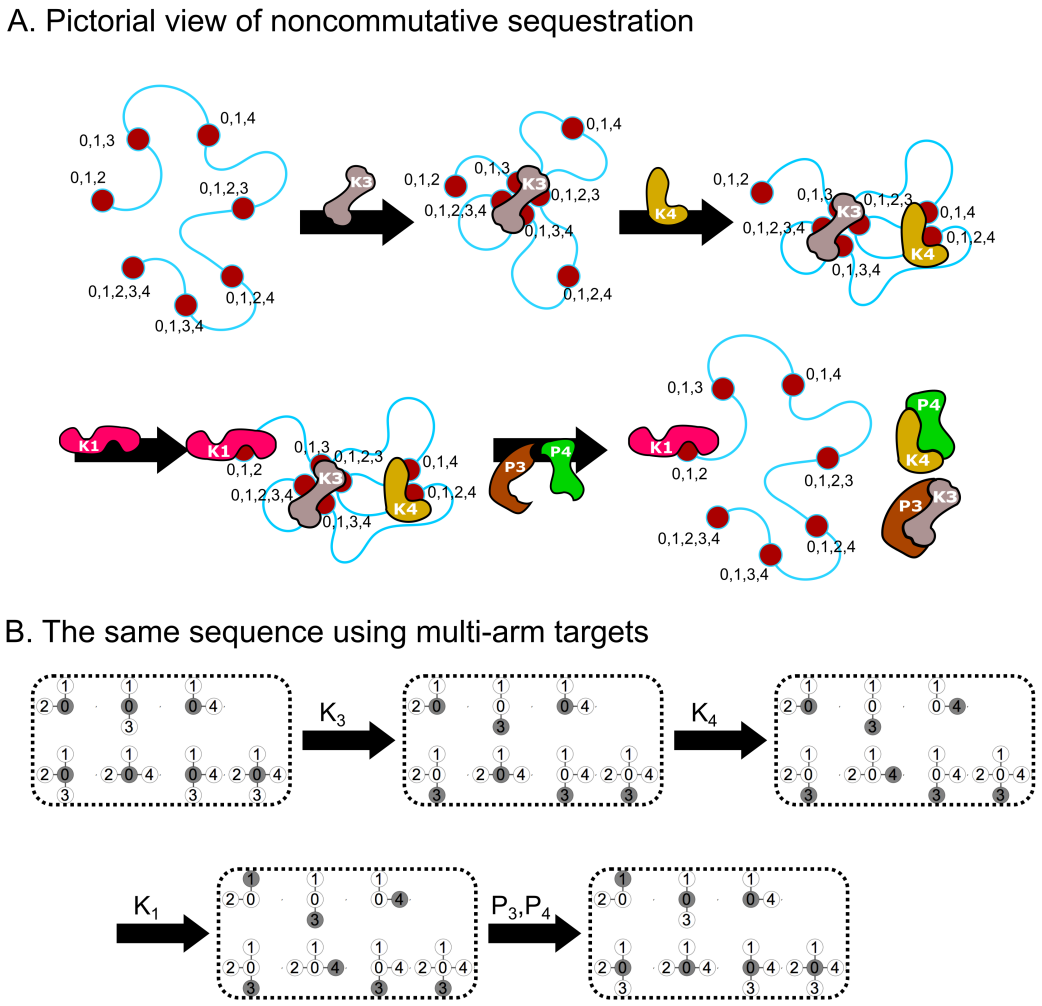

Figure 3.5: The sequestration network is a noncommutative model of gene regulation by chromosome folding. **(A)** A sequence of moves $K_3K_4K_1P_3P_4$ on a hypothetical chromosome with K and P actions represented as DNA-binding factors and K_1 playing the role of RNAP. Red circles correspond to genes and numbers correspond to allowed binding partners. **(B)** The same sequence in A represented as a collection of targets with up to $n = 4$ arms. For example, the target $\{0, 1, 2\}$ corresponds to the gene locus with states 1 and 2 in A. The filled circle represents the current state.

We derived (see below) that the number of reachable configurations scales with the number of regulator pairs n as

$$f(n) = 2^{2^{n-1}-1} - \sum_{m=2}^{n-1} \binom{n-1}{m} \left(2^{\Sigma_{k=3}^{m} \binom{m}{k-1}} - 1\right) \left(2^{\Sigma_{k=3}^{m} \binom{n-1}{k-1} - \binom{m}{k-1}}\right). \tag{3.7}$$

For $n = 1, 2, 3, 4, 5, 6$, this formula gives $f(n) = 1, 2, 7, 89, 16897, 780304385$ (Figure 3.6). We also relaxed the constraint that all genes have a 1 state (allowing for a total of $2^n - 1$ genes) and found that the number of configurations scales as $c_n = 2, 7, 94, 37701$ with $n = 1, 2, 3, 4$. The full model does not have an analytical solution, but it does have upper and lower bounds related to Eq. (3.7) (Materials and Methods section 3.4.7, S3 Fig).

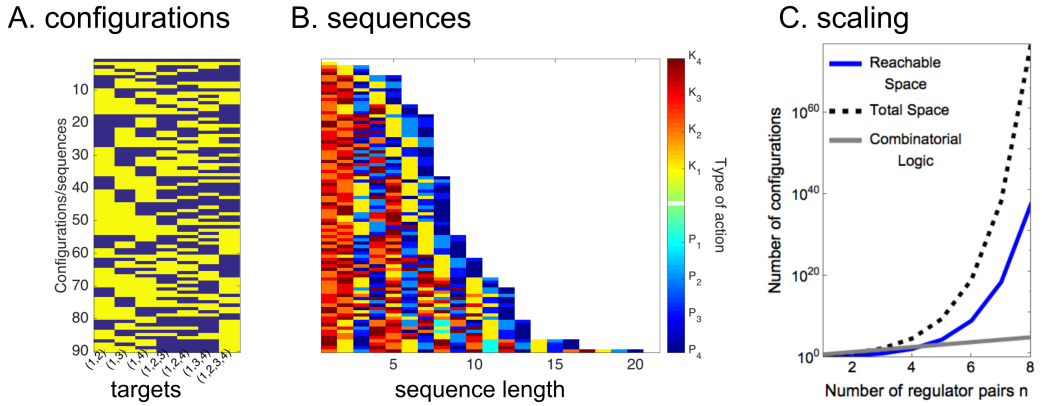

Figure 3.6: Scaling in the sequestration model is super-exponential.(A) A plot of all the allowed configurations of a set of targets of $n = 4$ regulator pairs in the sequestration model. Yellow represents targets that are ON, and blue those that are OFF. **(B)** A list of the sequences generating the corresponding states in A. K actions are shown in the red spectrum, and P in the blue. **(C)** A logarithmic plot of the scaling in the sequestration model. The total space is the $2^{2^{n-1}-1}$, the reachable space is calculated from Eq. (3.7), and the combinatorial model is 2^{2n}.

Combinatorial scaling laws of this sort are not uncommon [66, 100, 209]. Edwards and Glass [66] saw an explosion in the number of states when studying trajectories on n-cubes, and Green and Rees [100] saw a super-exponential jump when enumerating certain types of nonrepeating sequences on n letters. Furthermore, a similar small number (four) of factors are necessary and sufficient to reprogram fibroblasts to stem cells [265]. Together, these results indicate that sequences can far exceed the 2^n limit set by combinatorial regulation, and that only a few regulators are necessary to make large changes in the configuration of a cell.

3.2.7 Regulators act on the configuration vector in the sequestration model

The sequestration network with n regulator pairs (referred to as the n-*network*) is described using the $1 \times 2^n - 1$ *configuration vector* $\mathbf{x}$. This is a simpler description than the connectivity matrix because a target affected by K_i is necessarily affected by P_i. The entries of $\mathbf{x}$ are the states of each target g able to be controlled by $k \leq n$ of the regulator pairs. Each target g is a list $\{0, i_1, \ldots, i_k\}$ of the k regulators to which it responds. Because of their radial appearance, such targets are said to have k *arms* (see Figure 3.5B).

The regulators act on $\mathbf{x}$ according to the rules

$$K_i(\mathbf{x}_g) = \begin{cases} \mathbf{x}_g + i & \text{if } i \in g \text{ and } \mathbf{x}_g = 0 \\ \mathbf{x}_g & \text{else} \end{cases}$$
$$P_i(\mathbf{x}_g) = \begin{cases} 0 & \text{if } i \in g \text{ and } \mathbf{x}_g = i \\ \mathbf{x}_g & \text{else.} \end{cases} \tag{3.8}$$

Eq. (3.8) guarantees that the regulators are *orthogonal* in the sense that a target in state j is protected from K_i and P_i if $i \neq j$; and also *idempotent* in that $K_i^2 = K_i$. Furthermore, sequences of regulators are noncommutative unless the only actions are P's. This is a consequence of the fact that P's put all affected targets into the 0 state. Although these rules are different from the ratchet model, a formulation exists that generalizes the K's and P's to matrix operators consistent with both models (Materials and Methods section 3.4.9).

If $\mathbf{x}$ is restricted to the $2^{n-1} - 1$ targets all able to be regulated by K_1 and at least one other K, the network is said to be *reduced*; otherwise we say $\mathbf{x}$ is *full*. This distinction was used in Figure 3.5.

A *one-coloring* is a configuration of $\mathbf{x}$ that uses only one of the states and 0. For example, the configuration $\mathbf{x} = (1, 0, 0, 1, 1, 0, 0)$ in the full $n = 3$-network is a one-coloring of 1; so is the reduced network formed by $(\mathbf{x}_4, \mathbf{x}_5, \mathbf{x}_7) = (1, 1, 0)$. This concept is easily extended to $k > 1$-colorings. One-colorings are particularly important because they resemble the ON/OFF configurations of genes in an RNA-seq experiment, and we would like to know how many such configurations can be reached.

3.2.8 A simple counting argument for the connected one-colorings illustrates super-exponential scaling in the sequestration model

As in the ratchet model, finding the accessible states of the sequestration network amounts finding restricted patterns in $\mathbf{x}$. We determined that the restricted

one-colorings are those that violate a property referred to as *connectivity* (Materials and Methods section 3.4.6). A configuration of $\mathbf{x}$ is said to be connected if all $k \geq 3$-arm targets $g_i^{(k)} = \{0, i_1, \ldots, i_k\}$ match the state of at least one of $\binom{k}{2}$ of the 2-arm targets $\{0, i_1, i_2\}$,..., $\{0, i_{k-1}, i_k\}$ sharing the indices i. If the network is reduced, no k-arm target may be in the 1 state when all of 2-arm targets with which it overlaps (i.e., shares an index other than 1) are in the 0 state. This restricts the one-colorings and suggests a method to determine the scaling law for the model in Figure 3.5.

As an example, in the $n = 4$ network on the reduced set of $2^3 - 1$ targets illustrated in Figure 3.5, $\{0, 1, 3\}$ and $\{0, 1, 4\}$ both being 0 constrains $\{0, 1, 3, 4\}$ to be 0 as well. Furthermore, even though $\{0, 1, 2\}$ is in the 1 state, $\{0, 1, 2, 4\}$ and $\{0, 1, 2, 3, 4\}$ may be 0. It is only the two-arm targets that constrain the possible configurations: for example, the longer sequence

$$K_2K_4P_2K_3K_2P_4K_1P_3K_4P_1K_3P_4K_1P_2P_3$$

obtains the state $\mathbf{x} = (0, 0, 1, 0, 0, 0, 1)$ in which only the targets $\{1, 4\}$ and $\{0, 1, 2, 3, 4\}$ are ON, showing that $\{0, 1, 2, 3, 4\}$ need not be in the same state as $\{0, 1, 2, 3\}$, $\{0, 1, 2, 4\}$, or $\{0, 1, 3, 4\}$. In Figure 3.6A and B we show the allowed states and the sequences that generate them for $n = 4$; there are 90 out of a possible $2^{2^{4-1}-1} = 128$ configurations.

There are $2^{2^{n-1}-1}$ one-colorings on $2^{n-1} - 1$ targets. How many of these violate the connectivity rule? Suppose there are m 0's among the 2-arm targets. If $m = 1$, then $\binom{m}{k-1} = \binom{1}{k-1} = 0$ of the $k \geq 3$-arm targets are constrained to be 0, as there is always another 2-arm target (in the 1 state) that each k-arm target can match. If $m > 1$ and $k - 1 \leq m$, however, then $\binom{m}{k-1} > 0$, so $\binom{m}{k-1}$ k-arm targets whose states $\{i_1, \ldots, i_{k-1}\}$ are completely contained within the set of 2-arm targets $\{0, 1, j_1\}, \ldots, \{0, 1, j_m\}$ must be 0. Hence in any violation of the connectivity rules at least one of $\sum_{k=3}^{m} \binom{m}{k-1}$ k-arm targets will be in the 1 state and the remaining $\sum_{k=3}^{m} \binom{n-1}{k-1} - \binom{m}{k-1}$ k-arm targets will be 0 or 1. Furthermore, there are $\binom{n-1}{m}$ ways of specifying m 0's, so the total number of violations is

$$\sum_{m=2}^{n-1} \binom{n-1}{m} \left(2^{\sum_{k=3}^{m} \binom{m}{k-1}} - 1\right) \left(2^{\sum_{k=3}^{m} \binom{n-1}{k-1} - \binom{m}{k-1}}\right). \tag{3.9}$$

Subtraction from $2^{n-1} - 1$ gives Eq. (3.7).

3.2.9 The ratchet and sequestration networks divide the configuration space into orbits

Until now we have considered the reachable space of a single group of targets each starting in 0. An ensemble of networks could each start with their targets in some arbitrary state, and when a sequence is applied to the ensemble the different networks will in general span different configurations. Determining the number of *orbits* (defined precisely in Materials and Methods section 3.4.8) within the set of possible configurations tells us how many networks can be controlled in parallel.

Enumerating the reachable space for both the ratchet and sequestration networks involved finding configurations that violated at least one rule. If two configurations have distinct violations, then there is no way they can communicate using the regulators. Therefore, the different orbits are the groups of configurations having the same forbidden patterns. It is possible that a violation could be alleviated by an action that changes the state of an offending target, so we require that each orbit be immune to a subset of the regulators. This could be achieved in biological networks by locking targets in protective chromatin states or by shutting down certain cellular receptors.

We determined a recursive formula for the number of orbits in the ratchet network for an arbitrary n, m (Materials and Methods section 3.4.8). In Figure 3.7A we plot the orbits for the $n = 4, m = 2$ case. There is one large component of size B_n^{-m} and several smaller orbits of size B_i^{-j} with $i \leq n$ and $j \leq m$. There are only a handful of singleton orbits in Figure 3.7A, but the number of isolated states dominates the space as n, m increase.

We were unable to find a similar solution for the sequestration network because we lack a general solution for the number of states in the main orbit. However, Figure 3.7B shows the computationally discovered orbits for the full network on $2^n - 1$ targets. A nontrivial feature is that there are orbits which use all pairs of regulators, but which do not communicate with the main orbit. For example, the sequence K_2K_3 from $\mathbf{x} = (1, 0, 0, 0, 0, 0, 1)$ reaches the same configuration as the sequence K_1 starting from $\mathbf{x} = (0, 2, 3, 2, 2, 3, 0)$; these configurations are part of the same orbit because both violate the connectivity rule between $\mathbf{x}_7 = \{0, 1, 2, 3\}$ and the 2-arm targets $\mathbf{x}_4$, $\mathbf{x}_5$, and $\mathbf{x}_6$.

Another observation is that some pathways cannot be reversed by a legal action in the ratchet network orbits (indicated by a directed arrow in Figure 3.7), whereas there always exists a reversible path between configurations in the seques-

tration network orbits (no arrowheads). It can be proved that this is true in general for the sequestration network (Materials and Methods section 3.4.8). This feature permits orbits to be found computationally by looking for reversible one-step paths in the entire configuration space.

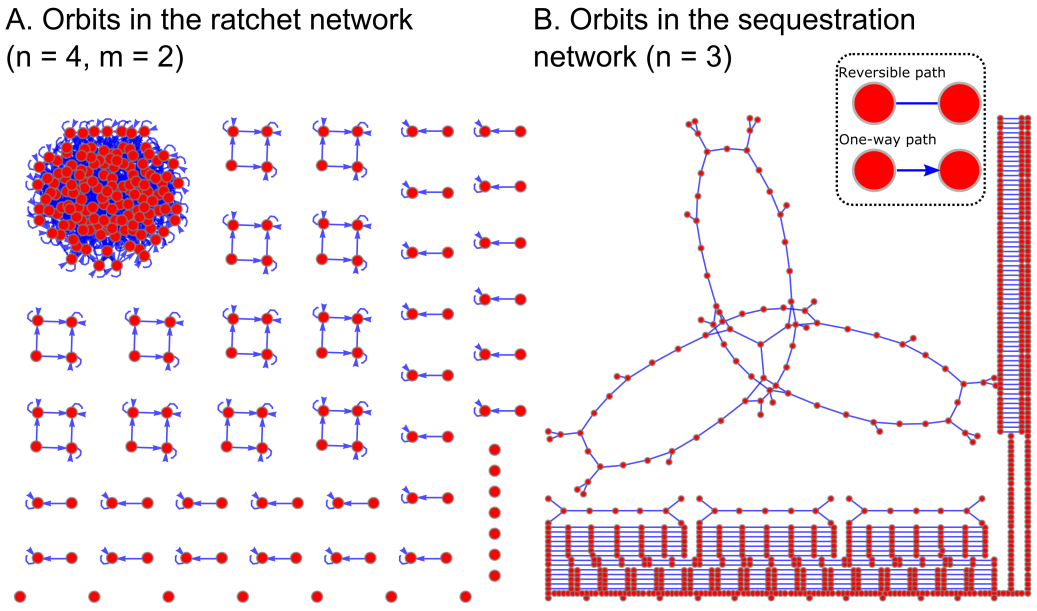

Figure 3.7: Noncommutative models induce orbits in the configuration space. Graphical representation of the orbits in **(A)** the $n = 4, m = 2$ ratchet network and **(B)** the full $n = 3$ sequestration network. Configurations are indicated by red circles, and those accessible to each other are connected with blue lines. Arrows in A indicate whether a path is irreversible.

The orbits are one explanation for the phenomenon the same signal can cause cells to behave differently [287]. More generally, the orbits demonstrate an intriguing symmetry between the targets responding to a restricted subset of the regulators on one hand, and the orbits restricted to the same subset on the other.

3.3. Discussion

In this paper we first show how noncommutative, sequential logic can relieve information bottlenecks in multilayer networks. Bottlenecks in combinatorial logic may occur whenever a downstream layer has fewer elements than the layer upstream, which poses the problem of how networks process complex signals without loss of information. Noncommutative solutions such as the ratchet and sequestration models, in which the number of configurations scales super-exponentially in the number of regulators (Eqs. (3.5) and (3.7)), permit longer, more complex messages to reach the targets via information "pulses." These pulses encode a large

diversity of signals into configurations of the targets that would otherwise be lost using combinatorial logic.

Noncommutativity has long been recognized as a central concept in control theory, because it allows systems with few controllers to explore a broader configuration space. For example, one generates z rotations in 3D by $\mathbf{R}_{-x}\mathbf{R}_y\mathbf{R}_x$, so control over z is generated by a pulse sequence of rotations in x and y, as in airplane control where roll and pitch generate yaw [190]. Infinitesimal motions in the form of generating matrices are translated into flows in a vector space by exponentiation. Because matrix multiplication is noncommutative, composition of flows is not simply the addition of generators, but rather a higher order polynomial of commutators of the generators given by the Baker-Campbell-Hausdorff formula [258]. Noncommutativity also appears in experimental physical chemistry where pulse sequences can prepare spin systems in nontrivial population configurations [47]. A formal description of these phenomena is based on the Heisenberg picture of quantum mechanics, wherein evolution of a system of many variables is given by a differential equation involving the commutator of a Hamiltonian operator.

The significance of noncommutative control for systems biology is that it becomes possible to independently control targets that would otherwise be activated by the same promiscuous regulator. In this paper, we argue that noncommutative sequences permit control over new directions in gene expression space, allowing more specific sets of targets to be controlled. Several studies have shown that TFs that can bind genes in one tissue type are in fact precluded from binding the same genes in another [15, 146]. The *C. elegans* TF LIN35 fails to bind targets in the germline that it binds in the intestine [146], and the SMARCA4 complex in mouse binds enhancer elements in heart, limb, and brain tissue in a tissue-specific manner [15]. One hypothetical explanation for these observations, based on the sequestration model, is that cell-type specific gene expression is the result of noncommutative sequences like K_1K_2 and K_2K_1 that silence certain promoters. The three-dimensional structure of the genome is a likely setting for this type of regulation.

Gene regulation is known to take place in three-dimensions, as observations of DNA looping [198], nonrandom chromosome packing [192], and clustered transcription factories [241] have shown. However, the factors that affect chromosome structure are non-specific. One such factor is the ubiquitous zinc finger protein CCCTC binding factor (CTCF) [174], which functions as both an activator of transcription by bringing enhancers and promoters together [111, 256] and as a

repressor by insulating genes [22, 120]. Epigenetic modifications, such as histone methylation and acetylation [104, 177, 305], also affect three-dimensional structure. In addition, DNA looping was observed in the context of allelic exclusion during B- and T-cell lineage specification where individual alleles were recruited to heterochromatic regions while the other underwent recombination [52, 236]. Consequently, the sequestration model predicts that temporal permutations of a small set of chromatin modifying factors could specify a large number of potential chromosomal conformations and lead to different expression states and corresponding cell fate decisions.

New technologies such RNA-seq and ChIP-seq can be used to test the predictions of the noncommutativity hypothesis at the genome level. Epigenetic drugs such as azacytidine and trichostatin A inhibit DNA methylation [184] and histone deacetylation [301], respectively, and have been shown to cause global changes in gene expression alone and in combination [62, 184]. The sequestration hypothesis predicts that perturbations to the three-dimensional structure of the chromosome are noncommutative, so distinct gene expression states may be reached by permuting the order in which epigenetic drugs are applied. While the sequestration model may underlie chromosome folding, the ratchet model could form the basis of phosphorylation networks. For example, mass spectrometry studies have revealed complex phosphorylation patterns [127, 220], though the number of kinases and phosphatases is comparatively small and the networks are highly interconnected [232, 279]. As phosphoproteins are the mediator of extracellular signals, ordered disruption of signaling pathways could also lead to distinct gene expression configurations.

Analogously, the ratchet model may aid in the specification of distinct neural activity patterns, owing to the fact that connections between the different hippocampal layers overlap [234, 240]. While superficial neurons can be activated in response to spatial cues, deeper layers can be selectively activated by time sequences of inputs [1, 41, 93]. These results suggest the hypothesis that neural networks may be noncommutative. In particular, experimental support exists for the role of the dentate gyrus in pattern separation and orthogonalization by way of ensuring that even quite similar memory representations use distinct subsets of neurons [49, 154]. The ratchet model, by ordering inputs in time, is one way of reaching these specific subsets if the number of input neurons is smaller than the number of targets neurons. Memories share many common elements, including shape, color, smell, and sound, which poses problems for recall. We hypothesize that older, "fuzzier" memories could be those relegated to very long ratchet sequences. According to

this hypothesis, memories are not forgotten, but are instead increasingly difficult to access, and memories that are not consolidated are those that never formed a unique ratchet sequence.

Beyond resolving bottlenecks and generating specificity, noncommutative actions offer a new interpretation of how cell fate decisions and other stepwise processes occur on abstract regulatory landscapes. The classical Waddington landscape view of development holds that cells decay to attractor configurations representing terminal outcomes [288]; this is consistent with a boolean network with many variables X converging to a fixed point [124]. In a static landscape, the final outcome is determined *a priori* by the nearest energy minimum. What then determines the initial configuration? In organisms such as Drosophila, maternal patterning of the embryo may account for this initial bias [257]; but in other organisms that employ mechanisms like multilineage priming [3, 177], it is not clear that every cell fate decision is made at the beginning.

Sequential logic allows cells to reach their final fate on a dynamic landscape. In the system of Figure 3.8A (top), for example, it is not possible for cells in the blue configuration to transition to the red fate by increasing X_2, because this involves an uphill climb. However, the regulators of genetic networks may also affect the landscape directly. This is seen in Figure 3.8A (bottom) where the sequence $K_1K_2P_1$ changes the landscape in such a way that the overall cost of reaching the same endpoint is much lower than the direct path (Figure 3.8A, top). This can be understood as the effect of regulators acting on additional variables V, which modulates the landscape in X space. For example, TFs can recruit chromatin regulators that modify global three-dimensional chromosome structure and future TF accessibility [27, 111, 241, 286], or kinases can sequester substrates in the nucleus to prevent their subsequent activation [45, 61]. Because sequential logic acts on the V's as well as the X's, changes that appear to be small in one dimension (Figure 3.8B, left) actually involve large excursions in the full space (Figure 3.8B, right). As a consequence, in noncommutative regulation, the landscape changes and cells can take on fates that were not accessible at the beginning.

Previous theoretical models have explored dynamic regulatory landscapes in the form of bifurcations [75, 125]. In these models, a set of kinetic parameters determines the positions of minima and maxima in the landscape. However, the noncommutative model advanced here is fundamentally different, in that using the regulators to move through X changes the landscape directly. This could happen, for example, if acting on X_1 with K_1 hides it from the effect of K_2. Uncoupling of

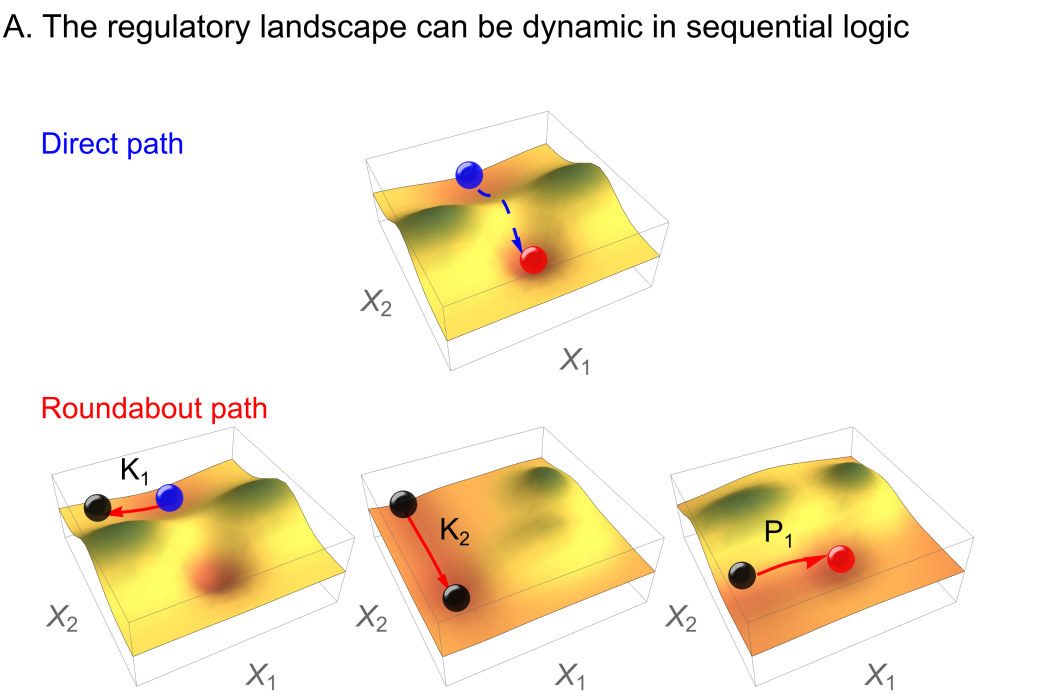

Figure 3.8: Sequential logic on regulatory landscapes. **(A)** The regulatory landscape for the 2-mRNA system X_1, X_2 for two hypothetical paths with configurations represented by balls. It is difficult to directly increase X_2 because of a potential barrier (top). In the roundabout path (bottom), visiting two intermediate configurations via $K_1 K_2 P_1$ results in an altered regulatory landscape. **(B)** The initial and final configurations in A projected onto (X_1, X_2) space (left) and (X_1, X_2, V_1) space (right). The regulators affect not only X_1 and X_2, but also an additional variable, denoted V_1, that alters the landscape of X_1 and X_2. The arrows indicate the instantaneous direction of the trajectory.

targets in this way may underlie the distinct effects of signals like FGF at different stages of development [132, 178, 249, 287]. It will be interesting to explore time series data for hints that some genes pulse ON and OFF in order to protect their

promoters from the actions of promiscuous regulators.

Multistep processes other than development can benefit from the type of noncommutative regulation highlighted in Figure 3.8. What seems like an intractable problem at the start becomes much more feasible if one realizes that the effects of actions change with time and context. This intuition is why thinking in terms of commutators $[A, B] = AB - BA$ can make complex problems more soluble: the desired effect is often what is leftover after performing and undoing a sequence of actions. Several examples illustrate this concept.

With its increased capacity for generating diversity, sequential logic is likely to be used in evolution. A recent theoretical example in social bacteria demonstrated that in evolving a new quorum sensing receptor-ligand pair, adding new receptors prior to ligands is preferred over the opposite path [68]. An analysis of the stability and catalytic activity of a family of bacterial β-lactamase mutants showed that the ability to evolve new substrate specificity is contingent on mutations that first stabilize the protein active site [229, 292]. Finally, biological networks evolve the same functions in different orders, but the order in which these functions arise dictates which other genotypes can be reached by neutral mutations [209]. These results suggest that permuted sequences of mutation events may have different fitness costs. With extensive artificial evolution experiments underway in protein engineering [229] and bacterial mutation accumulation [34], coupled with progress in sequencing technologies, it will be possible to test this hypothesis by permuting the conditions that promote mutation.

Sequential logic can also be applied in synthetic biology to build circuits with memory [85, 108, 161, 170]. In general, the toolkit that permits up- and downregulation of genes is small, with a few staples like Lac, Tet, and Ara [284]. Significant effort has been put into generating logic gate (AND/OR) promoters [43]. To further expand the toolkit, it has been proposed that more orthogonal regulators be developed [223]. We suggest that sequential logic may be a more promising strategy to scale up the number of targets that can be independently controlled by permuting in time a small number of controllers.

More broadly, sequential logic can be used to accomplish experimental goals not possible in single-step approaches. For example, in multiplexing mRNA detection in single cells, we previously used a sequential hybridization scheme that permits the number of barcodes to exponentially [165], whereas combinatorial schemes can only specify approximately 30 barcodes. We expect many single-cell experiments to benefit from a sequential strategy in which detours facilitate

achievement of the main goal with high efficiency.

Finally, our results connect outside of biology to strategic planning in social, political, and economic arenas. Anyone familiar with negotiating knows about the limitations inherent in trying to make interconnected groups of people move in specific directions, especially when the actions affect all participants at once. Multiparty negotiations and tournaments may benefit from time-ordered strategies in which enemies temporarily team up, or fringe interest groups are transiently pacified. Indeed, a conclusion from the sequestration model is that the most highly regulated targets need to be protected prior to satisfying the ones with fewer connections. Determining whether this prediction is borne out in congressional and international negotiations, for example, is an interesting question for political science. Evidence for noncommutative effects in games exists in that the initial seeding in a tournament can bias its outcome [102], and that long-term goals change players' strategies in in the repeated prisoner's dilemma [86]. In conclusion, the direct path to an outcome in a networks with many interacting parts may have many unintended and prohibitively expensive consequences. A multi-step strategy may achieve the same outcome with minimal cost and side effects.

3.4. Materials and Methods

3.4.1 The connectivity matrix with multiple targets

In this section we determine how many targets are controlled by the same regulators in the connectivity matrix $\mathbf{A}$. Then we extend $\mathbf{A}$ to more than 2 dimensions.

If $l_n = l_m = 1$ it is clear that each $\mathbf{A}_{i,j}$ corresponds to a single target and that each target appears only once. In general, however, a target can appear in multiple entries of $\mathbf{A}$ (cf. Eq. (3.6)). To see this, consider the bipartite graph formed by all the targets and all the K's, but none of the P's. The handshaking lemma from graph theory [175] says that the total number of edges is one half the sum of the degrees of each vertex, which is either l_n for a target or some number p_n for a K regulator. There are Nl_n total edges, so we find $\frac{1}{2}\left(Nl_n + np_n\right) = Nl_n$ or $p_n = \frac{N}{n}l_n$ for the number of links coming from each K. Similarly, the number of links emanating from each P is $p_m = \frac{N}{m}l_m$. In terms of the connectivity matrix, p_n and p_m correspond to the number of unique targets in each row and column, respectively.

Because K_1 connects to a fraction $\frac{p_n}{N}$ of the targets, it follows that K_1 and P_1 together connect to a fraction $\frac{p_n p_m}{N^2}$ of the targets. Therefore, the total number

of targets connecting to K_1 and P_1 is $M = N\left(\frac{p_n p_m}{N^2}\right) = \frac{p_n p_m}{N}$. Another way to see this is to consider one target in the intersection of K_1 and P_1. This one target uses up one of each of the regulators and one unit of connectivity, leaving a total of $M = \binom{n-1}{l_n-1}\binom{m-1}{l_m-1}$ ways to connect other targets to the same pair of regulators. It is easily verified that these two formulations for the number of targets per matrix entry M are equivalent. This illustrates that there is not simply a one-to-one correspondence between the entries of $\mathbf{A}$ and the targets.

There was nothing special about the labels K and P in the above paragraphs. Thus, the connectivity matrix can easily be extended to a u-dimensional *connectivity tensor* where u is the number of pools of regulators. Each pool has n_i regulators connecting to l_{ni} targets, and each target connects to $p_{ni} = \frac{N}{n_i} l_{ni}$ regulators of pool i, $\forall i \in \{1, \ldots, u\}$. The total number of targets and the total number of targets per entry are extensions of the $u = 2$ case, giving

$$N = \prod_{i=1}^{u} \binom{n_i}{l_{ni}} \tag{3.10}$$

distinct targets and

$$M = \frac{\prod_{i=1}^{u} p_{ni}}{N^{u-1}} = \prod_{i=1}^{u} \binom{n_i - 1}{l_{ni-1}} \tag{3.11}$$

targets controlled by one factor from each of the u pools. S1 Fig A shows an example network with $u = 3$ pools.

3.4.2 Counting configurations in combinatorial networks using the connectivity matrix

The number of configurations in combinatorial logic is the number of ways that N targets can each be bound by exactly u regulators, where each regulator comes from a different pool. In the main text we analyzed the case $u = 1$ and $l_n = 1$. Here we extend those results to arbitrary u and l_n.

First consider the case $u = 2$, corresponding to a pool of K's and a pool of P's. Whereas in the ratchet model, K_i and P_j acted separately on the entries of $\mathbf{A}$, in combinatorial logic the pair (K_i, P_j) is needed to switch $\mathbf{A}_{i,j}$ from 0 to 1. Many such pairs may be active at any one time. We write this formally as

$$(\{K\}, \{P\})[\mathbf{A}_{i,j}] = \begin{cases} 1 & \text{if } K_i \in \{K\} \text{ and } P_j \in \{P\} \\ 0 & \text{else,} \end{cases} \tag{3.12}$$

where $\{K\}$ denotes a subset of the K's. The notation $(\cdot, \cdot)$ means that a combination of factors acts on the target, instead of just a single factor.

If $l_n = l_m = 1$ there are $(2^n - 1)(2^m - 1) + 1$ ways to pick at least one of n K's and one of m P's, plus one way to pick nothing. If $l_m = 1$ and $l_n > 1$, then for a certain number $\alpha \leq n$ of the K's, any subset containing α or more K's has the same effect as activating all n K's at once. For example, in Eq. (3.6), the action of $(\{K_1, K_2\}, \{P_1, P_2\})$ is sufficient to activate all targets in the $n = m = 3$, $l_n = l_m = 2$ network. To determine α, recall that there are M targets in each entry of the connectivity matrix $\mathbf{A}$. Choosing i K's means that the total number of targets is $M \times i$, but a single column of $\mathbf{A}$ only contains p_m unique targets. Each target is connected to l_n K's, so for a target in the intersection of i K's and a single P, there are $l_n - i$ spots left over to choose $n - i$ K's and $l_m - 1$ spots left over to choose $m - 1$ P's, or $\binom{n-i}{l_n-i}\binom{m-1}{l_m-1}$ ways total. Using the principle of inclusion-exclusion [175] this means that α is the smallest i such that

$$M \times i - \sum_{i'=2}^{\min(i,l_n)} (-1)^{i'} \binom{i}{i'}\binom{n-i'}{l_n-i'}\binom{m-1}{l_m-1} \geq p_m. \tag{3.13}$$

By choosing α K's, the number of unique targets in a column of $\mathbf{A}$ that can be turned ON is exactly the number represented in that column. Because all subsets with $\alpha, \alpha+1, \ldots, n-1$ K's are redundant, here are only $(2^n - 1) - \sum_{i=\alpha}^{n-1}\binom{n}{i}$ subsets of K's that contribute to unique configurations, leaving a total of $\left[(2^n - 1) - \sum_{i=\alpha}^{n-1}\binom{n}{i}\right](2^m - 1)+1$ unique configurations.

If the P's also have redundant connections, the result generalizes to

Theorem 3.4.1. *The number of configurations in combinatorial logic with parameters n, m, l_n, l_m, and $u = 2$ is*

$$\begin{aligned}&(2^n - 1)(2^m - 1) + 1 \\ &\quad - \left(\sum_{i=\alpha}^{n-1}\binom{n}{i}\right)(2^m - 1) - (2^n - 1)\left(\sum_{i=\beta}^{m-1}\binom{m}{i}\right) + \left(\sum_{i=\alpha}^{n-1}\binom{n}{i}\right)\left(\sum_{i=\beta}^{m-1}\binom{m}{i}\right),\end{aligned} \tag{3.14}$$

where α (resp. β) is the smallest number of K's (resp. P's) having the same effect as all K's (resp. P's) at once.

This result is obtained by counting all pairings of K's and P's, and then subtracting those pairings that have a redundant effect. For example, any combination using K_3 is redundant in the connectivity matrix of Eq. (3.6). Finally, those pairings that were excluded twice are added back in.

This result generalizes to all u with slight modifications. Because one factor from each of u pools is now required, the combinatorial equation determining

state of a target is

$$\left(\{K\}_1, \{K\}_2, \ldots, \{K\}_u\right)\left[\mathbf{A}_{i,j,\ldots,k}\right] = \begin{cases} 1 & \text{if } K_{1i} \in \{K\}_1, K_{2j} \in \{K\}_2, \ldots, K_{uk} \in \{K\}_u \\ 0 & \text{else.} \end{cases} \tag{3.15}$$

Here the double subscript K_{ik} indicates the k^{th} factor in the i^{th} pool. Determining α_i for each pool i of regulators requires finding the pool $j \neq i$ which maximizes the number N_i of targets controlled in two dimensions. If we choose α_i or more regulators in the i^{th} pool, then there is a redundancy in the j^{th} dimension, whereas any choice of fewer than α_i regulators activates fewer than N_i targets. Write $N_i = \max_{j\neq i}\left\{\binom{n_i}{l_{ni}}\binom{n_j}{l_{nj}}\right\}$ the total number of targets and $p_{nj} = \frac{N_i}{n_j} l_{nj}$ the number of targets in any column of the the equivalent $n_i \times n_j$ connectivity matrix regulated by pools i and j. It is easy to see that these parameters reduce to their previous definitions for $u = 2$. Now define $M_i = \binom{n_i-1}{l_{ni}-1}\binom{n_j-1}{l_{nj}-1}$ as the number of targets in each entry of the equivalent $n_i \times n_j$ connectivity matrix. As above, α_i is now the smallest r such that

$$M_i \times r - \sum_{r'=2}^{\min(r,l_{ni})} (-1)^{r'} \binom{n_i - r'}{l_{ni} - r'}\binom{n_j - 1}{l_{nj} - 1} \geq p_{nj}. \tag{3.16}$$

Once α_i is determined for each pool i, the inclusion-exclusion sum can be extended using standard arguments [175]. Define by

$$S^{(k)} = \sum_{\sigma\in\binom{u}{k}} \left\{\prod_{i\in\sigma}\left(\sum_{j=\alpha_i}^{n_i-1}\binom{n_i}{j}\right)\prod_{i\notin\sigma}\left(2^{n_i}-1\right)\right\}, \tag{3.17}$$

where σ denotes all k-subsets of $\{1, \ldots, u\}$. Then we have the final result

Theorem 3.4.2. *The total number of configurations in combinatorial logic with u pools and parameters n_i, l_{ni}, $i \in \{1, \ldots, u\}$ is*

$$S = 1 + \sum_{k=0}^{u} (-1)^k S^{(k)}. \tag{3.18}$$

This result reduces to Theorem 3.4.1 when there are only $u = 2$ pools. At most there are $\prod_{i=1}^{u}\left(2^{n_i} - 1\right)$ ways to specify at least one target, corresponding to the 0^{th}-order term in Eq. (3.18). Increasing the connectivity through the l_{ni} can only reduce the number of configurations. This behavior is shown in S1 Fig B for the symmetric case that all the n_i and l_{ni} are equal. As u is increased the number of configurations increases dramatically, but the scaling is actually subexponential, i.e., less than 2^N. Increasing connectivity through l_{ni} shifts the curves to the right.

3.4.3 Using the connectivity matrix to establish a one-to-one correspondence between the ratchet network and the lonesum matrices

To establish the correspondence between the reachable configurations of ratchet network ($l_n = l_m = 1$, $T = 1$) and the lonesum matrices, we must show (i.) that $\mathbf{A}$ avoids the patterns $\begin{pmatrix} 1 & 0 \\ 0 & 1 \end{pmatrix}$ and $\begin{pmatrix} 0 & 1 \\ 1 & 0 \end{pmatrix}$ in any 2×2 sub-block, and (ii.) that any lonesum matrix can be constructed from K and P actions. First observe that the value 1 in $\mathbf{A}_{i,j}$ indicates the last K affecting that index must have followed a P, whereas 0 indicates the last P must have followed a K. For the first restriction we have $\begin{pmatrix} 1 & 0 \\ 0 & 1 \end{pmatrix}$ implies $\begin{pmatrix} P_1 \cdots K_1 & K_1 \cdots P_2 \\ K_2 \cdots P_1 & P_2 \cdots K_2 \end{pmatrix}$. This means P_2 follows K_1 follows P_1 follows K_2 follows P_2, which is a contradiction, showing that this 2×2 block is unreachable. The other five unique 2×2 blocks are all reachable with elementary sequences. This establishes point (i.) that the reachable configurations are a subset of the lonesum matrices.

To establish point (ii.) that the lonesum matrices are a subset of the reachable configurations, we use an equivalent formulation of the lonesum matrices as *staircase matrices* composed of the rows $a_j = (1, \ldots, 1, 0, \ldots, 0)$ with the last 1 appearing at position i_j subject to the constraint that $i_j \leq i_{j-1}$ for all $\forall j \in \{2, \ldots, n\}$ [141]. It is easy to see that the pattern of ones resembles an inverted staircase. We show via induction that any staircase matrix can be constructed from K and P actions. The n^{th} row is obtained by the sequence $K_n P_{i_n+1} \cdots P_m$ which leaves 1's at the first i_n indices and 0's at the remainder. Now assume that the k^{th} row is obtained by the sequence $K_k P_{i_k+1} \cdots P_m$ without affecting any of the rows $n, n-1, \ldots, k+1$. Then the sequence $K_{k-1} P_{i_{k-1}+1} \cdots P_m$ puts 1's at the first i_{k-1} indices of row $k-1$. Because $i_{k-1} \geq i_k \geq \cdots \geq i_n$, none of the $P_{i_{k-1}+1}, \ldots, P_m$ turn a 1 to a 0 in rows $n, n-1, \ldots, k+1, k$. This proves the induction hypothesis and shows that the staircases matrices are a subset of the reachable configurations.

Together with the fact that the reachable configurations are a subset of the staircase matrices, this implies that the reachable configurations and the lonesum matrices are in fact the same set, and we have

Theorem 3.4.3. *The number of reachable configurations in the (n, m) ratchet network with $l_n = l_m = 1$ and threshold 1 scales as the poly-Bernoulli numbers $B_m^{-n} = B_n^{-m}$.*

3.4.4 Inductive proof that all binary ON/OFF configurations are reachable in the ratchet network with threshold greater than 1

With $T = 2$, only targets in state 2 are ON. Once a 0-1 configuration of $\mathbf{A}$ is obtained, however, it is a simple matter to convert it into an ON/OFF configuration by applying all the K's. Here we use the fact that 1's can be reached from above and below to prove

Theorem 3.4.4. *In the ratchet network represented by the matrix* $\mathbf{A}$ *with* $l_n = l_m = 1$ *and threshold* $T = 2$*, all binary 0-1 configurations are reachable.*

Proof. We use an induction argument analogous to the proof of Theorem 3.4.3. Suppose that in row n a set of $r \leq m$ indices $\{n_j\} = \{n_{j_1}, \ldots, n_{j_r}\}$ should be ON. First prepare every target in row n in the 1 state using K_n, then use the sequence $K_n P_{j_{r+1}} \cdots P_{j_m}$ to obtain 2's at $\{n_{j_1}, \ldots, n_{j_r}\}$ and 1's at $\{n_{j_{r+1}}, \ldots, n_{j_m}\}$. Now assume that we can prepare rows $n, n-1, \ldots, k+1$ in a similar 1-2 configuration with the rest of the matrix 0. We want to show that we can add row k to this set without affecting any of the previous rows. Assuming that a set of $s \leq m$ indices $\{k_{j_1}, \ldots, k_{j_s}\}$ should be ON, apply the sequence $P_{j_1} \cdots P_{j_s} K_k^2 P_{j_{s+1}} \cdots P_{j_m}$ to obtain 2's at $\{k_{j_1}, \ldots, k_{j_s}\}$ and 1's at $\{k_{j_{s+1}}, \ldots, k_{j_m}\}$. Now, because $\{P_{j_1}, \ldots, P_{j_s}\} \cup \{P_{j_{s+1}}, \ldots, P_{j_m}\} = \{P_1, \ldots, P_m\}$, all 2's and 1's in rows $n, n-1, \ldots, k+1$ are now 1's and 0's, respectively. Applying the sequence $K_n K_{n-1} \cdots K_{k+1}$ reestablishes the 1-2 configuration we had prior to fixing row k and leaves 0's at rows $1, \ldots, k-1$. Now that row k is also in the proper 1-2 configuration, we have proved the induction hypothesis. Once all rows in the proper 1-2 configuration, the sequence $P_1 \cdots P_m$ obtains the matrix in the 0-1 configuration. Since this procedure can be repeated for any collection of indices $\{\{1_j\}, \ldots, \{n_j\}\}$, it follows that all binary 0-1 matrices are reachable. □

3.4.5 A recursive formula for the number of non-redundant sequences in the ratchet network

When the connectivity parameters l_n and l_m exceed 1, certain sequences in the threshold 1 ratchet network become redundant. Our goals in this section are to (i.) to characterize the redundant sequences by the number of K's and P's, and (ii.) count the non-redundant sequences. This will obtain an upper bound on the number of configurations.

We want the shortest sequences that can activate or (deactivate) all targets; any sequences longer than this are redundant. To see why this is so, we need the

concept of a *cycle*. We say that a target has gone through a cycle if has traversed the states 0, 1, 0 at some subsequent time points. We have the following lemma.

Lemma 3.4.5. *Any sequence that takes all targets through a cycle is redundant.*

Proof. The final configuration of any sequence is represented by the positions of the 1's and 0's of the connectivity matrix. Recall that $\mathbf{A}_{i,j} = 0$ if and only if all targets represented by $\mathbf{A}_{i,j}$ are OFF in the final configuration. Permute the rows and columns of $\mathbf{A}$ until it is in staircase form with $r \leq \min(n, m)$ steps, where a step is a group of adjacent rows or columns having the same number of 1's and 0's. The steps partition the rows and columns of $\mathbf{A}$ into subsets of indices $\{i_1, i_2, \ldots, i_r\}$ and $\{j_1, j_2, \ldots, j_r\}$ where the k^{th} step is defined by 1's at rows i_k to $i_{k+1} - 1$ and 0's at columns j_k to $j_{k+1} - 1$. Then the sequence $\prod_{k=1}^{r} K_{i_k} \cdots K_{i_{k-1}} P_{j_k} \cdots P_{j_{k-1}}$ obtains the desired configuration of 1's and 0's. Being able to write a staircase matrix for the final configuration means that every target ON in the final configuration occurs only where there are 1's in the matrix. These targets are never affected by a P in this procedure; they do not go through a cycle. Because any allowed configuration can be reached from this procedure, it follows that any sequence that uses a cycle is redundant. □

Knowing that the non-redundant sequences must avoid cycles, it suffices to find the longest sequences that can be written before cycles appear.

Lemma 3.4.6. *For each value of l_n (l_m), the maximum number of K's (P's) that can be used before all targets are activated (deactivated) is $n - l_n + 1$ ($m - l_m$).*

Proof. A sequence that activates all targets has no intervening P's. Recall that a single K activates at most $\frac{N}{n} l_n$ targets. Then, prior to the last K being used, the number of activated targets is $N - \frac{N}{n} l_n = \frac{N}{n}(n - l_n) \leq \frac{N}{n} l_n (n - l_n)$. This means there are at most $n - l_n$ groups of targets controlled by different K's. Thus, at most $n - l_n$ K's are used before the last K is used, and $n - l_n + 1$ K's must be sufficient to activate the complete set. The maximum number of P's that can be used is only $m - l_m$ because we can think of every sequence starting in the zero configuration as having been preceded by a single P; this modification puts the P's on equal footing with the K's. □

With this characterization of the non-redundant sequences our goal is to recursively eliminate sequences that use $n - l_n + 1$ K's and $m - l_m$ P's. We first find the number of sequences that use up to $m - l_m$ P's, which forms the top row

in each (n, m) block in S2 Fig. Then we use these values to recursively find the number of sequences using up to $n - l_n + 1$ K's. The strategy is to subtract from the total number of sequences at a given (l_n, l_m) all those sequences using the forbidden number of regulators in order to get the new total.

Denote by a_n^m the number of sequences using m P's when the total number of K's is n. If $m = 1$, then all $B_1^{-n} = 2^n$ sequences (except for the empty sequence) use a K and none use a P. If $m = 2$, the maximum number of P's that can be used is $m - l_m = 1$. Discarding the 2^n sequences with no P, the number of sequences using a single P is

$$a_n^1 = \frac{B_2^{-n} - 2^n}{2}. \tag{3.19}$$

Division by $m = 2$ is required to account for the fact that there are $\binom{m}{1} = m$ different ways of starting each sequence with a P, and we consider both of these equivalent. Having determined a_n^m, it is straightforward to determine a_n^{m+1}. Because there are $m + 1$ P's to choose from, there are $\binom{m+1}{m} a_n^m$ ways to write sequences with m P's, $\binom{m+1}{m-1} a_n^{m-1}$ ways to write sequences with $m - 1$ P's,..., $\binom{m+1}{0} 1$ ways to write sequences with 0 P's, the only remaining sequences are those with $m + 1$ P's. Knowing that the total number of sequences is B_m^{-n}, this leaves

$$a_n^{m+1} = \frac{B_m^{-n} - 2^n - \sum_{j=0}^{m} \binom{m+1}{j} a_n^j}{m+1} \tag{3.20}$$

total sequences using $m + 1$ P's when the total number of K's is n. Having determined this number, we can sum up all the sequences using $m - l_m$ P's to get the first row of the (n, m) block in S2 Fig. Denote by $c_n^m(l_n, l_m)$ the $l_m{}^{\text{th}}$ column and $l_n{}^{\text{th}}$ row of the (n, m) block. The column headers $c_n^m(1, l_m)$ are given by

$$c_n^m(1, l_m) = 2^n + \sum_{j=0}^{m-l_m} \binom{m}{j} a_n^j. \tag{3.21}$$

We can determine the row entries for $l_n > 1$ in the same way that we determined the column headers, the only difference being that the total number of sequences is $c_n^m(1, l_m)$, not B_m^{-n} unless $l_m = 1$. Denote by $b_m^n(l_m)$ the number of sequences using n K's when the total number of P's is m and the P connectivity is l_m. For fixed m, l_m and $n = 1$, there are

$$b_m^1(l_m) = 2^m - \sum_{j=0}^{l_m-1} \binom{m}{j}, \tag{3.22}$$

sequences, as all but the empty sequence use a single K. In complete analogy to (3.20) we find there are

$$b_m^{n+1}(l_m) = c_n^m(1, l_m) - \sum_{j=0}^{n-l_n+1} \binom{n+1}{j} b_m^j(l_m) \tag{3.23}$$

sequences using $n+1$ K's when the total number of P's is m. Unlike in the equation for a_n^m, there is no division by $n+1$ because all sequences starting with a different K are different. Finally, we can sum up all the sequences using $n-l_n+1$ K's to get

Theorem 3.4.7. *The number of minimal length sequences in the (n, m, l_n, l_m) ratchet network with threshold $T = 1$ using no more than $n - l_n + 1$ K's and $m - l_m$ P's is*

$$c_n^m(l_n, l_m) = \sum_{j=0}^{n-l_n+1} \binom{n}{j} b_m^j(l_m). \tag{3.24}$$

We used this formula to compute each entry in S2 Fig. Because of the complexity of this procedure, we checked it against a computer algorithm operating with the following steps. In step 1 find all B_m^{-n} sequences in the $l_n = l_m = 1$ case. In step 2 increase the connectivity (l_n or l_m) and find all sequences of a given length; group them by the configuration they generate. Some of these sequences will not appear in the list generated by step 1: for example, both K_1K_2 and K_2K_1 will be found in step 2. We are interested in index permutation e.g. $1 \to 3$, not letter permutation, so in step 3 delete all sequences in each length group not appearing in step 1. Repeat steps 1-3 with this new list of sequences until $l_n = n - 1$. This code, implemented in Matlab Version 2015b, gave exact agreement with Theorem 3.4.7.

3.4.6 Proof that the reachable configurations are equivalent to the connected one-colorings

We now show that rules restrict the reachable configurations of the sequestration model in the main text to the connected one-colorings of the reduced n-network.

Theorem 3.4.8. *There is a one-to-one correspondence between the reachable configurations of the reduced n-network and the connected one-colorings.*

Proof. The converse direction, reachable implies connected, is easier to prove and will be discussed first. Assume that all configurations in the reduced n-network so far reached are connected. The next configuration will be reached by turning all 0's to i's or all j's to 0's by application of K_i or P_j, respectively. The k-arm targets sharing state i with the 2-arm target $\{0, 1, i\}$ are either in the same state as some other 2-arm target $\{0, 1, i'\}$ or are in the 0 state. So application of K_i cannot change the connectivity of the configuration. Furthermore, a k-arm target can be in the j state only if the target $\{0, 1, j\}$ is in the j state, so these targets will

still be matched after application of P_j. Thus, any configurations reachable from a reachable configuration must be connected.

The forward direction, connected implies reachable, is less trivial. In order to prove that all connected one-colorings in the n-network are reachable, we will use the strong form of mathematical induction. Assume the theorem holds for all networks up to $n-1$. Embedded within the full n-network of 2^n-1 targets is the reduced n-network on 2^{n-1} targets. Within the reduced n-network is a set of 2^{n-2} targets able to access $\{0,1,2\}$ and all subsets (including $\varnothing$) of the integers $\{3,\ldots,n\}$. Thus, we can substitute $2 \to 1$ as the ON state in this embedded network and all connected one-colorings (of 2) will be reachable. The same holds in general for all 2^{n-k} targets able to access $\{0,1,k\}$ and all subsets of the integers $\{k+1,\ldots,n\}$. In each of these embedded networks the substitution $k \to 1$ as the ON state will enable us create any connected one-coloring.

Pick any connected one-coloring (of 1) in the n-network. Its *opposite* configuration is formed by the transformation at each target g of $1 \to 0$ and $0 \to k_{min}$, where $k_{min} = \min\left\{k \in g | \mathbf{x}_{\text{pos}(\{0,j,k\})} = 0\right\}$ is the smallest index that g shares with a corresponding 2-arm target at position $\text{pos}\left(\{0,j,k\}\right)$ of $\mathbf{x}$ (possibly in the full network) currently in the 0 state. The opposite of a connected one-coloring is clearly connected, because all the connected 1's are now 0, and all the 0's are in the same state as the 2-arm target $\{0,j,k_{min}\}$. If it is possible to reach the opposite configuration, then application of the sequence $K_1P_2\ldots P_n$ yields the desired one-coloring of the n-network.

To show that the opposite configuration of the chosen one-coloring is indeed reachable, isolate the embedded networks one-by-one by application of the sequence $K_kK_1P_k$ for $k = 2,\ldots,n$, so that the targets in the $n-k+1$-network are the only targets in the 0 state. By hypothesis, the connected one-colorings are reachable in all embedded networks which have at most $n-k$ states besides 0, 1, and k. The opposite configuration in the n-network is composed of connected one-colorings (of k) in each embedded network; these are are reachable. Therefore, the one-coloring of the n-network is reachable via $K_1P_2\ldots P_n$. This procedure holds for any one-coloring. □

3.4.7 Lower and upper bounds for the full n-network

How many configurations are reachable in the full n-network? Let this number be c_n. The following theorems derive lower and upper bounds for c_n in terms of the number of one-colorings.

Theorem 3.4.9. *The formula $f(n+1)$ for the number of connected one-colorings in the reduced $n+1$-network is a lower bound for c_n.*

Proof. The full $n+1$-network can be partitioned into a set of 2^n targets having a 1 and all subsets of $\{2,\ldots,n+1\}$, and 2^n-1 targets that lack 1 but have all nonempty subsets of $\{2,\ldots,n+1\}$. The latter set of targets is an embedded full n-network, while the former is the reduced $n+1$-network. All $2(n+1)$ letters are needed to form the one-colorings in the reduced $n+1$-network. Every one-coloring is finally obtained by applying some permutation of $K_1, P_2, \ldots, P_{n+1}$ to a configuration that uses (at most) the states $2,\ldots,n+1$ and 0, i.e., the full n-network. Because K_1 and P_1 do not affect the targets of the the embedded full n-network, there must be (at least) one sequence using only $\{K_2,\ldots,K_{n+1}\}$ and $\{P_2,\ldots,P_{n+1}\}$ that prepares the embedded full n-network in the aforementioned configuration, which means we may associate a one-coloring to (at least) one of the c_n sequences in the embedded full n-network. Therefore, multiple configurations in the full n-network may map to the same one-coloring in the reduced $n+1$-network. Conversely, if two one-colorings are different, they are distinguishable by their configurations immediately preceding the final $K_1, P_2, \ldots, P_{n+1}$ sequence, and must therefore map to different configurations in the full n-network. Together, these statements imply that the map from configurations in the full n-network to one-colorings in the reduced $n+1$-network is many-to-one, but the map from one-colorings to configurations in the full n-network is one-to-one. Therefore, $f(n+1) \le c_n$. □

Theorem 3.4.10. *An upper bound on c_n is*

$$\begin{aligned} &nf(n)+n(n-1)(f(n)-1)f(n-1)+\cdots+n!(f(n)-1)\cdots(f(2)-1)f(1)+1 \\ &\qquad=\sum_{k=1}^{n}(n)_k\left\{\prod_{j=n-k+2}^{n}(f(j)-1)\right\}f(n-k+1)+1, \end{aligned} \tag{3.25}$$

where $(n)_k = n(n-1)\cdots(n-k+1)$ is the falling factorial.

Proof. There are $nf(n)$ one-colorings in the full n-network, plus one origin. Each one of the one-colorings can be thought of as the origin of an $n-1$-network, which in turn generate $(n-1)f(n-1)$ one-colorings in an embedded $n-1$-network, for a total of

$$nf(n)(n-1)f(n-1)$$

configurations using 1, 2, and perhaps 0, hence termed two-colorings. However, one of the $f(n)$ one-colorings is the 0 state of the n-network, so it does not generate any

two-colorings. Thus, there are at most $1 + nf(n) + n(n-1)(f(n)-1)f(n-1)$ zero-, one-, and two-colorings. Now assume that the number of k-colorings is

$$n(n-1)\cdots(n-k+1)(f(n)-1)(f(n-1)-1) \\ \cdots(f(n-k+2)-1)f(n-k+1).$$

Of these,

$$n(n-1)\cdots(n-k+1)(f(n)-1)(f(n-1)-1)\cdots(f(n-k+2)-1)$$

are origins of an $n-k$-network, meaning they are actually $k-1$-colorings; they cannot generate any $k+1$-colorings. The remaining

$$n(n-1)\cdots(n-k+1)(f(n)-1)(f(n-1)-1) \\ \cdots(f(n-k+2)-1)(f(n-k+1)-1)$$

are genuine k-colorings which can generate $f(n-k)$ one-colorings in the $n-k$-network, or equivalently, $k+1$-colorings. Thus, the total number of zero-, one-, two-, $\ldots, k+1$-colorings is no more than

$$n(n-1)\cdots(n-k+1)(f(n)-1)(f(n-1)-1) \\ \cdots(f(n-k+2)-1)(f(n-k+1)-1).$$

This induction argument proves the statement. □

3.4.8 Properties of the orbits in the ratchet and sequestration network

First we define what it means to be an *origin* and an *orbit* in the threshold-1 ratchet network and determine the number of orbits as a function of n and m. Then we prove that the configurations in the sequestration network are defined by reversible paths.

A forbidden configuration in the ratchet network contains some row or column permutation of the pattern $\begin{pmatrix} 1 & 0 \\ 0 & 1 \end{pmatrix}$ on any 2×2 sub-block of the connectivity matrix $\mathbf{A}$. This is the minimum violation, but larger blocks may violate this pattern as well, for example $\begin{pmatrix} 1 & 0 \\ 0 & 1 \\ 1 & 0 \end{pmatrix}$ has 2 violations. Furthermore, application of any of the K's or P's in this sub-block will relieve at least one of these violations. Therefore, we define an i,j*-orbit* in the ratchet network as the locus of configurations having

a forbidden configuration on an $i \times j$ sub-block that does not use the corresponding set of i K's and j P's. The *origin* of any i,j-orbit is the configuration having all remaining $nm - ij$ entries of $\mathbf{A}$ equal to 0 (or all 1 to make the case of having only P actions symmetric with having only K's). A matrix $\mathbf{X}$ having the same forbidden $i \times j$ sub-block as an origin $\mathbf{Y}$ is not considered to be in the orbit of $\mathbf{Y}$ if (i.) there is no sequence of actions that transforms $\mathbf{Y}$ to $\mathbf{X}$, or (ii.) if the sequence involves one of the forbidden K's or P's. With these restrictions, the number of origins is equal to the number of orbits.

Denote by c_i^j the number of orbits in a ratchet network of size $n \times m$ with violations involving $i \leq n$ K's and $j \leq m$ P's. If $i = j = 2$ there are $2^{ij} - B_2^{-2} = 2$ forbidden configurations that turn into origins for the remaining $n - i$ K's and $n - j$ P's. There are more orbits in these smaller networks. For every $i', j' \geq 2$ there are $\binom{i}{i'}\binom{j}{j'}c_{i'}^{j'}B_{i-i'}^{-(j-j')}$ configurations reached by orbits using i' K's and j' P's. Only configurations *not* reached by these orbits are available as new origins when the number of K's and P's not to be used is i and j, respectively. Finally, there are $\binom{n}{i}\binom{m}{j}$ ways to specify $i \leq n$ K's and $j \leq m$ P's. Then we have

Theorem 3.4.11. *For a given set of $i \leq n$ K's and $j \leq m$ P's, the number of i,j-orbits is*

$$c_i^j = \left(2^{ij} - B_i^{-j}\right) - \sum_{\substack{i',j' \geq 2 \\ i'+j' \leq i+j-1}}^{i,j} \binom{i}{i'}\binom{j}{j'}c_{i'}^{j'}B'^{-(j-j')}_{i-i'}, \tag{3.26}$$

and the total number of i,j-orbits in the $n \times m$ ratchet network is

$$C_i^j(n,m) = \binom{n}{i}\binom{m}{j}c_i^j, \tag{3.27}$$

where

$$B'^{-(j-j')}_{i-i'} = \begin{cases} B_{i-i'}^{-(j-j')} & \text{if } i - i' > 0 \text{ and } j - j' > 0 \\ 2^{i-i'} & \text{if } j - j' = 0 \\ 2^{j-j'} & \text{if } i - i' = 0 \end{cases}. \tag{3.28}$$

The modification B' ensures that an orbit lacking allowable P's (K's) can still use K's (P's). A table of values of Eq. (3.27) is given in S4 Fig.

We noted in the main text that configuration in the sequestration network can be joined by reversible paths. A path K_iP_j or P_jK_i is *reversible* if a configuration reached by the sequence of actions w is also reached by the either the sequence wK_iP_j or wP_jK_i, but not wK_i or wP_j, respectively. Thus we can also prove

Theorem 3.4.12. *There always exists a reversible path between any two configurations in an orbit of the sequestration network.*

Proof. Let $\mathbf{x}$ be a configuration in an orbit using $m \leq n$ of the actions, and let P denote the locus of configurations reached from $\mathbf{x}$. We now need to show that P must be reversibly reached from the origin. Denote by $\overline{P}$ the complement of P, so that any $\mathbf{y} \in \overline{P}$ is reversibly reached from the origin. In order for there to be no reversible path between $\mathbf{x} \in P$ and $\mathbf{y} \in \overline{P}$, there must always be a state i such that K_i increases the number of targets $\{\cdot, i\}$ in the i state and P_i increases the number of targets $\{\cdot, i\}$ in the zero state. Now assume there is a configuration $\mathbf{z} \in P$ using all m allowed states. $\mathbf{z}$ must have at least one target in the 0 state, but this is un-allowed, because then $\mathbf{z}$ would violate the connection rule. Therefore, there is a maximum number $m' < m$ of states used by any $\mathbf{x} \in P$. Now assume there is a configuration $\mathbf{z}' \in P$ using all m' allowed states. But this implies that there is a single-arm target $\{0, j\}$ that must be in the zero state. Then the action K_j takes $\mathbf{z}'$ to a configuration $\mathbf{y} \in \overline{P}$ and P_j takes $\mathbf{y}$ to $\mathbf{z}$. This path must be reversible, and $\mathbf{z}'$ is reached reversibly from the origin. By induction we conclude that $m' = 0$ and that $P = \varnothing$. Finally, because any two configurations are reached reversibly from the origin, there is a reversible path between them. □

Theorem 3.4.12 defines the orbits of the sequestration network as those configurations connected by reversible paths.

3.4.9 A universal formulation of the actions as matrix operators

In this section we show how to write the K and P regulators as matrix operators in a manner consistent with both models considered in the paper. First we define the vector space $\mathcal{V}$ of configurations of the N targets, then we derive the operators that transform $\mathcal{V}$.

Let $\mathbf{x} \in \mathcal{V}$. For a network with N targets we require that $\sum_i x_i = N$. This means that $\mathbf{x}$ has at least N entries, and in general dim $\mathbf{x} \geq N$. Therefore, we cannot use the standard state space of N-dimensional vectors, because the operators will not conserve the number of targets. Each target has a 0 state. The number D of independent directions accessible from 0 is called the *dimension* of the network, and the number T of steps one can move along each dimension is called the *threshold*. In the ratchet model, each target has a single ladder of states with variable threshold, so $D = 1$ and T is allowed to vary; in the sequestration model $D = n$ but the threshold is $T = 1$.

Denote by A_{di} the fraction of the targets of type A in state $i \in \{0, 1, \ldots, T\}$ along dimension d. For a subset of the targets a K-type action causes population transfer between states (d, j) and (d, i) with $i = j+1$, and a P-type action the reverse. If a K regulator acts for a short time we can write the "reaction rate" equation as

$$\dot{x}_{A_j} = -g_A x_{A_j} \tag{3.29a}$$

$$\dot{x}_{A_i} = +g_A x_{A_j}, \tag{3.29b}$$

where $g_A > 0$ is a proportionality constant. This defines a matrix differential equation

$$\dot{\mathbf{x}} = \mathbf{G_{dj}} \cdot \mathbf{x} \tag{3.30}$$

with $\mathbf{x} \in \mathbb{R}^{N(DT+1)\times 1}$ the vector of populations of the $DT+1$ states of the N targets and $\mathbf{G_{dj}} \in \mathbb{R}^{N(DT+1)\times N(DT+1)}$ the block diagonal matrix of rate constants between the j and $j+1$ population states along dimension d. Eqs. (3.29) can be rewritten

$$\begin{pmatrix} \dot{x}_{A_j} \\ \dot{x}_{A_i} \end{pmatrix} = \begin{pmatrix} -g_A & 0 \\ g_A & 0 \end{pmatrix} \cdot \begin{pmatrix} x_{A_j} \\ x_{A_i} \end{pmatrix}. \tag{3.31}$$

Because $\mathbf{G_{dj}}$ is block diagonal, Eq. (3.30) can be solved by exponentiation on each block:

$$\begin{pmatrix} x_{A_j}(t) \\ x_{A_i}(t) \end{pmatrix} = \exp\left\{ \begin{pmatrix} -g_A & 0 \\ g_A & 0 \end{pmatrix} t \right\} \cdot \begin{pmatrix} x_{A_j}(0) \\ x_{A_i}(0) \end{pmatrix} = \begin{pmatrix} e^{-g_A t} & 0 \\ 1 - e^{-g_A t} & 1 \end{pmatrix} \cdot \begin{pmatrix} x_{A_j}(0) \\ x_{A_i}(0) \end{pmatrix}. \tag{3.32}$$

The restriction of the model from a continuous range of population states $x_{A_i} \in [0, 1]$ to the boolean values $\{0, 1\}$ formally emerges by considering the "reaction" K catalyzes on its targets to have gone to completion. We do this by taking the the limit $t \to \infty$ in Eq. (3.32) to get

$$\begin{pmatrix} x_{A_j}(t) \\ x_{A_i}(t) \end{pmatrix} = \begin{pmatrix} 0 & 0 \\ 1 & 1 \end{pmatrix} \cdot \begin{pmatrix} x_{A_j}(0) \\ x_{A_i}(0) \end{pmatrix}, \tag{3.33}$$

so that the matrix $\mathbf{K_{dj}}$ defined by

$$\mathbf{K_{dj}} = \lim_{t\to\infty} \exp\{\mathbf{G_{dj}} t\} \tag{3.34}$$

is the block diagonal matrix having 1's at (row, column) positions $\Big(1 + (d-1)T + i, 1 + (d-1)T + j\Big)$ of each block that responds to K in dimension d and admits population transfer between from j to i.

Because K acts on all targets at once, it is insensitive to the initial state j. Thus the matrix corresponding to the action of K is

$$\mathbf{K_d} = \prod_j \mathbf{K_{dj}}, \tag{3.35}$$

which is the block diagonal matrix having 1's at (row, column) positions

$$\Big(1+(d-1)\,T+1, 1+(d-1)\,T+0\Big), \ldots, \Big(1+(d-1)\,T+T, 1+(d-1)\,T+T-1\Big)$$
$$\text{and } \Big(1+(d-1)\,T+T, 1+(d-1)\,T+T\Big)$$

of each block that responds to K in dimension d.

This derivation can be repeated in the case that population goes in the opposite direction from at state j to a state $i < j$ using a different set of rate matrices $\mathbf{H_{dj}}$ corresponding to the reverse of Eq. (3.31). We obtain the block diagonal matrix $\mathbf{P_d}$ corresponding to the action of P in dimension d having 1's at (row, column) positions

$$\Big(1+(d-1)\,T+0, 1+(d-1)\,T+1\Big), \ldots, \Big(1+(d-1)\,T+T-1, 1+(d-1)\,T+T\Big)$$
$$\text{and } \Big(1+(d-1)\,T+0, 1+(d-1)\,T+0\Big)$$

of each block that responds to P in dimension d. Whereas $\mathbf{K_d}$ is sub-diagonal, $\mathbf{P_d}$ is super-diagonal.

The Baker-Campbell-Hausdorf expansion shows that $\mathbf{K_d}$ in Eq. (3.35) and in general any product of matrices $\mathbf{K_d}$ and $\mathbf{P_d}$ are generated by matrix exponentiation of commutators of the generators $\mathbf{G_{dj}}$, $\mathbf{H_{dj}}$. This is the origin of noncommutativity in both the ratchet and sequestration models.

An example in the sequestration network illustrates population transfer between states. In the $n = 2$ network on the targets A, B, and C the initial configuration of the network is represented by $\begin{pmatrix} A_0 & A_{11} & A_{21} & B_0 & B_{11} & B_{21} & C_0 & C_{11} & C_{21} \end{pmatrix}^T =$ $\begin{pmatrix} 1 & 0 & 0 & 1 & 0 & 0 & 1 & 0 & 0 \end{pmatrix}^T$. Only targets A and C can access dimension 1, and only targets B and C can access dimension 2. Therefore the $t \to \infty$ action of K_1 on

the network is given by

$$\begin{pmatrix} e^{-g_A t} & 0 & 0 & 0 & 0 & 0 & 0 & 0 & 0 \\ 1-e^{-g_A t} & 1 & 0 & 0 & 0 & 0 & 0 & 0 & 0 \\ 0 & 0 & 0 & 0 & 0 & 0 & 0 & 0 & 0 \\ 0 & 0 & 0 & 1 & 0 & 0 & 0 & 0 & 0 \\ 0 & 0 & 0 & 0 & 0 & 0 & 0 & 0 & 0 \\ 0 & 0 & 0 & 0 & 0 & 1 & 0 & 0 & 0 \\ 0 & 0 & 0 & 0 & 0 & 0 & e^{-g_C t} & 0 & 0 \\ 0 & 0 & 0 & 0 & 0 & 0 & 1-e^{-g_C t} & 1 & 0 \\ 0 & 0 & 0 & 0 & 0 & 0 & 0 & 0 & 1 \end{pmatrix} \begin{pmatrix} 1 \\ 0 \\ 0 \\ 1 \\ 0 \\ 0 \\ 1 \\ 0 \\ 0 \end{pmatrix} \xrightarrow[t\to\infty]{} \begin{pmatrix} 0 \\ 1 \\ 0 \\ 1 \\ 0 \\ 0 \\ 0 \\ 1 \\ 0 \end{pmatrix}. \tag{3.36}$$

Only A and C advance to state 1 and the number of targets (3) is conserved.

3.5. Supplementary Information

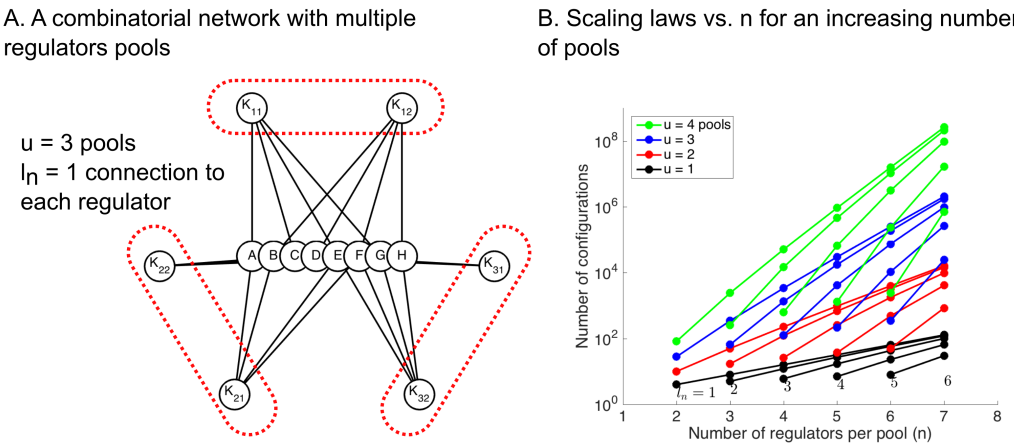

Figure S3.1: Scaling in combinatorial networks is sub-exponential. **(A)** An example network with $u = 3$ pools of $n = 2$ regulators each. A target is only ON if all u of its regulators bind. **(B)** Plots of Eq. (3.18) versus n for an increasing number of pools u and increasing redundancy l_n

		n	**2**					**3**					**4**					**5**					**6**				
		l_m	**1**	**2**	**3**	**4**	**5**	**1**	**2**	**3**	**4**	**5**	**1**	**2**	**3**	**4**	**5**	**1**	**2**	**3**	**4**	**5**	**1**	**2**	**3**	**4**	**5**
m	l_n																										
6	**1**		1394	1004	509	169	34	20266	11512	4207	947	122	237686	107336	29261	4681	406	2441314	884848	184183	21563	1298	22934774	6730424	1087829	95089	4054
	2							3991	2839	1399	439	79	72955	40255	13945	2865	315	999391	431311	109111	15511	1111	11467387	3914575	742945	75705	3675
	3												7855	5563	2713	833	143	175736	95906	32531	6431	656	2815849	1193353	292513	39393	2553
	4																	12986	9176	4451	1351	226	344884	187138	62773	12153	1188
	5																						19384	13678	6613	1993	328
5	**1**		454	289	119	29		4718	2283	653	103		41506	15481	3191	341		329462	95907	14597	1087		2441314	560449	64079	3389	
	2							1267	787	307	67		16275	7505	1965	265		164731	57331	10531	931		1441923	384713	51093	3073	
	3												2471	1521	581	121		38576	17451	4401	551		453537	153257	26697	2137	
	4																	4066	2491	941	191		75072	33617	8307	997	
	5																						6052	3697	1387	277	
4	**1**		146	78	24			1066	414	84			6902	1986	276			41506	8982	876			237686	39138	2724		
	2							391	199	55			3451	1235	215			25231	6511	751			164731	31283	2471		
	3												751	375	99			7976	2756	446			67081	16457	1721		
	4																	1226	606	156			15316	5192	806		
	5																						1816	892	226		
3	**1**		46	19				230	65				1066	211				4718	665				20266	2059			
	2							115	43				675	165				3451	571				16275	1869			
	3												215	77				1496	341				8673	1305			
	4																	346	121				2808	615			
	5																						508	175			
2	**1**		14					46					146					454					1394				
	2							31					115					391					1267				
	3												55					236					889				
	4																	86					424				
	5																						124				

Figure S3.2 (*preceding page*)**: Number of unique words in the threshold 1 ratchet network as a function of $n, m, l_n,$ and l_m found using Eq.** (3.24)**.** n and m increase the across the rows and up the columns. l_n and l_m increase down the columns and across the rows of the sub-blocks.

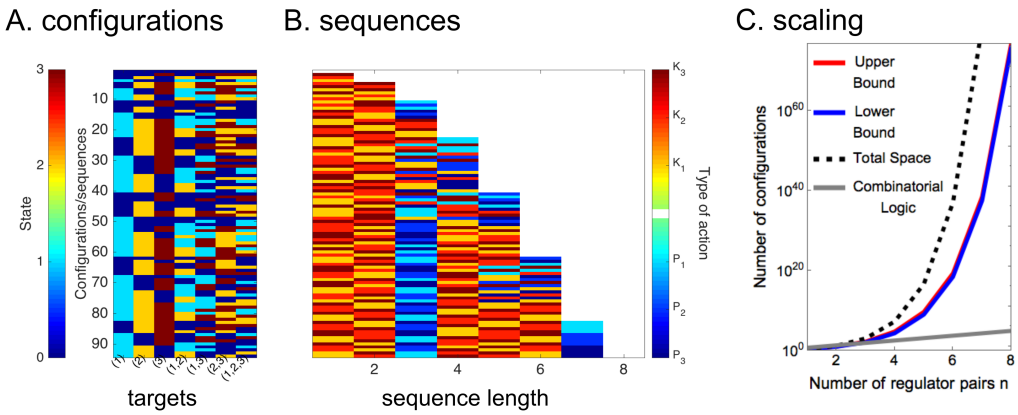

Figure S3.3: The full n-network model has upper and lower bounds. (A) A plot of all the allowed configurations of a set of targets controlled by n = 3 regulators pairs in the full n-network. Blue, cyan, yellow, and red correspond to states 0, 1, 2, and 3, respectively. **(B)** A list of the words generating the corresponding states in A. K actions are shown in the red spectrum, and P in the blue. **(C)** A logarithmic plot of the bounds on the full model. The total space is $\prod_{i=0}^{n}(i+1)^{\binom{n}{i}}$, the upper and lower bounds are calculated from Eqs. (3.25) and (3.7), respectively, and the combinatorial model is 2^{2n}.

		n	2					3					4					5					6				
		j	2	3	4	5	6	2	3	4	5	6	2	3	4	5	6	2	3	4	5	6	2	3	4	5	6
m	i																										
6	2		30					90	90				180	360	210			300	900	1050	450		450	1800	3150	2700	930
	3		120					360	3480				720	13920	22440			1200	34800	112200	151800		1800	69600	336600	910800	918120
	4		210					630	16830				1260	67320	484230			2100	168300	2421150	7348950		3150	336600	7263450	44093700	110096310
	5		180					540	45540				1080	182160	2939580			1800	455400	14697900	122372820		2700	910800	44093700	734236920	4044522780
	6		62					186	45906				372	183624	7339754			620	459060	36698770	674087130		930	918120	110096310	4044522780	49630551242
5	2		20					60	60				120	240	140			200	600	700	300		300	1200	2100	1800	620
	3		60					180	1740				360	6960	11220			600	17400	56100	75900		900	34800	168300	455400	459060
	4		70					210	5610				420	22440	161410			700	56100	807050	2449650		1050	112200	2421150	14697900	36698770
	5		30					90	7590				180	30360	489930			300	75900	2449650	20395470		450	151800	7348950	122372820	674087130
	6																										
4	2		12					36	36				72	144	84			120	360	420	180		180	720	1260	1080	372
	3		24					72	696				144	2784	4488			240	6960	22440	30360		360	13920	67320	182160	183624
	4		14					42	1122				84	4488	32282			140	11220	161410	489930		210	22440	484230	2939580	7339754
	5																										
	6																										
3	2		6					18	18				36	72	42			60	180	210	90		90	360	630	540	186
	3		6					18	174				36	696	1122			60	1740	5610	7590		90	3480	16830	45540	45906
	4																										
	5																										
	6																										
2	2		2					6	6				12	24	14			20	60	70	30		30	120	210	180	62
	3																										
	4																										
	5																										
	6																										

Figure S3.4 (*preceding page*)**: Number of orbits restricted from using i of the K's and j of the P's in the threshold 1 ratchet network as a function of n and m calculated using Eq.** (3.27)**.** n and m increase the across the rows and up the columns. i and j increase down the columns and across the rows of the sub-blocks.

Chapter 4

STRING THEORY MEETS BIOLOGY: APPLICATION OF ROTATIONAL DYNAMICS TO AUTONOMOUS DEVELOPMENT

4.1. Introduction

The fundamental problems in using combinatorial logic to explain development have been reviewed in section 1.3, and an alternative using sequential logic was proposed in chapter 3. The information bottleneck at the egg stage could be circumnavigated by extracting the information content of the adult in a stepwise fashion. However, the paradox remained unresolved as to how sequences could arise autonomously. As reviewed in section 1.1, the need for sequential processes is hardly surprising in experimental embryology. Inductive signals in the form of morphogen gradients initiate development [14, 233], and over time the cell translates these messages into tissue-specific gene expression profiles. Yet, it has been argued that such an "ordering process" adds no new information to instructions present in the egg, in the same way that a differential equation with boundary conditions provides no more information than the solution curve [117]. It was described in chapter 2 how regulation in the *tangent space* of gene expression led to a stepwise process in as related cells maintained their equipotential relationship over time. It is the aim of the current chapter to make this abstract theory more tangible by showing how imposition of conserved transcriptional activity translates into spatially-restricted gene expression. These goals are accomplished via a seemingly unrelated question: What happens to a string whose ends are subjected to twisting and bending?

Strings are bent and twisted due to the action of forces and torques supplied at their ends; it is desirable to predict the resultant shape and stability. Initial studies on strings were motivated by the problems of kinking in undersea cable [60, 159, 302], and wave propagation in wires [56, 274], but similar analyses have been extended to looping and supercoiling in DNA [87, 248]; see also [98] for a perspective. Exact results are possible when the string is cast in the form of the inflectional Euler elastica (see [28], [163], ch. XIX, [200] ch. 4, [272] ch. 2.7, and the Supplementary Information 4.5.1), a curved planar arc of fixed length, which may double back on itself to form loops. This well-studied model has shed much light on the elastic stability of strings.

One may want to know, for example, under what conditions planar loops "pop out" of the plane. A popular strategy for determining the loads that lead to pop out or kinking has been to use nonlinear stability analysis near a bifurcation in the string's energy [98, 159, 167, 196, 277, 278, 302]. The idea of this approach, when applied to the related problem of beam buckling, is to postulate a relationship between the axial and (sinusoidal) transverse displacements of a loaded elastic rod, and then to solve a differential equation for the amplitude of a particular mode as a function of the axial compression [296]. One may also relate the total energy of the deformed rod to the transverse displacement (cf. [272] ch. 1.11), an approach which when applied to the string led Maddocks to a bifurcation diagram in the deflection angle θ between the string axis and the line of action of the load [167]. The critical tension from the beam buckling problem (derived in [272] ch. 2.21) has also been related to the bending angle θ [278]. In reference [278], phase portraits in the (θ, θ') plane revealed qualitative differences in shape as the tension was tuned, from those with full loops ($\theta_{\max} \geq 2\pi$) to those that merely nutate ($0 < \theta_{\max} < 2\pi$); the analysis paralleled that of the heavy top precessing in time (see [13] ch. 6.30). Tension-displacement phase diagrams have also been used to determine when twisted strings whose ends are brought together pop out into loops [97, 196, 269, 277]. Thompson and Champneys originally made the distinction between wave-like helical loops, in which one turn of axial twist coincides with one turn of the helix, and localized loops with three twists; they derived equilibrium conditions relating the energy of the localized state to the moment and tension applied in the helical state [269]. Similarly, van der Heijden and coworkers described two behaviors in pretwisted strings whose ends were brought together: (i.) those that jumped into self-contacting loops before the ends met, and (ii.) those that smoothly made the transition through a circular ring [277]. In general, buckling relieves torsional strain—by reducing the angular deformation that must be accommodated—at the expense of increased bending strain; the critical point is where the two strains match [98]. In addition to these studies, others have explicitly measured pop out curves using specialized apparatus [97], derived perturbation expansions in the angular velocities [96], and analyzed vibrations in clamped elasticas [70]. This last study made use of the central idea [56, 57, 272] that first differences in space of forces and moments over small sections of the string result in second differences in time (i.e., acceleration) of spatial points of the material.

Instead of a stability analysis, one may want to know the explicit equation of the space curve of the string's central line. Although the planar elastica has a

closed-form solution, being loaded only with tension, the nonplanar loop is nontrivial because end shortening interacts with twist. The combined torques and tensions change the direction of all three so-called director basis vectors $\{\mathbf{d}_i\}$ [56, 57, 167, 200], which define an orthogonal basis that moves with the string. The directors are related to a fixed Euclidean coordinate system by elements of the Lie group $SO\,(3)$ of rigid rotations of a three-dimensional object. Furthermore, because twist and bending are accounted for using angular *rates* of the directors, the applied loads are actually members of the tangent space of $SO\,(3)$, known at the group identity as the Lie algebra $\mathfrak{so}\,(3)$. Fortunately, there is a well-development mathematical theory called Hamiltonian mechanics [12, 13, 119, 172] that prescribes how angular velocities change in a dynamical system with fixed energy. Previous authors have successfully used this framework to describe n-dimensional rotation, fluid flow, plasma dynamics, and heavy tops [33, 106, 173, 222]. The main idea is that since vector fields represent the tangent vectors of flows, it is possible, using the Legendre transform and a device called the Lie bracket, to find a new differential equation that maintains constant energy along vector fields of interacting forces. The Euler-Poincaré equations for the rotation of a body in three-dimensional space, for example, can be written as the Lie bracket of angular momentum and angular velocity. In turn, the Euler-Poincaré equations are a special case of the analysis using the more general semidirect product group, a group in which the symmetry of the free system is broken by the application of a force in a distinguished direction [106, 119, 172, 173]. This chapter examines the case when the symmetry of the string's director basis is broken by both axial and bending strains. It is concluded that the Euler-Poincaré equations represent the most parsimonious path between energy states of a string controlled only at its ends, but that in the case of more than one force, a closed form trajectory cannot be known in advance.

When stated as a constraint on information, string dynamics illuminate the problem of development by resolving the paradox of how a process can be deterministic but not realizable until the passage of time. To see how this works, imagine drawing the (unique) line through the tangent vectors of a *single* vector field starting at time zero; where would this line be if there were *two* overlaid fields? Following the vector field 2 for a short time means that the line traces a different tangent vector of field 1, just as following field 1 in reverse for a short time discloses a different tangent vector of field 2. The two tangent lines found by this procedure approximate the trajectory of the system when field 2 modifies field 1 (and vice versa). The (possibly non-integrable) field obtained as the time span approaches

zero is known formally as the Lie derivative. The Lie derivative of the two fields determines the trajectory at later times, but only because the input signals provide "steering assistance," not exact "GPS coordinates." We can't know final state until we follow the flow lines till their ends. If biological signals could be formulated as vector fields, they too would steer development on highly contingent trajectories set by their Lie brackets in the egg. This chapter develops such a formulation used conserved total RNA polymerase to represent the more abstract concept of constant total information. Just as torsion and curvature of a string are constrained by the total energy, conserved transcriptional activity determines the spatial variation of gene expression throughout the embryo. The emphasis on constants of motion imposes symmetry on the system via Noether's theorem [119], resulting in an autonomous theory of development that does not appeal to noise or stochasticity in expression dynamics.

4.2. Results

The Results are organized as follows. First in section 4.2.1, the differential equation in the arc length for the angular momentum of a looped string is derived, and the connection is made to the analogous problem of the heavy top. It is shown in section 4.2.2 how to account for pure twist of fibers about the central line; how twist interacts with looping to become torsion is addressed in section 4.2.3. The results of the Lie framework are compared with the classical Frenet-Serret equations using known equations for the angular velocities. It is concluded that differences emerge due to misalignment of forces and velocities along the length of the string. In section 4.2.4, the Zassenhaus expansion for mixed forces propagating from a localized point on the string is derived. The remaining sections 4.2.5-4.2.7 connect the string results to the problem of autonomous development. Section 4.2.5 presents a derivation of the rotational equations for the allocation of limited RNA polymerase, section 4.2.6 describes a rigid parametrization of a growing one-dimensional organism, and section 4.2.7 applies the model to interacting morphogen gradients during development. Supplementary derivations are found in the Materials and Methods section 4.4.

4.2.1 String looping without twist

Combinations of forces in strings lead to shapes not predicted by either force alone. Before studying combined forces, we show how to translate tension at the string ends into the evolution of the angular velocity of the binormal curvature

vector along the arc length of the string. Formulating force in the tangent space of allowed motions of the string makes it possible to treat the combinatorial problem in a unified way using Lie algebras.

According to Love [163], Kirchhoff was the first to make an analogy between the equations governing the periodic motion of pendula and the helical looping of strings. With the time variable t replaced by the spatial variable s, looping becomes the problem of how the principal unit vectors $(\mathbf{n}, \mathbf{b}, \mathbf{t})$ in the normal, binormal, and tangential directions rotate relative to a (moving) body-centered coordinate frame. The principal vectors are everywhere defined by drawing the unit normal out from the center of curvature to the origin of the body frame and orienting the unit tangent in the direction of motion; binormal is the direction mutually orthogonal to $\mathbf{n}$ and $\mathbf{b}$. Of course, there is no reason a point referred to an independent set $\{\mathbf{d}_i\}$ of mutually orthogonal vectors in the body frame at s should have the same coordinates relative to the principal frame. Derived and used in many works dealing with strings [56, 57, 95, 200, 274], the fundamental equation for updating the body position vector $\mathbf{d}$ in $\mathbb{R}^3$ is

$$\mathbf{d}' = \boldsymbol{\omega} \times \mathbf{d} = \begin{pmatrix} 0 & -\omega_3 & \omega_2 \\ \omega_3 & 0 & -\omega_1 \\ -\omega_2 & \omega_1 & 0 \end{pmatrix} \begin{pmatrix} d^1 \\ d^2 \\ d^3 \end{pmatrix} = \boldsymbol{\Omega} \cdot \mathbf{d}, \tag{4.1}$$

where the components of $\mathbf{d}$ are the positions coordinates of a point mass relative to the body-centered orthonormal basis $(\mathbf{d}_1, \mathbf{d}_2, \mathbf{d}_3)$, and $\boldsymbol{\omega}$ is the vector of rotational velocities (radians per length) about the three axes in the body. The *directors* $(\mathbf{d}_1, \mathbf{d}_2, \mathbf{d}_3)$ are initially parallel to the principal $(\mathbf{n}, \mathbf{b}, \mathbf{t})$ vectors and to the fixed Euclidean $(\mathbf{e}_1, \mathbf{e}_2, \mathbf{e}_3)$ basis, although they become misaligned as a result of the applied curvature, twist, and torsion. The vector $\boldsymbol{\omega}$ and the skew-symmetric matrix $\boldsymbol{\Omega}$ are related by the so-called *hat map* $\widehat{\ }\colon \mathbb{R}^3 \to \mathbb{R}^{3\times 3}$ in the obvious manner [119]; $\widehat{\ }$ can be extended to vectors in $\mathbb{R}^n$ (see [126] for one realization). To understand, for example, the total displacement $\omega_1 d^2 - \omega_2 d^1$ of of the third component of $\mathbf{d}$ when multiplying out Eq. (4.1), one uses a construction, due to Routh [231], for moving the north pole (axis 3) of a rotating globe: counterclockwise rotation about axis 1 increases the distance between the north pole and (the old) axis 2 by a circumferential arc length $\omega_1 d^2$ while leaving the distance to axis 1 fixed; subsequent counterclockwise rotation about (the new or old) axis 2 decreases the distance to (the old) axis 1 by $\omega_2 d^1$. Such are the only rotations that move the north pole, which is invariant to rotations about itself.

An alternative formulation for determining the space curve of a string relies entirely on the principal basis. In the Frenet-Serret equations, the principal basis is updated as

$$\mathbf{t}' = -\kappa\mathbf{n} \tag{4.2a}$$

$$\mathbf{n}' = \kappa\mathbf{t} - \tau\mathbf{n} \tag{4.2b}$$

$$\mathbf{b}' = \tau\mathbf{n}. \tag{4.2c}$$

There are only two distinguished velocities, viz. $\omega_2 = \kappa$ and $\omega_3 = \tau$, corresponding to the curvature and geometric torsion of the space curve $\mathbf{r}(s)$ of the central line [218]. In this basis, the normal direction, not $\mathbf{d}_1$, is chosen to rotate with the body. The principal $\mathbf{t}$ and body $\mathbf{d}_3$ tangents are assumed to be parallel, but points not on the central line are referred to different axes in the two formulations (4.1) and (4.2).

A loop is an instance of the inflectional Euler elastica, a well-known shape that also satisfies the pendulum equation $\theta'' = -\lambda^2 \sin\theta$ in the (azimuthal) Euler angle θ, where the rate of change of angular velocity $\omega_2 = \kappa = \theta'$ (and hence the bending moment) vanishes at the end point [28, 163, 200, 272, 296]. Loops can be fully described by the end tension $T = \lambda^2 E\mathbb{I}_2$(= force) which maintains the shape without any additional supports along s. For a loop localized to the xz plane, the bending moment is $E\mathbb{I}_2\kappa$ = force × dist., where E = force × dist.$^{-2}$ is the Young's modulus and $\mathbb{I}_2 = \frac{1}{\rho_0}\int_\Sigma \rho(x,z)(x^2+z^2)\,dxdz$ = dist.^{4} is the y component of the (diagonal) tensor $\frac{1}{\rho_0}\int \rho(x,y,z)(\mathbf{r}^2\mathbf{e}_i\otimes\mathbf{e}_i - \mathbf{r}\otimes\mathbf{r})\,d^3\mathbf{r}$ of the second moments of area about an axis through cross section Σ [13, 119, 200]; as in [200, 242], the mass density of $\rho(x,y,z)$ is normalized by the overall density ρ_0 at a particular cross section in order that $E\mathbb{I}$ have units of force × dist.^{2} The curvature $\kappa = \frac{x''z'-z''x'}{(z'+x')^{3/2}}$ [218] corresponds to the Frenet-Serret curvature and is determined by differentiation of the z and x coordinates of the elastica versus arc length s.

The elastica and Frenet-Serret pictures of the looped string are identical in the case of a planar loop, as we now show. In the absence of applied torques, the body-centered and fixed space bases at position s along the string are related to each other by a rotation matrix $g(s)$, which is an element of Lie group $G = SO(n)$ of n-dimensional rotations. So to write the (x,y,z) components of a position vector $\mathbf{r}$ relative to the moving body frame $(\mathbf{d}_1,\mathbf{d}_2,\mathbf{d}_3)$, one computes $\mathbf{R}(s) = g^{-1}(s)\,\mathbf{r}(s)$. Differentiating both sides and using the identity $(gg^{-1})' = g'g^{-1} + g(g^{-1})' = 0$ gives that

$$\mathbf{R}'(s) = -g^{-1}(s)\,g'(s)\,g^{-1}(s)\,\mathbf{r}(s) = -g^{-1}(s)\,g'(s)\,\mathbf{R}(s) = -\boldsymbol{\Omega}(s)\cdot\mathbf{R}(s), \tag{4.3}$$

where $g^{-1}g' = \boldsymbol{\Omega} = \widehat{\boldsymbol{\omega}}$ is the the angular velocity matrix, an element of the *Lie algebra* $\mathfrak{g}$ of G. The Lie algebra is the tangent space of the G at the origin of the group, i.e. the identity on $\mathbb{R}^n$. Using the vector $E\mathbb{I}$ of moments, there is conjugate to $\boldsymbol{\Omega}$ is an angular momentum matrix $p = \widehat{E\mathbb{I}\boldsymbol{\omega}}$ (also written $E\mathbb{I}\boldsymbol{\Omega} + \boldsymbol{\Omega}E\mathbb{I}$ for $E\mathbb{I}$ the diagonal *matrix* of moments), which evolves in the cotangent space $\mathfrak{g}^*$ of functions over $\mathfrak{g}$ under the action of $g \in G$ as per Hamilton's equations in presence of an applied torque:

$$p'(s) = [p(s), \boldsymbol{\Omega}(s)] + \boldsymbol{\Xi}(s) \tag{4.4a}$$

$$g'(s) = g(s)\,\boldsymbol{\Omega}(s). \tag{4.4b}$$

Eqs. (4.4) are derived from Hamilton's equations in the Materials and Methods section 4.4.1.1, and an alternative using Lie groups and Lie algebras is presented in section 4.4.1.3. In (4.4a), $p = \widehat{\mathbf{p}}$ is regarded as a skew-symmetric matrix of an angular momentum vector $\mathbf{p}$ with components $E\mathbb{I}_i\omega_i$, and $[\cdot,\cdot]$ is the matrix commutator. The situation $\boldsymbol{\Xi} = 0$ where the applied torque vanishes corresponds to an orbit in the cotangent space $T^*SO(n)$ of angular momenta associated with the rotational motion of n-dimensional bodies [172]. When $\boldsymbol{\Xi} \neq 0$, symmetry is broken, and angular momenta evolve in a reduced space $\mathfrak{se}(3)$ tangent to the group $SE(3) = SO(3) \times \mathbb{R}^3$ of rotations plus translation in a distinguished direction. For example, the so-called *semidirect product group* applies to the case of a heavy top where the fixed direction of gravity is known even in the rotating frame, leading to conservation of angular momentum about the vertical [106, 172, 173] .

The first result of this chapter is to show that the situation of the looped string is that of the top. Let a string localized to the xz plane be loaded axially with tension $\mathbf{T} = T\boldsymbol{\Gamma}_t$, with $\boldsymbol{\Gamma}_t$ the unit tangent vector relative to the fixed basis, given at any point by inverse rotation $g^{-1}(s)\,\boldsymbol{\chi}_t$ of the body tangent $(0,0,1)^T$. At any point s the radius of curvature $\boldsymbol{\varrho}$ has magnitude $\frac{1}{\|\boldsymbol{\kappa}\|} = \frac{1}{\kappa_2}$ in the body normal direction $\boldsymbol{\chi}_n = (1,0,0)^T$, and the component of the loading force along the string is $T\cos\theta$ (Figure 4.1A.i-ii). The moment $\boldsymbol{\varrho} \times \mathbf{F}$ of this force about the center of curvature is thus $\mathbf{p}(s) = \frac{T}{\kappa_2}\cos(\theta)\boldsymbol{\chi}_b$ in the binormal direction. Assuming that the angular velocity $\kappa_2 = \frac{\Delta\theta}{\Delta s}$ is constant over the infinitesimal length over which it acts, the moment of the tension force at a nearby point is $\mathbf{p}(s+\Delta s) = \frac{T}{\kappa_2}\cos(\theta+\Delta\theta)\boldsymbol{\chi}_b$. The change in the moment is the applied torque, and its magnitude is equal to

$$\begin{aligned}\|\Delta\mathbf{p}\| &= \frac{T}{\kappa_2}\left[\left(1 - \frac{1}{2!}(\theta+\Delta\theta)^2 + \frac{1}{4!}(\theta+\Delta\theta)^4 + \cdots\right) - \left(1 - \frac{1}{2!}\theta^2 - \frac{1}{4!}\theta^4 + \cdots\right)\right] \\ &= \frac{T}{\kappa_2}\Delta\theta\left(-\theta + \frac{1}{3!}\theta^3 + \cdots\right) + \mathcal{O}\left(\Delta\theta^2\right) = -\frac{T}{\kappa_2}\kappa_2\Delta s\sin\theta = -T\Delta s\sin\theta, \end{aligned} \tag{4.5}$$

for sufficiently small $\Delta\theta$. If $\mathbf{p}$ is directed along $\boldsymbol{\chi}_b$, then $\Delta\mathbf{p}$ is in the orthogonal direction defined

$$\boldsymbol{\chi}_b' = (\boldsymbol{\chi}_t \times \boldsymbol{\Gamma}_n)' = \boldsymbol{\chi}_t' \times \boldsymbol{\Gamma}_n = \boldsymbol{\chi}_n \times \boldsymbol{\Gamma}_n, \tag{4.6}$$

which can be used to replace $\sin\theta$ term in Eq. (4.5). Here the opposite perspective has been invoked to regard the reference normal as a constant while the body tangent and binormal change. Taking $\Delta s \to 0$, the extra force $\frac{d\mathbf{p}}{ds}$ that must be supplied to rotate the frame by an infinitesimal amount $d\theta$ is $\mathbf{p}' = \lambda^2 E\mathbb{I}_2 \boldsymbol{\Gamma}_n \times \boldsymbol{\chi}_n$. One checks that the units make sense for $E\mathbb{I}_2$ = force × dist.^{2}, λ = dist.$^{-1}$, and $\mathbf{p}$ = force × dist.

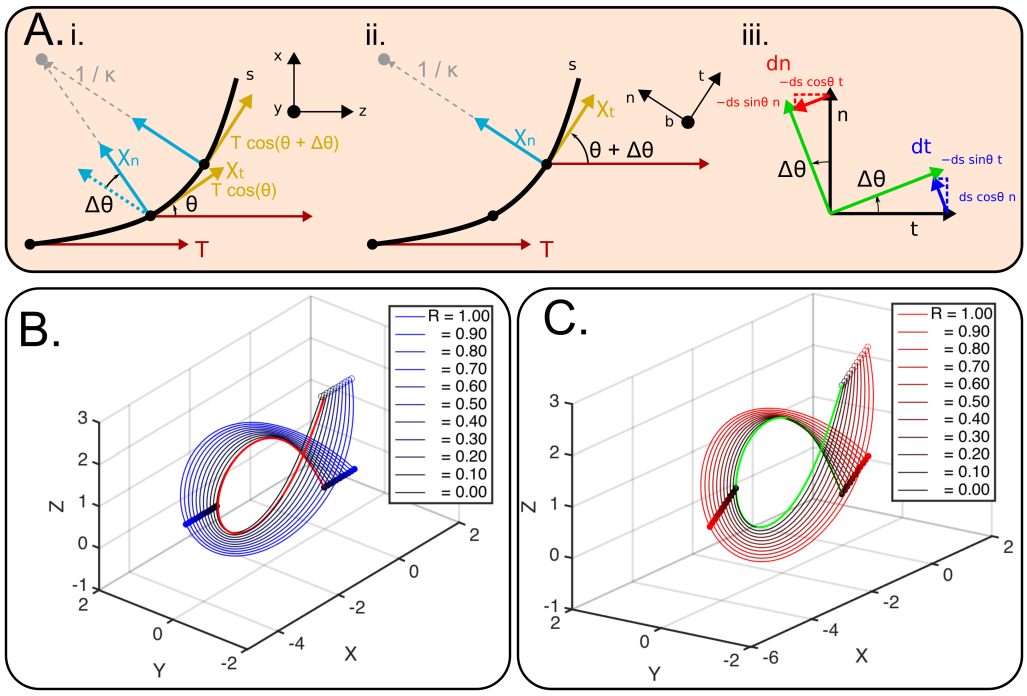

Figure 4.1: Looping of the Euler elastica. The Euler elastica with loading parameter $\lambda = \sqrt{\frac{T}{E\mathbb{I}}} = \sqrt{\frac{3}{10}}$, bending stiffness $E\mathbb{I}_1 = E\mathbb{I}_2 = 10$ and length $L = 10$ (plotted in bold in panels B and C) gives rises to curvature κ_2 (directed in the binormal direction along y) in a straight string originally parallel to z. **(A)** Diagram showing how looping is caused by tangential tension at different points along the string. Different tensions $\mathbf{T}(s)$ and $\mathbf{T}(s+ds)$ in a string loaded at the ends with $\|\mathbf{T}\| = T = 3$ cause rotation between frames *i.* and *ii.* by the amount $\Delta\theta$. The extra torque misaligns the body normal $\boldsymbol{\chi}_n$ (drawn in blue directed toward the center of curvature) and the fixed normal x. *iii.* Rotation of the (old) body frame $\boldsymbol{n}$ and $\boldsymbol{t}$ vectors due to the resultant moment (in the $\mathbf{b}$ direction) of the force $\mathbf{F}$ on a vector $d\mathbf{s}$ in the (old) tangential direction. **(B)** Integration of the Euler equations (4.8) leads to a planar loop of the central line ($R = 0$, black) identical to the Euler elastica (red). Overlaid twist $\tau_0 = \frac{2\pi}{L}$ results in rotation of the $R > 0$ fibers (blue) as per the screw velocity matrices (4.10) and (4.11). **(C)** The same as panel B with integration performed using the Frenet-Serret relations (4.1) on the central line, again in agreement with the Euler elastica (green). Filled circles indicate $s = 0$ and $s = 0.5L$; open circles $s = L$.

One can also verify that the extra force rotates the body frame by $\Delta\theta$. The change $\frac{d\mathbf{t}}{d\mathbf{s}} = \mathbf{r}''(s)$ of the tangent vector of a space curve is directed in the binormal direction, given by $\mathbf{t} \times \mathbf{n}$ [218].[1] Then using the vector triple product identity we find that the tangent changes by the amount

$$d\mathbf{t} = (\mathbf{t} \times \mathbf{n}) \times d\mathbf{s} = (\mathbf{t} \cdot d\mathbf{s})\,\mathbf{n} - (\mathbf{n} \cdot d\mathbf{s})\,\mathbf{t} = ds\cos(\Delta\theta)\mathbf{n} - ds\sin(\Delta\theta)\mathbf{t}, \quad (4.7)$$

corresponding to a counterclockwise rotation of the body-centered basis by $\Delta\theta$ (Figure 4.1A.iii). The applied force causing $d\mathbf{s}$ to differ from $\mathbf{t}$ and $\mathbf{n}$ is $\mathbf{p}' = \lambda^2 E\mathbb{I}_2 \mathbf{\Gamma}_n \times \boldsymbol{\chi}_n$.

The preceding arguments determine the applied torque $\boldsymbol{\Xi}$ in the looping problem. Recalling that $p = \widehat{\mathbf{p}}$, the differential equations for angular momentum evolution become

$$p'(s) = [p(s), \boldsymbol{\Omega}(s)] + \lambda^2 E\mathbb{I}_2 \left[\widehat{\mathbf{\Gamma}}_n(s) \times \widehat{\boldsymbol{\chi}}_n\right] \quad (4.8a)$$

$$\widehat{\mathbf{\Gamma}}_n'(s) = \left[\widehat{\mathbf{\Gamma}}_n(s), \boldsymbol{\Omega}(s)\right] \quad (4.8b)$$

$$g'(s) = g(s)\,\boldsymbol{\Omega}(s), \quad (4.8c)$$

where we have used the easily verified property of the hat map $\widehat{\mathbf{\Gamma} \times \boldsymbol{\chi}} = \left[\widehat{\mathbf{\Gamma}}, \widehat{\boldsymbol{\chi}}\right]$. The derivative of $\mathbf{\Gamma}_n = g^{-1}\boldsymbol{\chi}_n$ in (4.8b) keeps track of the evolving angle between $\mathbf{\Gamma}_n$ and $\boldsymbol{\chi}_n$, which are initially parallel (see Materials and Methods section 4.4.1.2).

With s replaced by t, and $\lambda^2 E\mathbb{I}_2$ by the gravitational moment, Eqs. (4.8) agree with the heavy top equations [106, 119, 172, 173]. Although the applied forces in the top and string are directed along different fixed vectors ($\mathbf{\Gamma}_n$ versus $\mathbf{\Gamma}_t$), geometry of similar triangles shows that both systems refer to the azimuthal angle θ, and hence the forms of the evolution equations are the same. A more subtle point is that the time (as opposed to spatial) rate of change of angular momentum has units force × dist. × time^{-1}, so that one understands division of $\Delta\mathbf{p}$ by the unitless quantity $\omega_2 \Delta t$ (instead of Δs) as an applied *torque* in the top problem, as opposed to an applied *force* in the string.

Figure 4.1B and C show the evolution of the central fiber ($R = 0$) of a string with $E\mathbb{I}_2 = 10$ and $T = 3$, corresponding to the Euler elastica shown in bold in both panels. Panel B is computed by specifying the initial tangent vector in the fixed basis at $s = 0$ and updating $g(s)$ by the angular momentum equations (4.8); rotation of the central line in the body frame is then evolved stepwise by adding $g^{-1}(s)\,\mathbf{\Gamma}_t(0)\,ds$. Panel C is calculated using the Frenet-Serret relations (4.2) with

[1] Note that because $\mathbf{n}$ is defined to be the outward normal, the lobe of the loop in Figure 4.1B and C lies in the $-x$ direction in order that the coordinate system at the origin be right-handed.

the curvature κ of the elastica used to get the new tangent vector $\mathbf{t}$ directly in fixed-space coordinates. The results are essentially identical, both to each other and to the elastica.

4.2.2 Looping with pure twist

Having reviewed the situation with a single force, we now introduce a second: twist. Twist is important because it distinguishes an additional direction, the axial one about which the fiber rotates. Although it is colloquial to use the terms interchangeably, twist is not the same as torsion; both make separate contributions to the axial strain of the director basis (see below). Twist is rotation of the $\mathbf{d}_1$ and $\mathbf{d}_2$ directors independently of the principal normal $\mathbf{n}$ and binormal $\mathbf{b}$ (see Figure 4.2B below), and thus it cannot affect the motion of the central line, a point originally made by Love [163]. Although the distinction will be important in section 4.2.3, in this section we show how to incorporate twist about looped space curves if it does not affect the principals. A useful analogy for twist is a bent candy cane: the painted-on red stripe twists about the central line $\mathbf{r}(s)$ at a rate dependent on arc length s, but no matter the number of wraps, the plane of the candy cane is always xz.

To model twist in a looped space curve, we need to introduce space-time constraints that express the connection between rotation at a fixed s and simultaneous translation along s. Because twist takes time to propagate, the string under combined twist and tension is actually a four-dimensional object parametrized in space $\mathbf{r}$ and time t. The dimensionality is reduced to two, however, by the *natural parametrization* $s \mapsto \mathbf{r}(s)$ of the string along its arc length [218]. If twist is a wave that propagates with velocity c in the s direction, then the time when the wave reaches arc length $s - \lambda$ is t, and the arc length accumulated when the clock reads $t + \mu$ is s. The spatial and temporal delays λ and μ are related by

$$\lambda = s - tc \tag{4.9a}$$

$$\mu = \frac{s}{c} - t, \tag{4.9b}$$

similar to those used in [56]. In Materials and Methods section 4.4.2 it is shown how Eqs. (4.9) partition the full four-dimensional configuration space into free and dependent coordinates, or more generally, into *vertical* and *horizontal* parts [32, 171]. The result is that the permitted elements of the Lie algebra $\mathfrak{g} = \mathfrak{se}(3)$ of the special Euclidean group $SE(3)$ are

$$\xi = \boldsymbol{\Omega} ds + cL_{g^{-1}}(v_t), \tag{4.10a}$$

or as a 4×4 matrix

$$\xi = \begin{pmatrix} \mathbf{\Omega} ds & cL_{g^{-1}}(v_t) \\ 0 & 0 \end{pmatrix}, \tag{4.10b}$$

with $L_{g^{-1}}$ representing left translation by g^{-1} of a unit step v_t in time. Materials and Methods section 4.4.2 also shows how ξ may be integrated to give a trajectory in the group. The result is

$$g(s + ds) = h(s) \exp(\mathbf{\Omega}(s) ds) + \mathbf{r}(s), \tag{4.11a}$$

or equivalently

$$g(s + ds) = \begin{pmatrix} h(s) \exp(\mathbf{\Omega}(s) ds) & \mathbf{r}(s) \\ 0 & 1 \end{pmatrix}, \tag{4.11b}$$

where $h \in SO(3)$ is a rigid rotation and $\mathbf{r} \in \mathbb{R}^3$ is a point on the space curve. Both Eqs. (4.10b) and (4.11b) agree with the semidirect product structure of $\mathfrak{se}(3)$ [106, 134, 172, 173]: the first is the screw velocity matrix of [73], and the second satisfies $g\big|_{s=0}$ = identity on $\mathbb{R}^4$. The group element $g(s)$ operates on four-dimensional vectors $(\mathbf{R}(s = 0), 1)^T$; if $\mathbf{\Omega}$ is a twist about the third body axis, then g rotates $\mathbf{d}_1$ and $\mathbf{d}_2$ about the tangent line at the translated position $\mathbf{r}(s)$. Thus we arrive at the intuitive notion of twist as rotation overlaid on the central line of the string, regardless of its shape.

Although the preceding exposition emphasized traveling waves, common experience says that twist waves in strings are stationary. For a twist wave to be a standing wave after it has reached the terminus, the ratio of its temporal period and spatial wavelength much be commensurate, i.e., the twists accumulated in time and space must agree at both ends (cf. [13] ch. 6.30 for the case of the top). Therefore, c must be rational; it drops out of the final equations after the standing wave has been established. Furthermore, a twist $\tau_0 = \frac{2\pi n}{L}$ of n rotations per unit length of the string has the angular velocity matrix $\mathbf{\Omega} = (0, 0, \tau_0)^{T\frown}$. With these values, Eqs. (4.10) and (4.11) give the twist about the central line of a looped string. As rotation about the body $\mathbf{d}_3 = \mathbf{t}$ axis leaves the central line unchanged, only body vectors with nonzero $\mathbf{d}_1$ and $\mathbf{d}_2$ components are subject to twist. The $R > 0$ lines in Figure 4.1B and C are rotations of the body vectors $(R, 0, 0)^T$.

4.2.3 Looping with torsion converted to localized spiraling

Pure twist of ζ radians per unit length about the central line does not leave room for any interactions with looping. According Love's formula in the 3-2-3 Euler

angles ψ, θ, and ϕ (Figure 4.1A and B; [200] ch. 5; [163] ch. XVIII) for the total axial strain, viz.

$$\kappa_3 = \frac{\partial \phi}{\partial s} + \frac{\partial \psi}{\partial s}\cos\theta = \frac{\partial \zeta}{\partial s} + \tau, \tag{4.12}$$

specifying $\kappa_3 = \tau_0 = \frac{\partial \zeta}{\partial s}$ in the previous section on pure twist meant zero torsion τ in the Frenet-Serret equations: the directors rotated, but the binormal stayed the same. In contrast, loading the string with $\tau_0 = \frac{2\pi n}{L}$ radians per length in torsion with $\frac{\partial \zeta}{\partial s} = 0$ twist means the principals rotate as well. The *spiraling* terms $\frac{\partial \psi}{\partial s}$ and $\frac{\partial \phi}{\partial s}$ partition τ into rotation $\frac{\partial \psi}{\partial s}\cos\theta$ of the directors and the normals about the fixed z axis and $\frac{\partial \phi}{\partial s} = \tau_0\left(1 - \cos\theta\right)$ of only the directors about the bent central line. These separate contributions to spiraling mean that the axial strains affecting the shape of the space curve are modified by bending.

The subtle differences between torsion, twist, and spiraling are illuminated by the short-string model of Figure 4.2. Spiraling will be the general term for axial strain the directors $\mathbf{d}_1$ and $\mathbf{d}_2$, which may (panel A) or may not (panel B) rotate with the principal normal $\mathbf{n}$ and binormal $\mathbf{b}$ of the space curve. Rotation about the fixed z axis is encompased by the angle ψ as *spatial* spiraling, while the remaining rotation about the string's tangent $\mathbf{d}_3$ is accounted for by ϕ as *localized* spiraling. Torsion only contributes to spatial spiraling, but twist does not only contribute to localized spiraling; thus $\frac{\partial \zeta}{\partial s} \neq \frac{\partial \phi}{\partial s}$. To see this another way, let the unbent ($\theta = 0$) string be loaded only with torsion τ_0; then $\mathbf{n}$ and $\mathbf{b}$ spiral around the z axis, tracing out the blue area of the tall string in panel A. Now if the string is bent, $\mathbf{n}$ and $\mathbf{b}$ spiral about a foreshortened z axis, accounting for only $\frac{\partial \psi}{\partial s}\cos\theta$ of the input torsion; the remainder $\frac{\partial \phi}{\partial s} = \tau_0\left(1 - \cos\theta\right)$ is converted into local spiraling (red area) of the directors relative to the principals. Next imagine a candy cane with $\frac{\partial \zeta}{\partial s} = \tau_0$ in twist being bent by compression of the ends (panel B). Although the space curve of the central line has no torsion, the stripe can still only rise by $\cos\theta$ along z (blue), the rest being twist about $\mathbf{d}_3$ (red). Relative to the fixed basis, $\mathbf{n}$ and $\mathbf{b}$ in panel B do not move. The two cases illustrate that local spiraling can be nonzero when twist is (panel A), and that spatial spiraling can be nonzero when twist isn't (panel B). Panel C shows that in general, spiraling may be broken into the two contributions from twist (green) and torsion (blue) for any bending angle θ. The director bases (black) of the short and tall strings must agree, but the principal bases (blue) need not. Bending converts equal fractions of twist and torsion into local spirals (highlighted in red), with the effect that overall torsion is reduced. One also sees that twist is akin to shear of the radial fibers: if the green areas vanished, the meridional coordinate of the $\mathbf{d}_1$ fiber would not vary along its length.

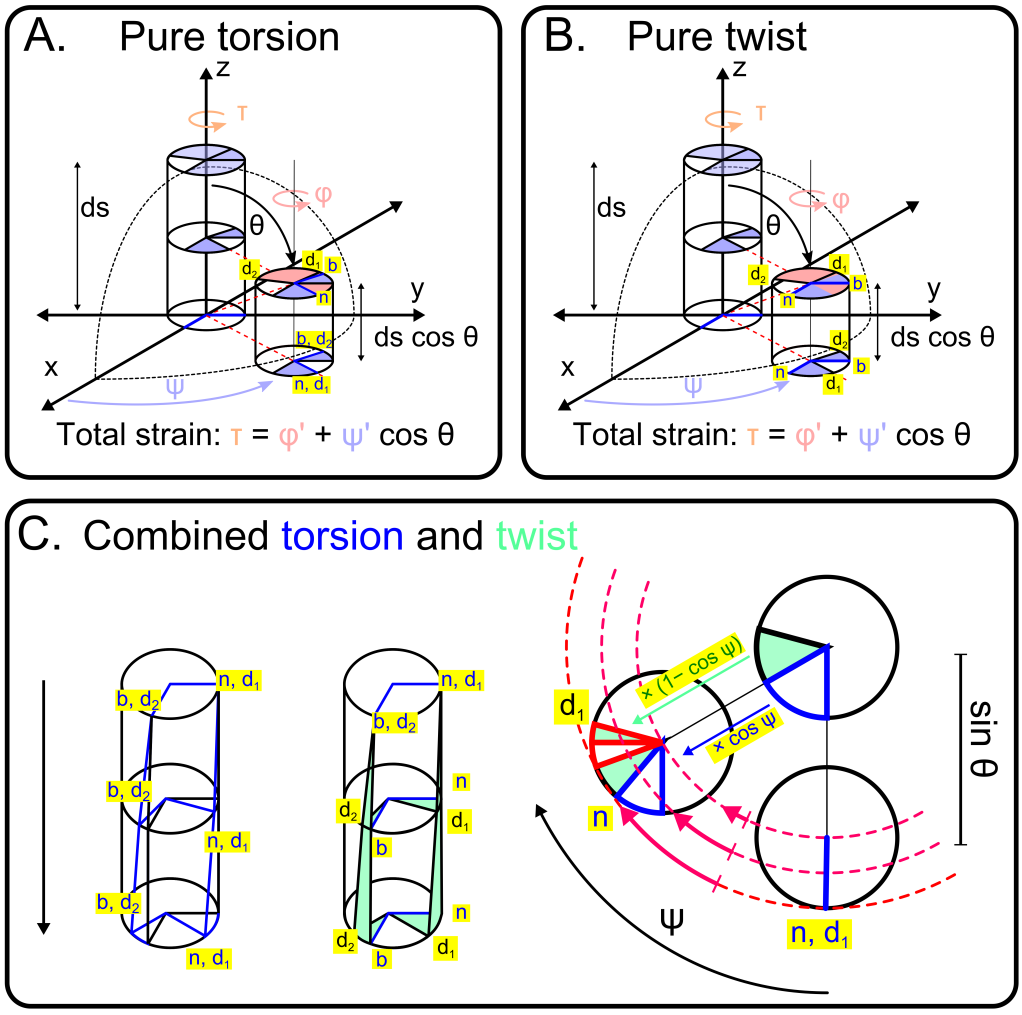

Figure 4.2: The difference between torsion and twist using the short string model. (A, B) Views of the straight and bent string having axial strain that is entirely torsional (A) or entirely in twisting (B). The bent string is projected onto the z axis to show its foreshortened height in that dimension, although its radial length is preserved. The Euler angles ψ, θ, and ϕ are indicated; rotation of the director basis vectors $\mathbf{d}_1$ and $\mathbf{d}_2$ due to ψ is shown in blue, and that due to ϕ in red. The principal $\mathbf{n}$ and $\mathbf{b}$ vectors rotate with the directors under torsional strain (A), but are stationary during twist (B). (**C**) A topdown view of the string shows that twist introduces shear of the short string fibers relative to the radius drawn from the long string. At any bending angle θ, a fraction $\cos\theta$ of twist (green) and torsion (blue) are both converted to spatial spiraling. The "missing" rotation is accounted for by local spiraling about string's axis (traced in red). The director $\mathbf{d}_1$ in the short string is parallel to that in the long string, but the normal spirals less due to bending.

The twist-torsion distinction is particularly relevant to the buckling of helical space curves, as discussed by in [269]. A helix of length L, height S, radius R and inclination angle $\frac{\pi}{2} - \theta$ is loaded with a total of n loops. It follows from the elementary geometry of "unwinding" the helix at its inclination angle that the input

strain about z is $\frac{2\pi n}{L} = \frac{\sin\theta}{R}$. Durning compression of the ends, $\tau = \frac{\cos\theta\sin\theta}{R}$ reduces the strain by a factor $\cos\theta$ (as per the usual formula, [200] ch. 1); the remaining strain $\frac{\partial\phi}{\partial s} = \tau_0\left(1-\cos\theta\right)$ goes into local spiraling. Buckling into a planar loop may reduce the string's total energy if the torsional rigidity $G\mathbb{J}$ exceeds the bending rigidities $E\mathbb{I}_1$ and $E\mathbb{I}_2$.

How bending and torsion combine to produce novel curves is the subject of the next two sections of this chapter. As in section 4.2.1, the approach is to find the differential force supplied at each point along s and represent it as an element of $\mathfrak{g}$. Just as looping distinguishes the y direction, so spiraling distinguishes z, the direction coincident with the axis of the undeformed string. It is assumed that all spiraling is due to torsion. Let the local spiraling moment be $G\mathbb{I}_l$, so that $G\mathbb{I}_l\tau_0$ is the torque (force × dist.) supplied to produce n turns over the length L of the unbent string. As a result of bending, local spiraling is converted in spatial spiraling, a mode which in general has a different moment of inertia $G\mathbb{J}$. At any point s the torque is directed along the body tangent $\boldsymbol{\chi}_t = \mathbf{d}_3$, and is decomposable into the cross product $\mathbf{M} = \boldsymbol{\varrho}\times\mathbf{F}$ of a (conserved) wrench force $\mathbf{F}$ acting on an orthogonal lever arm $\boldsymbol{\varrho}$. The lever arm is the radius of curvature, being of magnitude $\frac{1}{\kappa_2}$ and directed along the body normal $\boldsymbol{\chi}_n$. Thus the force $\mathbf{F} = \mathbf{M}\times\frac{1}{\|\boldsymbol{\varrho}\|^2}\boldsymbol{\varrho}$ responsible for spatial torquing has magnitude $G\mathbb{J}\tau_0\kappa_2$ in the direction of the body binormal $\boldsymbol{\chi}_b$. At $s=0$, $\boldsymbol{\chi}_b = \boldsymbol{\Gamma}_b$ is in the direction of the fixed y axis; later $\boldsymbol{\chi}_t$ accumulates an angle ψ relative to $\boldsymbol{\Gamma}_b$, reducing $\mathbf{F}$ by the cosine of this amount. The angular momentum supplied by the binormal torquing at two closely spaced points is $\mathbf{p}\left(s\right) = G\mathbb{J}\tau_0\kappa_2\cos\left(\psi\right)\times\frac{1}{\kappa_2}\boldsymbol{\chi}_t$ and $\mathbf{p}\left(s+ds\right) = G\mathbb{J}\tau_0\kappa_2\cos\left(\psi+\Delta\psi\right)\times\frac{1}{\kappa_2}\boldsymbol{\chi}_t$. As in Eq. (4.5), the extra moment responsible for the change is

$$\|\Delta\mathbf{p}\| = G\mathbb{J}\tau_0\Delta\psi\left(-\psi+\frac{1}{3!}\psi^3+\cdots\right)+\mathcal{O}\left(\Delta\psi^2\right) = -G\mathbb{J}\tau_0^2\Delta s\sin\psi. \tag{4.13}$$

Here, $G\mathbb{J}$ is the torsional rigidity, defined as the product of the shear modulus G and a factor $\mathbb{J}$ equal to the sum $\mathbb{I}_3$ of the area moments of x^2 and y^2 at an xy cross section (cf. [163] ch. XIV). This is in agreement with the earlier definition of section 4.2.1.

Next we want to use Eq. (4.13) to update the Euler equations (4.8). If $\mathbf{p}$ is directed along $\boldsymbol{\chi}_t$, then a similar argument leading to Eq. (4.6) shows that $\Delta\mathbf{p}$ is directed along the cross product $\boldsymbol{\chi}_b\times\boldsymbol{\Gamma}_b$. Using this to replace the factor $\sin\psi$ in Eq. (4.13), we find that in the limit $\Delta s\to 0$ the extra torque is supplied by a force $\mathbf{p}' = G\mathbb{J}\tau_0^2\boldsymbol{\Gamma}_b\times\boldsymbol{\chi}_b$ proportional to the angle between the body and fixed the binormals. One also checks that the units agree for $G\mathbb{J}$ = force × dist.^{2}, τ_0 = dist.$^{-1}$ and $\mathbf{p}$ = force × dist., as expected. With $p = \widehat{\mathbf{p}}$, the modified angular momentum

equations for the interaction of bending and torsion are

$$p'(s) = [p(s), \mathbf{\Omega}(s)] + \lambda^2 E \mathbb{I}_2 \left[\widehat{\mathbf{\Gamma}}_n(s), \widehat{\boldsymbol{\chi}}_n\right] + G\mathbb{J}\tau_0^2 \left[\widehat{\mathbf{\Gamma}}_b(s), \widehat{\boldsymbol{\chi}}_b\right] \tag{4.14a}$$

$$\widehat{\mathbf{\Gamma}}_n'(s) = \left[\widehat{\mathbf{\Gamma}}_n(s), \mathbf{\Omega}(s)\right] \tag{4.14b}$$

$$\widehat{\mathbf{\Gamma}}_b'(s) = \left[\widehat{\mathbf{\Gamma}}_b(s), \mathbf{\Omega}(s)\right] \tag{4.14c}$$

$$g'(s) = g(s)\,\mathbf{\Omega}(s). \tag{4.14d}$$

The middle two Eqs. (4.14) explicitly give the rotation of body frame relative to the fixed frame; they are not the same even though the body $\boldsymbol{\chi}_n$ and $\boldsymbol{\chi}_b$ vectors are defined to be orthogonal. The rotations in Eqs. (4.14b) and (4.14c) account for the extra torque in (4.14a). The conversion of some of τ_0 to spatial spiraling leaves $\tau_0(1-\cos\theta)$ available for local spiraling, being the ω_3 component of $\mathbf{\Omega}$ in the screw velocity equations (4.11). These modifications imply that torsion and bending are no longer known functions of s: they are differential equations that may only solved after traversing s.

The initial conditions of Eqs. (4.14) are also important for modeling the interactions between looping and spiraling. We measure θ relative to the tangent line at a point s_0 so that the supplied axial strain has its maximum value $\tau_0\cos(0)$ there. Physically, this means taking the tangent line for the undeformed string. No generality is lost because a twisted string can be rigidly rotated before the ends are brought together. In the limit $L \to \infty$ the undeformed line at s_0 approaches the fixed z axis. Also recall that before bending, the initial angular momentum is $G\mathbb{I}_l\tau_0$ for local spiraling, not $G\mathbb{J}\tau_0$ for spatial spiraling.

The importance of evolving $\kappa = \omega_2$ and $\tau = \omega_3$ simultaneously is illustrated schematically in Figure 4.3, panels A and D. Whereas the Euler equations (4.14) use the current direction of $\mathbf{\Gamma}_t$ and $\mathbf{\Gamma}_t$ to update all components of $\mathbf{\Omega}$, the Frenet-Serret equations (4.2) use a fixed κ and τ. The two methods are similar, except that the Euler equations result in additional bending at the ends of the string (panels B and D). Where along s one begins integrating also has an effect on the shape. Choosing $s_0 = 0.4L$ (C, F) results in the lower end of the Euler loop (C) being transposed to the right of the elastica, whereas the lower end of the Frenet-Serret loop lies to the left.

Why should the two methods differ in the case of mixed forces, but not in the case of a single force (as in Figure 4.1)? Section 2.2.3 in chapter 2 provides necessary and sufficient conditions for when the dynamics of a system controlled in the tangent space can be known in advance. When bending strain is supplied

singly, all potential energy is converted to kinetic in the form of rotation about a single axis. With nowhere else for the energy to go but into ω_2, it is possible to get the unique trajectory from the Legendre transformation of the total energy change by an angular velocity function $\mathbf{\Omega}(s)$ written down at a starting point s_0. The curvature of the planar elastica is the unique function giving the unique shape. In contrast, when two strains are supplied—in bending and spiraling, say—the energy can go into different degrees of freedom; the space curve in general fails to be unique. Chapter 2 outlines a theory of gradient and non-gradient systems, in which it is shown that multidimensional controls make the dynamics unknowable at the start. The dynamics can be made one-dimensional (i.e., parallel to a gradient) if the rotating angular velocity vector is given time to reorient to the direction of the applied forces. It is suggested here that misalignment of the forces and velocities in the Frenet-Serret equations violates the parsimony principle that each segment see the same increase in energy: by dissipating energy in the form of localized strains, the angular trajectory occasionally moves skew to the potential gradient. Certainly the predicted shape is a valid space curve, but realizing it would require additional inputs of energy in the form of localized strains. In contrast, the Euler-Poincaré equations are derived by minimizing the Lagrangian action functional [119], which predicts that the most likely path between the unstrained and strained states is the one that has the least deviation between level sets of the the potential. In this way, a sequential process á la those studied chapter 3 arises autonomously in the form the response of each segment of the string to a force imposed at the start. This theory could be falsified by measuring excess strain in strings forced into the shapes of Figure 4.3: the Euler-Poincaré string should have less localized strain than the Frenet-Serret one.

4.2.4 Looping with a propagating end-shortening force

Another way spiraling and looping can interact is by treating forces as *vector fields* on a certain Lie group; they evolve along each other over the body of the string and cause it to turn in space. The aim of this section is to show how to combine the fields and approximate the shape of a twisted string when a force propagates from its center.

In experiments [97, 269], a compressive end-shortening force applied to a pre-twisted causes looping. Propagation of the force means that different portions of the string see different values of the field representing it (Figure 4.4A). Consider dividing the string into many infinitesimal *segments* (black dots), a consecutive

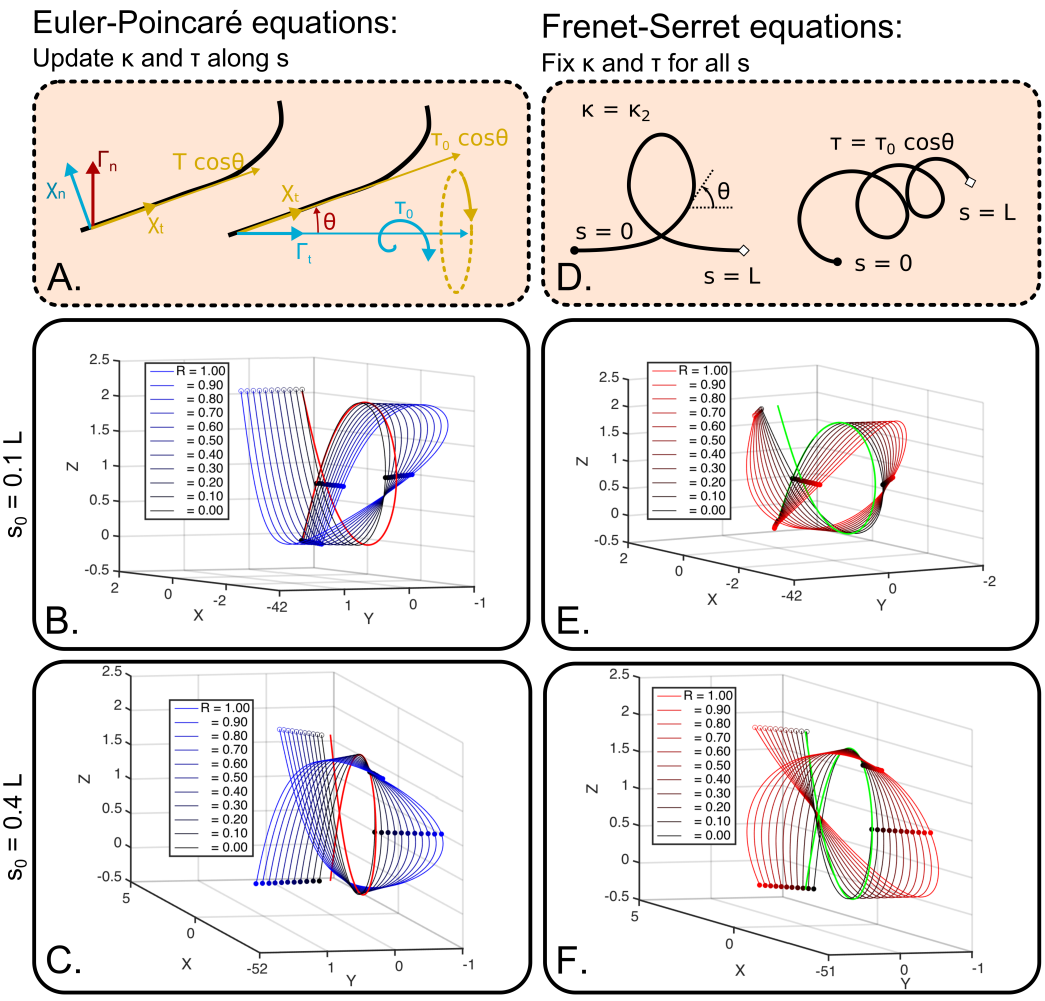

Figure 4.3: Strings with interacting forces. **(A, D)** Digram of distinguished directions. In the Euler picture (A), curvature and torsion are updated along s by extra torques applied in the normal and tangential directions. In the Frenet-Serret picture (D) curvature κ is a specified function of arc length s, and torsion τ is a function of the angle $\theta(s)$. **(B, E)** Integration of the Euler (B) and Frenet-Serret (E) equations starting from the point $s_0 = 0.1L$ for fibers of increasing distance from the central line. The central line ($R = 0$, black) experiences only spatial spiralling, while the $R > 0$ fibers (blue, red) experience local spiraling due to the screw velocity. **(C, F)** The same as panels B and E except that integration is started at $s_0 = 0.4L$. Parameters are $E\mathbb{I}_1 = E\mathbb{I}_2 = 10$, $G\mathbb{J} = 15$, $G\mathbb{I}_l = 1$, $L = 10$, $\tau_0 = \frac{2\pi}{L}$. Filled circles mark $s = 0$ and $s = 0.5L$; open circles $s = L$.

number of which define a *section*. In the Materials and Methods section 4.4.3.1, a model is described wherein stressed sections (red) push out into unstressed ones (blue). By Newton's third law, the unstressed sections push back, entangling more and more segments into the force wave, which propagates with velocity c. (It is sometimes convenient to think of the string moving with velocity $-c$ toward a

stationary origin s_0.) Equilibrium is reached when the numbers of right-pushing and left-pushing segments in any section are equal. Because vector fields represent velocities, it should be possible, from the space-time constraints in discussed in section 4.2.2, to write an equation versus space for the shape of the string under the loading force; conservation of energy makes this goal not strictly attainable.

The notion that forces take time to propagate motivates the introduction of the *flow* $\Phi^t_{\mathbf{X}}$ for time t along a vector field $\mathbf{X} \in \mathfrak{g}$. Flow is the solution curve to the differential equation

$$\dot{\sigma}(t) = \mathbf{X}(\sigma(t)) \tag{4.15}$$

for a path σ defined on G (cf. Eq. (4.49a) in Materials and Methods section 4.4.1.3). We say that vector fields $\mathbf{A}$ and $\mathbf{B}$—representing spiraling and bending—are the *exponential generators* of the their corresponding forces, because the formal solution of Eq. (4.15) is $\sigma(t) = \sigma(0)\exp(\mathbf{X}t)$. Due to the space-time constraints (4.9), the first temporal derivative $\dot{\sigma}$ in (4.15) is related to the spatial derivative $g'\Big|_{t=0} = \mathbf{X}$ of the rotation matrices; the higher derivatives are found from the Lie derivative, introduced below.

The first question is, what flow is relevant to strings? In the force propagation model, sections at the string ends saw only axial stress, while those in the middle experienced axial and bending strains. By the time the force wave represented by $\mathbf{B}$ reached the ends, its effect had changed (Figure 4.4B). But because space and time are equivalent, it is possible to relate the direction of field $\mathbf{B}$ at a point s in the present $t = 0$ to a point of origin s_0 in the past $t_0 < 0$. To make this connection precise, undo the spiraling force field $\mathbf{A}$ for a time Δt, and then apply $\mathbf{A}$ and $\mathbf{B}$ together for the same amount of time. The flow $\Phi = \Phi^{\Delta t}_{\mathbf{A}+\mathbf{B}} \circ \Phi^{-\Delta t}_{\mathbf{A}}$ maps the points of one *manifold* $\mathcal{M}$ onto another $\mathcal{N}$, each representing a different local section of the string. Now apply $\mathbf{B} \in T\mathcal{M}$ to the new coordinates $\Phi \circ z$ on $\mathcal{N}$; transform between tangent spaces using the chain rule and multiplying by a Jacobean "conversion" factor $D\Phi = \frac{d\Phi(z)}{dz}$ to get

$$\mathbf{B} = D\Phi \cdot D\Phi^{-1} \cdot \mathbf{B} = D\Phi \cdot \mathbf{B}\left(\Phi^{-1}\circ\right) =: \Phi_* \mathbf{B}. \tag{4.16}$$

This map $\Phi_* : T\mathcal{M} \to T\mathcal{N}$ is known as the *push forward* [172] because the vector field "catches up" with the coordinates (Figure 4.4B). The first derivative of Eq. (4.16), i.e.,

$$\mathbf{B}' = \mathcal{L}_{\mathbf{X}}\mathbf{B} := \frac{d}{dt} D\Phi \circ \mathbf{B} \circ \Phi^{-1}\Big|_{t=0} = [\mathbf{X}, \mathbf{B}], \tag{4.17}$$

is the *Lie derivative* of $\mathbf{B}$ along $\mathbf{X}$ (see Materials and Methods section 4.4.3.2).

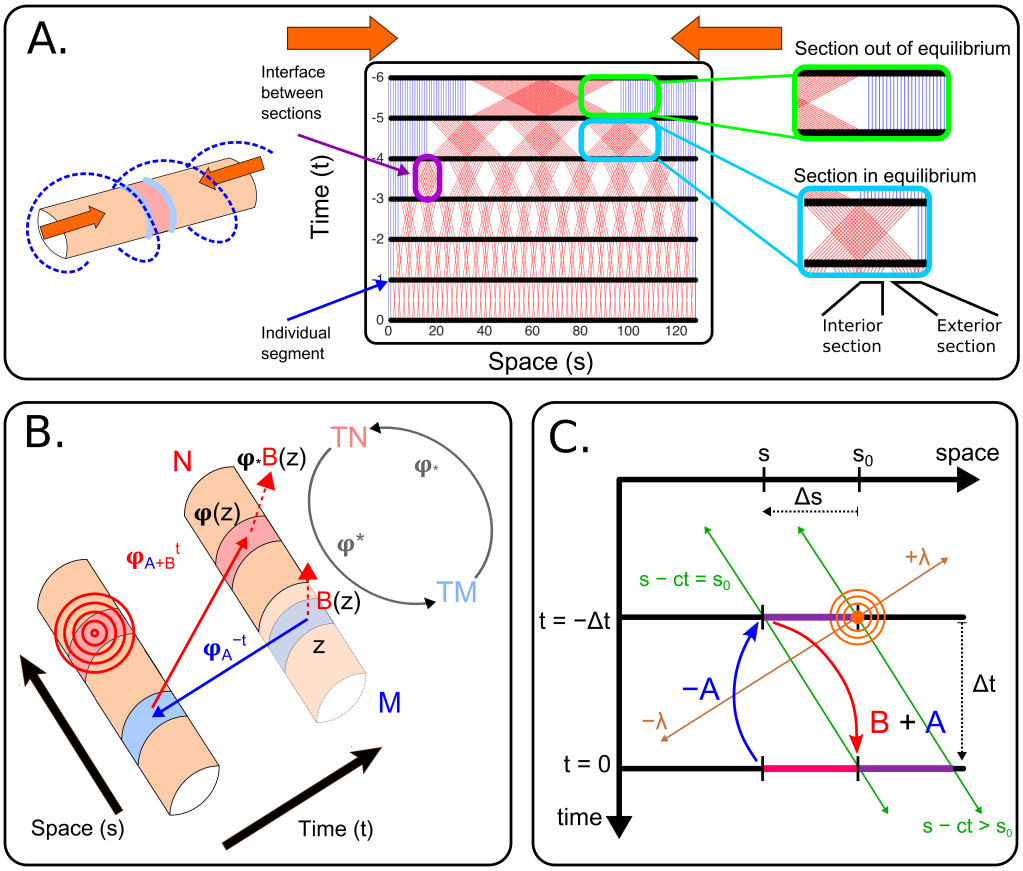

Figure 4.4: Propagation of a force in the presence of background twist. **(A)** Establishment of equilibrium in a twisted and bent string. Each infinitesimal segment of the string is represented by a black dot. The force exerted during a single time step by one section of the string on another is shown by a red line; unstressed segments are connected to themselves in blue. The stress pattern evolves by Newton's third law: unopposed exterior sections push outward, while opposed interior sections reverse the stress direction. The initial force has the strength of $n = 16$ segments. (*Inset*) Equilibrium is established in a finite section in one time step. **(B)** Change in the direction of a vector field (representing a force) at different points of the string. The map Φ changes the history of the finite section $\mathcal{M}$ of the string (experiencing only spiral motion) into $\mathcal{N}$ (experiencing end-shortening and spiraling) by reverse flow along $\mathbf{A}$ (blue) and forward flow along $\mathbf{A} + \mathbf{B}$ (red). The vector field push forward map Φ_* is the expression of the force of manifold $\mathcal{M}$ on manifold $\mathcal{N}$. Blue sections of the string have been exposed to twist only ($\Phi^t_{\mathbf{A}}$), while red sections have been exposed to twist and end-shortening ($\Phi^t_{\mathbf{A+B}}$). **(C)** Illustration of space-time constraints in a rigid string on which the end-shortening force acts over time. In the absence of this force, sections (violet) keep the same s over time (magenta), but in the presence of a force at s_0, they move toward the source at rate $-c$ along s. Backward flow along $\mathbf{A}$ (blue) and forward flow along $\mathbf{A} + \mathbf{B}$ (red) shifts the force at s_0 at $t = -\Delta t$ to s at $t = 0$. The delay λ is the size of the shift measured from s. Each infinitesimal segment has the same value of $\Delta\lambda = \Delta s - c\Delta t$ because the propagation velocity c does not vary with s.

It is shown in Materials and Methods 4.4.3.3 that the higher order derivatives of $\mathbf{B}$ along the path defined by Φ are

$$\mathbf{B}^{(n)} = \frac{d^n}{dt^n} \mathrm{Ad}_{\exp \mathbf{B}t} \circ \mathrm{Ad}_{\exp -\mathbf{A}t} \circ \mathbf{B}\Big|_{t=0} = \sum_{k=0}^{n} \binom{n}{k} (-1)^k \, \mathrm{ad}_{\mathbf{B}}^{n-k} \circ \mathrm{ad}_{\mathbf{A}}^{k} \circ \mathbf{B}, \quad (4.18)$$

and that they are related by a multiplicative factor to the *Zassenhaus coefficients* of the expansion $\exp\{(\mathbf{A}+\mathbf{B})\,\Delta t\}$ for the simultaneous application of two matrix operators [263, 297]; their calculation, which has been the subject of much previous research in mathematical physics [48, 263], is greatly facilitated by the simple binomial expansion of Eq. (4.18).

With the derivatives (4.18) it is possible to approximate the angular velocity matrix $\mathbf{\Omega}$ as a polynomial in s. Letting $\mathbf{A}+\mathbf{B} = g^{-1}(s_0)\, g'(s_0)$ be the velocity field at an origin of force propagation, the velocity $\mathbf{\Omega}^{(1)}$ at an arbitrary s may be found by the n^{th}-order Zassenhaus expansion as

$$\begin{aligned}\mathbf{\Omega}^{(1)}(s) &= \frac{1}{\Delta s} \log\left[\exp\{(\mathbf{A}+\mathbf{B})\,\Delta s\} \cdot \exp(-\mathbf{A}\Delta s)\right] \\ &= \frac{1}{\Delta s} \log\left[\exp\left(\mathbf{B}^{(n)} \frac{(s-s_0)^n}{n!}\right) \cdots \exp\left(\mathbf{B}' \frac{(s-s_0)^2}{2!}\right) \cdot \exp(\mathbf{B}(s-s_0))\right].\end{aligned} \quad (4.19)$$

The sense in which $\Delta s = s - s_0$ is increasing is shown in Figure 4.4C. Also shown is how increments $\Delta\lambda$ of the spatial delay parameter (brown) pick out the next space-time trajectory (green) of material points that, Δs away from the origin s_0, experience the force after a time delay Δt. Of course, we should really be using elements $\xi \in \mathfrak{se}(3) \times \mathbb{R}^3 = \mathfrak{so}(3) \times \mathbb{R}^3 \times \mathbb{R}^3$ of the full semidirect product Lie algebra with two conserved directions, but if we knew those derivatives, the path in $\mathfrak{se}(3) \times \mathbb{R}^3$ would be completely solved. Our objective is to find an approximation using the reduced Lie algebra $\mathfrak{so}(3)$ whose elements are simply the generators of three dimensional rotations; e.g., $\mathbf{A} \in \mathfrak{so}(3)$ is just the spiral rotation $(0, 0, \tau_0)^{T\frown}$. With the approximation $\mathbf{\Omega}^{(1)}(s)$, Eqs. (4.14b) and (4.14c) can be integrated to give the evolution for all s of the normal and binormal directions $\mathbf{\Gamma}_n$ and $\mathbf{\Gamma}_b$ relative to the fixed basis. Inserting these into Eq. (4.14a) gives the evolution of the momentum p as a function of s, and by extension, the angular velocities $\mathbf{\Omega} = \widehat{(E\mathbb{I})^{-1}\mathbf{p}}$ in $\mathfrak{se}(3) \times \mathbb{R}^3$.

Figure 4.5 shows the $\mathcal{O} = 10$ Zassenhaus approximation for a string initiated from different points s_0. As in section 4.2.3, it is assumed that the tangent line at s_0 of the full solution (4.14) is loaded with localized spiraling torque in the amount $G\mathbb{I}_l\tau_0$, which is then converted to spatial spiraling as the ends are brought together.

The initial normal $\mathbf{n}$ is a $90°$ rotation of $\mathbf{t}$ in the xz plane, and $\mathbf{b}$ is in the direction of $\mathbf{t} \times \mathbf{n}$. The magenta curves approximate the full solution especially well near s_0, although not as well when Δs increases (panels A and B). Nevertheless, the approximation has the form of a loop and in addition begins to turn over at the midpoint of the string. Interestingly, all curves have excess out-of-plane motion—rotation about the x direction, being spanned by the cross product of the axes of bending and spiraling strain. The approximation also does much better than the green "continuation" lines, which plot the resultant free rotation at angular velocity $\mathbf{\Omega}(s_0)$ when the applied torques are suddenly terminated, a consequence of Newton's first law. Also shown in panel C is a series of approximations of increasing order, demonstrating that the curves converge after a certain number of retained terms in Eq. (4.19). In summary, the Zassenhaus expansion is a reasonable approximation of the true curve, but it cannot reproduce the solution to arbitrary accuracy.

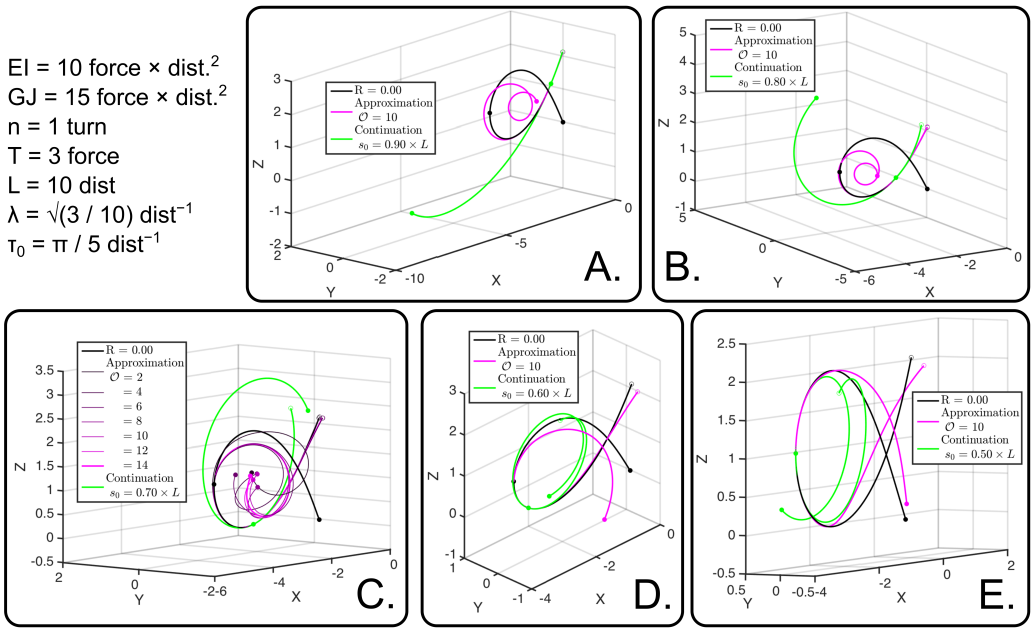

Figure 4.5: The Zassenhaus approximation of a propagating end-shortening force. The central line (black) of a twisted and looped string is re-plotted (magenta) using an expansion of the Zassenhaus formula (4.19) for the angular velocity and integrated from (**A**) $s_0 = 0.9L$, (**B**) $s_0 = 0.8L$, (**C**) $s_0 = 0.7L$, (**D**) $s_0 = 0.6L$, and (**E**) $s_0 = 0.5L$. The continuation from s_0 in the absence of other forces is plotted in green. The string parameters are indicated in the top left panel. Panel C shows the convergence of a series of approximations. Solid circles mark $s = 0$, $s = \frac{L}{2}$, and s_0; open circles $s = L$. Integration is performed with 10^4 points in all panels, except in higher orders in C when the approximation becomes numerically unstable.

With the Zassenhaus approximation, the future evolution of the string is guessed at the origin. In order to get this information, it was necessary to let the group

elements g and the velocities ξ in Eq. (4.49a) be expanded to arbitrary distances Δs from s_0; only after the momenta p were computed could the permitted velocities be found. But there was no guarantee during this procedure that the forces were being applied in the same direction as the velocities. For the change dE in the energy to be always parallel to a gradient, applied forces can only put energy into rotation; misalignment results in energy dissipation. The inability to fully recover the Euler-Poincaré solution with the Zassenahus expansion reflects significant constraints on both string looping and organismal development: the vector fields of interacting forces are not the derivatives of known functions of a single variable s. If the velocities do not take time to align to the one-dimensional coordinate parallel to the energy gradient, the approximation will miss crucial information about the future. The requirement for the temporal dimension is shown in Figure 4.4B and C where adjacent points on the string are related by a roundabout path in time, not by direct traversal of space. Establishing how these concepts relate to developing organisms is the subject of the remaining sections of this chapter.

4.2.5 Rotational dynamics of transcription with limited RNA polymerase

Having discussed the way in which forces combine in strings, it remains to be shown how the results apply to development. Development is fundamentally the coordination of gene expression in time and space. Transcription of genes in a tissue-specific manner requires appropriate allocation of limited transcriptional resources, a constraint ultimately set by the nutrient availability in the environment. The goal of the remaining sections is to show that limited RNA polymerase (RNAP) leads to tissue-specific gene expression. The basis for this view is the observation that Euler's rotational equations (4.4) emerge due to a constraint on total energy. Here, RNAP represents the more abstract concept that information in the egg stage is conserved throughout development. In order for the Euler-Poincaré equations to apply, it needs to be established what is rotating in genetic networks. To this end, an analogy using a transcript cost function and transiting RNAP is presented next.

Once x_i units of RNAP are allocated to a locus i on the chromosome, a total of z_i copies of gene i are transcribed. But the relation between x_i and z_i depends on many factors, including gene length, the presence of cofactors, and the chromatin landscape. All of these may be subsumed into a cost function $\mathbb{I}_i$ = RNAP × trans.$^{-1}$ for the amount of RNAP required to transcribe one unit of gene i. The conversion between RNAP and transcripts is then $z_i = \mathbb{I}_i^{-1} x_i$. In an extended embryo composed of many cells, the transcription rates are actually *spatial rates* or *pitches* κ_{ij} = dist.$^{-1}$

that quantify the distance in space needed to be traversed for the RNAP allocation vector to rotate (by $90°$) between the orthogonal j and i axes. Then (negative) allocation to locus i varies at a spatial rate $X_i = \sum_j x_j \kappa_{ij}$ = RNAP × dist.$^{-1}$. For $n = 3$ genes, the outflow rates $\kappa_{ij} = \epsilon_{ij}^k \kappa_k$ correspond to rotational dynamics about axis k.

Although rotations *about* body axes makes sense for three-dimensional strings, rotation *between* axes is a more fundamental concept in gene networks (Figure 4.6A). One understands the new viewpoint by introducing (mixed) tensor quantities $\mathbb{J}_i^j$, $\mathbb{I}^{ji}$, $\mathbb{I}_{ji}$, and κ_i^j as conversions *from* i to j. In Materials and Methods section 4.4.4 we introduce for the spatial RNAP transfer and transcription *rates*

$$X_i = x_j \kappa_i^j \tag{4.20a}$$

$$Z^i = \kappa_i^j \mathbb{I}^{ik} \mathbb{I}_{kl} z^l, \tag{4.20b}$$

where $\mathbb{J}_l^j := \mathbb{I}^{jk}\mathbb{I}_{kl}$ is a unitless conversion factor giving the worth of transcripts produced at locus j in terms of transcripts produced at i by a single unit of RNAP, and where the RNAP and mRNA *amounts* are related by

$$x_i = \mathbb{I}_{ij} z^j. \tag{4.21}$$

Here, $\mathbb{I}_{ij}$ = RNAP × trans.$^{-1}$ is the cost function that measures the worth in RNAP at i of one transcript from j. From Eq. (4.21), it is possible to show that

$$X_i = \mathbb{I}_{ij} Z^j, \tag{4.22}$$

which identifies X_i as a momentum and Z^j as a velocity in gene expression space (cf. the convention in Materials and Methods section 4.4.1.1). For simplicity, the tensor $\mathbb{I}_{ij}$ is 0 if $i \neq j$, corresponding to the case that transcripts at i can only come from RNAP at i (see Materials and Methods section 4.4.4).

The velocities Z^i and the conjugate momenta X_i are more natural quantities to study than the absolute amounts z^i and x_i, because momenta and energy are conserved in rotational systems in $\mathbb{R}^3$ [13]. These concepts are not merely abstract constructions, but quantities having tangible influence on transcription. The constraints on the transcriptional system may be expressed

$$\sum_{i=1}^{n} X_i^2 = X^2 \tag{4.23a}$$

$$\sum_{i=1}^{n} \frac{X_i^2}{\mathbb{I}_i} = E. \tag{4.23b}$$

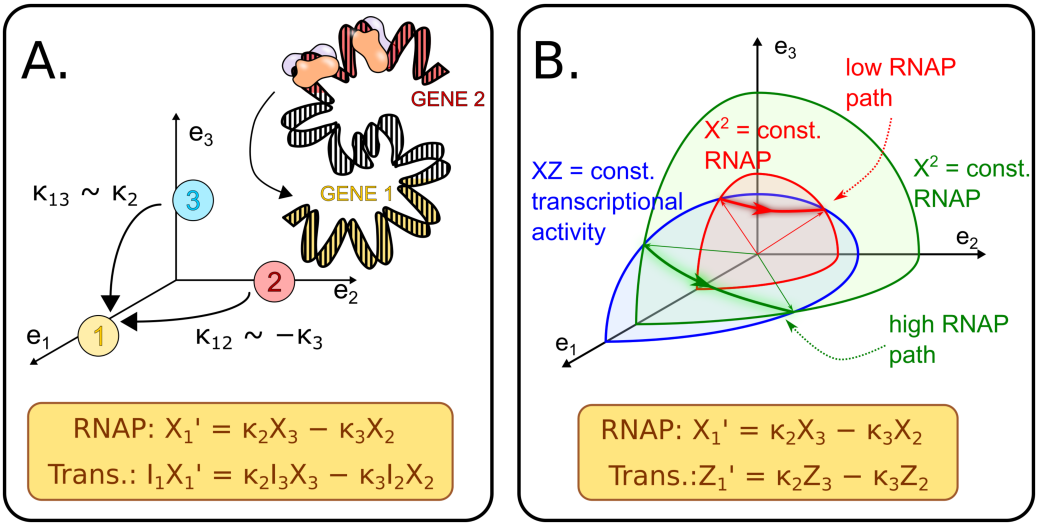

Figure 4.6: Rotational dynamics of RNAP and transcription illustrated using the energy ellipsoid. (**A**) RNAP flows from loci 2 and 3 to locus 1 at angular rates $\kappa_{\text{to,from}}$ with units of dist.$^{-1}$, inducing changes in the transcription rates. Signs follow from association $\kappa^{\text{to}}_{\text{from}} = \kappa^{\text{row}}_{\text{col}}$ with the angular velocity matrix $\widehat{\boldsymbol{\kappa}}$. The quantity $\mathbb{I}_i$ is the cost function for the number of units of RNAP to produce a single transcript of gene i. (**B**) Evolution of the transcription rates on the energy ellipsoid (blue) for low (red) and high (green) levels of RNAP. The allowed transcription rates are intersect the spheres because RNAP is conserved. RNAP is represented as a sphere because it has unit worth at each gene, whereas transcription is an ellipsoid because different genes have different requirements for RNAP.

Eqs. (4.23) specify the momentum sphere and energy ellipsoid, respectively, demarcating the allowed motions of the system by their intersection [13]. For $n = 3$, Eq. (4.23b) is the only constraint (the $\mathbb{I}_i$'s being fixed), but for larger n there are additional invariants of motion [119, 168, 230]. Conservation of momentum means that the vector X_i traces out a sphere in RNAP rate space (Figure 4.6B). The intersection of the momentum sphere with the energy ellipsoid defines the allowed pairings of RNAP allocation- and mRNA transcription rates. Because *transcriptional activity* E is conserved, the transcription rate vector Z^i traces out a curve on an ellipsoid with semiaxes $\sqrt{\mathbb{I}_i}$ and weighted radius $\sqrt{E}$; it is not a sphere because the transcription costs are different. The reason for measuring RNAP outflow X_i and transcription inflow with Z^i (cf. the position of the indices in Eqs. (4.20); see Materials and Methods section 4.4.4) is now clear: only those covector-vector pairings $\langle X_i, Z^i \rangle = \text{const.}$ that conserve RNAP during transfer between loci are permitted. Any two states $V^{(1)} = \left(X_i^{(1)}, Z^{i(1)}\right)$ and $V^{(2)} = \left(X_i^{(2)}, Z^{i(2)}\right)$ are compatible if they can be mutually reached by rigid rotation of the radius of the momentum sphere. In terms of the canonical two-form on vector fields (see Materials and Methods section

4.4.1 and [172] ch. 2),

$$\begin{aligned}\Omega\left(V^{(1)}, V^{(2)}\right) &= X_i^{(1)}\Omega^\flat Z^{i(2)} - \Omega^\sharp X_i^{(2)} Z^i(2) \\ &= X_i^{(1)}\mathbb{I}_i X_i^{(1)} - X_i^{(1)}\mathbb{I}_i X_i^{(1)} = 0,\end{aligned} \tag{4.24}$$

states 1 and 2 lie along a Hamiltonian flow of the transcriptional system that preserves total transcriptional activity. In this way, the constraint leads to different expression states throughout the body of the organism.

The spatial rates X_i and Z^j can be expressed in terms of the experimentally accessible amounts x_i and z^j. Differentiate Eq. (4.21) and substitute into Eq. (4.20a) to get $x_i' = \left(\mathbb{I}_{ij} z^j\right)' = x_j \kappa_i^j = \mathbb{I}_{jl} z^l \kappa_j^i$. Using skew-symmetry of the $\widehat{\boldsymbol{\kappa}}$ we arrive at the transcriptional analog of the Euler equations

$$\left(\mathbb{I}_{ij} z^j\right)' = -\kappa_i^j \mathbb{I}_{jl} z^l, \tag{4.25}$$

expressing the change in transcripts produced at each locus over space. For diagonal costs $\mathbb{I}_{ij} = \mathbb{I}_j \delta_{ij}$ and $n = 3$ genes we find explicitly

$$\begin{aligned}\begin{pmatrix}\mathbb{I}_{11}z^1\\ \mathbb{I}_{22}z^2\\ \mathbb{I}_{33}z^3\end{pmatrix}' &= \boldsymbol{\kappa} \times z = \left[\hat{\boldsymbol{\kappa}}, \hat{z}\right] = \begin{pmatrix}0 & -\kappa_1^2 & \kappa_3^1\\ \kappa_1^2 & 0 & -\kappa_2^3\\ -\kappa_3^1 & \kappa_2^3 & 0\end{pmatrix}\begin{pmatrix}\mathbb{I}_{11}z^1\\ \mathbb{I}_{22}z^2\\ \mathbb{I}_{33}z^3\end{pmatrix} \\ &= \begin{pmatrix}\kappa_3^1\mathbb{I}_{33}z^3 - \kappa_1^2\mathbb{I}_{22}z^2\\ \kappa_1^2\mathbb{I}_{11}z^1 - \kappa_2^3\mathbb{I}_{33}z^3\\ \kappa_2^3\mathbb{I}_{22}z^2 - \kappa_1^2\mathbb{I}_{22}z^2\end{pmatrix} = \begin{pmatrix}\kappa_3^1\mathbb{I}_{33}z^3 + \kappa_2^1\mathbb{I}_{22}z^2\\ \kappa_1^2\mathbb{I}_{11}z^1 + \kappa_3^2\mathbb{I}_{33}z^3\\ \kappa_2^3\mathbb{I}_{22}z^2 + \kappa_2^1\mathbb{I}_{22}z^2\end{pmatrix},\end{aligned} \tag{4.26a}$$

or in terms of single indices

$$\begin{pmatrix}\mathbb{I}_1 z_1\\ \mathbb{I}_2 z_2\\ \mathbb{I}_3 z_3\end{pmatrix}' = \begin{pmatrix}\kappa_{13}\mathbb{I}_3 z_3 + \kappa_{12}\mathbb{I}_2 z_2\\ \kappa_{21}\mathbb{I}_1 z_1 + \kappa_{23}\mathbb{I}_3 z_3\\ \kappa_{32}\mathbb{I}_2 z_2 + \kappa_{12}\mathbb{I}_2 z_2\end{pmatrix}, \tag{4.26b}$$

using the $\kappa_{\text{col}}^{\text{row}} = \kappa_{\text{from}}^{\text{to}} \mapsto \kappa_{\text{to,from}} = -\kappa_{\text{from,to}} \leftarrow\!\shortmid -\kappa_{\text{to}}^{\text{from}} = -\kappa_{\text{row}}^{\text{col}}$ convention for the association $\kappa_j^i \mapsto \kappa_{i,j}$ now that there is no need for tensor indices. Eqs. (4.26) are important because they relate the tangent space of rates (X_i, Z^j) to the base space of mRNA copy number, which is really what determines cell fate. Thus the absolute amounts x_i and z^i of RNAP and transcripts evolve via the Euler equations for rotational motion.

The last equalities in Eqs. (4.26) describes the picture in Figure 4.6A where the net change in the number of transcripts at a gene is due to the inflow

(or outflow for $\kappa_{ij} < 0$) of RNA polymerase from all other genes. With only three genes, the $\sharp$ map from forms (covectors) to vectors of the Hodge dual of a two form $[\star(\mathbf{e}_i \wedge \mathbf{e}_j)]^\sharp = \mathbf{e}_i \times \mathbf{e}_j = \mathbf{e}_k$ is a third vector (see [162] ch. 3 and [172] ch. 4), recovering the simple picture of rotation about an axis. Thus we have shown that the change in allocation of RNAP is between gene loci is analogous to rotational dynamics in $\mathbb{R}^3$.

4.2.6 Parametrization of a growing organism as a rigid body

Although rotational dynamics apply to transcriptional systems, it is not clear that they apply to developmental systems, which grow in extent as time progresses. In order to complete the analogy between development and strings, we need a coordinate system that parametrizes the growing organism as a rigid body. Specifically, we need to identify the spatial coordinate implied by the prime in Eq. (4.26). It will be shown in this section that the transformation to logarithmic scale by $s \mapsto \log s$ is the one we desire.

In a simple model of mitosis (Figure 4.7A), every cell replicates itself during a certain time window. In a one-dimensional model of the process, beginning at time $t_0 < 0$, a cell at position $x(t) = s$ with spatial extent cds replicates in time dt, increasing the length of the organism by $c_0 ds$. As a result of this growth, the k^{th} cell in the array moves k units to the right relative to a fixed origin. Then the velocity of cell k is

$$v_k = \lim_{dt\to 0} \frac{x_k(t+dt) - x_k(t)}{dt} = \lim_{dt\to 0} \frac{x_k(t) + kc_0 dt - x_k(t)}{dt} = kc_0. \tag{4.27}$$

Eq. (4.27) defines the spatially varying constraint $c = kc_0$ between time and space in the organism (cf. Eqs. (4.9)). If the temporal μ and spatial λ delays are held fixed, then we lose no generality in choosing the present ($t = 0$) in (4.9a) to make the velocity measurement (4.27). Differentiating the spatial constraint shows that

$$d\lambda = ds - kc_0 dt - tc_0 dk = 0 \implies ds\Big|_{t=0} = kc_0 dt. \tag{4.28}$$

In the continuous limit $k \to s$; then we may introduce the transformed variable $s' = \log s$, which satisfies the string condition $ds' = c_0 dt$. In other words, the velocity $\frac{ds'}{dt} = c_0$ does not vary in space. The foregoing argument shows that the logarithmic parametrization is the relevant length scale for growing systems.

The transformed coordinate $s' = \log s$ parametrizes the growing organism as a rigid body. It can be shown that a line drawn in the (t, s) plane (no primes) through a cell at position s in the present time $t = 0$ to its immediate ancestor at

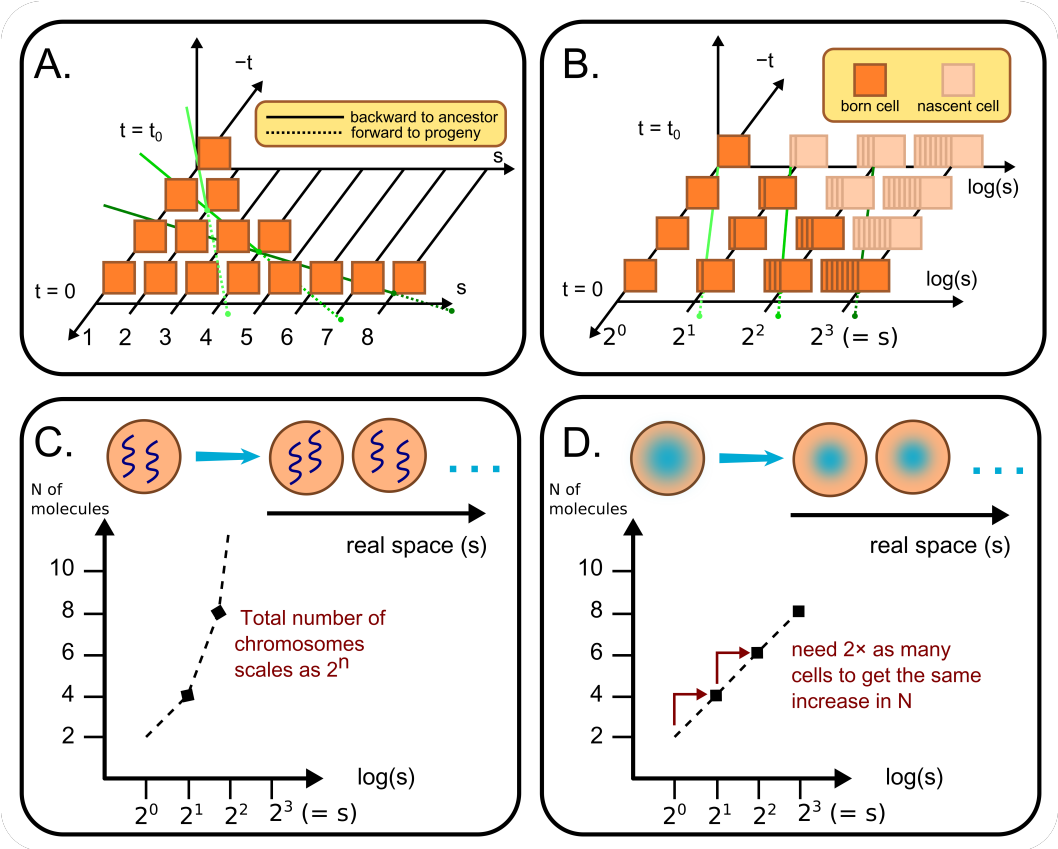

Figure 4.7: Parametrization of a growing one-dimensional organism as a rigid body. (**A**) Dividing cells originating from a single progenitor at $t_0 < 0$ move rightward with increasing horizontal velocity, quantified by the slope of the solid green lines connecting a cell to its immediate ancestor. Tracing the lines backward (solid) and forward (dashed) shows the cell's position in space-time if the relationship c between space and time were constant. (**B**) Transforming the spatial dimension as $s' = \log s$ makes the space-time relationship constant: each cell moves by the same multiple of its position at each time step. Distances between cells at $t = 0$ are preserved at t_0. (**C**) The total amount of a molecule that increases exponentially in the transformed coordinate s' is not conserved. (**D**) The total amount of a molecule that is diluted at each cell division and traces out a straight line versus $s' = \log s$ is conserved; it marks out distance in the transformed coordinate, because twice as many cells must be collected at each step to obtain a constant increase in the number of molecules observed.

$\frac{s}{2}$, one division time τ earlier, intercepts the horizontal $s = 0$ line through cell 1 at $t = 2\tau\left(\frac{1}{s} - 1\right) < 0$ (Figure 4.7A). By connecting each cell to the principal ancestor at the origin of space, one reads off its origin in time by the t-intercept. In contrast, each segment of a twisted string has a unique "ancestor" at t_0, namely, an earlier version of itself. Because dividing cells were born at different times, s does not parametrize the organism as a rigid body. In other words, in the growing organism the connection one-form ω (Materials and Methods section 4.4.2) depends explicitly

on space, whereas in the rigid string it is invariant. In the transformed coordinate system, lines drawn through cells in the present to their immediate ancestors are parallel with slope c_0 (Figure 4.7B). Extending these lines back $-\frac{t_0}{\tau}$ generations in t connects cells in the present to a unique ancestor in the past. There is no contradiction here because parallel lines *do* meet: at $t = -\infty$, the ultimate origin of time. No organism starts life as a dimensionless point, so picking t_0 is equivalent to choosing a time when the generational lines of each cell are still parallel. Because the parameterization s' preserves distance between the cells at all times between $t = 0$ and $t = t_0$, it is a rigid one.

4.2.7 Autonomous development from strained gene expression profiles

Distinct cell fates are characterized by different gene expression profiles, resulting from the allocation of RNAP and other factors to different genomic loci via morphogen gradients [14, 233]. In this section, we consider the hypothesis that morphogen gradients act on in the tangent space of gene expression; then the information they convey must be in the form of "steering assistance" rather than explicit "GPS" coordinates.

Let the nondecreasing function Θ_{x_i} be the cumulative distribution of RNAP seen at locus i across the spatial extent of the organism: by position s in the organism, locus i will have seen a fraction $\Theta_{x_i}(s)$ of the RNAP that it ultimately will see. With $s' = \log s$ the natural parametrization of the growing organism, the distribution of RNAP is log-transformed as well: if s is $\log\Theta$-distributed, then $\log s$ is Θ-distributed. With the appropriate Jacobean $s' = \log s \implies ds' = \frac{1}{s}ds$, common RNAP distributions are

$$\Theta(l) = \frac{\sqrt{2}}{\sqrt{\pi}\sigma}\int_0^l \exp\left(\frac{-(s'-\mu)^2}{2\sigma^2}\right)ds' \quad \text{(normal)}$$

$$\to \Theta\left(e^l\right) = \frac{\sqrt{2}}{\sqrt{\pi}\sigma}\int_1^{e^l}\frac{1}{s}\exp\left(\frac{-(\log s-\mu)^2}{2\sigma^2}\right)ds \quad \text{(lognormal)} \quad (4.29a)$$

$$\Theta(l) = \int_0^l \lambda\exp(-\lambda s')ds' \quad \text{(exponential)}$$

$$\to \quad \Theta\left(e^l\right) = \int_1^{e^l}\lambda s^{-\lambda-1}ds \quad \text{(log-exponential)} \quad (4.29b)$$

$$\Theta(l) = \frac{1}{\ell}\int_0^l ds' \quad \text{(uniform)}$$

$$\to \quad \Theta\left(e^l\right) = \frac{1}{\log L}\int_1^{e^l}\frac{1}{s}ds \quad \text{(log-uniform).} \quad (4.29c)$$

(See Figure 4.8A below for examples of each distribution in log-transformed coor-

dinates.) In Notice that in the log-transformed distributions the lower limit of s is 1 instead of 0, corresponding to the extent of a single cell, the smallest unit. Also note that if the upper limit of s' is $\ell = \log L$, then $s = L$ is the spatial extent of the organism.

The log-uniform distribution is special because it has the form of an arc length of an undeformed string, i.e., a line versus s' with unit slope. In contrast to a replicated molecule such as the chromosome, which scales exponentially in s' (Figure 4.7C), a molecule with fixed total amount is diluted at each cell division and is distributed according to (4.29c) (Figure 4.7D). Intuitively, at each step in s', one needs to count twice as many cells to count the same number of molecules. The assumption that RNAP (or the nutrients in the environment converted into it) is constant implies that the pitch of its distribution among genes obeys the same laws as the balance of angular momentum and angular velocity at different points along the string. We next make this analogy precise.

The applied torques in Eq. (4.14a) are of the form a force multiplied by the cross product of a fixed and body-referenced direction. The forces $\lambda^2 E\mathbb{I}$ and $G\mathbb{J}\tau_0^2$ measure the (constant) rate of change of the Euler angles θ and ψ, which are the components of curvature in the normal and binormal directions. One can easily see that twist $\tau_0 = \frac{\partial \psi}{\partial s} = \frac{2\pi n}{L}$ is a constant curvature, but to see that λ is as well requires closer examination of the elastica equations. In fact, the authors of [65] showed that a wave traveling in an elastic medium and having the shape of the Euler elastica naturally moves a material point in a circular arc, corresponding to a constant curvature. In the general case, the curvature $k_{ij}^2 = \frac{\left(x_i'' x_j' - x_j'' x_i'\right)^2}{\left(x_i'^2 + x_j'^2\right)^3}$ varies with the arc length parameter [218].

For a vector of input distributions $\boldsymbol{\Theta}\left(s'\right)$, one computes k_{ij}^2 from the rate at which the projection of $\boldsymbol{\Theta}^0$ on the $\left(\Theta_{x_i}^0, \Theta_{x_j}^0\right)$ plane bends away at an angle θ_{ij} from the diagonal (Figure 4.8B, left). The resultant strain is interpreted as the preferential allocation of RNAP to locus i over j (for counterclockwise deviation $\theta_{ij} > 0$), so that by some value $s' = s'_{1/2}$, locus i has seen 50% of its total RNAP allotment, whereas locus j has necessarily seen less than 50%. Yet because RNAP is shared, an arbitrary input distribution $\boldsymbol{\Theta}^0$ will be deformed into a new distribution $\boldsymbol{\Theta}$ so as not to violate the conservation laws. Let $\boldsymbol{\Omega} = \widehat{\boldsymbol{\kappa}}$ be the skew-symmetric matrix of pitches of the angles θ_{ij} versus s'. Then the angular momentum $p = \widehat{\mathbb{I}\boldsymbol{\kappa}}$ of RNAP in

the $n = 3$ gene system is assumed to evolve as

$$p'(s) = [p(s'), \mathbf{\Omega}(s')] + \sum_{i=1}^{3} \mathbb{I}_i k_i^2(s') \left[\widehat{\mathbf{\Gamma}}_i, \widehat{\boldsymbol{\chi}}_i(s')\right] \tag{4.30a}$$

$$\widehat{\mathbf{\Gamma}}_i'(s') = \left[\widehat{\mathbf{\Gamma}}_i(s), \mathbf{\Omega}(s')\right] \tag{4.30b}$$

$$g'(s') = g(s')\,\mathbf{\Omega}(s'), \tag{4.30c}$$

where $\mathbf{\Gamma}_i = g^{-1}\boldsymbol{\chi}_i$ is a unit vector in the direction of locus i at position s'. That is, the same chemical force that increased RNAP at locus i at s_0' now increases (and decreases) RNAP at other loci in the direction specified by $\mathbf{\Gamma}_i$. Eqs. (4.30) need to be solved by traversing developmental space, or equivalently, developmental time. Only after seeing all $s' \in [0, \ell]$ can the evolution in the tangent space be projected onto the base space of expression states. Also note that Eq. (4.30a) implicitly assumes a diagonal cost function $\mathbb{I}$ and makes the identification $k_{jl} = \epsilon^i_{jl} k_i$. Latin k is reserved for the curvature of the input distributions, and Greek κ for the output angular velocities.

To illustrate how gene expression evolves along the length of our one-dimensional organism, Figure 4.8 shows the simulated response to input gradients (4.29a)-(4.29c) of RNAP in $n = 3$ genes 1, 2, and 3 (panel A). Figure 4.8B (right) shows the effect of Eqs. (4.30) on the evolution of the input vector $\mathbf{\Theta}^0(s') = \left(\Theta^0_{x_1}(s'), \Theta^0_{x_2}(s'), \Theta^0_{x_3}(s')\right)$ of RNAP allocation rates at each locus in the one-dimensional organism, parametrized by $s' \in [0, \log(10)]$. Because Eqs. (4.30) can result in un-realistic values of the Θ_{x_i} (i.e., greater than 1 or less than 0), only the range of s' indicated by the solid lines of the input distribution are included in the distorted distribution. Whereas the input distribution (black) is nondecreasing in s and $\Theta^0_{x_3}$, the distorted distribution (blue) clearly increases and decreases. Yet the resulting vector $\mathbf{\Theta}(s')$ is still a cumulative distribution, for the simple reason that the $\Theta^0_{x_3}$ gradient has been distorted: in the undistorted state, the diluted molecule 3 marks out distance in the transformed coordinate (cf. Figure 4.7D). Figure 4.8A shows the RNAP density (red curves) at the three loci, computed from the derivative of the monotonic cumulative distributions $\Theta^0_{x_i}$ (blue curves). In contrast, in panel C, the densities are computed over the regions which Θ_i is increasing. It is clear that RNAP is distributed in a multimodal manner at the three loci, especially at locus 3. Dividing by the cost functions $\mathbb{I}_i$ gives the transcript density in arbitrary units across the organism (right). In this case, $\mathbb{I}_1 = 3$ is the smallest of the three cost functions, and correspondingly gene 1 has the highest level of transcripts. In summary, an input signal $\mathbf{\Theta}^0$ of RNAP allocation rates in the tangent space has been transformed

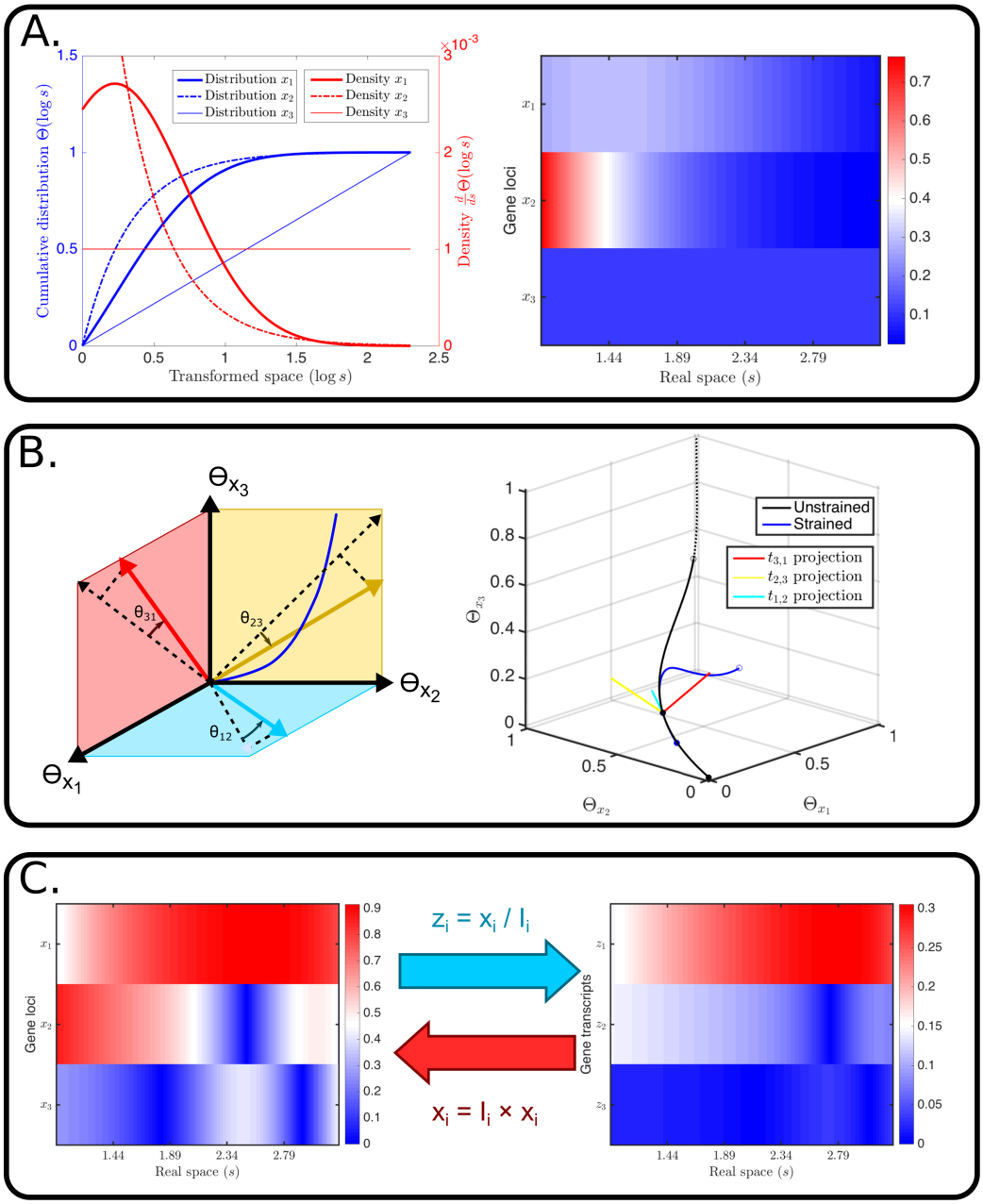
A.
Distribution x_1
Distribution x_2
Distribution x_3
Density x_1
Density x_2
Density x_3
Cumulative distribution $\Theta(\log s)$
Density $\frac{d}{ds}\Theta(\log s)$
Transformed space ($\log s$)
Gene loci
Real space (s)
B.
Θ_{x_3}
Θ_{x_2}
Θ_{x_1}
θ_{31}
θ_{23}
θ_{12}
Unstrained
Strained
$t_{3,1}$ projection
$t_{2,3}$ projection
$t_{1,2}$ projection
C.
Gene loci
Real space (s)
$z_i = x_i / l_i$
$x_i = l_i \times x_i$
Gene transcripts

into gene expression in a one-dimensional developing organism as a consequence of conserved transcriptional activity.

4.3. Discussion

We have achieved two broad goals in this chapter. First we have generalized the interaction of twist and looping in physical strings as differential equations for the angular momentum versus arc length. Second, we have shown how rotational dynamics apply to gene networks and how they reshape gene expression profiles in space. Unifying these disparate concepts is the theme that evolution in the tangent space rather than the base space (of angular strains or expression levels) provides a way to determine the future without knowing it ahead of time. It remains in this section to discuss the implications for autonomous development.

The most important conclusion from the string equations in sections 4.2.1-4.2.4 is that the shape (i.e., the "future") of the string is determinant not because of the heterogeneity of the individual segments (i.e., cells), but because of their interdependence. The principal equations (4.8), (4.14), and (4.30) of these sections are differential equations in the arc length coordinate s for a string with bending stiffness $E\mathbb{I}$ and torsional rigidity $G\mathbb{J}$. In the case of pure twist about the central line (section 4.2.1), loops remain planar, and torsional rigidity does not affect looping. But in strings and in biological systems, forces may interact in ways not predicted by either force alone. In order to account for this interaction, it was necessary to break up the applied torque (M or m in references [60, 196, 277, 278, 302]) into its contributions from spiral and bending strains; then the dynamics could be reduced to that of a top in a gravitational field. In fact, the analogy to the heavy top was pointed

Figure 4.8 (*preceding page*)**: Autonomous evolution of gene expression in the presence of strained gradients of RNA polymerase.** (**A**) Input RNAP distributions at three loci versus the transformed coordinate (left) and real space (right). Locus 1 is gaussian distributed in s' ($\mu = 0.1\ell$, $\sigma = 0.5\ell$), locus 2 exponentially ($\lambda = 3\ell$), and locus 3 uniformly. The density of RNAP at locus 2 in real space (bottom) is substantially higher than at the other loci. (**B**) Straining the cumulative RNAP allocation profiles. The three-dimensional plots show the cumulative fraction of RNAP allocated to gene i compared to genes j and k. Strain is measured by the angular deviation of the tangent lines $t_{i,j}$ from the identity line (where RNAP is allocated with no bias). The unstrained profile (black) is subject to the angular momentum evolution equations (4.30) initiated from $s' = 0.1\ell$, and bends to accommodate the constraint of constant total RNAP (blue). (**C**) Conversion of the output RNAP allocation profiles in real space s (left) to gene expression profiles (right) by the diagonal cost functions $\mathbb{I}_i$. Parameters are $\mathbb{I}_1 = 3$, $\mathbb{I}_2 = 6$, $\mathbb{I}_3 = 12$, $\ell = \log(10)$ (in s'), and $L = 10$ (in s). The dotted regions of the profile in B are excluded because the RNAP fraction goes above 1.

out by van der Heijden and coworkers [278], although their analysis was primarily on finding the critical points at which twisted rods buckled into loops. While their strategy was to determine M from the evolution of the angular velocities in the tangent space $TSO(3)$, ours is the complementary approach of directly evolving M in the cotangent space $T^*SO(3)$. The equivalence of these perspectives follows from the corresponding equivalence of the Lie-Poisson and Euler-Poincaré (Eq. (4.49b)) equations for the time (or arc length) evolution of the momentum rate of change of the Hamiltonian ($\frac{\partial H}{\partial \mu_i} = \xi^i$) and the angular velocity rate of change of the Lagrangian (i.e., $\frac{\partial L}{\partial \xi^i} = \mu_i$) , respectively; they are converted into each other by the Legendre transform [33]. The terms $\lambda^2 E\mathbb{I}$ and $\tau_0^2 G\mathbb{J}$ are forces (constant in the case of the elastica) whose resultants change the angular momentum when the Euler angles θ and ψ between and about the fixed z axis are nonzero. The angular momentum is converted into angular velocity using the moments of inertia, which then update the direction of the tangent vector. In this way, the configuration of the string is controlled by the memory of what it looked like when straight. "Memory" is not merely a mathematical convenience; it is the manifestation of connections between segments of the string which register stress as the string is strained. By virtue of the space-time constraints, symmetry provides the bridge between past and present.

The alternative to updating the angular momentum locally via the Euler equations is to specify curvature and torsion for all s and evolve the angular velocities using the Frenet-Serret relations (4.2), or to approximate the dynamics using the Zassenhaus expansion (4.19). In the case of a single (bending) force, the Euler and Frenet-Serret pictures are equivalent, although small but noticeable differences at the ends emerge when bending strains combine with spiraling. The discrepancy is a consequence of the fact that the string is not a conservative system, unless certain conditions are met. When there is only a single bending force, the angular trajectory of the azimuth θ is fully determined from the derivative of the strain energy. When two angles are strained by forces f and g, the equation $dE = fd\theta + gd\psi$ for the distribution of energy between them is underdetermined: ΔE is not sufficient to determine the angular trajectory. The parsimony principle of section 2.2.4 provides an additional constraint that the forces "add up" to the direction orthogonal to the current trajectory. Because no energy is lost to dissipation, all segments stay on the same level set of the potential as the string is transformed from straight to curved over time, and no internal strains develop between segments. This is also the content of Theorem 2.2.5, which states that it is only possible to know the (space or time)

trajectory in advance if the net force is one-dimensional, at all points orthogonal to the trajectory. The problem is that the orthogonal direction is not guaranteed to be a 90° rotation when the basis is skew, as when the angles are strained by different amounts (see Figure 2.1 in chapter 2). The Frenet-Serret equations and the Zassenhaus expansion postulate a form for $\mathbf{\Omega}$ for all s that may or may not agree with the applied strains; in contrast, the Euler-Poincaré equations update the force p' at every step with the new direction of the body frame, effectively making the dynamics one-dimensional. In this way, the Euler-Poincaré equations increase the energy in the most parsimonious way: parallel to the energy gradient.

Is there any reason the Euler-Poincaré picture should apply in the current setup? Surely the forces felt at any given segment need not be orthogonal to the current angular velocity vector. The reason that these equations apply is that the string is controlled only at its ends; there is no mechanism to increase or decrease energy at intermediate points along the arc length. Furthermore, we know the total increase in energy by virtue of specifying the total amount of curvature and twist in advance. Therefore, every segment must see the same increase dE in the energy. In these rarefied circumstances, the only way to obtained the strained string from straight is to take the most direct path, putting all energy into rotation and dissipating none. In contrast, real strings are dissipative. It may be that the endpoint strain energy is not specified, or that there is some way for excess strain to be added or frozen in midway between the string ends. The prediction of the current theory is that a string forced into an arbitrary shape will show localized strains the Euler-Poincaré string lacks.

The results of this chapter allow us to make the following logical progression pertaining to combinatorial logic in development. If development is not known ahead of time in the egg stage, then the dynamics cannot be one-dimensional: strains in the RNAP distribution at time zero point will have different effects at later times. Because the controls f, g on gene expression x, y are noncommutative—in the sense that $\frac{\partial f}{\partial y} - \frac{\partial g}{\partial x} \neq 0$ (see sections 1.2 and 2.2.1 and Figure 1.1B)—it is not possible for cells to flow downhill on the surface $\phi = fx + gy$ without reorienting at each step, although the surface itself may be smooth. With controls in the tangent space having nonzero curl, the projected dynamics in gene expression space circulate as well (cf. section 2.2.2). Thus the potential is not a gradient potential, fixed at all times from the start. Reversing the foregoing logic implies that if the dynamics are *not* noncommutative, then they are *not* not known ahead of time. Or what is the same thing, if the dynamics are commutative (i.e., combinatorial), they are known

at the start. The preponderance of evidence suggests that animals require time to develop, the implication being that in the egg there is an information bottleneck to the reading out the future. Put another way, a differential equation for cell fate is not sufficient to characterize the adult at the egg stage if it can't be integrated.

The concept of mixing forces to steer the shape of a string is an attractive analogy in developmental biology where gradients of chemical signals control cell fate. Information for the adult is stored in the DNA of the egg, but there are simply insufficient signals to address it to each gene in every cell at the start. In order to extract the information without appealing to a *deus ex machina* influence to guide the embryo to its final state, each space-time fragment should contain the same amount of information. With the total information context fixed, each progressive change in transcription guides the interconnected group of cells down an energy gradient in gene expression space. But with transcription in constant flux, the gradient direction changes over time. Contrast this dynamic picture with the static Waddington landscape where the "downhill" direction is known at every point from the start. In order to make the differential equation for development integrable, it must be checked at each step that the integration path is still downhill. By the time we have done so, development is over.

In order to make the string analogy complete, it was necessary to find an analog of the angular momentum. We showed in section 4.2.5 that a core component of the transcription machinery, RNA polymerase, can serve in this capacity if its total amount is fixed. While useful, this ansatz should not be taken literally: RNAP is merely a substitute for the more abstract quantity called information. In a complex organism, cells of different tissues transcribe distinct sets of genes, meaning that RNAP must be variably allocated to each locus across the length of the organism. Specifically, the organism remembers the spatial rates (measured in units of RNAP per distance) at which the amount of RNAP at locus i changes between adjacent cells in the same way that the deformed string remembers being straight. It is easy to see the basis for this conservation law: allocating a large amount of RNAP/information early on means that there is less to go around later.

If RNAP is momentum, then transcriptional activity—defined as the spatial rate at which transcripts of type i vary been adjacent cells—is the energy. RNAP represents the fundamental activity unit, having equal ability to transcribe genes at all loci. However, transcripts are not all created equal, with some genes requiring many units of RNAP to produce a single mRNA. The seemingly abstract notion of rotation in transcriptional networks is just the net flow of mRNA from one locus to

another across space. The same calculus occupies traders in currencies who seek the soundest specie in which to store their wealth, a quantity with universal value. Before transcripts can transit, they must be converted into a common currency, such as RNAP, with equal valuation at all loci. We understood this in Figure 4.6 as the intersection of an RNAP sphere, with equal axes in all gene "directions," and a transcriptional activity ellipsoid, with longer axes in the direction of more costly genes. In higher dimensions than three, one no longer speaks of rotation *about* an axis, but rather of rotations *in* a two-dimensional plane (see [162] ch. 4). This concept is much more transparent in transcriptional systems than strings because we always speak about transfer from one gene to another, never about rotation *of* a single gene. The concept generalize to any number of genes. For an n-dimensional system that evolves as its Lie bracket, one may write the momentum as $\mathbf{M} = \mathbb{I}\boldsymbol{\Omega} + \boldsymbol{\Omega}\mathbb{I}$ as the product of a skew-symmetric and a diagonal matrix, giving that the amount of RNAP involved in the $i \to j$ transfer is $(\mathbb{I}_i + \mathbb{I}_j)\,\Omega_{ij}$. The n-dimensional Euler-Poincaré equations define $\binom{n}{2}$ differential equations of the form $(\mathbb{I}_i + \mathbb{I}_j)\,\dot{\Omega}_{ij} = (\mathbb{I}_i - \mathbb{I}_j)\sum_k \Omega_{ik}\Omega_{kj}$ for each of the pairs of genes, modulo an applied force [73]. Therefore, in the general case, no transfer is privileged by how we choose to write the skew-symmetric matrix $\boldsymbol{\Omega}$ (see [126] for one option). In this chapter, networks are limited to $n = 3$ genes, in which case there is only one integral invariant of the motion, namely the energy. In higher dimensional systems it is well known that other conserved quantities [168, 119] circumscribe the transcriptional activity. In fact, for a matrix evolving in time as the Lie bracket with some n-dimensional angular velocity, the traces of the n powers of the matrix are constants of the motion [230]. It is the subject of future research to ascribe biological meaning to the higher order constraints. While it was also assumed that RNAP acts locally—only RNAP at i affects transcripts at i—the possibility for nonzero off-diagonal terms in the tensor $\mathbb{I}_{ij}$ presages the more general case of gene regulatory interactions.

Essential to our results on the interpretation of morphogen gradients in section 4.2.6 was the parametrization of the growing organism using a log-transformed distance coordinate. This choice permitted distances between spatial points to be preserved in time, an essential feature of rigid objects. The log-transformed parameter s' makes sense because twice as many cells are needed to count the same total number of molecules in a mitosing cell that partitions half its components between two daughters upon division. Such a parametrization may not describe very early development when rapid division occurs while the egg maintains constant size, or in embryos that grow in 2- and 3D. The decoupling of real space and transformed

space is rationalized by recalling that cells differ due to their molecular makeup, not their physical location per se. In section 4.2.7, for example, the organism itself did not bend like a string: only the distribution of RNAP to a gene changed.

More fundamental than the log-transformed distance coordinate is the equivalence of space and time. If pairwise distances are preserved, neighboring cells are like a kymograph, representing phased versions of an ancestor cell at different stages of its life. As a consequence of space-time equivalence, the transcriptional states of neighbors are related to each other based on their distance from a common ancestor. Another way to understand the relationship is by extending the wealth analogy introduced above. Investments may be denominated in different currencies, so that when the exchange rates are not constant, and investor stands to gain or lose depending on when he chooses to repatriate his returns. If a U.S. investor's holdings denominated in Yen produce a $\lambda_1 = 10\%$ return while over the same time period the U.S. dollar depreciates by $\lambda_2 = -5\%$, then his profit in dollar terms is $(1+\lambda_2)^{-1} \times (1+\lambda_1) \times 1 = 1.16$ times his initial dollar investment. Undoing the action of holding dollars alone and applying the combined action of buying Yen and investing it clearly leads to a different point along the dollar axis than simply holding dollars. By virtue of their having a common origin, the distance "Δ\$" accumulated between the alternative strategies is found by going backward and forward in time as in Figure 4.4. An added complication is that a holder of Yen can anticipate appreciation of the dollar; she can charge the U.S. investor a premium to "hedge" his Yen investment against its reduced ability to repurchase dollars later. Using the present framework of stress and strains to formulate the economics of how beliefs about valuations in the future affect exchange rates in the present will be an interesting topic for future research.

It is interesting to relate our results to other studies that have explored the role of forces in development. Elasticity in particular has been shown to be relevant to tissue growth in plants [37, 19, 140, 156], leaf venation [149], invagination of the morphgenic furrow in flies [58, 187], initial alignment of the anterior-posterior axis in fish [51], and even looping in the intestine [235]. The primary result is that complex forms are generated during development by context-specific responses of the connected tissue to a common signal. For example, the faster growth rate of the gut tube or leaf mesophyll vis-á-vis the underlying mesendoderm or epidermis resulted in either loops [235] or cracks [149], respectively, a consequence of the constraint of tissue connectivity. By combining global polarity and genetic "identity" factors with applied gradients of growth rates, Kenneway and coworkers demonstrated how com-

binatorial interactions in the tangent space led to autonomous formation of shapes as complex as the Snapdragon corolla tube [140]. This study intriguingly assumed that genetic factors modulate the magnitude, but not direction, of the growth rate vectors, reiterating the theme that shape is predetermined, but unrealized until time has passed. A similar demonstration was made in *Arabidopsis* embryos where the (genetic) effect of a cell wall-remodeling hormone was modulated by the local strain felt by the growing cells [19]. The yolk and vitelline membrane of *Drosophila* embryos were shown to modulate the depth and width, respectively, of the invaginating morphogenic furrow as the cells underwent a combination of active and passive isochoric deformations [58, 187]. Importantly, the different deformation rates controlled the allowable forms, echoing the results here that the effect of two strains cannot be known at the start. Spatial constraints are also operative when organelles compete for scarce cytoplasmic resources [94], which can result in interior cells of a colony being smaller and more compressed than their more peripheral counterparts [4]. The contribution of this chapter is to suggest that elasticity may operate on the more abstract space of gene regulation. Indeed, there is evidence for such a notion in nodal flow in left-right polarity in mouse [197, 266] and germ band extension in *Drosophila* [64]; both processes result in differential gene expression in tissues where the forces are felt (reviewed in [109]). Finally, the hypothesis that limited resources constrain form in a certain morphospace [250] suggests that evolution balances adaptions by their perceived value in different environments.

It is also useful to compare our results with studies that have found a role for the temporal dimension in cell decision-making. Palau-Ortin and colleagues observed path-dependence in the selection of the stable state in a bistable region of phase space in a noise-driven model of contact inhibition [206]. Selection could largely be accounted for by the equilibrium pattern of the previous monostable region along the path, although a critical burn-in time was necessary for the system to forget the very first state. Here, memory of the penultimate state shows that the rate variables (where the cells are poised to go) and state variables (where they are) have equally important roles in decision-making. On the other hand, Nené and coworkers showed that the relative speeds and asymmetry of two signals could bias selection in a bistable circuit, with faster decisions making the system less sensitive to asymmetry [194]. Although both studies relied to some extent on noise for the initial symmetry-breaking, the effect on gene expression could not be realized until the passage of time. Our model does not include noise, but does require a deterministic signal (the input gradients) at the very start.

In conclusion, the ideas presented in this chapter are one solution to the problem of autonomous development. When they act in the tangent space, a small number of signals evolve over time to produce novel outcomes that are neither possible nor knowable at the egg stage. Because they steer cells rather than address them to new positions, signals in the tangent space are just as agnostic to the final outcome as the cells themselves. This new viewpoint removes the need for a *deus ex machina* argument at time zero, an inescapable feature of regulation directly in the base space of gene expression. We argued that the evolution of the space curve of string or the developmental trajectory of a cell could not be known in advance due to the multi-dimensional nature of the strains. The new model is a significant step forward from static Waddington picture and answers the question of why cells do not start at the end if they know the end at the start: the directions of the forces in the tangent space controlling the spatial rates of expression do not always point downhill; by the time their direction is verified at every step, development is complete. It was suggested that an alternative to reading out all the information at once in the egg state is to require each time step to process an equally-sized information fragment. That different shapes result when the parsimony principle is violated was used in support of a mechanism whereby sequential processes arise autonomously. New technologies that probe the spatial variation of gene expression at the single-cell level [157, 244] will be indispensable in the search for evidence that the connectedness and common origin of dividing cells determine their fates to the same, if not greater, extent than heterogenous decision-making.

4.4. Materials and Methods

4.4.1 Vector fields and the derivation of Hamilton's equations

4.4.1.1 *Hamilton's equations*

The following is a derivation of Hamilton's equations (4.4) applied to rotational motion; the reader is referred to [134, 172] in particular for additional exposition. The analysis uses a number of central concepts from the differential geometry of vector fields, for which [13] chs. 7 and 8 and [255] chs. 4, 5, and 7 are good references.

Velocity and momentum of an n-dimensional object make up a $2n$-dimensional symplectic vector space in which each vector has a unique conjugate.

In this space, (bold face) vector fields and their commutators have the form

$$\mathbf{X} = \Omega^i \frac{\partial}{\partial q^i} + \Xi_i \frac{\partial}{\partial p_i} \tag{4.31a}$$

$$\begin{aligned}
[\mathbf{X}, \mathbf{Y}] =& \Omega^i_{\mathbf{X}} \frac{\partial \Omega^j_{\mathbf{Y}}}{\partial q^i} \frac{\partial}{\partial q^j} + \Omega^i_{\mathbf{X}} \frac{\partial \Xi^{\mathbf{Y}}_j}{\partial q^i} \frac{\partial}{\partial p_i} + \Xi^{\mathbf{X}}_i \frac{\partial \Omega^j_{\mathbf{Y}}}{\partial p_i} \frac{\partial}{\partial q^j} + \Xi^{\mathbf{X}}_i \frac{\partial \Xi^{\mathbf{Y}}_j}{\partial p_i} \frac{\partial}{\partial p_i} \\
& - \Omega^i_{\mathbf{Y}} \frac{\partial \Omega^j_{\mathbf{X}}}{\partial q^i} \frac{\partial}{\partial q^j} - \Omega^i_{\mathbf{Y}} \frac{\partial \Xi^{\mathbf{X}}_j}{\partial q^i} \frac{\partial}{\partial p_i} - \Xi^{\mathbf{Y}}_i \frac{\partial \Omega^j_{\mathbf{X}}}{\partial p_i} \frac{\partial}{\partial q^j} - \Xi^{\mathbf{Y}}_i \frac{\partial \Xi^{\mathbf{X}}_j}{\partial p_i} \frac{\partial}{\partial p_i} \\
=& \left[\boldsymbol{\Omega}_{\mathbf{X}}, \boldsymbol{\Omega}_{\mathbf{Y}}\right] + \left[\boldsymbol{\Xi}^{\mathbf{X}}, \boldsymbol{\Xi}^{\mathbf{Y}}\right] + \left[\boldsymbol{\Omega}_{\mathbf{X}}, \boldsymbol{\Xi}^{\mathbf{Y}}\right] + \left[\boldsymbol{\Xi}^{\mathbf{X}}, \boldsymbol{\Omega}_{\mathbf{Y}}\right] \\
=& \left[\boldsymbol{\Omega}_{\mathbf{X}}, \boldsymbol{\Omega}_{\mathbf{Y}}\right] + \left[\boldsymbol{\Xi}^{\mathbf{X}}, \boldsymbol{\Xi}^{\mathbf{Y}}\right].
\end{aligned} \tag{4.31b}$$

To show that the last two terms vanish, observe that the (unadorned) momentum vector $\Xi_{\mathbf{Z}}$ can be written under the hat map (4.1) as $\widehat{\mathbb{I}\Omega_{\mathbf{Z}}} = \mathbb{A}\widehat{\Omega}_{\mathbf{Z}} + \widehat{\Omega}_{\mathbf{Z}}\mathbb{A}$, where $\mathbb{A} = \frac{1}{\rho_0}\int \rho(\mathbf{R})\,\mathbf{R}\otimes\mathbf{R}d^n\mathbf{R}$ is a symmetric matrix which is diagonal in the body basis relative to the center of mass [119]. Together with the skew symmetry of $\widehat{\Omega}_{\mathbf{Z}}$, this tensor can be commuted as $\widehat{\Omega}_{\mathbf{Z}}\mathbb{A} = \mathbb{A}^T\widehat{\Omega}^T_{\mathbf{Z}} = -\mathbb{A}\widehat{\Omega}_{\mathbf{Z}}$ when multiplying on the left. Then

$$\begin{aligned}
\left[\widehat{\Omega}_{\mathbf{X}}, \widehat{\Xi}^{\mathbf{Y}}\right] + \left[\widehat{\Xi}^{\mathbf{X}}, \widehat{\Omega}_{\mathbf{Y}}\right] &= \left[\widehat{\Omega}_{\mathbf{X}}, \mathbb{A}\widehat{\Omega}_{\mathbf{Y}} + \widehat{\Omega}_{\mathbf{Y}}\mathbb{A}\right] + \left[\mathbb{A}\widehat{\Omega}_{\mathbf{X}} + \widehat{\Omega}_{\mathbf{X}}\mathbb{A}, \widehat{\Omega}_{\mathbf{Y}}\right] \\
&= \left(\widehat{\Omega}_{\mathbf{X}}\mathbb{A}\widehat{\Omega}_{\mathbf{Y}} - \mathbb{A}\widehat{\Omega}_{\mathbf{Y}}\widehat{\Omega}_{\mathbf{X}}\right) + \left(\widehat{\Omega}_{\mathbf{X}}\widehat{\Omega}_{\mathbf{Y}}\mathbb{A} - \widehat{\Omega}_{\mathbf{Y}}\mathbb{A}\widehat{\Omega}_{\mathbf{X}}\right) \\
&\quad + \left(\mathbb{A}\widehat{\Omega}_{\mathbf{X}}\widehat{\Omega}_{\mathbf{Y}} - \widehat{\Omega}_{\mathbf{Y}}\mathbb{A}\widehat{\Omega}_{\mathbf{X}}\right) + \left(\widehat{\Omega}_{\mathbf{X}}\mathbb{A}\widehat{\Omega}_{\mathbf{Y}} - \widehat{\Omega}_{\mathbf{Y}}\widehat{\Omega}_{\mathbf{X}}\mathbb{A}\right) \\
&= \left(\widehat{\Omega}_{\mathbf{X}}\mathbb{A}\widehat{\Omega}_{\mathbf{Y}} - \mathbb{A}\widehat{\Omega}_{\mathbf{Y}}\widehat{\Omega}_{\mathbf{X}}\right) + \left(\widehat{\Omega}_{\mathbf{X}}\widehat{\Omega}_{\mathbf{Y}}\mathbb{A} - \widehat{\Omega}_{\mathbf{Y}}\mathbb{A}\widehat{\Omega}_{\mathbf{X}}\right) \\
&\quad + \left(-\widehat{\Omega}_{\mathbf{X}}\mathbb{A}\widehat{\Omega}_{\mathbf{Y}} + \mathbb{A}\widehat{\Omega}_{\mathbf{Y}}\widehat{\Omega}_{\mathbf{X}}\right) + \left(-\widehat{\Omega}_{\mathbf{X}}\mathbb{A}\widehat{\Omega}_{\mathbf{Y}} + \widehat{\Omega}_{\mathbf{Y}}\mathbb{A}\widehat{\Omega}_{\mathbf{X}}\right) = 0.
\end{aligned} \tag{4.32}$$

Reversing the hat map of the quantities on the l.h.s. of Eq. (4.32) gives the desired result in Eq. (4.32) for the Lie bracket of vector fields.

A special vector field $\mathbf{X}_H$ represents the change dH of an energy function $H : \mathbb{R}^{2n} \to \mathbb{R}$, but rotated 90° clockwise. The condition $dH = 0$ that energy is conserved along a path parametrized by s is expressed by the vanishing of

$$dH(s) = \frac{\partial H}{\partial q}dq + \frac{\partial H}{\partial p}dp = \begin{pmatrix} \frac{\partial H}{\partial p} & -\frac{\partial H}{\partial q} \end{pmatrix} \begin{pmatrix} 0 & \mathbf{I} \\ -\mathbf{I} & 0 \end{pmatrix} \begin{pmatrix} dq \\ dp \end{pmatrix} = \Omega\left(\mathbf{X}_H(s)\right), \tag{4.33}$$

with $\mathbf{I}$ the identity on $\mathbb{R}^n$. The canonical two-form Ω (not to be confused with the vector $\Omega_{\mathbf{Z}}$) defined in (4.33) takes as input $\mathbf{X}_H$ and an additional vector field $\mathbf{Y}$ over $\mathbb{R}^{2n}$; it returns 0 if $\mathbf{Y}$ is parallel to $\mathbf{X}_H$, or what is the same thing, orthogonal to the Legendre transform of H (see [106] section 1 and [172] ch. 2).

Eq. (4.33) shows that Ω operating on $\mathbf{X}_H$ defines a one-form $\Theta = \theta_i(p,q)\,dq^i$. Then Ω may be written as the differential

$$d\Theta = d\theta_i \wedge dq^i = \left(\frac{\partial\theta_i}{\partial p_j}dp_j + \frac{\partial\theta_i}{\partial q^j}dq^j\right) \wedge dq^i = \frac{\partial\theta_i}{\partial p_j}dp_j \otimes dq^i - \frac{\partial\theta_i}{\partial p^j}dq^i \otimes dp_j \quad (4.34)$$

in the direction of the input vector fields ([13] ch. 7). The wedge product $dp_j \wedge dq^i = dp_i \otimes dq^i - dq_i \otimes dp_j$ is the volume element in the $2n$-symplectic vector space spanned by p_j and q^i; it is nonzero only if $i = j$ because there is only direction skew-orthogonal to any vector in a symplectic space (see Appendix 1.5.1 and [13] ch. 8). Observe that with an input field $\mathbf{X}$ the first term of Eq. (4.34) can be written

$$\frac{\partial\theta_i}{\partial p_j}dp_j(\mathbf{X})\,dq^i = \Xi_j^{\mathbf{X}}\frac{\partial\theta_i}{dp_j}dq^i, \quad (4.35)$$

and similarly for $\mathbf{Y}$. The Lie derivative $\mathcal{L}_{\mathbf{X}}(\Theta) = \mathbf{X}(\Theta)$, introduced in Materials and Methods section 4.4.3.2, has the additional property of being a derivation, viz.

$$\begin{aligned}\mathcal{L}_{\mathbf{X}}\Theta = \mathcal{L}_{\mathbf{X}}\left(\theta_j dq^j\right) &= \mathcal{L}_{\mathbf{X}}(\theta_j)\,dq^j + \theta_j\mathcal{L}_{\mathbf{X}}\left(dq^j\right) \\ &= \left(\Omega^i_{\mathbf{X}}\frac{\partial\theta_j}{\partial q^i} + \Xi_i^{\mathbf{X}}\frac{\partial\theta_j}{\partial p_i}\right)dq^j + \theta_j\Omega^i_{\mathbf{X}}\frac{\partial}{\partial q^i}dq^j \end{aligned} \quad (4.36a)$$

implying when the substitution $\theta_i = p_i$ is made that

$$\Xi_i^{\mathbf{X}}\frac{\partial\theta_j}{\partial p_i}dq^j = \mathbf{X}(\Theta) - \Theta(\mathbf{X}) \quad (4.36b)$$

(with implicit summation over i, j). With this substitution in Eq. (4.34), the version in coordinates

$$\Omega(\mathbf{X},\mathbf{Y}) = d\Theta(\mathbf{X},\mathbf{Y}) = \Xi^{\mathbf{X}}\cdot\Omega_{\mathbf{Y}} - \Xi^{\mathbf{Y}}\cdot\Omega_{\mathbf{X}} \quad (4.37a)$$

assumes the coordinate-free form

$$\begin{aligned} d\Theta(\mathbf{X},\mathbf{Y}) =& \mathbf{X}(\Theta)\circ\mathbf{Y} - \Theta(\mathbf{X})\circ\mathbf{Y} - \mathbf{Y}(\Theta)\circ\mathbf{X} - \Theta(\mathbf{Y})\circ\mathbf{X} \\ &= \mathbf{X}(\Theta\circ\mathbf{Y}) - \mathbf{Y}(\Theta\circ\mathbf{X}) - \Theta([\mathbf{X},\mathbf{Y}]), \end{aligned} \quad (4.37b)$$

expressing the well-known result (see [172] ch. 4, [255] ch. 7) for the derivative of a one-form.

Now, substitute $\Theta = p_i dq^i$ in Eq. (4.37b) and observe that $\Theta\circ\mathbf{Z} = p\cdot\Omega_{\mathbf{Z}}$. Use of the chain rule then gives

$$\begin{aligned}\Omega(\mathbf{X},\mathbf{Y}) &= \mathbf{X}(p\cdot\Omega_{\mathbf{Y}}) - \mathbf{Y}(p\cdot\Omega_{\mathbf{X}}) - p(\Omega_{\mathbf{X}}\cdot\Omega_{\mathbf{Y}} - \Omega_{\mathbf{Y}}\cdot\Omega_{\mathbf{X}}) \\ &= dp\cdot\mathbf{X}(\Omega_{\mathbf{Y}}) - dp\cdot\mathbf{Y}(\Omega_{\mathbf{X}}) - p\cdot\mathrm{ad}_{\Omega_{\mathbf{X}}}(\Omega_{\mathbf{Y}}), \end{aligned} \quad (4.38a)$$

while at the same time contracting Eq. (4.33) with vector field $\mathbf{Y}$ yields

$$\Omega(\mathbf{X},\mathbf{Y}) = \frac{\partial H}{\partial q}\Omega_{\mathbf{Y}} + \frac{\partial H}{\partial p}\Xi^{\mathbf{Y}}. \tag{4.38b}$$

Upon collecting like terms and evaluating the dp's, one finds Hamilton's equations for the evolution of momenta p and the velocities q that preserve level sets of H:

$$\frac{\partial H}{\partial q} = \Xi^{\mathbf{X}} - \mathrm{ad}^*_{\mathbf{\Omega_X}}(p) = p'(s) \tag{4.39a}$$

$$\frac{\partial H}{\partial p} = -\Omega_{\mathbf{X}} = g^{-1}(s)\, g'(s) = q'(s). \tag{4.39b}$$

In Eqs. (4.38) and (4.39), the vector $\Omega_{\mathbf{Z}}$ and the covector p are regarded as elements of the Lie algebra $\mathfrak{g}$ and its dual $\mathfrak{g}^*$, respectively. The vector adjoint ad_η with $\eta \in \mathfrak{g}$ satisfies the relation $\langle \mu, \mathrm{ad}_\eta(\xi)\rangle = \langle \mathrm{ad}^*_\eta(\mu), \xi\rangle$ with the covector adjoint ad^*_η in the pairing between $\mu \in \mathfrak{g}^*$ and $\xi \in \mathfrak{g}$. The adjoint action of a Lie algebra on itself is defined from the differential of the Adjoint action by

$$\mathrm{ad}_\eta(\xi) = T_e\left(L_g \circ R_{g^{-1}}\right)\circ\xi = T_e L_g R_{g^{-1}}\circ\xi + L_g T_e R_{g^{-1}}\circ\xi \to \eta\circ\xi - \xi\circ\eta \tag{4.40}$$

as $g = \exp(t\eta) \to e$ at the identity of the Lie group G. Under the association $p \leftrightarrow \widehat{p}$ and $\mathbf{\Omega_X} \leftrightarrow \widehat{\Omega}_{\mathbf{X}}$ of vectors to skew-symmetric matrices via the hat map (4.1), the ad and ad^* operations in Eqs. (4.38a) and (4.39a) become synonymous with the Lie bracket or matrix commutator. Finally, by dropping the subscript $\mathbf{X}$ we obtain Euler's equations for the evolution of the angular momentum along the string in the presence of an applied torque:

$$p'(s) = [p(s), \mathbf{\Omega}(s)] + \mathbf{\Xi}(s) \tag{4.4a}$$

$$g'(s) = g(s)\,\mathbf{\Omega}(s). \tag{4.4b}$$

The association of elements of $\mathfrak{g}, \mathfrak{g}^*$ with skew-symmetric matrixes is made throughout the Results section 4.2 and in the sequel. Eq. (4.4a) is sometimes known as the Euler-Poincaré or Lie-Poisson equation [119, 172], because the angular momentum p is the *fiber derivative* or *Legendre transformation* of the Lagrangian L, and the angular velocity $\mathbf{\Omega}$ that of the hamiltonian H; the change in one can be expressed as the (co)adjoint ad (ad^*) of the the other.

4.4.1.2 *Keeping track of a fixed direction*

Here we derive the result $\widehat{\mathbf{\Gamma}}'_n(s) = \left[\widehat{\mathbf{\Gamma}}_n(s), \mathbf{\Omega}(s)\right]$ of (4.8b) in the Results section 4.2.1 that for $\mathbf{\Gamma}_n = g^{-1}\boldsymbol{\chi}_n$, the body-coordinate representation of the fixed x direction.

Introduce an auxiliary parameter t so that the fixed and body normal agree at $t = 0$, viz. $\mathbf{\Gamma}_n (s+t)\Big|_{t=0} = \boldsymbol{\chi}_n (t)\Big|_{t=0}$. The role of t is to pick out a reference vector for $\mathbf{\Gamma}_n$ and define rotations relative to it. Then in the equation

$$\mathbf{\Gamma}_n (t+s) = g^{-1} (t+s)\, \boldsymbol{\chi}_n (t)\,, \tag{4.42}$$

the matrix $g^{-1}(s+t) \to e$ as $t \to 0$. Advancing along the string by a short amount ds gives the normal as $\mathbf{\Gamma}_n (t+s+ds) = g^{-1}(t+s+ds)\, \boldsymbol{\chi}_n (t)$. One gets in the limit that the derivative is

$$\widehat{\mathbf{\Gamma}}'_n (s+t)\Big|_{t=0} = \lim_{ds\to 0} \frac{g^{-1}(t+s+ds) - g^{-1}(t+s)}{ds} \mathbf{\Gamma}_n (s+t)\Big|_{t=0}. \tag{4.43}$$

However, the matrix $\mathbf{\Omega}$ is tangent to g at the origin e; then we may differentiate the identity $\mathbf{I} = gg^{-1}$ with respect to s and let both $t, ds \to 0$ to find $(g^{-1})'\Big|_{t=0} = -g^{-1}g'g^{-1}\Big|_{t=0} = -\mathbf{\Omega}$. Thus we conclude

$$\widehat{\mathbf{\Gamma}}'_n (s) = -\mathbf{\Omega}(s) \cdot \mathbf{\Gamma}(s) = \left[\widehat{\mathbf{\Gamma}}_n (s), \mathbf{\Omega}(s)\right] \tag{4.44}$$

for all s (cf. [12] Lemma 2 ff. and [172] ch. 9.1). This important modification keeps track of the rotation of the body frame for updating the angular momentum p.

4.4.1.3 *Alternative derivation of the Euler equations*

Energy conservation is ultimately what causes dynamical systems like the string to change direction and explore different regions of the underlying phase space. Here we use this principle to arrive at Euler's equations (4.4) from the perspective of Lie groups and Lie algebras.

Let $g \in G$ be points in a Lie group G, $\xi \in \mathfrak{g}$ the infinitesimal velocity generators in the Lie algebra, and $\mu \in \mathfrak{g}^*$ the associated momenta in the dual Lie algebra. Conservation of the energy function $H : \mathbb{R}^{2n} \to \mathbb{R}$ means that over a region $V \ni (z, \overline{z})$ bounded by ∂V in a symplectic phase space

$$\oint_{\partial V} H(z,\overline{z})\, d\overline{z} = \int \int_V \frac{\partial H}{\partial z} dz \wedge d\overline{z} = -\int \int_V \frac{\partial H}{\partial z} d\overline{z} \wedge dz = 0, \tag{4.45}$$

or upon collecting $d\overline{z}$ terms of and evaluating dz in the ξ direction

$$H = \int \frac{\partial H}{\partial z} \wedge dz = \int dz \wedge L_H = 0 \tag{4.46a}$$

$$dH = \xi \wedge L_H = 0. \tag{4.46b}$$

Here, the coordinate $\overline{z}$ is conjugate to z in the sense that dz and $d\overline{z}$ form the boundary ∂V of the volume element V [13], and the Legendre transform

$$L_H \cdot w = \frac{d}{dt} H\left(z + tw\right)\Big|_{t=0} = \frac{\partial H}{\partial z} \cdot w \tag{4.47}$$

denotes the increase of H in the direction w [106, 172]. Without loss of generality, we may associate $\xi \in \mathfrak{g}$ and $\mu \in \mathfrak{g}^*$, belonging to conjugate vector spaces, with dz and L_H so that the pairing (4.46b) becomes

$$dH = \langle \xi, \mu \rangle_\Omega = [\xi, \mu] \,, \tag{4.48}$$

where $\langle \cdot, \cdot \rangle_\Omega$ denotes the pairing under the canonical two-form (regarded as a map from $\mathfrak{g}^*$ to $\mathfrak{g}$ via the symplectic matrix $\begin{pmatrix} 0 & \mathbf{I} \\ -\mathbf{I} & 0 \end{pmatrix}$; see Materials and Methods section 4.4.1.1 and [172] ch. 2), and $[\cdot, \cdot]$ is the Lie bracket. The geometric intuition is that orthogonal velocities and momenta form the border of a region whose (directed) volume is the energy increment. Evaluation of dH in its direction of maximum increase means composing the increment vector with an orthogonal direction vector; maintaining level sets of H means the direction vector is parallel to the increment vector.

The condition $dH = 0$ is a constraint on the allowed pairings (ξ, μ) of infinitesimal translation in $\mathfrak{g}, \mathfrak{g}^*$. Consequently, momentum can be regarded as a function $\mu : G \times \mathbb{R} \to \mathfrak{g}^*$ defined on G for a given value of the energy (cf. [106]). Because $\xi = g'\Big|_{t=0}$ are the s-derivatives of $g = \exp \xi t$ at the identity, the variation of μ with s can be written

$$\mu'\Big|_{s=0} = \frac{d}{ds} \mu \left(g + g' s + \frac{1}{2} g'' s^2 + \cdots \right)\Big|_{s=0} = \frac{\partial \mu}{\partial g} \xi = \mathbf{X}_\xi \left(\mu \right) , \tag{4.49a}$$

or what is the same thing

$$\begin{aligned} \left(\mu_i \frac{\partial}{\partial g^i} \right)'\Big|_{s=0} &= \frac{\partial}{\partial s} \left(\mu_i \frac{\partial}{\partial g^i} \right) \left(g^j + \xi^j s + \cdots \right)\Big|_{s=0} = \frac{\partial \mu_i}{\partial g^j} \xi^j \frac{\partial}{\partial g^i} + \mu_i \xi^j \frac{\partial^2}{\partial g^j \partial g^i} \\ &= \xi^j \frac{\partial \mu_i}{\partial g^j} \frac{\partial}{\partial g^i} - \mu_i \frac{\partial \xi^j}{\partial g^i} \frac{\partial}{\partial g^j} = [\mathbf{X}_\xi, \mathbf{X}^\mu] \,, \end{aligned} \tag{4.49b}$$

where in the second line we have used Eq. (4.65) from Materials and Methods section 4.4.3.2. Here, $\mathbf{X}_\xi = \xi^i \frac{\partial}{\partial g^i}$ is the vector field corresponding the velocity vector ξ, and $\mathbf{X}^\mu = \mu_i \frac{\partial}{\partial g^i}$ is the corresponding covector field for μ. Eq. (4.49b) and the condition $\xi = g'\Big|_{t=0}$ are another version of Euler's equations (4.4), now in terms of vector fields; they may be supplemented with an applied torque field. Eq. (4.49a) is the equation for flow of a curve along a vector field (used in the Results section 4.2.4).

4.4.2 The connection one-form

This section expands the notion of free and constrained coordinates, introduced in section 4.2.2, to the more general scheme of vertical and horizontal coordinates, and shows how the latter are expressed using the connection one-form. See [32, 171] for more details.

Let $\mathcal{Q} \subseteq \mathbb{R}^n$ and $\mathcal{E} = \mathcal{Q} \times \mathcal{P} \subseteq \mathbb{R}^{2n}$ be two manifolds representing the base space and the configuration space of a kinematical system. The projection mapping $\pi : \mathcal{E} \to \mathcal{Q}$ from the full configuration space to the realized body coordinates induces a mapping π_* between the tangent spaces defined by $T\pi : T\mathcal{E} \to T\mathcal{Q}$. The kernel of π_* at a point $q \in \mathcal{Q}$ defines the elements $\xi \in \mathfrak{g}$ of the Lie algebra of (infinitesimal generators of) motions of the body that are tangent to the orbit of the actions $g \in G$ of the Lie group through q. The horizontal lift of a vector $u \in T\mathcal{Q}$ is the unique vector $v^{\mathrm{h}} = \operatorname{hor} u \in T\mathcal{E}$ satisfying $\pi_* (v^h) = u$. The vector v has a unique decomposition into a horizontal part $v^{\mathrm{h}} \in \mathcal{H} \subseteq T\mathcal{E}$ and a vertical part $v^{\mathrm{v}} = v - v^{\mathrm{h}} \in \mathcal{V} \subseteq T\mathcal{E}$. Because $T\pi (v^{\mathrm{v}}) = 0$, it is clear that only vertical vectors in $\mathcal{V}$ represent allowed motions of the body, whereas horizontal vectors in $\mathcal{H}$ specifically fail the constraints on the system. In this way, horizontal vectors v are defined by nonzero values of the *connection one-form* $\omega (v)$, which in (fixed-space) coordinates is written

$$\omega (q)\, dq = d\mathbf{r} + A (q)\, dt, \tag{4.50}$$

naturally partitioning a tangent vector into its free $d\mathbf{r}$ and constrained dt parts. The connection one-form ω operates on tangent vectors v_q at q and returns 0 if the sum of the free $ds \left(\frac{\partial}{\partial s}\right)$ and constrained $A dt \left(\frac{\partial}{\partial t}\right)$ parts of the local field $\left(\frac{\partial}{\partial s}, \frac{\partial}{\partial t}\right)$ vanishes.

The map $g' g^{-1} \to g' \to g^{-1} g'$ from fixed to body coordinates is well-known to be accomplished by applying the Adjoint map $T_g \operatorname{Ad}_{g^{-1}}$ in the tangent space at g to both sides of (4.50). For the particular space-time constraints introduced in (4.9a), it is clear that $A = -c \in \mathbb{R}^3$ (with units of dist. $\times$ time^{-1}). Now, let $d\mathbf{r} = g^{-1} g' = \xi$ be the body-coordinate representation of an element of $\mathfrak{g}$, which is naturally interpreted as an angular velocity. Let $T_g R_{g^{-1}} (v_t)$ be a fixed-coordinate representation of dt. Then the connection one-form

$$\omega (q)\, dq = T_g A d_g \xi - c T_g R_{g^{-1}} (v_t) =: d\lambda \tag{4.51}$$

describes the variation in the spatial delay (4.9a) of the allowed pairs $(d\mathbf{r}, dt)$; it is zero for a single front of the twist wave followed through space-time. But when the string is observed at a fixed time (say the present $t = 0$), the segments accumulate delay $d\lambda = \|d\mathbf{r}\| = ds$, with no translation in t. There must be a new constraint on $d\mathbf{r}$

to make the variation $d\lambda$ vanish. The most general one-form we can write to express this constraint is

$$\begin{aligned}\omega(q)\,dq &= T_g \operatorname{Ad}_g(\alpha dx + \beta dy + \gamma dz)\\ &= T_g \operatorname{Ad}_g[\alpha' ds \star (dy \wedge dz) + \beta' ds \star (dz \wedge dx) + \gamma' ds \star (dx \wedge dy)]\\ &= T_g \operatorname{Ad}_g \star(\Omega^\flat)\,ds = \operatorname{Ad}_g \boldsymbol{\Omega} ds. \end{aligned} \tag{4.52}$$

Here $\boldsymbol{\Omega} ds$ is the skew-symmetric matrix (again a one-form) corresponding to the two-form $\Omega^\flat(x_i, x_j) \sim dx^i \wedge dx^j$ via the Hodge $\star$ operator from k-forms to $(n-k)$-forms, and the $\flat$ operator from vectors to forms is defined in the sense that $\Omega^\flat(x_i, x_j)\, x^j = \Omega^\flat(x_i) = \omega_j^i x^j$ is a linear function over x_j (see [172] chs. 2 and 4). Equating the two pictures (4.51) and (4.52) ensures that the same twist wavefront is observed at the origin of time as in the present; the equality gives a condition for the permitted elements of $\mathfrak{g}$:

$$\begin{aligned} T_g \operatorname{Ad}_{g^{-1}}(\omega(q))\,dq =& \xi - cT_g \operatorname{Ad}_{g^{-1}} R_{g^{-1}}(v_t) = \boldsymbol{\Omega} ds\\ \Longrightarrow\ \xi =& \boldsymbol{\Omega} ds + cT_g L_{g^{-1}}(v_t), \end{aligned} \tag{4.10a}$$

or equivalently

$$\xi = \begin{pmatrix} \boldsymbol{\Omega} ds & cT_g L_{g^{-1}}(v_t) \\ 0 & 0 \end{pmatrix}. \tag{4.10b}$$

Using the fact that $\xi = g^{-1} g'$, we can left-multiply (4.10) by g and integrate over s to solve for the path of the group variables in the configuration space. Because $\mathfrak{se}(3) = \mathfrak{so}(3) \times \mathbb{R}^3$ is a direct product space, integration is performed on the rotations and translations separately. Since rotations $h \in \mathfrak{so}(3)$ satisfy

$$h'(s) = \lim_{ds \to 0} \frac{h(s+ds) - h(s)}{ds} = h(s)\,\boldsymbol{\Omega}(s), \tag{4.54}$$

we can use the fact that

$$h'(s)\,ds = h(s)\,(\mathbf{I} + \boldsymbol{\Omega}(s)\,ds - \mathbf{I}) \approx h(s) \exp(\boldsymbol{\Omega}(s)\,ds) - h(s) \tag{4.55}$$

to write

$$h(s+ds) \approx h(s) + h'(s)\,ds = h(s) \exp(\boldsymbol{\Omega}(s)\,ds). \tag{4.56}$$

Let $\mathbf{X}_t(g)$ be the vector field at g of translation in time at time t, defined in the sense that $\mathbf{X}_t(g)(p) = v_t$ for a curve $g(t) \in G$ parametrized in time. Then the left action of g on $\mathfrak{g}$ in Eqs. (4.10) is found by the chain rule (see [172] ch. 9) to be

$$\begin{aligned} v_0 &= T_e L_e \mathbf{X}_0(e)(p) = T_e L_{g^{-1}} L_g \mathbf{X}_t(e)(p)\\ &= T_g L_{g^{-1}}(T_e L_g \mathbf{X}_t(e))(g \circ p) = T_g L_{g^{-1}} \mathbf{X}_t(g)(g \circ p) = T_g L_{g^{-1}} v_t, \end{aligned} \tag{4.57}$$

showing that the time-translation vector field is invariant as time increases. Then we may replace $T_g L_{g^{-1}} v_t$ with v_0 in Eqs. (4.10). By letting $g \to e$ at the origin of time in Eqs. (4.10) and recognizing that $d\mathbf{r}$ is an infinitesimal translation in $\mathbb{R}^3$ along the space curve $\mathbf{r}(s)$, viz.

$$\xi = \boldsymbol{\Omega}(t) + cT_g L_{g^{-1}} v_t \xrightarrow{t\to 0} d\mathbf{r} = 0 + cv_0, \tag{4.58}$$

it is further possible to replace $T_g L_{g^{-1}} v_t$ with $\frac{1}{c} d\mathbf{r}$. Altogether, substituting Eqs. (4.56) and (4.58) in (4.10) and integrating each term give for an element $g \in \mathfrak{se}(3)$,

$$g(s + ds) = h(s) \exp(\boldsymbol{\Omega}(s)\, ds) + \mathbf{r}(s), \tag{4.11a}$$

or equivalently

$$g(s + ds) = \begin{pmatrix} h(s) \exp(\boldsymbol{\Omega}(s)\, ds) & \mathbf{r}(s) \\ 0 & 1 \end{pmatrix}. \tag{4.11b}$$

4.4.3 Sending vector fields between manifolds

4.4.3.1 *Force equilibrium*

A model of force equilibration was introduced in section 4.2.4. Suppose that compressive forces push on the ends of a string of length L starting at time $t_0 < 0$ (Figure 4.4A). Let a *segment* of a string be an infinitesimal piece of length dL. A contiguous region of segments of length dL define a *section* of length ΔL. The following is a characterization of the condition that such a string be in force equilibrium after a finite time.

At a time $t_0 < 0$, the section $\left(\frac{L}{2} - (n-1)\, dL, \frac{L}{2}\right)$ containing n segments pushes against the equally sized section $\left(\frac{L}{2}, \frac{L}{2} + (n-1)\, dL\right)$ to its right; the integer n is also proportional to the strength of the applied force. In the figure, stresses between segments are indicated by red lines, whereas unstressed segments are connected to themselves in blue. Segments in the *interior* sections $\left(\frac{L}{2} - \frac{n-1}{2} dL, \frac{L}{2}\right)$ and $\left(\frac{L}{2}, \frac{L}{2} + \frac{n-1}{2} dL\right)$ are opposed by sections to the right and left, respectively, but segments in the *exterior* sections $\left(\frac{L}{2} - (n-1)\, dL, \frac{L}{2} - \frac{n-1}{2} dL\right)$ and $\left(\frac{L}{2} + \frac{n-1}{2} dL, \frac{L}{2} + (n-1)\, dL\right)$ are not opposed by an equal number of segments in $\left(\frac{L}{2} - \frac{3(n-1)}{2} dL, \frac{L}{2} - (n-1)\, dL\right)$ on the left and $\left(\frac{L}{2} + \frac{n-1}{2} dL, \frac{L}{2} + \frac{3(n-1)}{2} dL\right)$ on the right, respectively. Thus, by Newton's third law, the latter segments must push back on the exterior segments in the subsequent time step.

Precisely, let the length be defined by $L = 2^m \times 2N$, with N half the number of sections and $n = 2^m$ the number of segments per section before any force

has been applied, also proportional to the ultimate strength of the force. The the interval permutation function is

$$\sigma_k\left(\mathcal{I}_i \mid k\right) = \begin{cases} \overline{\mathcal{I}_i} & \text{if } i \in [N-k, N+k+1] \\ \mathcal{I}_i & \text{else,} \end{cases} \tag{4.60}$$

where $\overline{\mathcal{I}}$ is the association $j \leftrightarrow 2^{m-k} - j$, indexed by k, among the elements of $\mathcal{I}$.

The process of pushing out continues, with the number of sections involved at time step $k+1$ satisfying the recursion $a_{k+1} = 2a_k + 2$, and the number of *interfaces* equal to $\frac{a_{k+1}}{2}$, beginning with $a_1 = 2$. This is understood from Figure 4.4A where interfaces are represented by intersections of the stress lines. The number ν of segments in each section at step $k+1$ is $\frac{n}{2^k} = 2^{m-k}$. Equilibrium is reached as $\nu \to 1$ when the number of right-pushing and left-pushing segments in any section are equal; it occurs at time $t = 0$.

4.4.3.2 *Push forward, pull back, and the Lie derivative*

Here we use the language of manifolds to represent forces on strings as vector fields, as introduced in section 4.2.4. Vector fields map spatial points to the tangent vectors of the curve through them. The advantage of a vector field formulation of twisting and bending is that it facilitates combining forces by the Lie bracket of their representative fields. End shortening will be represented by $\mathbf{B}$ and twist by $\mathbf{A}$.

In general, flow (see Eq. (4.15)) of a vector field $\mathbf{B}$ along $\mathbf{A}$ may change $\mathbf{B}$. In coordinates, the vector field $\mathbf{B}$ on a manifold $\mathcal{M}$ is $b^j \frac{\partial}{\partial z^j}$. If $\mathcal{M}$ is the configuration space of a section of the string, then the map $\Phi : \mathcal{M} \to \mathcal{N}$ transforms the section by changing its history (Figure 4.4B). If there has been no propagation ($c = 0$), then $\mathcal{M}$ is the section containing point z, whereas in the presence of a force ($c \neq 0$), z becomes $\Phi(z) \in \mathcal{N}$ through a spatial shift λ. The path $\Phi = \Phi^t_{\mathbf{A}+\mathbf{B}} \circ \Phi^{-t}_{\mathbf{A}}$ represents undoing spiraling and then applying spiral strain in the presence of end-shortening.

By the change-of-variables theorem for vector fields [128], one writes $\mathbf{B}$ on $\mathcal{M}$ as

$$\mathbf{B} = b^i(z)\frac{\partial}{\partial z^j} = \frac{d\left(\Phi \circ z\right)^i}{dz^j} b^j(z) \frac{\partial}{\partial\left(\Phi \circ z\right)^i} = D\Phi \cdot \mathbf{B}_\Phi. \tag{4.61}$$

The new field acts on coordinates $\Phi \circ z$ of $\mathcal{N}$ as

$$\mathbf{B}_\Phi(\Phi\circ) = D\Phi^{-1} \cdot \mathbf{B}(\Phi\circ) = D\Phi^{-1} \cdot b^j(\Phi\circ) \frac{\partial}{\partial\left(\Phi \circ z\right)^i}(\Phi\circ) =: \Phi^* \mathbf{B}, \tag{4.62}$$

where the map $\Phi^* : T\mathcal{N} \to T\mathcal{M}$ between tangent spaces is the *pull back* [172], so defined because the "advanced" vector field $\mathbf{B}_\Phi$ on $\mathcal{N}$ is brought back to $\mathcal{M}$ as a new vector field $\Phi^*\mathbf{B}$. If $\mathbf{B}_\Phi = \Phi_*\mathbf{B}$ is the push forward of $\mathbf{B}$ onto $\mathcal{N}$ (cf. Eq. (4.16)), then it is clear that

$$\Phi_*\Phi^*\mathbf{B} = D\Phi \cdot \Phi^*\mathbf{B} \circ \Phi^{-1} = D\Phi \cdot D\Phi^{-1} \cdot \mathbf{B}\left(\Phi^{-1} \circ \Phi\right) = \mathbf{B}, \tag{4.63}$$

showing that the pull back is the inverse of the push forward, and vice versa. As a result $\mathbf{B}$ sends points in different directions on $\mathcal{M}$ and $\mathcal{N}$ (Figure 4.4B). The differential D denotes the Jacobean matrix $D\Phi = \frac{d\Phi(z)}{dz} = \Phi$, reflecting the fact that Φ is the exponential map $\exp(\mathbf{X}t) = \mathbf{I} + t\mathbf{X} + t^2\frac{1}{2!}\mathbf{X} \circ \mathbf{X} + \cdots$ for matrix operators (cf. [172] ch. 9.1).

The *Lie derivative* $\mathcal{L}_\mathbf{X}\mathbf{B}$ of $\mathbf{B}$ along $\mathbf{X}$ is [172, 255]

$$\mathcal{L}_\mathbf{X}\mathbf{B} = \lim_{t\to 0}\frac{1}{t}\left(\Phi_*\mathbf{B} - \mathbf{B}\right)\Big|_{t=0} = \frac{d}{dt}D\Phi \circ \mathbf{B} \circ \Phi^{-1}\Big|_{t=0}. \tag{4.64}$$

By pushing $\mathbf{B}$ on $\mathcal{M}$ forward onto an ever-closer manifold $\mathcal{N}$ in the direction of $\mathbf{X}$, Eq. (4.64) gives the first order change in $\mathbf{B}$ along $\mathbf{X}$; it may be written $[\mathbf{X}, \mathbf{B}] = \mathbf{X} \circ \mathbf{B} - \mathbf{B} \circ \mathbf{X}$. Another way to get the result that the Lie derivative is represented by the *Lie brackets* is to assume that $\mathbf{X} = a^i(z)\frac{\partial}{\partial z^i} \approx a^i\frac{\partial}{\partial z^i}$ is approximately constant over a small ball containing z. Taking the derivative of $\mathbf{X}$ (still assuming it to be constant) with respect to z^j then gives that $\frac{\partial a^i}{\partial z^j}\frac{\partial}{\partial z^i} = -a^i\frac{\partial^2}{\partial z^j z^i}$ (see [255] ch. 5). Regarding $\mathbf{B} = b^i(z)\frac{\partial}{\partial z^i}$ as a function f of z, we may substitute into the definition $\mathcal{L}_\mathbf{X} f = \mathbf{X}(f)$ of the derivative of f in the direction of $\mathbf{X}$ to find that

$$\begin{aligned}\mathcal{L}_\mathbf{X}\mathbf{B}(z) =& \left(\mathcal{L}_\mathbf{X} b^j(z)\right)\frac{\partial}{\partial z^i} + b^j(z)\left(\mathcal{L}_\mathbf{X}\frac{\partial}{\partial z^i}\right) \\ =& a^i\frac{\partial b^j}{\partial z^i}\frac{\partial}{\partial z^j} + a^i b^j\frac{\partial^2}{\partial z^i z^j} = a^i\frac{\partial b^j}{\partial z^i}\frac{\partial}{\partial z^j} - b^j\frac{\partial a^i}{\partial z^j}\frac{\partial}{\partial z^i} \\ =& \mathbf{X} \circ \mathbf{B}(z) - \mathbf{B} \circ \mathbf{X}(z) = [\mathbf{X}, \mathbf{B}](z),\end{aligned} \tag{4.65}$$

so that a vector field applied to a function is the (negative) Lie bracket of that field and the field representing function's derivative. Together, Eqs. (4.64) and (4.65) show that the direction $\mathbf{B}$ takes when made to flow along $\mathbf{X}$ is the difference between its direction after flowing on $\mathbf{X}$, and what it would have been had the points only travelled on $\mathbf{X}$. In general, the difference in the paths is not zero, and we have a new controllable direction on the manifold.

4.4.3.3 *The Zassenhaus expansion*

This section explains the Zassenhaus expansion, introduced in section 4.4 for approximating the angular velocity matrix at points distant from the origin of a force. The higher order derivatives of the Adjoint action of $SO(3)$ on its Lie algebra $\mathfrak{so}(3)$ are shown to approximate the motion in $\mathfrak{se}(3) \times \mathbb{R}^3 = \mathfrak{so}(3) \times \mathbb{R}^3 \times \mathbb{R}^3$.

The manifolds $\mathcal{M} \ni s$ and $\mathcal{N} \ni s_0$ are connected via the space-time constrains (4.9). Undo spiral strain $\mathbf{A}$ for time $-\Delta t$ and apply bending strain $\mathbf{B}$ in the presence of $\mathbf{A}$ for Δt to get that the transformation from $\mathcal{M}$ to $\mathcal{N}$ is $\Phi = \Phi^{\Delta t}_{\mathbf{A}+\mathbf{B}} \circ \Phi^{-\Delta t}_{\mathbf{A}}$ (see Figure 4.4B and C). The flow $\Phi^{\Delta t}_{\mathbf{A}+\mathbf{B}}$ must at every instant satisfy the n-fold iterates of differential equation (4.15). If the path may be divided into n equally-sized segments as

$$\exp\{(\mathbf{A}+\mathbf{B})\,\Delta t\} = \exp\left(\mathbf{C}_n \Delta t^n\right) \circ \cdots \circ \exp\left(\mathbf{C}_2 \Delta t^2\right) \circ \exp\left(\mathbf{B}\Delta t\right) \circ \exp\left(\mathbf{A}\Delta t\right), \tag{4.66}$$

then the derivatives of $\mathbf{A}+\mathbf{B}$ along $\mathbf{A}$ at the i^{th} step must equal the derivatives of the i^{th} term on the r.h.s (indexing the $\mathbf{A}$ term as $i=0$ and $\mathbf{B}$ as $i=1$). At $\Delta t = 0$, the only remaining term is

$$\mathbf{B}^{(i-1)} = i!\mathbf{C}_i. \tag{4.67}$$

Notice that there is no $\mathbf{A}$ term because the Lie derivative of $\mathbf{A}$ along itself is 0. We lose no generality in taking the propagation velocity c to be unity and replacing the time shift Δt with its attendant spatial shift $\Delta s = s - s_0$. We then have that the flow Φ along the propagated force field is

$$\begin{aligned}&\exp\{(\mathbf{A}+\mathbf{B})\,\Delta t\} \circ \exp\left(-\mathbf{A}\Delta t\right)\\ &\quad = \exp\left(\mathbf{B}^{(n)}\frac{(s-s_0)^n}{n!}\right) \circ \cdots \circ \exp\left(\mathbf{B}'\frac{(s-s_0)^2}{2!}\right) \circ \exp\left(\mathbf{B}\,(s-s_0)\right).\end{aligned} \tag{4.68}$$

This result relates the flow Φ to the changes in the generator $\mathbf{B}$, which are multiplied instead of added as in a usual Taylor series. The logarithm of this quantity is used to derive the approximation (4.19) for the angular velocities in the semidirect product group from those in $\mathfrak{so}(3)$.

To calculate the coefficient $\mathbf{B}'$ in (4.68), we need to know how $\mathbf{A}+\mathbf{B}$ changes along the path $\Phi = \Phi^{\Delta t}_{\mathbf{A}+\mathbf{B}} \circ \Phi^{-\Delta t}_{\mathbf{A}}$ as $\Delta t \to 0$. In the sequel we replace $\Delta t \mapsto t$ because there is no notion of absolute time. By the product rule we evaluate

the Lie derivative as

$$\begin{aligned}
\mathcal{L}_{\mathbf{A}+\mathbf{B}}\mathcal{L}_{\mathbf{A}^{-1}}(\mathbf{A}+\mathbf{B}) &= \frac{d}{dt} D\Phi^t_{\mathbf{A}+\mathbf{B}} \cdot D\Phi^{-t}_{\mathbf{A}} \cdot (\mathbf{A}+\mathbf{B}) \circ \Phi^t_{\mathbf{A}} \circ \Phi^{-t}_{\mathbf{A}+\mathbf{B}}\Big|_{t=0} \\
&= \frac{d}{dt} \Phi^t_{\mathbf{A}+\mathbf{B}} \circ \Phi^{-t}_{\mathbf{A}} \circ (\mathbf{A}+\mathbf{B}) \circ \Phi^t_{\mathbf{A}} \circ \Phi^{-t}_{\mathbf{A}+\mathbf{B}}\Big|_{t=0} \\
&= \big((\mathbf{A}+\mathbf{B}) \cdot \Phi^t_{\mathbf{A}+\mathbf{B}} \circ \Phi^{-t}_{\mathbf{A}} \circ (\mathbf{A}+\mathbf{B}) \circ \Phi^t_{\mathbf{A}} \circ \Phi^{-t}_{\mathbf{A}+\mathbf{B}} \\
&\quad - \Phi^t_{\mathbf{A}+\mathbf{B}} \circ \mathbf{A} \cdot \Phi^{-t}_{\mathbf{A}} \circ (\mathbf{A}+\mathbf{B}) \circ \Phi^t_{\mathbf{A}} \circ \Phi^{-t}_{\mathbf{A}+\mathbf{B}} \\
&\quad + \Phi^t_{\mathbf{A}+\mathbf{B}} \circ \Phi^{-t}_{\mathbf{A}} \circ (\mathbf{A}+\mathbf{B}) \circ \mathbf{A} \cdot \Phi^t_{\mathbf{A}} \circ \Phi^{-t}_{\mathbf{A}+\mathbf{B}} \\
&\quad - \Phi^t_{\mathbf{A}+\mathbf{B}} \circ \Phi^{-t}_{\mathbf{A}} \circ (\mathbf{A}+\mathbf{B}) \circ \Phi^t_{\mathbf{A}} \circ (\mathbf{A}+\mathbf{B}) \cdot \Phi^{-t}_{\mathbf{A}+\mathbf{B}}\big)\Big|_{t=0} \\
&= (\mathbf{A}+\mathbf{B}) \circ (\mathbf{A}+\mathbf{B}) - \mathbf{A} \circ (\mathbf{A}+\mathbf{B}) \\
&\quad + (\mathbf{A}+\mathbf{B}) \circ \mathbf{A} - (\mathbf{A}+\mathbf{B}) \circ (\mathbf{A}+\mathbf{B}) \\
&= [\mathbf{B}, \mathbf{A}]\,. \qquad (4.69)
\end{aligned}$$

Under the association $\mathbf{X} = a^i \frac{\partial}{\partial x^i} \mapsto a^i \mapsto \widehat{X}$ under the hat map (4.1), the Lie bracket $[\cdot,\cdot]$ becomes the matrix commutator. Observe that the same result is obtained by replacing $\mathbf{A}+\mathbf{B} \mapsto \mathbf{B}$. Thus to a first approximation the direction of $\mathbf{B}$ at two points s and s_0 exposed to end-shortening for different amounts of time differ by $(s-s_0)[\mathbf{B},\mathbf{A}]$. In a similar fashion one can evaluate the second derivative

$$\frac{d^2}{dt^2} D\Phi^t_{\mathbf{B}} \cdot D\Phi^{-t}_{\mathbf{A}} \cdot \mathbf{B} \circ \Phi^t_{\mathbf{A}} \circ \Phi^{-t}_{\mathbf{B}}\Big|_{t=0} = [\mathbf{A},[\mathbf{A},\mathbf{B}]] - 2[\mathbf{B},[\mathbf{A},\mathbf{B}]]\,. \qquad (4.70)$$

The operation $e^{\mathbf{X}t} \cdot \mathbf{B} \cdot e^{-\mathbf{X}t}$ is known as the capital Adjoint $\mathrm{Ad}_{\exp \mathbf{X}t}\mathbf{B}$, and its derivative at the identity $t=0$ is well known to be the lower-case adjoint $\mathrm{ad}_{\mathbf{X}}\mathbf{B} = [\mathbf{X},\mathbf{B}]$. Then using the fact that the n^{th} iterate of the product rule is $(fg)^{(n)} = \sum_k \binom{n}{k} f^{(n-k)} g^{(k)}$, and that composition $\circ$ is the same as multiplication for matrix operators, we find that the n^{th} Zassenhaus coefficient is

$$\mathbf{B}^{(n)} = \frac{d^n}{dt^n} \mathrm{Ad}_{\exp \mathbf{B}t} \circ \mathrm{Ad}_{\exp -\mathbf{A}t} \circ \mathbf{B}\Big|_{t=0} = \sum_{k=0}^{n} \binom{n}{k} (-1)^k \,\mathrm{ad}^{n-k}_{\mathbf{B}} \circ \mathrm{ad}^k_{\mathbf{A}} \circ \mathbf{B}, \qquad (4.18)$$

after mapping back to vector fields by inverting the hat map. This may also be seen directly in terms of vector fields by noting that if

$$\mathrm{Ad}_{\exp \mathbf{X}t} \circ \mathbf{B} = \sum_k \frac{1}{k!} \,\mathrm{ad}^k_{\mathbf{X}} \circ \mathbf{B} t^k \qquad (4.71a)$$

holds for a single element $g = \exp \mathbf{X}t$ (cf. [145] ch. 2.9 and [297]), then the n^{th} term of the expansion $\mathrm{Ad}_h \circ \mathrm{Ad}_g$ for a second operator $h = \exp \mathbf{Y}t$

$$\begin{aligned}\mathrm{Ad}_{\exp \mathbf{Y}t} \circ \mathrm{Ad}_{\exp \mathbf{X}t} \circ \mathbf{B} &= \mathrm{Ad}_{\exp \mathbf{Y}t} \circ \sum_k \frac{1}{k!} \mathrm{ad}_{\mathbf{X}}^k \circ \mathbf{B} \\ &= \sum_{n-k} \frac{1}{(n-k)!} \mathrm{ad}_{\mathbf{Y}}^{n-k} \circ \sum_k \frac{1}{k!} \mathrm{ad}_{\mathbf{X}}^k \circ \mathbf{B} t^k t^{n-k} \\ &= \sum_n \sum_k \frac{1}{n!} \frac{n!}{(n-k)!k!} \mathrm{ad}_{\mathbf{Y}}^{n-k} \circ \mathrm{ad}_{\mathbf{X}}^k \circ \mathbf{B} t^n \end{aligned} \tag{4.71b}$$

is the only surviving term when taking the n^{th} derivative at $t = 0$, recovering Eq. (4.18) when $\mathbf{Y} = \mathbf{B}$ and $\mathbf{X} = -\mathbf{A}$. Eq. (4.18) is in agreement with Eqs. (4.69) and (4.70); together with Eq. (4.68), it specifies how a force field $\mathbf{B}$ propagates in space and time.

4.4.4 The transcription rate tensor

This section shows how derive the relationships between the tensor quantities in section 4.2.5, and clarifies the precise meanings of upper and lower indices.

Let the spatial rate of RNAP transfer out of locus i to all other loci j be expressed by the covector

$$X_i = x_j \kappa_i^j, \tag{4.20a}$$

with units of RNAP × dist.$^{-1}$. Lower indices denote the contravariant components of a vector relative to a covariant (row) basis, and upper indices the covariant components relative to a contravariant (column) basis [79]. Although outflow of spent RNAP from i measures its own turnover rate there, inflow of fresh RNAP measures the local transcription rate. As transcription at each of the loci have different efficiencies, the rate at locus i may be expressed

$$Z^i = \kappa_j^i \mathbb{I}^{jk} \mathbb{I}_{kl} z^l, \tag{4.20b}$$

with units of trans. × dist.$^{-1}$; the sum is over diagonal indices in corresponding positions. The quantity $\mathbb{I}_{kl}$ = RNAP × trans.$^{-1}$ is a cost function that measures the worth in RNAP at k of one transcript from l; the reciprocal $\mathbb{I}^{jk}$ = RNAP^{-1} × trans. expresses the number of transcripts at j resulting from the transfer of a single unit of RNAP from k. The product $\mathbb{J}_j^i = \mathbb{I}^{ik}\mathbb{I}_{kj}$ $(= \mathbb{I}_{jk}\mathbb{I}^{ki})$ is a unitless conversion matrix giving the worth of transcripts (amount of RNAP) from j at locus i in terms of transcripts (RNAP) produced at i (j) by a single unit of RNAP (transcript) freed from j (i); it is singular because if 1 transcript at i is worth α transcripts of j and β of k, then j is worth α^{-1} of i and $\alpha^{-1}\beta$ of k, showing that the j^{th} row of $\mathbb{J}_j^i$ is the i^{th} row multiplied by a constant.

The contrasting perspectives for RNAP and transcripts require X_i to be a row vector, and Z^i a column; the relationship between them is assumed to be

$$x_i = \mathbb{I}_{ij} z^j, \tag{4.21}$$

as the RNAP freed from j is not converted back to transcripts. Although $\mathbb{I}_{ij}$ looks like a matrix, it is actually a double covariant tensor (being the contravariant components of a covariant basis) that turns the column vector z^j into a row. When the two-form $\mathbb{I}(z)(w)$ is regarded as a function over the second second vector input, the matrix of the linear operator $\mathbb{I}(z)$ must be interpreted as sending contravariant basis vectors e_i (columns) to covariant ones e^i (rows) by transposition, making the mapping the transpose $(\mathbb{I}_{ij})^T = \mathbb{I}^i_j$ of the tensor [172]. The tensor index conventions $\mathbb{T}^{\text{row}}_{\text{col}} = \mathbb{T}^{\text{to}}_{\text{from}}$ and $\mathbb{T}_{\text{to,from}}$ make precise the notion of reversed transfer from transcripts to RNAP:

$$\begin{aligned}
\mathbb{I}_{ij} z^j &= \begin{pmatrix} \mathbb{I}_{11} & \mathbb{I}_{12} & \mathbb{I}_{13} \end{pmatrix} \begin{pmatrix} \mathbb{I}_{21} & \mathbb{I}_{22} & \mathbb{I}_{32} \end{pmatrix} \begin{pmatrix} \mathbb{I}_{31} & \mathbb{I}_{32} & \mathbb{I}_{33} \end{pmatrix} \begin{pmatrix} z^1 \\ z^2 \\ z^3 \end{pmatrix} = z^j (\mathbb{I}_{ij})^T \\
&= z^j \mathbb{I}^i_j = \begin{pmatrix} z^1 & z^2 & z^3 \end{pmatrix} \begin{pmatrix} \mathbb{I}^1_1 & \mathbb{I}^1_2 & \mathbb{I}^1_3 \\ \mathbb{I}^2_1 & \mathbb{I}^2_2 & \mathbb{I}^2_3 \\ \mathbb{I}^3_1 & \mathbb{I}^3_2 & \mathbb{I}^3_3 \end{pmatrix} := \begin{pmatrix} y^1 & y^2 & y^3 \end{pmatrix} = y^i,
\end{aligned} \tag{4.72}$$

which is a vector that acts on the covector x_i from the left instead of the right. Therefore, the transpose is associated with reversal of RNAP flow.

One obtains the relationship (4.22) between the transcription and RNAP allocation rates in the following way. From Eqs. (4.20a) and (4.21) it follows that

$$X_i = x_j \kappa^j_i = \mathbb{I}_{jl} z^l \kappa^j_i = \mathbb{I}_{jl} \left(\mathbb{I}^{lk} \mathbb{I}_{kn} z^n \right) \kappa^j_i = \mathbb{J}^k_j Z^j \mathbb{I}_{ki} = Z^j \mathbb{I}_{ji}, \tag{4.73}$$

where the fourth equality follows by multiplying Eq. (4.20b) for $Z^j = \kappa^j_i \mathbb{I}^{ik} \mathbb{I}_{kn} z^n$ by $\mathbb{I}_{ki}$ and using the fact that the $\mathbb{I}_{ki} \mathbb{I}^{ik} = 1$ for transfer of RNAP away from and back to locus k. Note also that in the last equality $\mathbb{J}^k_j$ acts on $\mathbb{I}_{ki}$, a quantity in terms of RNAP amounts; we do not have to assume it operates directly on the transcription rate Z^j. In a diagonal basis we recover the single-index convention with $\mathbb{I}_{ii} \to \mathbb{I}_i$ being the conversion of transcripts to RNAP at locus i to produce a single transcript of gene i. The case in which diagonalization is not possible corresponds to the one of gene-gene regulation: transcripts at locus j affects transcription at locus i by transfer of RNAP via the off-diagonal components of $\mathbb{I}_{ij}$.

4.5. Supplementary Information

4.5.1 The inflectional elastica

The shapes of the inextensible rod that can be maintained with terminal forces and bending moments alone are solution to Euler's problem of the elastica. When restricted to the plane, the elastica has curvature in the amount $\kappa = \kappa_2$ projected along the principal binormal, and no axial curvature. This section describes how to find the solution curve using elliptic integrals. The curve can be differentiated twice to find the angular velocity, which interacts with axial twist. The development follows [28, 272]; additional information can be found in [65, 200] regarding the elastica, or [242] ch. 9 regarding moment balance. The curve will be localized in the xz plane, and the Euler angle θ will define the inclination of the tangent vector relative to the fixed z axis.

The elastica is said to be *inflectional* or *non-inflectional* depending on whether or not the bending moment $\frac{\partial\theta}{\partial s}$ vanishes at any point along s, including the endpoints. At such points, the graph $x(z)$ has an inflection point separating regions of positive curvature (opening down, toward positive x in our schemes, see footnote 1) and negative curvature (opening up). Inflections occurring at the end points indicate vanishing of the bending moments and hence of the applied torque. However, the angle $\theta(0) = \alpha$ need not be zero at the inflections, and it may be written in the form

$$p = \sin\left(\frac{\alpha}{2}\right). \tag{4.74}$$

Elasticas with non-vanishing end moments must be maintained by torques as well as tensions; they are not considered here.

It is initially assumed that a string of length L lies along the fixed z axis. As the ends at $s = 0$ and $s = L$ are brought together due to a compressive force, the string deforms in the xz plane. The components of the compressive force $\mathbf{F}$ parallel and perpendicular to the z axis are $F\cos(\theta)$ and $F\sin(\theta)$. The Bernoulli relationship between the curvature and (magnitude of) the bending moment $\mathbf{M}$ for shapes localized to the xz plane is

$$M = E\mathbb{I}_2\frac{d\theta}{ds}, \tag{4.75}$$

so that positive curvature is supported by a counterclockwise moment (a vector pointing to positive y) at the $s = 0$ face. The Young's modulus E has units of force $\times$ dist.$^{-2}$, while the second moment of area in the y direction

$$\mathbb{I}_2 = \frac{1}{\rho_0}\int_\Sigma \rho(x,z)\, x(s)\, z(s)\, dxdz \tag{4.76}$$

has units of dist.[4] Here, $\frac{\rho(x,y)}{\rho_0}$ is the unitless mass density, which is unity when mass is equally distributed over face Σ. Then the moment (4.75) is measured in force $\times$ dist. Opposing (4.75) is the end force $\mathbf{F}$ acting perpendicular to a cross sectional face Σ of area $A(s)$ with lever arm x measured from an inflection point at $s = 0$; its moment, assuming a constant area $A(s) = A$ is

$$x\frac{F}{A} = xT \tag{4.77}$$

where $T > 0$ is the pressure exerted by $\mathbf{F}$ on the xy cross section at s. Vanishing of the differential of the two moments (4.75) and (4.77) across a small section ds of the rod implies

$$\begin{aligned} M &= E\mathbb{I}_2\frac{d\theta}{ds} + xT \\ \frac{dM}{ds} &= E\mathbb{I}_2\frac{d^2\theta}{ds^2} + T\sin(\theta) = 0 \\ \theta''(s) &= -\lambda^2\sin(\theta(s)), \end{aligned} \tag{4.78}$$

where $\lambda = \sqrt{\frac{T}{E\mathbb{I}_2}}$ is an adjustable parameter, and $\frac{dx}{ds} = \sin\theta$. Eq. (4.78) is the governing differential equation for the elastica with height profile $x(z)$.

To integrate (4.78), observe that $\frac{1}{2}\frac{d}{ds}(\theta')^2 = \theta'\theta''$. Multiplication by the integrating factor θ' gives

$$\frac{1}{2}\left(\frac{d\theta}{ds}\right)^2 = \int -\lambda^2\sin(\theta(z))\frac{d\theta}{ds}ds = -\lambda^2\cos\theta + C, \tag{4.79}$$

wherein the initial conditions $\theta(0) = \alpha$ and $\theta'(0) = 0$ give $C = \lambda^2\cos\alpha$. The length of the string is thus constrained to be

$$\begin{aligned} L = \int_0^L ds &= \int_0^L \frac{d\theta}{\sqrt{2}\lambda\sqrt{\cos\theta - \cos\alpha}} = \int_{\theta(0)}^{\theta(L)} \frac{d\theta}{2\lambda\sqrt{\sin^2\frac{\alpha}{2} - \sin^2\frac{\theta}{2}}} \\ &= \frac{1}{2\lambda}\int_{\theta(0)}^{\theta(L)} \frac{d\theta}{p\sqrt{1-\sin^2(\phi)}} = \frac{1}{2\lambda}\int_{\theta(0)}^{\theta(L)} \frac{d\theta}{p\cos\phi}, \end{aligned} \tag{4.80}$$

where the quantities

$$\sin\frac{\theta}{2} =: \sin\left(\frac{\alpha}{2}\right)\sin\phi =: p\sin\phi \tag{4.81a}$$

and

$$\frac{d\theta}{d\phi} = \frac{2p\cos\phi}{\cos\left(\frac{\theta}{2}\right)} = \frac{2p\cos\phi}{\sqrt{1-\sin^2\left(\frac{\theta}{2}\right)}} = \frac{2p\cos\phi}{\sqrt{1-p^2\sin^2\phi}} \tag{4.81b}$$

have been introduced using p as defined in (4.74) above.[2] N.B.: ϕ is *not* the Euler angle of the same name, but the elliptic amplitude, defined below. Substituting (4.81b) into (4.80) and evaluating at an intermediate arc length s gives

$$s = \frac{1}{\lambda}\int_{\phi(\theta(0))}^{\phi(\theta(s))} \frac{d\phi}{p\cos\phi}\frac{d\theta}{d\phi} = \frac{1}{\lambda}\int_{\phi(\theta(0))}^{\phi(\theta(s))} \frac{d\phi}{\sqrt{1-p^2\sin^2\phi}}. \tag{4.82}$$

The lower limit $\phi(0)$ is found from the condition $\sin\frac{\theta(0)}{2} = \sin\frac{\alpha}{2} = p\sin\phi(0) = p$, which implies $\phi(0) = \frac{\pi}{2} + 2n\pi$. Separation of the integral shows that

$$\begin{aligned}
\lambda s &= -\int_0^{\frac{\pi}{2}} \frac{d\phi}{\sqrt{1-p^2\sin^2\phi}} + \int_0^{\phi(\theta(s))} \frac{d\phi}{\sqrt{1-p^2\sin^2\phi}} \\
&= -\mathcal{K}(p) + \mathcal{K}(\phi(s)\,|\,p) \\
\lambda s + \mathcal{K}(p) &= \int_0^{\phi} \frac{dt}{\sqrt{1-p^2\sin^2 t}},
\end{aligned} \tag{4.83}$$

where we have introduced $\mathcal{K}(p) = \mathcal{K}\left(\frac{\pi}{2}\,|\,p\right)$ for the (complete) elliptic integral of the first kind, also known as the elliptic quarter period. The angle

$$\phi = \mathrm{am}\left\{\lambda s + \mathcal{K}(p)\,|\,p\right\} \tag{4.84}$$

is defined as the *amplitude* of the dimensionless arc length $\lambda s + \mathcal{K}(p)$ via the Jacobi elliptic functions

$$\sin\left(\mathrm{am}\left\{\lambda s + \mathcal{K}(p)\,|\,p\right\}\right) = \mathrm{sn}\left(\lambda s + \mathcal{K}(p)\,|\,p\right) \tag{4.85a}$$

$$\cos\left(\mathrm{am}\left\{\lambda s + \mathcal{K}(p)\,|\,p\right\}\right) = \mathrm{cn}\left(\lambda s + \mathcal{K}(p)\,|\,p\right). \tag{4.85b}$$

Intuitively, p is the elliptical eccentricity parameter, equal to 0 for a circle. The the amplitude ϕ is just the angle on a unit circle needed to trace an arc of length $s + \frac{\mathcal{K}(p)}{\lambda}$ on an ellipse of the same area. Conversely, the argument of the amplitude function (4.84) is the elliptic arc length (in units of λ) swept out by a circular angle ϕ.

The upper bound $\phi(s)$ of (4.82) is found using Eq. (4.79) for $\theta' = \lambda\sqrt{\sin^2\frac{\alpha}{2} - \sin^2\frac{\theta}{2}}$ when $\theta' = 0$ at $s = L$. Along with the definition (4.74) for p, this gives $\sin\left(\frac{\theta(L)}{2}\right) = p\sin\phi(L) = \pm\sin\left(\frac{\alpha}{2}\right) = \pm p$, or $\sin\phi(L) = \pm 1$, which implies $\phi(L) = \frac{\pi}{2} + m\pi$. The first nontrivial solution of Eq. (4.82) occurs for $n = 0$ and

[2] Note also that transformation of the limits of (4.80) using the map $\theta : \mathcal{M} \to \mathcal{N}$ depends on the transformation $\int_{\mathcal{M}} \theta^*\omega = \int_{\mathcal{N}=\theta\circ\mathcal{M}} \omega\circ\theta$, where $\omega \in \mathcal{N}^*$ is a k-form over $\mathcal{N}$, and the transpose map $\theta^*\omega$ is a form over $\mathcal{M}^*$, evaluated by the coordinate transformation $\theta\circ\mathcal{M}$. See [13] ch. 7 for more details.

$m = 1$, which results in

$$\lambda L + \mathcal{K}(p) = \int_0^{\frac{3\pi}{2}} \frac{dt}{\sqrt{1 - p^2 \sin^2 t}} = 3\mathcal{K}(p)$$
$$\lambda L = 2\mathcal{K}(p), \tag{4.86}$$

thereby providing a relationship between the string length L and the elliptic eccentricity p.

The object is ultimately to find the x and z coordinates of the transformed string. Using

$$x' = \sin\theta = 2\sin\left(\frac{\theta}{2}\right)\cos\left(\frac{\theta}{2}\right) = 2p\sin(\phi)\sqrt{1 - p^2\sin^2\phi}$$
$$z' = \cos\theta = 1 - 2\sin^2\frac{\theta}{2} = 2\left(1 - p^2\sin^2\phi\right) - 1, \tag{4.87}$$

we may integrate to get

$$\begin{aligned} x &= \int_0^x \frac{dx}{ds}ds = \int_{\phi(s(0))}^{\phi(s(x))} \frac{dx}{ds}\frac{ds}{d\phi}d\phi = \int_{\phi(s(0))}^{\phi(s(x))} \frac{2p\sin(t)\sqrt{1 - p^2\sin^2 t}}{\lambda\sqrt{1 - p^2\sin^2 t}}dt \\ &= \frac{2p}{\lambda}\int_{\phi(s(0))}^{\phi(s(x))} \sin t dt = -\frac{2p}{\lambda}\left(\cos\phi(s) - \cos\phi(0)\right) \\ &= -\frac{2p}{\lambda}\left[\cos\left(\mathrm{am}\left\{\lambda s + \mathcal{K}(p) \mid p\right\}\right) - \cos\left(\mathrm{am}\left\{\mathcal{K}(p) \mid p\right\}\right)\right] \\ &= -\frac{2p}{\lambda}\,\mathrm{cn}\left(\lambda s + \mathcal{K}(p) \mid p\right) \end{aligned} \tag{4.88}$$

and

$$\begin{aligned} z &= \int_0^z \frac{dz}{ds}ds = \int_{\phi(s(0))}^{\phi(s(z))} \frac{dz}{ds}\frac{ds}{d\phi}d\phi = \int_{\phi(s(0))}^{\phi(s(z))} \frac{2\left(1 - p^2\sin^2 t\right) - 1}{\lambda\sqrt{1 - p^2\sin^2 t}}dt \\ &= \frac{2}{\lambda}\int_{\phi(s(0))}^{\phi(s(z))} \sqrt{1 - p^2\sin^2 t} - \int_{\phi(s(0))}^{\phi(s(z))} \frac{1}{\lambda\sqrt{1 - p^2\sin^2 t}} \\ &= \frac{2}{\lambda}\left(\mathcal{E}(\phi(s) \mid p) - \mathcal{E}(\phi(0) \mid p)\right) - \frac{1}{\lambda}\left(\mathcal{K}(\phi(s) \mid p) - \mathcal{K}(\phi(0) \mid p)\right) \\ &= \frac{2}{\lambda}\left(\mathcal{E}\left(\mathrm{am}\left\{\lambda s + \mathcal{K}(p) \mid p\right\} \mid p\right) - \mathcal{E}\left(\mathrm{am}\left\{\mathcal{K}(p) \mid p\right\} \mid p\right)\right) \\ &\quad - \frac{1}{\lambda}\left(\mathcal{K}\left(\mathrm{am}\left\{\lambda s + \mathcal{K}(p) \mid p\right\} \mid p\right) - \mathcal{K}\left(\mathrm{am}\left\{\mathcal{K}(p) \mid p\right\} \mid p\right)\right) \\ &= \frac{2}{\lambda}\left(\mathcal{E}\left(\mathrm{am}\left\{\lambda s + \mathcal{K}(p) \mid p\right\} \mid p\right) - \mathcal{E}\left(\mathrm{am}\left\{\mathcal{K}(p) \mid p\right\} \mid p\right)\right) - \frac{1}{\lambda}\left(\lambda s + \mathcal{K}(p) - \mathcal{K}(p)\right) \\ &= -s + \frac{2}{\lambda}\left(\mathcal{E}\left(\mathrm{am}\left\{\lambda s + \mathcal{K}(p) \mid p\right\} \mid p\right) - \mathcal{E}\left(\mathrm{am}\left\{\mathcal{K}(p) \mid p\right\} \mid p\right)\right), \end{aligned} \tag{4.89}$$

where $\mathcal{E}\left(\frac{\pi}{2} \mid p\right) = \mathcal{E}(p)$ is the (complete) elliptic integral of the second kind defined in the obvious way on the second and third lines of (4.89). In the last line of (4.88),

we have used the fact that the amplitude $\mathrm{am}\{\mathcal{K}(p) \mid p\}$ of the complete elliptic integral is the angle required to subtend one quarter of the elliptical circumference, i.e., $\frac{\pi}{2}$, to eliminate the second cosine term. In the second-to-last line of (4.89), one uses $\mathcal{K}(\mathrm{am}\{x \mid p\} \mid p) = x$, which literally says that the arc length covered by an angle sufficient to cover the arc length x is x.

Note that Eq. (4.89) is of the form $z = -s + \Delta s$. For the case of zero deformation $\Delta s = 0$, the z limits satisfy $z(0) = 0$, as expected, but also $z(L) = -L$. Therefore, (4.89) inverts the ends of the rod. This can be dealt with in simulations by preemptively inverting the rod by $s \mapsto -s$.

In measuring derivatives g' and p' of the rotation matrices g and the angular momentum p in Eq. (4.4) it is important to take into account the direction in which s is increasing. Starting at the center of the rod and moving rightward to $s = L$ means ds is always positive, even if the z coordinate decreases.

4.5.2 Perspective drawing of spheres

The circles in Figure 4.2 and 4.6 are drawn in a three-dimensional perspective using a skew axis in the xy to represent z. The transformation is exact using the metric tensor prescription outlined here. Additional background can be found in [79].

Representation of three-dimensional objects on a two-dimensional canvas is defined by a rank-deficient linear projection mapping $\mathbb{P}_M : \mathbb{R}^3 \to \mathbb{R}^2$ onto a skew plane $M \subseteq \mathbb{R}^2$ spanned by vectors $\mathbf{v}^1, \mathbf{v}^2$ as

$$\mathbb{P}_M(\mathbf{w}) = \left[\mathbf{v}^j \otimes \mathbf{e}_i\right]\mathbf{w} = \begin{pmatrix} \mathbf{v}^1 \cdot \mathbf{E}_1 & \mathbf{v}^1 \cdot \mathbf{E}_2 & \mathbf{v}^1 \cdot \mathbf{E}_3 \\ \mathbf{v}^2 \cdot \mathbf{E}_1 & \mathbf{v}^2 \cdot \mathbf{E}_2 & \mathbf{v}^2 \cdot \mathbf{E}_3 \end{pmatrix} \begin{pmatrix} w^1 \\ w^2 \\ w^3 \end{pmatrix} = \begin{pmatrix} \mathbf{v}^1 \cdot \mathbf{w} \\ \mathbf{v}^2 \cdot \mathbf{w} \end{pmatrix}, \tag{4.90}$$

where w^1, w^2, w^3 are the components of $\mathbf{w}$ relative to the standard Euclidean basis $\{\mathbf{E}_i\}$ fixed to the body's center of mass. Obviously, $\mathbb{P}_M(\mathbf{w}) = \mathbf{w}$ for any vector $\mathbf{w} \in M$, because

$$\mathbb{P}_M(\mathbf{w}) = \begin{pmatrix} \mathbf{v}^1 \cdot (w_1\mathbf{v}^1 + w_2\mathbf{v}^2) \\ \mathbf{v}^2 \cdot (w_1\mathbf{v}^1 + w_2\mathbf{v}^2) \end{pmatrix} = \begin{pmatrix} w_1 \\ w_2 \end{pmatrix} = \mathbf{w}. \tag{4.91}$$

But if $\mathbf{w}$ has components not in M, it will suffer angular distortion due to the unequal sharing of the out-of-plane components among $\mathbf{v}^1$ and $\mathbf{v}^2$. The goal of perspective drawing is to find, for an arbitrary view angle (azimuthal and meridional), the basis vectors that make the third dimension appear undistorted.

The projection of a vector is *faithful* if it preserves magnitude, namely if $\mathbf{w}$ and $\mathbb{P}_M(\mathbf{w}) = \mathbb{P}_M\left(w^1\mathbf{E}_1 + w^2\mathbf{E}_2 + w^3\mathbf{E}_3\right) = w_1\mathbf{v}^1 + w_2\mathbf{v}^2$ have the same norm relative to the covariant and contravariant basis sets (see below). It is first assumed that Z can be projected faithfully into M using the metric tensor, and a drawing scheme is proposed. It is then shown that this projection is faithful using concepts from the problem of simple shear in continuum mechanics.

4.5.2.1 *The metric tensor method*

The illusion of depth is accomplished using the *metric tensors* g^{ij} and g_{ij}, which measure the dot products between pairs of covariant $\mathbf{x}^i, \mathbf{x}^j$ and contravariant $\mathbf{x}_i, \mathbf{x}_j$ basis vectors, respectively, of M. Let the vectors $\mathbf{x}_1$ and $\mathbf{x}^2$ be the standard orthonormal basis vectors of the (x, y) Euclidean plane.[3] Precisely, $\mathbf{x}_1 \cdot \mathbf{x}^2 = 0$, while $\|\mathbf{x}_1\| = \|\mathbf{x}^2\| = 1$. We seek to define a rotated set of basis vectors $\mathbf{x}^1$ and $\mathbf{x}_2$ that also satisfy $\mathbf{x}_i \cdot \mathbf{x}^j = \delta_i^j$, but which possibly do not have unit magnitude. These vectors are projections of a local (X, Y, Z) frame that rotates with the body. Let the $\mathbf{x}_2$ direction in the rotated system represent $-Z$, and let $\mathbf{x}^1$ be orthogonal to it (Figure S4.1A). The angle between (positive) $\mathbf{x}_1$ and $\mathbf{x}_2$ axes is ϕ, and that between $\mathbf{x}_1$ and $\mathbf{x}^1$ is $\frac{\pi}{2} - \phi$. From the usual definition of the dot product, it is readily found that

$$\mathbf{x}_1 \cdot \mathbf{x}^1 = \left\|\mathbf{x}^1\right\| \cos\left(\frac{\pi}{2} - \phi\right) \implies \left\|\mathbf{x}^1\right\| = \frac{1}{|\sin\phi|} \tag{4.92a}$$

$$\mathbf{x}_2 \cdot \mathbf{x}^2 = \|\mathbf{x}_2\| \cos\left(\frac{\pi}{2} - \phi\right) \implies \|\mathbf{x}_2\| = \frac{1}{|\sin\phi|}. \tag{4.92b}$$

Since the components of the metric tensors are found by $g_{ij} = \mathbf{x}_i \cdot \mathbf{x}_j$ and $g^{ij} = \mathbf{x}^i \cdot \mathbf{x}^j$, all that remains in the definition of g are the (symmetric) cross terms:

$$\mathbf{x}^1 \cdot \mathbf{x}^2 = \frac{1}{\sin\phi} \cos\left(\frac{\pi}{2} + \phi\right) = -\frac{\cos\phi}{\sin\phi} \tag{4.93a}$$

$$\mathbf{x}_1 \cdot \mathbf{x}_2 = \frac{1}{\sin\phi} \cos(\phi) = \frac{\cos\phi}{\sin\phi}. \tag{4.93b}$$

Thus transformation from contravariant to covariant is given by

$$g^{ij} = \begin{pmatrix} \frac{1}{\sin^2\phi} & -\cot\phi \\ -\cot\phi & 1 \end{pmatrix}, \tag{4.94a}$$

and from covariant to contravariant by

$$g_{ij} = \begin{pmatrix} 1 & \cot\phi \\ \cot\phi & \frac{1}{\sin^2\phi} \end{pmatrix}. \tag{4.94b}$$

[3] In general, bold face will denote basis vectors, and unadorned quantities their components; so x^1 is the covariant component of the contravariant basis vector $\mathbf{x}_1$ in the expression $x^1\mathbf{x}_1$.

Of course, when $\phi = 0$, we recover the situation where $\mathbf{x}_1 = \mathbf{x}^1$, $\mathbf{x}_2 = \mathbf{x}^2$, etc., so that arbitrary vectors $\mathbf{w} \in \mathbb{R}^n$ take the form $\mathbf{w} = w^1\mathbf{x}_1 + \ldots + w^n\mathbf{x}_n$.

The metric tensor can be used to express new vectors in terms of the old by

$$\mathbf{x}^1 = g^{11}\mathbf{x}_1 + g^{12}\mathbf{x}_2 \tag{4.95a}$$

$$\mathbf{x}_2 = g_{21}\mathbf{x}^1 + g_{22}\mathbf{x}^2. \tag{4.95b}$$

Inserting (4.95b) into (4.95a) gives

$$\begin{aligned}\mathbf{x}^1 &= g^{11}\mathbf{x}_1 + g^{12}\left(g_{21}\mathbf{x}^1 + g_{22}\mathbf{x}^2\right) \\ &= \frac{g^{11}}{1 - g^{12}g_{21}}\mathbf{x}_1 + \frac{g^{12}g_{22}}{1 - g^{12}g_{21}}\mathbf{x}^2,\end{aligned} \tag{4.96a}$$

and similarly

$$\mathbf{x}_2 = \frac{g_{21}g^{11}}{1 - g_{21}g^{12}}\mathbf{x}_1 + \frac{g_{22}}{1 - g_{21}g^{12}}\mathbf{x}^2. \tag{4.96b}$$

Thus, transformation between the rectangular $(\mathbf{x}_1, \mathbf{x}^2)$ and rotated $(\mathbf{x}^1, \mathbf{x}_2)$ basis sets can be accomplished by

$$\mathbf{x}^1 = \frac{1/\sin^2\phi}{1 + \cot^2\phi}\mathbf{x}_1 - \frac{\cos\phi/\sin^3\phi}{1 + \cot^2\phi}\mathbf{x}^2 = \mathbf{x}_1 - \cot(\phi)\mathbf{x}^2 \tag{4.97a}$$

$$\mathbf{x}_2 = \frac{\cos\phi/\sin^3\phi}{1 + \cot^2\phi}\mathbf{x}_1 + \frac{1/\sin^2\phi}{1 + \cot^2\phi}\mathbf{x}^2 = \cot(\phi)\mathbf{x}_1 + \mathbf{x}^2. \tag{4.97b}$$

Therefore, the matrix

$$\mathbf{A}_\phi := \begin{pmatrix} 1 & -\cot\phi \\ \cot\phi & 1 \end{pmatrix} \tag{4.98}$$

can be inverted to solve the linear equation

$$\begin{pmatrix} 0 \\ -1 \end{pmatrix} = \mathbf{A}_\phi \begin{pmatrix} x^1_\phi \\ x_{2,\phi} \end{pmatrix} \tag{4.99}$$

for the (x^1, x_2) components of the basis vectors $(\mathbf{x}_1, \mathbf{x}^2)$ representing the Z basis vector with coordinates $(0, -1)$ relative to the rotated $(\mathbf{x}^1, \mathbf{x}_2)$ system. Figure S4.1A, lower, shows that two ellipses (a^1, b^1) and (a^2, b^2) with horizontal and vertical semiaxes a and b can be drawn on top of an ellipse (r^1, r^2) where

$$a^1 = r^1 + r^3\left|x^1_\phi\right| \tag{4.100a}$$

$$b^1 = r^3\left|x_{2,\phi}\right| \tag{4.100b}$$

$$a^2 = r^3\left|x^1_\phi\right| \tag{4.100c}$$

$$b^2 = r^2 + r_3\left|x_{2,\phi}\right| \tag{4.100d}$$

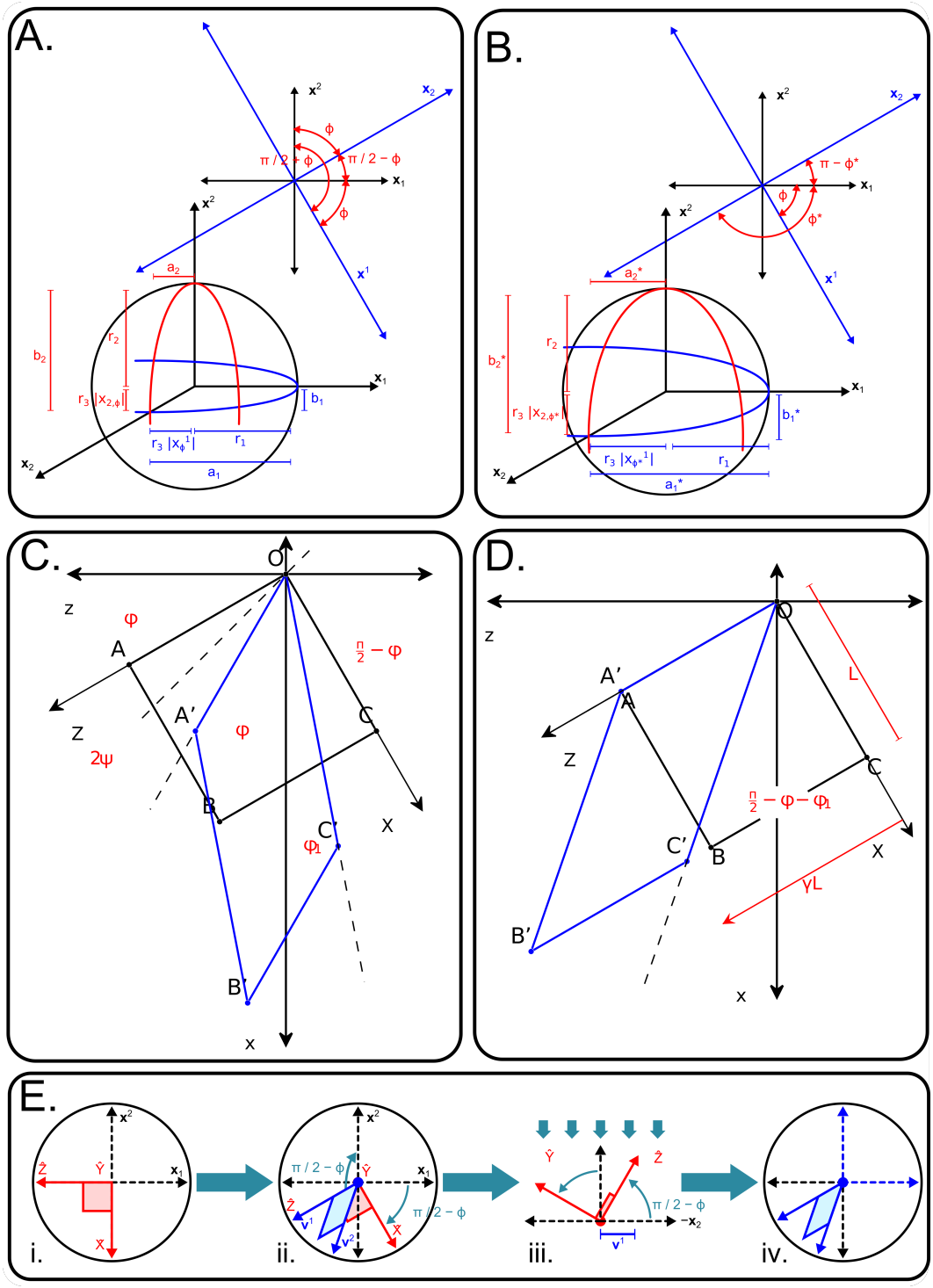
A.
B.
C.
D.
E.
i.
ii.
iii.
iv.

that will intersect at a point $\left(r^3\left|x^1_\phi\right|, r^3\left|x_{2,\phi}\right|\right)$ of the standard Euclidean plane, with r^3 the magnitude of the semiaxis in the third dimension of an ellipsoid (r^1, r^2, r^3).

The matrix

$$\mathbb{A}^{-1} = \left[\mathbf{A}^{-1}_\phi \begin{pmatrix} 0 \\ -1 \end{pmatrix}, \mathbf{A}^{-1}_\phi \begin{pmatrix} 1 \\ 0 \end{pmatrix}\right] = \begin{pmatrix} -\sin\phi\cos\phi & \sin^2\phi \\ -\sin^2\phi & -\sin\phi\cos\phi \end{pmatrix} \tag{4.101}$$

defines a transformation from body coordinates to the references basis, referring direction vectors $(X, Z)^T$ in the body to their components (x^1, x_2) relative to the fixed coordinate system $(\mathbf{x}_1, \mathbf{x}^2)$ (see Figure S4.1E for the sense in which the body element is defined). In particular, Eq. (4.101) refers a sphere in the third quadrant to the standard basis after it has been rotated by ϕ.

Eqs. (4.100) are not the only ellipses with vertices on $\mathbf{x}_1, \mathbf{x}^2$ that have intersections on $-\mathbf{x}_2$. Positive rotation by an angle ϕ is the same as a negative rotation by $\phi^* = \frac{\pi}{2} - \phi$. By making the transformation $\phi \mapsto \phi^*$ one gets the matrix

$$\mathbf{A}_{\phi^*} := \begin{pmatrix} 1 & \tan\phi \\ -\tan\phi & 1 \end{pmatrix} \tag{4.102}$$

and the linear equation

$$\begin{pmatrix} 1 \\ 0 \end{pmatrix} = \mathbf{A}_{\phi^*} \begin{pmatrix} x_{1,\phi^*} \\ x^2_{\phi^*} \end{pmatrix} \tag{4.103}$$

for the rectangular coordinates of the body basis vector $(1, 0)$ in the rotated $(\mathbf{x}^1, \mathbf{x}_2)$ system. In general, $\mathbf{A}_{\phi_1}$ and $\mathbf{A}_{\phi_2}$ define different bases $(\mathbf{x}^1, \mathbf{x}_2)$, but if the angles are chosen such that $\phi_2 = \frac{\pi}{2} - \phi_1$, then the vectors will overlap. As shown in in Figure

---

Figure S4.1 (*preceding page*)**: Projection mapping and shear.** (**A, B**) Two rotated bases for drawing a three-dimensional sphere in two-dimensions. The horizontal and vertical ellipses defined by Eqs. (4.100) are shown in blue and red. For the sphere $r^1 = r^2 = r^3 = 100$. The rotations are defined by $\phi = \frac{\pi}{6}$ (A) and $\phi^* = \frac{\pi}{3}$ (B). The $-\mathbf{x}_2$ axis is a faithful projection of the $\hat{Z}$ (A) or $\hat{X}$ (B) axis. Insets show the definitions of the angles, with the unit vectors drawn to reflect their different magnitudes. (**C, D**) Simple shear defined by the rotation angle ϕ of an XZ element relative to a square element in the fixed basis $\left(-\mathbf{x}_1, -\mathbf{x}^2\right)$. The square element $OABC$ with side length $L = 5$ in the third quadrant undergoes stretches $\alpha = \cot\phi$ and α^{-1} along vectors parallel to $\overline{OC'}$ and $\overline{OA'}$ (C), followed by negative rotation of 2ψ (D), resulting in shear by γL of $\overline{BC}$ relative to $\overline{OA}$. (**E**) Shearing of an XZ element of the body (*i.*) is equivalent to faithful projection of the basis vectors. Rotation by ϕ about $\hat{Y}$ and subsequent rotation of $\frac{\pi}{2} - \phi$ about $\hat{X}$ (*ii.*) preserves an amount $\sin\phi$ of the $\hat{Z}$ when it is projected on principal axis $\mathbf{v}^1$ in the $\left(\mathbf{x}_1, \mathbf{x}^2\right)$ plane (*iii.*). The projection is faithful because the rotated basis $\left(\mathbf{x}^1, \mathbf{x}_2\right)$ has unit vectors with magnitude $\frac{1}{|\sin\phi|}$ (*iv.*).

S4.1B, lower, the analogous set of ellipses (4.100) for $\mathbf{A}_{\phi^*}$, viz.

$$a^{1*} = r^1 + r^3 \left| x^1_{\phi^*} \right| \tag{4.104a}$$

$$b^{1*} = r_3 \left| x_{2,\phi^*} \right| \tag{4.104b}$$

$$a^{2*} = r^3 \left| x^1_{\phi^*} \right| \tag{4.104c}$$

$$b^{2*} = r^2 + r^3 \left| x_{2,\phi^*} \right| \tag{4.104d}$$

are different from Eqs. (4.100), but they still intersect the original ellipse (r^1, r^2) on $-\mathbf{x}_2$. If fact, because the $\phi \mapsto \phi^*$ transformation exchanges of the roles of $\mathbf{x}^1$ and $-\mathbf{x}_2$ relative to the rectangular basis, Figure S4.1B is simply a $90°$ rotation of panel A. To see this explicitly, note that the analogous matrix to Eq. (4.101) is

$$\mathbb{A}^{*-1} = \left[\mathbf{A}^{-1}_{\phi^*} \begin{pmatrix} 0 \\ -1 \end{pmatrix}, \mathbf{A}^{-1}_{\phi^*} \begin{pmatrix} 1 \\ 0 \end{pmatrix} \right] = \begin{pmatrix} \cos\phi \sin\phi & \cos^2\phi \\ -\cos^2\phi & \cos\phi \sin\phi \end{pmatrix}. \tag{4.105}$$

Then the matrix

$$\left[\mathbf{A}^{-1}_{\phi} \begin{pmatrix} 0 \\ -1 \end{pmatrix}, \mathbf{A}^{-1}_{\phi^*} \begin{pmatrix} 1 \\ 0 \end{pmatrix} \right] = \begin{pmatrix} -\sin\phi \cos\phi & \cos^2\phi \\ -\sin^2\phi & \cos\phi \sin\phi \end{pmatrix}. \tag{4.106}$$

has a vanishing determinant, showing the columns of this transformation are linearly dependent: the body vector $\hat{Z} = (0, -1)^T$ is mapped by $\mathbf{A}^{-1}_{\phi}$ to the same vector as $\hat{X} = (1, 0)^T$ is by $\mathbf{A}^{-1}_{\phi^*}$. This completes the prescription of drawing ellipsoids in two dimensions, assuming $\hat{Z}$ is faithfully represented by $-\mathbf{x}_2$.

4.5.2.2 *Faithful projections and shear*

Having shown how to draw the the Z axis of a sphere in two dimensions, it remains to be shown that this operation is well-defined. To accomplish this goal, we show how a faithful projection map is the same as isochoric *simple shear* of the Euclidean plane. Before stating the result, we introduce some terminology; further background may be found in reference [50], ch. 2. In the problem of isochoric (volume-preserving) simple shear, one layer (the horizontal, say) of a rectangular area element translates by a factor γ relative to another. The linear transformation

$$\mathbf{F} = \begin{pmatrix} 1 & \gamma \\ 0 & 1 \end{pmatrix} = \mathbf{RU} = \mathbf{VR}, \tag{4.107}$$

is broken down into a stretch $\mathbf{U}$ ($\mathbf{V}$) along two so-called *principal axes*, followed (preceded) by a rotation $\mathbf{R}$. $\mathbf{F}$ is known as the *deformation gradient*, and it sends

vectors in a body-centered *material basis* to equivalent positions in a *fixed basis*. Matrices $\mathbb{A}^{-1}$ and $\mathbb{A}^{*-1}$ of Eqs. (4.101) and (4.105) also refer material vectors to a fixed basis, but without changing the their relative angles.

Let $(-x^1, -x_2) = (z, x)$ be the coordinates of an orthonormal fixed basis (relative to $(-\mathbf{x}_1, -\mathbf{x}^2)$), and (Z, X) an orthonormal material basis oriented at a positive angle ϕ from the fixed basis. In Figure S4.1C, the material basis is an element in the third quadrant with $+Z$ originally ($\phi = 0$) aligned with z and $+X$ with x. If shearing preserves area, $\det \mathbf{U} = \det \mathbf{V} = 1$, and the relationship between the two bases is

$$\begin{pmatrix} Z \\ X \end{pmatrix} = \mathbf{R}^T \mathbf{V}^{-1} \begin{pmatrix} z \\ x \end{pmatrix} = \begin{pmatrix} \cos\phi & -\sin\phi \\ \sin\phi & \cos\phi \end{pmatrix} \begin{pmatrix} \alpha^{-1} & 0 \\ 0 & \alpha \end{pmatrix} \begin{pmatrix} z \\ x \end{pmatrix} = \begin{pmatrix} \alpha^{-1} z \cos\phi - \alpha x \sin\phi \\ \alpha^{-1} z \sin\phi + \alpha x \cos\phi \end{pmatrix}. \tag{4.108}$$

(Observe that $\mathbf{R}^T$ in Eq. 4.108 corresponds to a counterclockwise rotation of $\phi > 0$, the result of undoing a clockwise one.) A square in the material basis (Z, X) is bounded by the lines $Z = 0$ and $X = 0$; these values in Eq. (4.108) determine the lines

$$x = \alpha^{-2} \cot(\phi) z \tag{4.109a}$$

$$x = -\alpha^{-2} \tan(\phi) z, \tag{4.109b}$$

which get transformed into the unit square if the shear is undone. At $\phi = 0$, the complementary stretches α and α^{-1} operating respectively on the z and x coordinates transform the material points as

$$(z, \alpha z) \mapsto (\alpha z, z) \tag{4.110a}$$

$$\left(z, \alpha^{-1} z\right) \mapsto \left(\alpha z, \alpha^{-2} z\right). \tag{4.110b}$$

As shown in Figure S4.1C, Eq. (4.110a) transforms the leg $\overline{OA}$ into $\overline{OA'}$ by reflection over the dashed $45°$ line, preserving the angle ϕ relative to one of the axes. The angle ϕ and the corresponding ϕ_1, defined by $\overline{OC'}$, satisfy

$$\tan\phi = \frac{1}{\alpha} = \alpha^{-1} \tag{4.111a}$$

$$\tan\phi_1 = \frac{\alpha^{-2}}{\alpha} = \alpha^{-3}, \tag{4.111b}$$

as seen by putting $z = 1$ in Eqs. (4.110). From Eqs. (4.109), the sheared shape is bounded by the lines

$$x = \alpha^{-1} z \tag{4.112a}$$

$$x = -\alpha^{-3} z. \tag{4.112b}$$

Eq. (4.112a) defines the material element that shortens in Figure S4.1C, whereas (4.112b) defines the one that lengthens; clearly they need not be orthogonal.

Shear is completed by a negative rotation of $2\psi = 2\left(\frac{\pi}{4} - \phi\right)$ that reorients axis (4.112a) with the body Z axis, in agreement with the interpretation of shear as a shift by a factor γ in one direction. From Figure S4.1D the shift factor may be calculated as

$$\begin{aligned}\gamma &= \tan\left(\frac{\pi}{2} - \phi - \phi_1\right) = \frac{1}{\tan\left(\phi + \phi_1\right)} \\ &= \frac{1 - \tan\phi\tan\phi_1}{\tan\phi + \tan\phi_1} = \frac{1 - \alpha^{-1}\alpha^{-3}}{\alpha^{-1} + \alpha^{-3}} = \frac{\alpha^2 - \alpha^{-2}}{\alpha + \alpha^{-1}} = \alpha - \alpha^{-1}.\end{aligned} \tag{4.113}$$

The quadratic (4.113) is readily solved to give the relationship

$$\alpha = \frac{\gamma}{2} + \sqrt{1 + \frac{\gamma^2}{4}}; \tag{4.114}$$

together with (4.111a) and the double angle formula, it gives as well that

$$\phi = \frac{1}{2}\tan^{-1}\left(\tan 2\phi\right) = \frac{1}{2}\tan^{-1}\left(\frac{2}{\alpha - \alpha^{-1}}\right) = \frac{1}{2}\tan^{-1}\left(\frac{2}{\gamma}\right). \tag{4.115}$$

Eqs. (4.113)-(4.115) are well-known results from continuum mechanics. They illustrate the important fact that simple shear is completely characterized by either γ, α, or ϕ. Although ϕ is restricted by (4.115) to the range $\left(0, \frac{\pi}{4}\right)$, negative shears may be defined by the observation made above that a positive rotation by ϕ is the same as a negative rotation $\phi^* = \frac{\pi}{2} - \phi$. If the material element is an element of the fourth quadrant with $+Z$ originally aligned with $-\mathbf{x}_1$ and $+X$ with $-\mathbf{x}^2$, then negative rotation by ϕ^* defines the same element $OABC$ in Figures S4.1C and D, but with the line $\overline{OC}$ preserved during shear instead of $\overline{OA}$. One reasons this by the convention that the stretch α in Eqs. (4.109)-(4.112) was arbitrarily assigned to the line sloping at the cotangent of the rotation angle.

Having introduced the parameters that define simple shear, we are in a position to state the following result:

Theorem 4.5.1. *A projection map $\mathbb{P}_M : \mathbb{R}^3 \to \mathbb{R}^2$ of a vector in $\mathbf{R}^3$ onto a plane $M \subseteq \mathbb{R}^2$ is faithful if and only if the basis vectors $\mathbf{v}^1, \mathbf{v}^2$ of M represent a simple shear of the standard basis of $\mathbb{R}^2$.*

Proof. To show sufficiency, consider the sequence in Figure S4.1E. Suppose the sphere is oriented so that an observer looks down the body Y axis onto an element of the third quadrant of the ZX plane (panel i.). Projection in this orientation

is clearly faithful, because the basis vectors $\hat{Z}$ and $\hat{X}$ map to unit vectors in the $-\mathbf{x}_1 = -\mathbf{x}^1$ and $-\mathbf{x}^2 = -\mathbf{x}_2$ directions in the fixed basis. Then any vector in the ZX plane has the same magnitude when referred to coordinates of M. Next suppose that $\hat{Y}$ is exposed by rotation of the sphere about through $\frac{\pi}{2} - \phi$ about some vector in the ZX plane (panel ii.). What vector should rotate with $\hat{Y}$ in order that $\hat{Z}$ be faithfully projected into M? If the ZX element is first rotated through a counterclockwise angle ϕ, then the Z and Y vectors rotate together (panel iii.). Some information in the Z direction is lost, however, when only $\sin\phi$ in that direction is projected onto the fixed $\mathbf{x}_2$ axis (panel iii.). But use of the metric tensor in Eq. (4.92b) in the rotated basis shows that $\|\mathbf{x}_2\| = \frac{1}{|\sin\phi|}$, so that

$$\left\|\mathbb{P}_M\left(\hat{Z}\right)\right\| = \|\sin\phi\cdot\mathbf{x}_2\| = |\sin\phi|\cdot\left|\frac{1}{\sin\phi}\right| = 1. \tag{4.116}$$

Thus the requirement that $\hat{Z}$ be faithfully projected entails rotation by ϕ. But prior rotation of a ZX area element by ϕ is equivalent to simple shear of that element. Therefore, the projected vectors $\mathbb{P}_M\left(\hat{Z}\right) = \mathbf{v}^1$ and $\mathbb{P}_M\left(\hat{X}\right) = \mathbf{v}^2$ define the sides of a skew element in M. Another way to understand why shear is faithful in $\hat{Z}$ is that the deformation gradient (4.107) leaves the Z axis invariant if the X coordinate is zero (see Figure S4.1C and D).

To prove the only if direction, we seek conditions in which the original $\hat{Z}$ unit vector and the planar $\mathbf{v}^1$ direction vector satisfy $\mathbb{P}_M\left(\hat{Z}\right)\cdot\mathbf{v}^1 = 1$ and $\mathbb{P}_M\left(\hat{Z}\right)\cdot\mathbf{v}^2 = 0$, so that two unit vectors from different bases have the same magnitude. First define by N the plane spanned by $\mathbf{x}^1$ and $\mathbf{x}^2$, and let the angle between $\mathbb{P}_N\left(\hat{Z}\right)$ and $-\mathbf{x}_1$ when the planes ZX and N are superimposed be ϕ. Then $\mathbb{P}_N\left(\hat{Z}\right)$ has magnitude $\frac{1}{|\sin\phi|}$ in the planar $-\mathbf{x}_2$ direction, as prescribed by the metric tensor (4.92b). But the vector $-\mathbf{x}_2 \in N$ onto which $\hat{Z}$ is projected undergoes a stretch of $\alpha^{-1} = \tan\phi$, by virtue of its being along the principal shear axis $x_2 = \alpha^{-1}x^1$ (cf. Eq. (4.112a)). Then,

$$\mathbb{P}_N\left(\hat{Z}\right)\cdot(-\mathbf{x}_1) = \left\|\mathbb{P}_N\left(\hat{Z}\right)\right\|\cdot\|-\mathbf{x}_1\|\cdot\cos\phi = \left(\frac{1}{\sin\phi}\cdot\tan\phi\right)\cdot(1)\cdot\cos\phi = 1. \tag{4.117}$$

By hypothesis, a rectangular element bounded by unit vectors $-\mathbf{x}_1$ and $-\mathbf{x}^2$ in the plane N undergoes isochoric shear into vectors $\mathbf{v}^1$ and $\mathbf{v}^2$ in a plane M. Then $-\mathbf{x}_1$ and $\mathbf{v}^1$ are related by a rigid rotation $\mathcal{R}_\phi(-\mathbf{x}_1) = \mathbf{v}^1$ through an angle ϕ, and the matrix for projection onto N (cf. Eq. (4.90)) is $\mathbf{f}_j \otimes \mathbf{E}_i$ for basis vectors $\mathbf{f}_j$ of N and $\mathcal{R}_\phi(\mathbf{f}_j)$ of M. Regarding $-\mathbf{x}_1$ as a linear function over $\mathbb{P}_N\left(\hat{Z}\right)$ and using the metric tensor g_{ij} to transform from an orthonormal $(\mathbf{v}^1, \mathbf{v}_2)$ to a skew $(\mathbf{v}^1, \mathbf{v}^2)$ basis of M,

we find that

$$\begin{aligned}
\mathbb{P}_N\left(\hat{Z}\right)\cdot\left(-\mathbf{x}_1\right) &= \left\langle \mathbb{P}_N\left(\hat{Z}\right), \mathcal{R}_{-\phi}\left(\mathbf{v}_1\right)\right\rangle = \left\langle \mathcal{R}_\phi\left(\mathbb{P}_N\left(\hat{Z}\right)\right), \mathbf{v}_1\right\rangle \\
&= \left\langle \left[\mathcal{R}_\phi\left(-\mathbf{x}_1\right)\otimes\mathbf{E}_i + \mathcal{R}_\phi\left(-\mathbf{x}^2\right)\otimes\mathbf{E}_i\right]\hat{Z}, \mathbf{v}_1\right\rangle \\
&= \left\langle \left[\mathbf{v}^1\otimes\mathbf{E} + \mathbf{v}_2\otimes\mathbf{E}_i\right]\hat{Z}, \mathbf{v}_1\right\rangle \\
&= \left\langle \left[\left(1+g_{11}\right)\mathbf{v}^1\otimes\mathbf{E}_i + g_{12}\mathbf{v}^2\otimes\mathbf{E}_i\right]\hat{Z}, \mathbf{v}_1\right\rangle \\
&= \left\langle \mathbb{P}_M\left(\hat{Z}\right), \mathbf{v}_1\right\rangle = \mathbb{P}_M\left(\hat{Z}\right)\cdot\mathbf{v}_1, \qquad (4.118)
\end{aligned}$$

comparison of which to Eq. (4.117) allows us to conclude that $\mathbb{P}_M\left(\hat{Z}\right)\cdot\mathbf{v}_1 = 1$. Then if $\mathbf{v}_1$ has unit magnitude, $\mathbb{P}_M\left(\hat{Z}\right)$ does as well. Therefore, shearing of the basis elements of the Euclidean plane leads to faithful projection of $\hat{Z}$. □

The consequence of Theorem 4.5.1 is that the rotated basis defined by the metric tensor is a faithful projection of $\hat{Z}$. Although some information is necessarily destroyed because we cannot see all of the Z axis, the underlying plane onto which it is projected has been distorted to such an extent so as to preserve the illusion of depth.

BIBLIOGRAPHY

1. Agster KL, Fortin NJ, Eichenbaum H. The hippocampus and disambiguation of overlapping sequences. J Neurosci. 2002; 22: 5760–5768.
2. Ajo-Franklin CM, Drubin DA, Eskin JA, Gee EPS, Landgraf D, Phillips I, Silver PA. Rational design of memory in eukaryotic cells. Genes Dev. 2007; 21: 2271–2276. DOI: 10.1101/gad.1586107.
3. Akashi K, He X, Chen J, Iwasaki H, Niu C, Steenhard B, Zhang J, Haug J, Li L. Transcriptional accessibility for genes of multiple tissues and hematopoietic lineages is hierarchically controlled during early hematopoiesis. Blood. 2003; 101: 383–389. DOI: 10.1182/blood-2002-06-1780.
4. Aland S, Hatzikirou H, Lowengrub J, Voigt A. A Mechanistic Collective Cell Model for Epithelial Colony Growth and Contact Inhibition. Biophys J. 2015; 109: 1347–1357. DOI: 10.1016/j.bpj.2015.08.003.
5. Albeck JG, Mills GB, Brugge JS. Frequency-modulated pulses of ERK activity transmit quantitative proliferation signals. Mol Cell. 2013; 49: 249–261. DOI: 10.1016/j.molcel.2012.11.002.
6. Alon U. Network motifs: theory and experimental approaches. Nat Rev Genet. 2007; 8: 450–461. DOI: 10.1038/nrg2102.
7. Anderson JC, Voigt CA, Arkin AP. Environmental signal integration by a modular AND gate. Mol Syst Biol. 2010; 3. DOI: 10.1038/msb4100173.
8. Antebi YE, Linton JM, Klumpe H, Bintu B, Gong M, Su C, McCardell R, Elowitz MB. Combinatorial Signal Perception in the BMP Pathway. Cell. 2017; 170: 1184–1196. DOI: 10.1016/j.cell.2017.08.015.
9. Appel B, Givan LA, Eisen JS. Delta-Notch signaling and lateral inhibition in zebrafish spinal cord development. BMC Dev Biol. 2001; 1. DOI: 10.1186/1471-213X-1-13.
10. Araya CL, Kawli T, Kundaje A, Jiang L, Wu B, Vafeados D, Terrell R, Weissdepp P, Gevirtzman L, Mace D, Niu W, Boyle AP, Xie D, Ma L, Murray JI, Reinke V, Waterston RH, Snyder M. Regulatory analysis of the C. elegans genome with spatiotemporal resolution. Nature. 2014; 512: 400–405. DOI: 10.1038/nature13497.
11. Arias CF, Herrero MA, Stern CD, Bertocchini F. A molecular mechanism of symmetry breaking in the early chick embryo. Sci Rep. 2017; 7: 15776. DOI: 10.1038/s41598-017-15883-8.
12. Arnold VI. On the differential geometry of infinite-dimensional Lie groups and its application to the hydrodynamics of perfect fluids. In: Vladimir I. Arnold - Collected Works. Ed. by A Givental, B Khesin, A Varchenko, V Vassiliev, O Viro. Vol. 2, 33–69.
13. Arnold VI. Mathematical Methods of Classical Mechanics. Vol. 60. Graduate Texts in Mathematics. Springer-Verlag; 1983. Chap. 6-8.
14. Ashe HL, Briscoe J. The interpretation of morphogen gradients. Development. 2006; 133: 385–394. DOI: 10.1242/dev.02238.

15. Attanasio C, Nord AS, Zhu Y, Blow MJ, Biddie SC, Mendenhall EM, Dixon J, Wright C, Hosseini R, Akiyama JA, Holt A, Plajzer-Frick I, Shoukry M, Afzal V, Ren B, Bernstein BE, Rubin ER, Visel A, Pennacchio LA. Tissue-specific SMARCA4 binding at active and repressed regulatory elements during embryogenesis. Genome Res. 2014; 24: 920–929. DOI: 10.1101/gr.168930.113.
16. Ausländer S, Ausländer, Müller M, Wieland M, Fussenegger M. Programmable single-cell mammalian biocomputers. Nature. 2012; 487: 123–127. DOI: 10.1038/nature11149.
17. Bajoghli B, Aghaallaei N, Soroldoni D, Czerny T. The roles of Groucho/Tle in left-right asymmetry and Kupffer's vesicle organogenesis. Dev Biol. 2007; 303: 347–361. DOI: 10.1016/j.ydbio.2006.11.020.
18. Balaji S, Babu MM, Iyer LM, Luscombe NM, Aravind L. Comprehensive analysis of combinatorial regulation using the transcriptional regulatory network of yeast. J Mol Biol. 2006; 360: 213–227. DOI: 10.1016/j.jmb.2006.04.029.
19. Bassel GW, Stamm P, Mosca, de Reuille PB, Gibbs DJ, Winter R, Janka A, Holdsworth MJ, Smith RS. Mechanical constraints imposed by 3D cellular geometry and arrangement modulate growth patterns in the *Arabidopsis* embryo. Proc Natl Acad Sci U S A. 2014; 111: 8685–8690. DOI: 10.1073/pnas.1404616111.
20. Basu S, Gerchman Y, Collins CH, Arnold FH, Weiss R. A synthetic multicellular system for programmed pattern formation. Nature. 2005; 434: 1130–1134. DOI: 10.1038/nature03461.
21. Bedzhov I, Zericka-Goetz M. Self-organizing properties of mouse pluripotent cells initiate morphogenesis upon implantation. Cell. 2014; 156: 1032–1044. DOI: 10.1016/j.cell.2014.01.023.
22. Bell AC, West AG, Felsenfeld G. The protein CTCF is required for the enhancer blocking activity of vertebrate insulators. Cell. 1999; 98: 387–396. DOI: 10.1016/S0092-8674(00)81967-4.
23. Berks M, Kay RR. Combinatorial control of cell differentiation by cAMP and DIF-1 during development of Dictyostelium discoideum. Development. 1990; 110: 977–984.
24. Bessa J, Gebelein B, Pichaud F, Casares F, Mann RS. Combinatorial control of Drosophila eye development by eyeless, homothorax, and teashirt. Genes Dev. 2002; 16: 2415–2427. DOI: 10.1101/gad.1009002.
25. Bhattacharjee S, Renganaath K, Mehrotra R, Mehrotra S. Combinatorial Control of Gene Expression. Biomed Res Int. 2013; 2013: 1–11. DOI: 10.1155/2013/407263.
26. Bhattacharya S, Zhang Q, Andersen ME. A deterministic map of Waddington's epigenetic landscape for cell fate specification. BMC Syst Biol. 2011; 5. DOI: 10.1186/1752-0509-5-85.
27. Biddie SC, John S, Sabo PJ, Thurman RE, Johnson TA, Schiltz RL, Miranda TB, Sung MH, Trump S, Lightman SL, Vinson C, Stamatoyannopoulos JA, Hager GL. Transcription Factor AP1 Potentiates Chromatin Accessibility

and Glucocorticoid Receptor Binding. Mol Cell. 2011; 43: 145–155. DOI: 10.1016/j.molcel.2011.06.016.

28. Bigoni D, Bosi F, Misseroni D, Dal Corso F, Noselli G. New phenomena in nonlinear elastic structures: from tensile buckling to configurational forces. In: Extremeley Deformable Structures. Vol. 562. CISM International Centre for Mechanical Sciences, 55–153. DOI: 10.1007/978-3-7091-1877-1.
29. Bintu L, Buchler NE, Garcia HG, Gerland U, Hwa T, Kondev J, Phillips R. Transcriptional regulation by the numbers: models. Curr Opin Genet Dev. 2003; 15: 116–124. DOI: 10.1016/j.gde.2005.02.007.
30. Bisgrove BW, Essner JJ, Yost HJ. Regulation of midline development by antagonism of lefty and nodal signaling. Development. 1999; 126: 3253–3262.
31. Bisgrove BW, Essner JJ, Yost HJ. Multiple pathways in the midline regulate concordant brain, heart and gut left-right asymmetry. Development. 2000; 127: 3567–3579.
32. Bloch AM, Krishnaprasad PS, Marsden JE, Murray RM. Nonholonomic Mechanical Systems with Symmetry. Arch Rational Mech Anal. 1996; 136: 21–99. DOI: 10.1007/BF02199365.
33. Bloch A, Krishnaprasad PS, Marsden JE, Ratiu TS. The Euler-Poincaré equations and double bracket dissipation. Commun Math Phys. 1996; 175: 1–42. DOI: 10.1007/BF02101622.
34. Blount ZD, Borland CZ, Lenski RE. Historical contingency and the evolution of a key innovation in an experimental population of Escherichia coli. Proc Natl Acad Sci U S A. 2008; 105: 7899–7906. DOI: 10.1073/pnas.0803151105.
35. Bonnet J, Subsoontorn P, Endy D. Rewritable digital data storage in live cells via engineered control of recombination directionality. Proc Natl Acad Sci U S A. 2012; 109: 8884–8889. DOI: 10.1073/pnas.1202344109.
36. Bozhkov PV, Filonova LH, Suarez MF, Helmersson A, Smertenko AP, Zhivotovsky B, von Arnold S. VEIDase is a principal caspase-like activity involved in plant programmed cell death and essential for embryonic pattern formation. Cell Death Differ. 2004; 11: 175–182.
37. Bozorg B, Krupinski P, Jönsson H. Stress and strain provide positional and directional cues in development. PLoS Comput Biol. 2014; 10: e1003410. DOI: 10.1371/journal.pcbi.1003410.
38. Brewbaker C. A combinatorial interpretation of the poly-Bernoulli numbers and two Fermat analogues. Integers. 2008; 8: A02. URL: http://www.eudml.org/doc/130297.
39. Brkljacic J, Grotewold E. Combinatorial control of plant gene expression. Biochim Biophys Acta. 2017; 1860: 31–40. DOI: 10.1016/j.bbagrm.2016.07.005.
40. Bronson JE, Mazur WW, Cornish VW. Transcription factor logic using chemical complementation. Mol Biosyst. 2008; 4: 56–58. DOI: 10.1039/b713852k.

41. Brown TI, Ross RS, Keller JB, Hasselmo ME, Stern CE. Which way was I going? Contextual retrieval supports the disambiguation of well learned overlapping navigational routes. J Neurosci. 2010; 30: 7414–7422. DOI: 10.1523/JNEUROSCI.6021-09.2010.
42. Brunskill EW, Park JS, Chung E, Chen F, Magella B, Potter SS. Single cell dissection of early kidney development: multilineage priming. Development. 2014; 141: 3093–3101. DOI: 10.1242/dev.110601.
43. Buchler NE, Gerland U, Hwa T. On schemes of combinatorial transcription logic. Proc Natl Acad Sci U S A. 2003; 100: 5136–5141. DOI: 10.1073/pnas.0930314100.
44. Cai AQ, Radtke K, Linville A, Lander AD, Nie Q, Schilling TF. Cellular retinoic acid-binding proteins are essential for hindbrain patterning and signal robustness in zebrafish. Development. 2012; 139: 2150–2155. DOI: 10.1242/dev.077065.
45. Cai L, Dalal CK, Elowitz MB. Frequency-modulated nuclear localization bursts coordinate gene regulation. Nature. 2008; 455: 485–490. DOI: 10.1038/nature07292.
46. Carmena A, Gisselbrecht S, Harrison J, Jiménez F, Michelson AM. Combinatorial signaling codes for the progressive determination of cell fates in the Drosophila embryonic mesoderm. Genes Dev. 1998; 12: 3910–3922. DOI: 10.1101/gad.12.24.3910.
47. Carravetta M, Levitt MH. Long-lived nuclear spin states in high-field solution NMR. J Am Chem Soc. 2004; 126: 6228–6229. DOI: 10.1021/ja0490931.
48. Casas F, Murua A, Nadinic M. Efficient computation of the Zassenhaus formula. Comput Phys Commun. 1977; 183: 2386–2391. DOI: 10.1016/j.cpc.2012.06.006.
49. Chadwick MJ, Maguire DHMA. Decoding overlapping memories in the medial temporal lobes using high-resolution fMRI. Learn Mem. 2011; 18: 742–746. DOI: 10.1101/lm.023671.111.
50. Chadwick P. Continuum Mechanics: Concise Theory and Problems. Dover Publications, Inc.; 1999.
51. Chai J, Hamilton AL, Krieg M, Buckley CD, Riedel-Kruse IH, Dunn AR. A force balance can explain local and global cell movements during early zebrafish development. Biophys J. 2015; 109: 407–414. DOI: 10.1016/j.bpj.2015.04.029.
52. Chan EAW, Teng G, Corbett E, Choudhury KR, Bassing CH, Krangel DGSMS. Peripheral subnuclear positioning suppresses *Tcrb* recombination and segregates Tcrb alleles from RAG2. Proc Natl Acad Sci U S A. 2013; 110: E4628–E4637. DOI: 10.1073/pnas.1310846110.
53. Chang HH, Hemberg M, Barahona M, Ingber DE, Huang S. Transcriptome-wide noise controls lineage choice in mammalian progenitor cells. Nature. 2008; 453: 544–547. DOI: 10.1038/nature06965.
54. Chubb JR. Symmetry breaking in development and stochastic gene expression. Wiley Interdiscip Rev Dev Biol. 2017; 6: e284. DOI: 10.1002/wdev.284.

55. Church GM, Gao Y, Kosuri S. Next-generation digital information storage in DNA. Science. 2012; 337: 1628. DOI: 10.1126/science.1226355.
56. Coleman BD, Dill EH. Flexure waves in elastic rods. J Acoust Soc Am. 1992; 91: 2663–2673. DOI: 10.1121/1.402974.
57. Coleman BD, Dill EH, Lembo M, Lu Z, Tobias I. On the Dynamics of Rods in the Theory of Kirchhoff and Clebsch. Arch Rational Mech Anal. 1993; 121: 339–359. DOI: 10.1007/BF00375625.
58. Conte V, Muñoz JJ, Miodownik M. A 3D finite element model of ventral furrow invagination in the Drosophila melanogaster embryo. J Mech Behav Biomed Mater. 2008; 1: 188–198. DOI: 10.1016/j.jmbbm.2007.10.002.
59. Cox III RS, Surette MG, Elowitz MB. Programming gene expression with combinatorial promoters. Mol Syst Biol. 2007; 3. DOI: 10.1038/msb4100187.
60. Coyne J. Analysis of the formation and elimination of loops in twisted cable. IEEE J Ocean Eng. 1990; 15: 72–83. DOI: 10.1109/48.50692.
61. Dalal CK, Cai L, Lin Y, Rahbar K, Elowitz MB. Pulsatile dynamics in the yeast proteome. Curr Biol. 2014; 24: 2189–2194. DOI: 10.1016/j.cub.2014.07.076.
62. Dannengerg LO, Edenberg HJ. Epigenetics of gene expression in human hepatoma cells: expression profiling the response to inhibition of DNA methylation and histone deacetylation. BMC Genomics. 2006; 7. DOI: 10.1186/1471-2164-7-181.
63. Davidich MI, Bornholdt S. Boolean network model predicts cell cycle sequence of fission yeast. PLoS ONE. 2008; 3: e1672. DOI: 10.1371/journal.pone.0001672.
64. Desprat N, Supatto W, Pouille PA, Beaurepaire E, Farge E. Tissue deformation modulates twist expression to determine anterior midgut differentiation in Drosophila embryos. Dev Cell. 2008; 15: 470–477. DOI: 10.1016/j.devcel.2008.07.009.
65. Domokos G, Ruina A. A Circle construction based on elastostatics and hydordynamics. Mech Res Commun. 1993; 20: 181–185. DOI: 10.1016/0093-6413(93)90054-R.
66. Edwards R, Glass L. Combinatorial explosion in model gene networks. Chaos. 2000; 10: 691–704. DOI: 10.1063/1.1286997.
67. Eiraku M, Takata N, Ishibashi H, Kawada M, Sakakura E, Okuda S, Sekiguchi K, Adachi T, Sasai Y. Self-organizing optic-cup morphogenesis in three-dimensional culture. Nature. 2011; 472: 51–56. DOI: 10.1038/nature09941.
68. Eldar A. Social conflict drives the evolutionary divergence of quorum sensing. Proc Natl Acad Sci U S A. 2011; 108: 13635–13640. DOI: 10.1073/pnas.1102923108.
69. Essner JJ, Vogan KJ, Wagner MK, Tabin CJ, Yost HJ, Brueckner M. Left-right development: Conserved function for embryonic nodal cilia. Nature. 2002; 418: 37–38. DOI: 10.1038/418037a.
70. Fang J, Chen J. Deformation and vibration of a spatial elastica with fixed end slopes. Int J Solids Struct. 2013; 50: 824–831. DOI: 10.1016/j.ijsolstr.2012.11.011.

71. Farzadfard F, Lu TK. Genomically Encoded Analog Memory with Precise *In vivo* DNA Writing in Living Cell Populations. Science. 2014; 346: 1256272. DOI: 10.1126/science.1256272.
72. Fauré A, Naldi A, Chaouiya C, Thieffry D. Dynamical analysis of a generic Boolean model for the control of the mammalian cell cycle. Bioinformatics. 2006; 22: e124–e131. DOI: 10.1093/bioinformatics/btl210.
73. Federov YN, Kozlov VV. Various aspects of *n*-dimensional rigid body dynamics. In: Dynamical Systems in Classical Mechanics. Vol. 168. Advance in the Mathematical Sciences.
74. Fernandez-Rodriguez J, Yang L, Gorochowski TE, Gordon DB, Voigt CA. Memory and Combinatorial Logic Based on DNA Inversions: Dynamics and Evolutionary Stability. ACS Synth Biol. 2015; 4: 1361–1372. DOI: 10.1021/acssynbio.5b00170.
75. Ferrell Jr JE. Bistability, bifurcations, and Waddington's epigenetic landscape. Curr Biol. 2012; 22: R458–R466. DOI: 10.1016/j.cub.2012.03.045.
76. Filion GJ, van Bemmel JG, Braunschweig U, Talhout W, Kind J, Ward LD, Brugman W, de Castro Genebra de Jesus I, Kerkhoven RM, Bussemaker HJ, Steensel B van. Systematic protein location mapping reveals five principal chromatin types in *Drosophila* cells. Cell. 2010; 143: 212–224. DOI: 10.1016/j.cell.2010.09.009.
77. Fisher S. Complex Variables: Second Edition. Dover Publications, Inc.; 1999. Chap. 2.
78. Flores GV, Duan H, Yan H, Nagaraj R, Fu W, Zou Y, Noll M, Banerjee U. Combinatorial signaling in the specification of unique cell fates. Cell. 2000; 103: 75–85. DOI: 10.1016/S0092-8674(00)00106-9.
79. Flügge W. Tensor Analysis and Continuum Mechanics. Springer-Verlag; 1972. Chap. 1,7.
80. Foley AC, Skromne I, Stern CD. Reconciling different models of forebrain induction and patterning: a dual role for the hypoblast. Development. 2000; 127: 3839–3854.
81. Fossat N, Ip CK, Jones VJ, Studdert JB, Khoo PL, Lewis SL, Power M, Tourle K, Loebel DA, Kwan KM, Behringer RR, Tam PP. Context-specific function of the LIM homeobox 1 transcription factor in head formation of the mouse embryo. Development. 2015; 142: 2069–2079. DOI: 10.1242/dev.120907.
82. Freeman BT, Jung JP, Ogle BM. Single-Cell RNA-Seq of Bone Marrow-Derived Mesenchymal Stem Cells Reveals Unique Profiles of Lineage Priming. PLoS One. 2015; 10: e0136199. DOI: 10.1371/journal.pone.0136199.
83. Frieda KL, Linton JM, Hormoz S, Choi J, Chow KK, Singer ZS, Budde MW, Elowitz MB, Cai L. Synthetic recording and in situ readout of lineage information in single cells. Nature. 2017; 541: 107–111. DOI: 10.1038/nature20777.

84. Friedland AE, Lu TK, Wang X, Shi D, Church G, Collins JJ. Synthetic gene networks that count. Science. 2009; 324: 1199–1202. DOI: 10.1126/science.1172005.
85. Fritz G, Buchler NE, Hwa T, Gerland U. Designing sequential transcription logic: a simple genetic circuit for conditional memory. Syst Synth Biol. 2007; 1: 89–98. DOI: 10.1007/s11693-007-9006-8.
86. Fudenberg D, Maskin E. Evolution and cooperation in noisy repeated games. In: Papers and Proceedings of the Hundred and Second Annual Meeting of the American Economic Association. Vol. 80, 274–279. URL: http://www.jstor.org/stable/2006583.
87. Fuller F. The writhing number of a space curve. Proc Natl Acad Sci U S A. 1971; 68: 815–819.
88. Garcia-Martinez V, Y Macias D G, Garcia-Lobo JM, Francia MV, Fernandez-Teran MA, Hurle JM. Internucleosomal DNA fragmentation and programmed cell death (apoptosis) in the interdigital tissue of the embryonic chick leg bud. J Cell Sci. 1993; 106: 201–208. DOI: 10.1038/sj.cdd.4401330.
89. Gardner TS, Cantor CR, Collins JJ. Construction of a genetic toggle switch in Escherichia coli. Nature. 2000; 403: 339–342. DOI: 10.1038/35002131.
90. Gerhart J. 1998 Warkany lecture: signaling pathways in development. Teratology. 1999; 60: 226–239. DOI: 10.1002/(SICI)1096-9926(199910)60:4<226::AID-TERA7>3.0.CO;2-W.
91. Gerhart J, Kerschner M. Cells, Embryos, and Evolution. Blackwell Science; 1997.
92. Ghosh P, Pannunzio NR, Hatfull GF. Synapsis in phage Bxb1 integration: selection mechanism for the correct pair of recombination sites. J Mol Biol. 2005; 349: 331–348. DOI: 10.1016/j.jmb.2005.03.043.
93. Ginther MR, Walshand DF, Ramus SJ. Hippocampal neurons encode different episodes in an overlapping sequence of odors task. J Neurosci. 2011; 31: 2706–2711. DOI: 10.1523/JNEUROSCI.3413-10.2011.
94. Goehring NW, Hyman AA. Organelle growth control through limiting pools of cytoplasmic components. Curr Biol. 2012; 22: R330–R339. DOI: 10.1016/j.cub.2012.03.046.
95. Goriely A, Tabor M. Nonlinear dynamics of filaments. IV Spontaneous looping of twisted elastic rods. Proc R Soc Lond A. 1998; 454: 3183–3202. DOI: 10.1098/rspa.1998.0297.
96. Goriely A, Tabor M. The Nonlinear Dynamics of Filaments. Nonlinear Dynamics. 2000; 21: 101–133. DOI: 10.1023/A:100836652.
97. Goss VGA, van der Heijden GHM, Thompson JMT, Neukirch S. Experiments on Snap Buckling, Hysteresis and Loop Formation in Twisted Rods. Exp Mech. 2005; 45: 101–111. DOI: 10.1177/0014485105052318.
98. Goyal S, Perkins NC, Lee CL. Nonlinear dynamics and loop formation in Kirchhoff rods with implications to the mechanics of DNA and cables. J Comput Phys. 2005; 209: 371–389. DOI: 10.1016/j.jcp.2005.03.027.
99. Graf T, Stadtfeld M. Heterogeneity of embryonic and adult stem cells. Cell Stem Cell. 2008; 3: 480–483. DOI: 10.1101/gr.2584104.

100. Green JA, Rees D. On semi-groups in which $x^r = x$. Mathematical Proceedings of the Cambridge Philosophical Society. 1952; 48: 35–40. DOI: 10.1017/S0305004100027341.
101. Green JB, New HV, Smith JC. Responses of embryonic Xenopus cells to activin and FGF are separated by multiple dose thresholds and correspond to distinct axes of the mesoderm. Cell. 1992; 71: 731–739. DOI: 10.1016/0092-8674(92)90550-V.
102. Groh C, Moldovanu B, Sela A, Sunde U. Optimal seedings in elimination tournaments. Economic Theory. 2008; 49: 59–80. DOI: 10.1007/s00199-008-0356-6.
103. Guelzim N, Bottani S, Bourgine P, Képès F. Topological and causal structure of the yeast transcriptional regulatory network. Nat Genet. 2002; 31: 60–63. DOI: 10.1038/ng873.
104. Guertin MJ, Lis JT. Mechanisms by which transcription factors gain access to target sequence elements in chromatin. Curr Opin Genet Dev. 2013; 23: 116–123. DOI: 10.1016/j.gde.2012.11.008.
105. Guet CC, Elowitz MB, Hsing W, Leibler S. Combinatorial synthesis of genetic networks. Science. 2002; 296: 1466–1470. DOI: 10.1126/science.1067407.
106. Guillemin V, Sternberg S. The moment map and collective motion. Ann Phys. 1980; 127: 220–253. DOI: 10.1016/0003-4916(80)90155-4.
107. Guo G, Huss M, Tong GQ, Wang C, Li Sun L, Clarke ND, Robson P. Resolution of cell fate decisions revealed by single-cell gene expression analysis from zygote to blastocyst. Dev Cell. 2010; 18: 675–685. DOI: 10.1016/j.devcel.2010.02.012.
108. Ham TS, Lee SK, Keasling JD, Arkin AP. Design and construction of a double inversion recombination switch for heritable sequential genetic memory. PLoS One. 2008; 3: e2815. DOI: 10.1371/journal.pone.0002815.
109. Hamada H. Role of physical forces in embryonic development. Semin Cell Dev Biol. 2015; 47-48: 88–91. DOI: 10.1016/j.semcdb.2015.10.011.
110. Hamilton FS, Wheeler GN, Hoppler S. Difference in XTcf-3 dependency accounts for change in response to beta-catenin-mediated Wnt signalling in Xenopus blastula. Development. 2001; 128: 2063–2073.
111. Handoko L, Xu H, Li G, Ngan CY, Chew E, Schnapp M, Lee CW, Ye C, Ping JL, Mulawadi F, Wong E, Sheng J, Zhang Y, Poh T, Chan CS, Kunarso G, Shahab A, Bourque G, Cacheux-Rataboul V, Sung WK, Ruan Y, Wei CL. CTCF-mediated functional chromatin interactome in pluripotent cells. Nat Genet. 2011; 43: 630–638. DOI: 10.1038/ng.857.
112. Hasty J, McMillen D, Collins JJ. Engineered gene circuits. Nature. 2002; 420: 224–230. DOI: 10.1038/nature01257.
113. He X, Samee MA, Blatti C, Sinha S. Thermodynamics-based models of transcriptional regulation by enhancers: the roles of synergistic activation, cooperative binding and short-range repression. PLoS Comput Biol. 2010; 6: e1000935. DOI: 10.1371/journal.pcbi.1000935.

114. Henrique D, Hirsinger E, Adam J, Le Roux I, Pourquié O, Ish-Horowicz D, Lewis J. Maintenance of neuroepithelial progenitor cells by Delta-Notch signalling in the embryonic chick retina. Curr Biol. 1997; 7: 661–670. DOI: 10.1016/S0960-9822(06)00293-4.
115. Hermsen R, Tans S, ten Wolde PR. Transcriptional regulation by competing transcription factor modules. PLoS Comput Biol. 2006; 2: 1552–1560. DOI: 10.1371/journal.pcbi.0020164.
116. Hikasa H, Sokol SY. Wnt signaling in vertebrate axis specification. Cold Spring Harb Perspect Biol. 2013; 5: a007955. DOI: 10.1101/cshperspect.a007955.
117. Hinegardner R, Engelberg J. Biological complexity. J Theor Biol. 1983; 104: 7–20. DOI: 10.1016/0022-5193(83)90398-3.
118. Hirata J, Nakagoshi H, Nabeshima Y, Matsuzaki F. Asymmetric segregation of the homeodomain protein Prospero during Drosophila development. Nature. 1995; 377: 627–630. DOI: 10.1038/377627a0.
119. Holm DD. Geometric Mechanics Part II: Rotating, Translating and Rolling. Imperial College Press; 2011. Chap. 2,6,8.
120. Hou C, Zhao H, Tanimoto K, Dean A. CTCF-dependent enhancer-blocking by alternative chromatin loop formation. Proc Natl Acad Sci U S A. 2008; 105: 20398–20403. DOI: 10.1073/pnas.0808506106.
121. Hsiao V, Hori Y, Rothemund PW, Murray RM. A population-based temporal logic gate for timing and recording chemical events. A population-based temporal logic gate for timing and recording chemical events. 2016; 12. DOI: 10.15252/msb.20156663.
122. Hu M, Krause D, Greaves M, Sharkis S, Dexter M, Heyworth C, Enver T. Multilineage gene expression precedes commitment in the hemopoietic system. Genes Dev. 1997; 11: 774–785. DOI: 10.1101/gad.11.6.774.
123. Hua S, Kittler R, White KP. Genomic antagonism between retinoic acid and estrogen signaling in breast cancer. Cell. 2009; 137: 1259–1271. DOI: 10.1016/j.cell.2009.04.043.
124. Huang S. Systems biology of stem cells: three useful perspectives to help overcome the paradigm of linear pathways. Philos Trans R Soc Lond B Biol Sci. 2011; 366: 2247–2259. DOI: 10.1098/rstb.2011.0008.
125. Huang S, Guo YP, May G, Enver T. Bifurcation dynamics in lineage-commitment in bipotent progenitor cells. Dev Biol. 2007; 305: 695–713. DOI: 10.1016/j.ydbio.2007.02.036.
126. Hurtado JE, Sinclair AJ. Hamel coefficients for the rotational motion of an *N*-dimensional rigid body. Proc R Soc Lond A. 2004; 460: 3613–3630. DOI: 10.1098/rspa.2004.1320.
127. Huttlin EL, Jedrychowski MP, Elias JE, Goswami T, Rad R, Beausoleil SA, Villén J, Haas W, Sowa ME, Gygi SP. A tissue-specific atlas of mouse protein phosphorylation and expression. Cell. 2010; 143: 1174–1189. DOI: 10.1016/j.cell.2010.12.001.

128. Isidori A. Nonlinear Control Systems: An Introduction. Vol. 72. Communications and Control Engineering Series. Springer-Verlag; 1989. Chap. Appendix A.
129. Isshiki T, Pearson B, Holbrook S, Doe CQ. Drosophila neuroblasts sequentially express transcription factors which specify the temporal identity of their neuronal progeny. Cell. 2001; 106: 511–521. DOI: 10.1016/S0092-8674(01)00465-2.
130. Iwanaszko M, Kimmel M. NF-$\varkappa$B and IRF pathways: cross-regulation on target genes promoter level. BMC Genomics. 2015; 16. DOI: 10.1186/s12864-015-1511-7.
131. Iwasaki H, Mizuno S, Arinobu Y, Ozawa H, Mori Y, Shigematsu H, Takatsu K, Tenen DG, Akashi K. The order of expression of transcription factors directs hierarchical specification of hematopoietic lineages. Genes Dev. 2006; 20: 3010–3021. DOI: 10.1101/gad.1493506.
132. Iyengar L, Wang Q, Rasko JE, McAvoy JW, Lovicu FJ. Duration of ERK1/2 phosphorylation induced by FGF or ocular media determines lens cell fate. Differentiation. 2007; 75: 662–668. DOI: 10.1111/j.1432-0436.2007.00167.x.
133. Jaitin DA, Kenigsberg E, Keren-Shaul H, Elefant N, Paul F, Zaretsky I, Mildner A, Cohen N, Jung S, Tanay A, Amit I. Massively parallel Single-Cell RNA-seq for marker-free decomposition of tissues into cell types. Science. 2014; 343: 776–779. DOI: 10.1126/science.1247651.
134. Jurdjevic V. Geometric Control Theory. Cambridge University Press; 1997. Chap. 11,12.
135. Kalmar T, Lim C, Hayward P, Muñoz-Descalzo S, Nichols J, Garcia-Ojalvo J, Martinez Arias A. Regulated fluctuations in nanog expression mediate cell fate decisions in embryonic stem cells. PLoS Biol. 2009; 7: e1000149. DOI: 10.1371/journal.pbio.1000149.
136. Kaneko M. Poly-Bernoulli numbers. Journal de théorie des nombres de Bordeaux. 1997; 9: 221–228. DOI: 10.5802/jtnb.197.
137. Kaplan T, Li XY, Sabo PJ, Thomas S, Stamatoyannopoulos JA, Biggin MD, Eisen MB. Quantitative models of the mechanisms that control genome-wide patterns of transcription factor binding during early Drosophila development. PLoS Genet. 2011; 7: e1001290. DOI: 10.1371/journal.pgen.1001290.
138. Kauffman SA. Metabolic stability and epigenesis in randomly constructed genetic nets. J Theor Biol. 1969; 22: 437–467. DOI: 10.1016/0022-5193(69)90015-0.
139. Kellogg RA, Tian C, Lipniacki T, Quake SR, Tay S. Digital signaling decouples activation probability and population heterogeneity. eLife. 2015; 4: e08931. DOI: 10.7554/eLife.08931.
140. Kennaway R, Coen E, Green A, Bangham A. Generation of diverse biological forms through combinatorial interactions between tissue polarity and growth. PLoS Comput Biol. 2011; 7: e1002071. DOI: 10.1371/journal.pcbi.1002071.

141. Kim HK, Krotov DS, Lee JY. Poly-Bernoulli numbers and lonesum matrices. arXiv. 2011; 1103.4884. DOI: 10.1016/j.laa.2012.11.027.
142. Kim TH, Saadatpour A, Guo G, Saxena M, Cavazza A, Desai N, Jadhav U, Jiang L, Rivera MN, Orkin SH, Yuan GC, Shivdasani RA. Single-Cell Transcript Profiles Reveal Multilineage Priming in Early Progenitors Derived from Lgr5(+) Intestinal Stem Cells. Cell Rep. 2016; 16: 2053–2060. DOI: 10.1016/j.celrep.2016.07.056.
143. Kimmel CB, Law RD. Cell lineage of zebrafish blastomeres. III. Clonal analyses of the blastula and gastrula stages. Dev Biol. 1985; 108: 94–101. DOI: 10.1016/0012-1606(85)90012-0.
144. Kramer BP, Fischer C, Fussenegger M. BioLogic gates enable logical transcription control in mammalian cells. Biotechnol Bioeng. 2004; 87: 478–484. DOI: 10.1002/bit.20142.
145. Kubo R, Toda M, Hashitsume N. Statistical Physics II: Nonequilibrium Statistical Mechanics. Vol. 31. Springer Series in Solid-State Science. Springer-Verlag; 1978. Chap. 2.
146. Kudron M, Niu W, Lu Z, Wang G, Gerstein M, Snyder M, Reinke V. Tissue-specific direct targets of *Caenorhabditis elegans* Rb/E2F dictate distinct somatic and germline programs. Genome Biol. 2013; 14: R5. DOI: 10.1186/gb-2013-14-1-r5.
147. Kumar RM, Cahan P, Shalek AK, Satija R, DaleyKeyser A, Li H, Zhang J, Pardee K, Gennert D, Trombetta JJ, Ferrante TC, Regev A, Daley GQ, Collins JJ. Deconstructing transcriptional heterogeneity in pluripotent stem cells. Nature. 2014; 516: 56–61. DOI: 10.1038/nature13920.
148. La Manno G, Soldatov R, Hochgerner H, Zeisel A, Petukhov V, Kastriti M, Lonnerberg P, Furlan A, Fan J, Liu Z, van Bruggen D, Guo J, Sundstrom E, Castelo-Branco G, Adameyko I, Linnarsson S, Kharchenko P. RNA velocity in single cells. bioRxiv. 2017; DOI: 10.1101/206052.
149. Laguna MF, Bohn S, Jagla EA. The Role of Elastic Stresses on Leaf Venation Morphogenesis. PLoS Comput Biol. 2008; 4: e1000055. DOI: 10.1371/journal.pcbi.1000055.
150. Lahav G, Rosenfeld N, Sigal A, Geva-Zatorsky N, Levine AJ, Elowitz MB, Alon U. Dynamics of the p53-Mdm2 feedback loop in individual cells. Nat Genet. 2004; 36: 147–150. DOI: 10.1038/ng1293.
151. Lawson KA, Meneses JJ, Pedersen RA. Clonal analysis of epiblast fate during germ layer formation in the mouse embryo. Development. 1991; 113: 891–911.
152. Leibfried A, Müller S, Ephrussi A. A Cdc42-regulated actin cytoskeleton mediates Drosophila oocyte polarization. Development. 2013; 140: 362–371. DOI: 10.1242/dev.089250.
153. Letsou W, Cai L. Noncommutative Biology: Sequential Regulation of Complex Networks. PLoS Comput Biol. 2016; 12: e1005089. DOI: 10.1371/journal.pcbi.1005089.

154. Leutgeb JK, Leutgeb S, Moser MB, Moser MI. Pattern separation in the dentate gyrus and CA3 of the hippocampus. Science. 2007; 315: 961–966. DOI: 10.1126/science.1135801.
155. Li Q, Ha TS, Okuwa S, Wang Y, Wang Q, Millard SS, Smith DP, Volkan PC. Combinatorial rules of precursor specification underlying olfactory neuron diversity. Curr Biol. 2013; 23: 2481–2490. DOI: 10.1016/j.cub.2013.10.05.
156. Liang H, Mahadevan L. The shape of a long leaf. Proc Natl Acad Sci U S A. 2009; 106: 22049–22054. DOI: 10.1073/pnas.0911954106.
157. Lignell A, Kerosuo L, Streichan SJ, Cai L, Bronner ME. Identification of a neural crest stem cell niche by Spatial Genomic Analysis. Nat Commun. 2017; 8: 1830. DOI: 10.1038/s41467-017-01561-w.
158. Lin Y, Sohn CH, Dalal CK, Cai L, Elowitz MB. Combinatorial gene regulation by modulation of relative pulse timing. Nature. 2015; 527: 54–58. DOI: 10.1038/nature15710.
159. Liu FC. Kink formation and rotational response of single and multistrand electromechanical cables. Tech. rep. N-1403. Naval Construction Battalion Center.
160. Liu F, van den Broek O, Destrée O, Hoppler S. Distinct roles for Xenopus Tcf/Lef genes in mediating specific responses to Wnt/beta-catenin signalling in mesoderm development. Development. 2005; 132: 5375–5385. DOI: 10.1242/dev.02152.
161. Lou C, Liu X, Ni M, Huang Y, Huang Q, Huang L, Jiang L, Lu D, Wang M, Liu C, Chen D, Chen C, Chen X, Yang L, Ma H, Chen J, Ouyang Q. Synthesizing a novel genetic sequential logic circuit: a push-on push-off switch. Mol Syst Biol. 2010; 6. DOI: 10.1038/msb.2010.2.
162. Lounesto P. Clifford Algebras and Spinors. Vol. 286. London Mathematical Society Lecture Note Series. Cambridge University Press; 2001. Chap. 3,7.
163. Love AEH. A Treatise on the Mathematical Theory of Elasticity. Dover Publications, Inc.; 1944. Chap. II,XIV,XVIII,XIX.
164. Lu H, Ward MG, Adeola O, Ajuwon KM. Regulation of adipocyte differentiation and gene expression-crosstalk between TGFβand wnt signaling pathways. Mol Bio Rep. 2013; 40: 5237–5245. DOI: 10.1007/s11033-013-2623-2.
165. Lubeck E, Coskun AF, Zhiyentayev T, Ahmad M, Cai L. Single-cell *in situ* RNA profiling by sequential hybridization. Nat Methods. 2014; 11: 360–361. DOI: 10.1038/nmeth.2892.
166. Ma HW, Kumar B, Ditges U, Gunzer F, Buer J, Zeng AP. An extended transcriptional regulatory network of *Escherichia coli* and analysis of its hierarchical structure and network motifs. Nucleic Acids Res. 2004; 32: 6643–6649. DOI: 10.1093/nar/gkh1009.
167. Maddocks JH. Stability of nonlinearly elastic rods. Arch Rational Mech Anal. 1984; 85: 311–354. DOI: 110.1007/BF00275737.

168. Mankov SV. Note on the integration of Euler's equation of the dynamics of an n-dimensional rigid body. Funct Anal Appl. 1976; 10: 328–329. DOI: 10.1007/BF01076037.
169. Marco E, Karp RL, Guo G, Robson P, Hart AH, Trippa L, Yuan GC. Bifurcation analysis of single-cell gene expression data reveals epigenetic landscape. Proc Natl Acad Sci U S A. 2014; 111: E5643–E5650. DOI: 10.1073/pnas.1408993111.
170. Margulies D, Felder CE, Melman G, Shanzer A. A molecular keypad lock: a photochemical device capable of authorizing password entries. J Am Chem Soc. 2007; 129: 347–354. DOI: 10.1021/ja065317z.
171. Marsden JE, Montgomery R, Raitu T. Ehresmann connections an holonomy. Vol. 88. Memoirs of the American Mathematical Society. American Mathematical Society; 1990.
172. Marsden JE, Raitu TS. Introduction to Mechanics and Symmetry. Vol. 17. Texts in Applied Mathematics. Springer-Verlag; 1994.
173. Marsden JE, Raitu T, Weinstein A. Semidirect products and reduction in mechanics. Trans Amer Math Soc. 1984; 281: 147–177. DOI: 10.1090/S0002-9947-1984-0719663-1.
174. Marsman J, Horsfield JA. Long distance relationships: Enhancer-promoter communication and dynamic gene transcription. Biochim Biophys Acta. 2012; 18-19: 1217–1227. DOI: 10.1016/j.bbagrm.2012.10.008.
175. Martin GE. Counting: The Art of Enumerative Combinatorics. Springer; 2001. 27–31, 153–160.
176. Messina DN, Glasscock J, Gish W, Lovett M. An ORFeome-based analysis of human transcription factor genes and the construction of a microarray to interrogate their expression. Genome Res. 2004; 14: 2041–2047. DOI: 10.1101/gr.2584104.
177. Mikkelsen TS, Ku M, Jaffe DB, Issac B, Lieberman E, Giannoukos G, Alvarez P, Brockman W, Kim TK, Koche RP, Lee W, Mendenhall E, O'Donovan A, Presser A, Russ C, Xie X, Meissner A, Wernig M, Jaenisch R, Nusbaum C, Lander ES, Bernstein BE. Genome-wide maps of chromatin state in pluripotent and lineage-committed cells. Nature. 2007; 448: 553–560. DOI: 10.1038/nature06008.
178. Min H, Danilenko DM, Scully SA, Bolon B, Ring BD, Tarpley JE, DeRose M, Simonet WS. Fgf-10 is required for both limb and lung development and exhibits striking functional similarity to Drosophila branchless. Genes Dev. 1998; 12: 3156–3161. DOI: 10.1101/gad.12.20.3156.
179. Moignard V, Woodhouse S, Haghverdi L, Lilly AJ, Tanaka Y, Wilkinson AC, Buettner F, Macaulay IC, Jawaid W, Diamanti E, Nishikawa SI, Piterman N, Kouskoff V, Theis FJ, Fisher J, Göttgens B. Decoding the regulatory network of early blood development from single-cell gene expression measurements. Nat Biotechnol. 2015; 33: 269–276. DOI: 10.1038/nbt.3154.
180. Moody SA. Fates of the blastomeres of the 32-cell-stage Xenopus embryo. Dev Biol. 1987; 122: 300–319. DOI: 10.1016/0012-1606(87)90296-X.

181. Moon TS, Lou C, Tamsir A, Stanton BC, Voigt CA. Genetic programs constructed from layered logic gates in single cells. Nature. 2012; 491: 249–253. DOI: 10.1038/nature11516.
182. Moris N, Pina C, Arias AM. Transition states and cell fate decisions in epigenetic landscapes. Nat Rev Genet. 2016; 17: 693–703. DOI: 10.1038/nrg.2016.9.
183. Moro SI, Tolboom M, Khayat PS, Roelfsema PR. Neuronal activity in the visual cortex reveals the temporal order of cognitive operations. J Neurosci. 2010; 30: 16293–16303. DOI: 10.1523/JNEUROSCI.1256-10.2010.
184. Mossman D, Kim KT, Scott RJ. Demethylation by 5-aza-2'-deoxycytidine in colorectal cancer cells targets genomic DNA whilst promoter CpG island methylation persists. BMC Cancer. 2010; 10. DOI: 10.1186/1471-2407-10-366.
185. Motegi F, Zonies S, Hao Y, Cuenca AA, Griffin E, Seydoux G. Microtubules induce self-organization of polarized PAR domains in Caenorhabditis elegans zygotes. Nat Cell Biol. 2011; 13: 1361–1367. DOI: 10.1038/ncb2354.
186. Mtango NR, Latham KE. Differential expression of cell cycle genes in rhesus monkey oocytes and embryos of different developmental potentials. Biol Reprod. 2008; 78: 254–266. DOI: 10.1095/biolreprod.107.064931.
187. Muñoz JJ, Barrett K, Miodownik M. A deformation gradient decomposition method for the analysis of the mechanics of morphogenesis. J Biomech. 2007; 40: 1372–1380. DOI: 10.1016/j.jbiomech.2006.05.006.
188. Munro E, Nance J, Priess JR. Cortical flows powered by asymmetrical contraction transport PAR proteins to establish and maintain anterior-posterior polarity in the early C. elegans embryo. Dev Cell. 2004; 7: 413–424. DOI: 10.1016/j.devcel.2004.08.001.
189. Murphy KF, Balázsi G, Collins JJ. Combinatorial promoter design for engineering noisy gene expression. Proc Natl Acad Sci U S A. 2007; 104: 12726–12731. DOI: 10.1073/pnas.0608451104.
190. Murray RM, Sastry SS. Nonholonomic motion planning: steering using sinusoids. IEEE Transactions on Automatic Control. 1993; 38: 700–716. DOI: 10.1109/9.277235.
191. Naganathan SR, Fürthauer S, Nishikawa M, Jülicher F, Grill SW. Active torque generation by the actomyosin cell cortex drives left-right symmetry breaking. eLife. 2014; 3: e04165. DOI: 10.7554/eLife.04165.
192. Nagano T, Lubling Y, Stevens TJ, Schoenfelder S, Yaffe E, Dean W, Laue ED, Tanay A, Fraser P. Single-cell Hi-C reveals cell-to-cell variability in chromosome structure. Nature. 2013; 502: 59–64. DOI: 10.1038/nature12593.
193. Nelson DE, Ihekwaba AE, Elliott M, Johnson JR, Gibney CA, Foreman BE, Nelson G, See V, Horton CA, Spiller DG, Edwards SW, McDowell HP, Unitt JF, Sullivan E, Grimley R, Benson N, Broomhead D, Kell DB, White MR. Oscillations in NF-$\varkappa$B signaling control the dynamics of gene expression. Science. 2004; 306: 704–708. DOI: 10.1126/science.1099962.

194. Nené NR, Garca-Ojalvo J, Zaikin A. Speed-dependent cellular decision making in nonequilibrium genetic circuits. PLoS One. 2012; 7: e32779. DOI: 10.1371/journal.pone.0032779.
195. Neph S, Stergachis AB, Reynolds A, Sandstrom R, Borenstein E, Stamatoyannopoulos J. Circuitry and dynamics of human transcription factor regulatory networks. Cell. 2012; 150: 1274–1286. DOI: 10.1016/j.cell.2012.04.040.
196. Neukirch S, van der Heijden GHM, Thompson JMT. Writhing instabilities of twisted rods: From infinite to finite length. J Mech Phys Solids. 2002; 50: 1175–1191. DOI: 10.1016/S0022-5096(01)00130-2.
197. Nonaka S, Shiratori H, Saijoh Y, Hamada H. Determination of left-right patterning of the mouse embryo by artificial nodal flow. Nature. 2002; 418: 96–99. DOI: 10.1038/nature00849.
198. Noordermeer D, de Wit E, Klous P, van de Werken H, Simonis M, Lopez-Jones M, Eussen B, Klein A, Singer RH, de Laat W. Variegated gene expression caused by cell-specific long-range DNA interactions. Nat Cell Biol. 2011; 13: 944–951. DOI: 10.1038/ncb2278.
199. O'Keefe DD, Thomas SR, Bolin K, Griggs E, Edgar BA, Buttitta LA. Combinatorial control of temporal gene expression in the Drosophila wing by enhancers and core promoters. BMC Genomics. 2012; 13. DOI: 10.1186/1471-2164-13-498.
200. O'Reilly OM. Modeling Nonlinear Problems in the Mechanics of Strings and Rods: The Role of the Balance Laws. Vol. 60. Interaction of Mechanics and Mathematics. Springer Nature; 2017. Chap. 1,3-5.
201. Ohnishi Y, Huber W, Tsumura A, Kang M, Xenopoulos P, Kurimoto K, Oleś AK, Araúzo-Bravo MJ, Saitou M, Hadjantonakis AK, Hiiragi T. Cell-to-cell expression variability followed by signal reinforcement progressively segregates early mouse lineages. Nat Cell Biol. 2014; 16: 27–37. DOI: 10.1038/ncb2881.
202. Okabe N, Xu B, Burdine RD. Fluid dynamics in zebrafish Kupffer's vesicle. Dev Dyn. 2008; 237: 3602–3612. DOI: 10.1002/dvdy.21730.
203. Olsson A, Venkatasubramanian M, Chaudhri VK, Aronow BJ, Salomonis N, Singh H, Grimes HL. Single-cell analysis of mixed-lineage states leading to a binary cell fate choice. Nature. 2016; 537: 698–702. DOI: 10.1038/nature19348.
204. Oppenheim RW. Naturally occurring cell death during neural development. Trends Neurosci. 2005; 8: 487–493. DOI: 10.1016/0166-2236(85)90175-4.
205. Pagán-Westphal SM, Tabin CJ. The transfer of left-right positional information during chick embryogenesis. Cell. 1998; 93: 25–35. DOI: 10.1016/S0092-8674(00)81143-5.
206. Palau-Ortin D, Formosa-Jordan P, Sancho JM, Ibañes M. Pattern selection by dynamical biochemical signals. Biophys J. 2015; 108: 1555–1565. DOI: 10.1016/j.bpj.2014.12.058.

207. Paul F, Arkin Y, Giladi A, Kenigsberg DAJE, Keren-Shaul H, Winter D, Lara-Astiaso D, Gury M, Weiner A, David E, Cohen N, Lauridsen FK, Haas S, Schlitzer A, Mildner A, Ginhoux F, Jung S, Trumpp A, Porse BT, Tanay A, Amit I. Transcriptional Heterogeneity and Lineage Commitment in Myeloid Progenitors. Cell. 2015; 16: 1663–1677. DOI: 10.1016/j.cell.2015.11.013.
208. Paulsen M, Legewie S, Eils R, Karaulanov E, Niehrs C. Negative feedback in the bone morphogenetic protein 4 (BMP4) synexpression group governs its dynamic signaling range and canalizes development. Proc Natl Acad Sci U S A. 2011; 108: 10202–10207. DOI: 10.1073/pnas.1100179108.
209. Payne JL, Wagner A. Constraint and contingency in multifunctional gene regulatory circuits. PLoS Comput Biol. 2013; 9: e1003071. DOI: 10.1371/journal.pcbi.1003071.
210. Perea-Gomez A, Camus A, Moreau A, Grieve K, Moneron G, Dubois A, Cibert C, Collignon J. Initiation of gastrulation in the mouse embryo is preceded by an apparent shift in the orientation of the anterior-posterior axis. Curr Biol. 2004; 14: 197–207. DOI: 10.1016/j.cub.2004.01.030.
211. Peric-Hupkes D, Meuleman W, Pagie L, Bruggeman SW, Solovei I, Brugman W, Gräf S, Flicek P, Kerkhoven RM, van Lohuizen M, Reinders M, Wessels L, van Steensel B. Molecular maps of the reorganization of genome-nuclear lamina interactions during differentiation. Mol Cell. 2010; 38: 603–613. DOI: 10.1016/j.molcel.2010.03.016.
212. Peter IS, Faure E, Davidson EH. Predictive computation of genomic logic processing functions in embryonic development. Proc Natl Acad Sci U S A. 2012; 109: 16434–16442. DOI: 10.1073/pnas.1207852109.
213. Petkova MD, Little SC, Liu F, Gregor T. Maternal origins of developmental reproducibility. Curr Biol. 2014; 24: 1283–1288. DOI: 10.1016/j.cub.2014.04.028.
214. Petkova MD, Tkačik G, Bialek W, Wieschaus EF, Gregor T. Optimal decoding of information from a genetic network. ArXiv e-prints. 2016; arXiv: 1612.08084 [q-bio.MN].
215. Pfeiffer A, Shi H, Tepperman JM, Zhang Y, Quail PH. Combinatorial complexity in a transcriptionally centered signaling hub in Arabidopsis. Mol Plant. 2014; 7: 1598–1618. DOI: 10.1093/mp/ssu087.
216. Picco V, Hudson C, Yasuo H. Ephrin-Eph signalling drives the asymmetric division of notochord/neural precursors in Ciona embryos. Development. 2007; 134: 1491–1497. DOI: 10.1242/dev.003939.
217. Pina C, Fugazza C, Tipping AJ, Brown J, Soneji S, Teles J, Peterson C, Enver T. Inferring rules of lineage commitment in haematopoiesis. Nat Cell Biol. 2012; 14: 287–294. DOI: 10.1038/ncb2442.
218. Pogorelov AV. Differential Geometry. Trans. by LF Boron. P Noordhoff N.V.; 1967. Chap. 1-3.
219. Pronk CJ, Rossi DJ, Månsson R, Attema JL, Norddahl GL, Chan CK, Sigvardsson M, Weissman IL, Bryder D. Elucidation of the phenotypic, functional, and molecular topography of a myeloerythroid progenitor cell hierar-

chy. Cell Stem Cell. 2007; 1: 428–442. DOI: 10.1016/j.stem.2007.07.005.

220. Qi Y, Fan P, Hao Y, Han B, Fang Y, Feng M, Cui Z, Li J. Phosphoproteomic analysis of protein phosphorylation networks in the hypopharyngeal gland of honeybee workers (Apis mellifera ligustica). J Proteome Res. 2015; 14: 4647–4661. DOI: 10.1021/acs.jproteome.5b00530.
221. Raharjo I, Gaudet J. Gland-specific expression of C. elegans hlh-6 requires the combinatorial action of three distinct promoter elements. Dev Biol. 2007; 302: 295–308. DOI: 10.1016/j.ydbio.2006.09.036.
222. Raitu T. The motion of the free *n*-dimensional rigid body. Indiana University Mathematics Journal. 1980; 29: 609–629. DOI: 10.1512/iumj.1980.29.29046.
223. Rao CV. Expanding the synthetic biology toolbox: engineering orthogonal regulators of gene expression. Curr Opin Biotechnol. 2012; 23: 689–694. DOI: 10.1016/j.copbio.2011.12.015.
224. Rätzel V, Marwan M. Gene expression kinetics in individual plasmodial cells reveal alternative programs of differential regulation during commitment and differentiation. Dev Growth Differ. 2015; 57: 408–420. DOI: 10.1111/dgd.12220.
225. Remányi A, Schöler HR, Wilmanns M. Combinatorial control of plant gene expression. Nat Struct Mol Biol. 2004; 11: 812–815. DOI: 10.1038/nsmb820.
226. Rhee DY, Cho DY, Zhai B, Slattery M, Ma L, Mintseris J, Wong CY, White KP, Celniker SE, Przytycka TM, Gygi SP, Obar RA, Artavanis-Tsakonas S. Transcription factor networks in Drosophila melanogaster. Cell Rep. 2014; 8: 2031–2043. DOI: 10.1016/j.celrep.2014.08.038.
227. Rivera-Pérez JA, Mager J, Magnuson T. Dynamic morphogenetic events characterize the mouse visceral endoderm. Dev Biol. 2003; 261: 470–487. DOI: 10.1016/S0012-1606(03)00302-6.
228. Roach PJ. Multisite and hierarchal protein phosphorylation. J Biol Chem. 1991; 266: 14139–14141.
229. Romero PA, Arnold FH. Exploring protein fitness landscapes by directed evolution. Nat Rev Mol Cell Biol. 2008; 10: 866–876. DOI: 10.1038/nrm2805.
230. Rosensteel G. Dynamical Symmetry of Rotating Many-Body Systems from Galaxies to Nuclei. In: Proceedings of the International Conference on Many-body Physics, 339–350.
231. Routh EJ. The Advanced Part of a Treatise on the Dynamics of a System of Rigid Bodies. MacMillan and Co.; 1905. Chap. I.
232. Sacco F, Perfetto L, Castagnoli L, Cesareni G. The human phosphatase interactome: An intricate family portrait. FEBS Lett. 2012; 586: 2732–2739. DOI: 10.1016/j.febslet.2012.05.008.
233. Sanson B. Generating patterns from fields of cells. Examples from Drosophila segmentation. EMBO Rep. 2001; 2: 1083–1088. DOI: 10.1093/embo-reports/kve255.

234. Sasaki T, Minamisawa G, Takahashi N, Matsuki N, Ikegaya Y. Reverse optical trawling for synaptic connections in situ. J Neurophysiol. 209; 102: 636–643. DOI: 10.1152/jn.00012.2009.
235. Savin T, Kurpios NA, Shyer AE, Florescu P, Liang H, Mahadevan L, Tabin CJ. On the growth and form of the gut. Nature. 2011; 476: 57–62. DOI: 10.1038/nature10277.
236. Sayegh CE, Jhunjhunwala S, Riblet R, Murre C. Visualization of looping involving the immunoglobulin heavy-chain locus in developing B cells. Genes Dev. 2005; 19: 322–327. DOI: 10.1101/gad.1254305.
237. Sayut DJ, Niu Y, Sun L. Construction and Enhancement of a Minimal Genetic AND Logic Gate. Appl Environ Microbiol. 2010; 75: 637–642. DOI: 10.1128/AEM.01684-08.
238. Schiebinger G, Shu J, Tabaka M, Cleary B, Subramanian V, Solomon A, Liu S, Lin S, Berube P, Lee L, Chen J, Brumbaugh J, Rigollet P, Hochedlinger K, Jaenisch R, Regev A, Lander E. Reconstruction of developmental landscapes by optimal-transport analysis of single-cell gene expression sheds light on cellular reprogramming. bioRxiv. 2017; DOI: 10.1101/191056.
239. Schilstra MJ, Nehaniv CL. Bio-logic: gene expression and the laws of combinatorial logic. Artif Life. 2008; 14: 121–133. DOI: 10.1162/artl.2008.14.1.121.
240. Schmidt B, Marrone DF, Markus EJ. Genomic antagonism between retinoic acid and estrogen signaling in breast cancer. Behav Brain Res. 2012; 226: 56–65. DOI: 10.1016/j.bbr.2011.08.039.
241. Schoenfelder S, Sexton T, Chakalova L, Cope NF, Horton A, Andrews S, Kurukuti S, Mitchell JA, Umlauf D, Dimitrova DS, Eskiw CH, Luo Y, Wei CL, Ruan Y, Bieker JJ, Fraser P. Preferential associations between co-regulated genes reveal a transcriptional interactome in erythroid cells. Nat Genet. 2010; 42: 53–61. DOI: 10.1038/ng.496.
242. Sechler ES. Elasticity in Engineering. Dover Publications, Inc.; 1968. Chap. 2.
243. Segel LA, Handelman GH. Mathematics Applied to Continuum Mechanics. Dover Publications, Inc.; 1987. Chap. 4,5.
244. Shah S, Lubeck E, Zhou W, Cai L. In Situ Transcription Profiling of Single Cells Reveals Spatial Organization of Cells in the Mouse Hippocampus. Neuron. 2016; 92: 342–357. DOI: 10.1016/j.neuron.2016.10.001.
245. Sharifi-Zarchi A, Totonchi M, Khaloughi K, Karamzadeh R, Araúzo-Bravo MJ, Baharvand H, Tusserkani R, Pezeshk H, Chitsaz H, Sadeghi M. Increased robustness of early embryogenesis through collective decision-making by key transcription factors. BMC Syst Biol. 2015; 9. DOI: 10.1186/s12918-015-0169-8.
246. Shea MA, Ackers GK. The OR control system of bacteriophage lambda. A physical-chemical model for gene regulation. J Mol Biol. 1985; 181: 211–230. DOI: 10.1016/0022-2836(85)90086-5.
247. Shi J, Chen Q, Li X, Zheng X, Zhang Y, Qiao J, Tang F, Tao Y, Zhou Q, Duan E. Dynamic transcriptional symmetry-breaking in pre-implantation

mammalian embryo development revealed by single-cell RNA-seq. Development. 2015; 142: 3468–3477. DOI: 10.1242/dev.123950.

248. Shi Y, Hearst JE. The Kirchhoff elastic rod, the nonlinear Schrödinger equation, and DNA supercoiling. J Chem Phys. 1994; 101: 5186–5200. DOI: 10.1063/1.468506.
249. Shifley ET, Kenny AP, Rankin SA, Zorn AM. Prolonged FGF signaling is necessary for lung and liver induction in *Xenopus*. BMC Dev Biol. 2012; 6. DOI: 10.1186/1471-213X-12-27.
250. Shoval O, Sheftel H, Shinar G, Hart Y, Ramote O, Mayo A, Dekel E, Kavanagh K, Alon U. Evolutionary trade-offs, Pareto optimality, and the geometry of phenotype space. Science. 2012; 336: 1157–1160. DOI: 10.1126/science.1217405.
251. Simske JS, Kim SK. Sequential signalling during Caenorhabditis elegans vulval induction. Nature. 1995; 375: 142–146. DOI: 10.1038/375142a0.
252. Singh AM, Hamazaki T, Hankowski KE, Terada N. A heterogeneous expression pattern for Nanog in embryonic stem cells. Stem Cells. 2007; 25: 2534–2542. DOI: 10.1634/stemcells.2007-0126.
253. Siuti P, Yazbek J, Lu TK. Synthetic circuits integrating logic and memory in living cells. Nat Biotechnol. 2013; 31: 448–452. DOI: 10.1038/nbt.2510.
254. Soulé C. Graphic Requirements for Multistationarity. ComPlexUs. 2003; 1: 123–133. DOI: 10.1159/000076100.
255. Spivak M. A Comprehensive Introduction to Differential Geometry. Publish or Perish, Inc.; 1994. Chap. 4,5,7.
256. Splinter E, Heath H, Kooren J, Palstra RJ, Klous P, Grosveld F, Galjart N, de Laat W. CTCF mediates long-range chromatin looping and local histone modification in the β-globin locus. Genes Dev. 2006; 20: 2349–2354. DOI: 10.1101/gad.399506.
257. St Johnston D, Nüsslein-Volhard C. The origin of pattern and polarity in the Drosophila embryo. Cell. 1992; 68: 201–219. DOI: 10.1016/0092-8674(92)90466-P.
258. Sternberg S. Lie Algebras. Book online; 2004. 7–32. URL: Book%20online:%20www.math.harvard.edu/~shlomo.
259. Stolt CC, Lommes P, Sock E, Chaboissier M, Schedl A, Wegner M. The Sox9 transcription factor determines glial fate choice in the developing spinal cord. Genes Dev. 2003; 17: 1677–1689. DOI: 10.1101/gad.259003.
260. Sugimori M, Nagao M, Bertrand N, Parras CM, Guillemot F, Nakafuku M. Combinatorial actions of patterning and HLH transcription factors in the spatiotemporal control of neurogenesis and gliogenesis in the developing spinal cord. Developmentl. 2007; 134: 1617–1629. DOI: 10.1242/dev.001255.
261. Sul JY, Wu CW, Zeng F, Jochems J, Lee MT, Kim TK, Peritz T, Buckley P, Cappelleri DJ, Maronski M, Kim M, Kumar V, Meaney D, Kim J, Eberwine J. Transcriptome transfer produces a predictable cellular phenotype. Proc Natl Acad Sci U S A. 2009; 106: 7624–7629. DOI: 10.1073/pnas.0902161106.

262. Sulston JE, Schierenberg E, White JG, Thomson JN. The embryonic cell lineage of the nematode Caenorhabditis elegans. Dev Biol. 1983; 100: 64–119. DOI: 10.1016/0012-1606(83)90201-4.
263. Suzuki M. On the convergence of exponential operators—the Zassenhaus formula, BCH formula and systematic approximants. Commun Math Phys. 1977; 57: 193–200. DOI: 10.1007/BF016141616.
264. Symes K, Smith JC. Gastrulation movements provide an early marker of mesoderm induction in Xenopus laevis. Development. 1987; 101: 339–349.
265. Takahashi K, Yamanaka S. Induction of pluripotent stem cells from mouse embryonic and adult fibroblast cultures by defined factors. Cell. 2006; 126: 663–676. DOI: 10.1016/j.cell.2006.07.024.
266. Tanaka Y, Okada Y, Hirokawa N. FGF-induced vesicular release of Sonic hedgehog and retinoic acid in leftward nodal flow is critical for left-right determination. Nature. 2005; 435: 172–177. DOI: 10.1038/nature03494.
267. Tanay A, Regev A, Shamir R. Conservation and evolvability in regulatory networks: the evolution of ribosomal regulation in yeast. Proc Natl Acad Sci U S A. 2005; 102: 7203–7206. DOI: 10.1073/pnas.0502521102.
268. Thomas R. Boolean formalization of genetic control circuits. J Theor Biol. 1973; 42: 563–585. DOI: 10.1016/0022-5193(73)90247-6.
269. Thompson JMT, Champneys AR. From Helix to Localized Writhing in the Torsional Post-Buckling of Elastic Rods. Proc R Soc Lond A. 1996; 452: 117–138. DOI: 10.1098/rspa.1996.0007.
270. Thomson M, Gunawardena J. Unlimited multistability in multisite phosphorylation systems. Nature. 2009; 460: 274–277. DOI: 10.1038/nature08102.
271. Thomson M, Liu SJ, Zou LN, Smith Z, Meissner A, Ramanathan S. Pluripotency factors in embryonic stem cells regulate differentiation into germ layers. Cell. 2011; 145: 875–889. DOI: 10.1016/j.cell.2011.05.017.
272. Timoshenko SP, Gere JM. Theory of Elastic Stability. McGraw-Hill Book Company; 1961. Chap. 1,2.
273. Treutlein B, Brownfield DG, Wu AR, Neff NF, Mantalas GL, Espinoza FH, Desai TJ, Krasnow MA, Quake SR. Reconstructing lineage hierarchies of the distal lung epithelium using single-cell RNA-seq. Nature. 2014; 509: 371–375. DOI: 10.1038/nature13173.
274. Tso WK. On the Motion of a Curved and Twisted Rod. Acta Mech. 1993; 13: 163–178. DOI: 10.1007/BF01586790.
275. Valentine JW, Collins AG, Porter Meyer C. Morphological complexity increase in metazoans. Paleobiology. 1994; 20: 131–142. DOI: 10.1017/S0094837300012641.
276. van den Brink SC, Baillie-Johnson P, Balayo T, Hadjantonakis AK, Nowotschin S, Turner DA, Arias AM. Symmetry breaking, germ layer specification and axial organisation in aggregates of mouse embryonic stem cells. Development. 2014; 141: 4231–4342. DOI: 10.1242/dev.113001.
277. van der Heijden GHM, Neukirch S, Goss VGA, Thompson JMT. Instability and self-contact phenomena in the writhing of clamped rods. Int J Mech Sci. 2003; 45: 161–196. DOI: 10.1016/S0020-7403(02)00183-2.

278. van der Heijden GHM, Thompson JMT. Helical and Localised Buckling in Twisted Rods: A Unified Analysis of the Symmetric Case. Nonlinear Dynamics. 2000; 21: 71–99. DOI: 10.1023/A:1008310425967.
279. Varjosalo M, Keskitalo S, Van Drogen A, Nurkkala H, Vichalkovski A, Aebersold R, Gstaiger M. The protein interaction landscape of the human CMGC kinase group. Cell Rep. 2013; 3: 1306–1320. DOI: 10.1016/j.celrep.2013.03.027.
280. Verzi MP, Hatzis P, Sulahian R, Philips J, Schuijers J, Shin H, Freed E, Lynch JP, Dang DT, Brown M, Clevers H, Liu XS, Shivdasani RA. TCF4 and CDX2, major transcription factors for intestinal function, converge on the same cis-regulatory regions. Proc Natl Acad Sci U S A. 2015; 107: 15157–15162. DOI: 10.1073/pnas.1003822107.
281. Vickaryous MK, Hall BK. Human cell type diversity, evolution, development, and classification with special reference to cells derived from the neural crest. Biol Rev Camb Philos Soc. 2006; 81: 425–455. DOI: 10.1017/S1464793106007068.
282. Vogel C, Chothia C. Protein Family Expansions and Biological Complexity. PLoS Comput Biol. 2006; 2: e48. DOI: 10.1371/journal.pcbi.0020048.
283. Vogelstein B, Kinzler KW. Cancer genes and the pathways they control. Nat Med. 2004; 10: 789–799. DOI: 10.1038/nm1087.
284. Voight CA. Genetic parts to program bacteria. Curr Opin Biotechnol. 2006; 23: 548–557. DOI: 10.1016/j.copbio.2006.09.001.
285. Vonica A, Brivanlou AH. The left-right axis is regulated by the interplay of Coco, Xnr1 and derrière in Xenopus embryos. Dev Biol. 2007; 303: 281–294. DOI: 10.1016/j.ydbio.2006.09.039.
286. Voss TC, Schiltz RL, Sung MH, Yen PM, Stamatoyannopoulos JA, Biddie SC, Johnson TA, Miranda TB, John S, Hager GL. Dynamic Exchange at Regulatory Elements during Chromatin Remodeling Underlies Assisted Loading Mechanism. Cell. 2011; 146: 544–554. DOI: 10.1016/j.cell.2011.07.006.
287. Wada N, Nohno T. Differential Response of Shh Expression Between Chick Forelimb and Hindlimb Buds by FGF-4. Dev Dyn. 2001; 221: 402–411. DOI: 10.1002/dvdy.1150.
288. Waddington CH. The cybernetics of development. In: The Strategy of the Genes. George Allen & Unwin Ltd.; 1957. 11–58.
289. Wang B, Kitney RI, Joly N, Buck M. Engineering modular and orthogonal genetic logic gates for robust digital-like synthetic biology. Nat Commun. 2011; 2. DOI: 10.1038/ncomms1516.
290. Wang J, Xu L, Wang E. Potential landscape and flux framework of nonequilibrium networks: robustness, dissipation, and coherence of biochemical oscillations. Proc Natl Acad Sci U S A. 2008; 105: 12271–12276. DOI: 10.1073/pnas.0800579105.
291. Wang J, Xu L, Wang E, Huang S. The potential landscape of genetic circuits imposes the arrow of time in stem cell differentiation. Biophys J. 2010; 99: 29–39. DOI: 10.1016/j.bpj.2010.03.058.

292. Wang X, Minasov G, Shoichet BK. Evolution of an Antibiotic Resistance Enzyme Constrained by Stability and Activity Trade-offs. J Mol Bio. 2002; 320: 85–95. DOI: 10.1016/S0022-2836(02)00400-X.
293. Wang Z, Oron E, Nelson B, Razis S, Ivanova N. Distinct lineage specification roles for NANOG, OCT4, and SOX2 in human embryonic stem cells. Cell Stem Cell. 2012; 10: 440–454. DOI: 10.1016/j.stem.2012.02.016.
294. Warmflash A, Sorre B, Etoc F, Siggia ED, Brivanlou AH. A method to recapitulate early embryonic spatial patterning in human embryonic stem cells. Nat Methods. 2014; 11: 847–854. DOI: 10.1038/nmeth.3016.
295. Weinreb C, Wolock S, Tusi BK, Socolovsky M, Klein AM. Fundamental limits on dynamic inference from single-cell snapshots. Proc Natl Acad Sci U S A. 2018; 115: E2467. DOI: 10.1073/pnas.1714723115.
296. Weiss EL. Column Buckling–An Elementary Example of A Bifurcation. In: Bifurcation Theory and Nonlinear Eigenvalue Problems. Ed. by JB Keller, S Antman, 1–16.
297. Wilcox RM. Exponential Operators and Parameter Differentiation in Quantum Physics. J Math Phys. 1967; 8: 962–982. DOI: 10.1063/1.1705306.
298. Wilson NK, Foster SD, Wang X, Knezevic K, Schütte J, Kaimakis P, Chilarska PM, Kinston S, Ouwehand WH, Dzierzak E, Pimanda JE, Bruijn MF de, Göttgens B. Combinatorial transcriptional control in blood stem/progenitor cells: genome-wide analysis of ten major transcriptional regulators. Cell Stem Cell. 2010; 7: 532–542. DOI: 10.1016/j.stem.2010.07.016.
299. Xu Z, Xing S, Shan Q, Gullicksrud JA, Bair TB, Du Y, Liu C, Xue HH. Cutting Edge: β-Catenin-Interacting Tcf1 Isoforms Are Essential for Thymocyte Survival but Dispensable for Thymic Maturation Transitions. J Immunol. 2005; 198: 3404–3409. DOI: 10.4049/jimmunol.1602139.
300. Yan L, Yang M, Guo H, Yang L, Wu J, Li R, Liu P, Lian Y, Zheng X, Yan Y, Huang J, Li M, Wu X, Wen L, Lao K, Li R, Qiao J, Tang F. Single-cell RNA-Seq profiling of human preimplantation embryos and embryonic stem cells. Nat Struct Mo Biol. 2013; 20: 1131–1139. DOI: 10.1038/nsmb.2660.
301. Yoshida M, Kijima M, Akita M, Beppu T. Potent and specific inhibition of mammalian histone deacetylase both in vivo and in vitro by trichostatin A. J Biol Chem. 1990; 265: 17174–17179.
302. Zajac EE. Stability of Two Planar Loop Elasticas. J Appl Mech. 1962; 29: 136–142. DOI: 10.1115/1.3636445.
303. Zeisel A, Muñoz-Manchado AB, Codeluppi S, Lönnerberg P, La Manno G, Juréus A, Marques S, Munguba H, He L, Betsholtz C, Rolny C, Castelo-Branco G, Hjerling-Leffler J, Linnarsson S. Cell types in the mouse cortex and hippocampus revealed by single-cell RNA-seq. Science. 2015; 347: 1138–1142. DOI: 10.1126/science.aaa1934.
304. Zeng F, Baldwin DA, Schultz RM. Transcript profiling during preimplantation mouse development. Dev Biol. 2004; 272: 483–496. DOI: 10.1016/j.ydbio.2004.05.018.

305. Zentner GE, Tesar PJ, Scacheri PC. Epigenetic signatures distinguish multiple classes of enhancers with distinct cellular functions. Genome Res. 2011; 21: 1273–1283. DOI: 10.1101/gr.122382.111.
306. Zernicka-Goetz M, Morris SA, Bruce AW. Making a firm decision: multi-faceted regulation of cell fate in the early mouse embryo. Nat Rev Genet. 2009; 10: 467–477. DOI: 10.1038/nrg2564.
307. Zhan J, Ding B, Ma R, Ma X, Su X, Zhao Y, Liu Z, Wu J, Liu H. Develop reusable and combinable designs for transcriptional logic gates. Mol Syst Biol. 2010; 6. DOI: 10.1038/msb.2010.42.
308. Zhou Q, Anderson DJ. The bHLH transcription factors OLIG2 and OLIG1 couple neuronal and glial subtype specification. Cell. 2002; 109: 61–73. DOI: 10.1016/S0092-8674(02)00677-3.
309. Zinzen RP, Girardot C, Gagneur J, Braun M, Furlong EE. Combinatorial binding predicts spatio-temporal cis-regulatory activity. Nature. 2009; 462: 65–70. DOI: 10.1038/nature08531.
310. Zullo JM, Demarco IA, Piqué-Regi R, Gaffney DJ, Epstein CB, Spooner CJ, Luperchio TR, Bernstein BE, Pritchard JK, Reddy KL, Singh H. DNA sequence-dependent compartmentalization and silencing of chromatin at the nuclear lamina. Cell. 2012; 149: 1474–1487. DOI: 10.1016/j.cell.2012.04.035.